UNIVERSITÄTSKLINIKUM HAMBURG-EPPENDORF

Klinik und Poliklinik für Neurologie

Prof. Dr. med. Götz Thomalla
Prof. Dr. med. Tim Magnus

Alterations of Brain Network Macro- and Microstructure in Vascular Cognitive Impairment

Dissertation

zur Erlangung des Doktorgrades PhD
an der Medizinischen Fakultät der Universität Hamburg.

vorgelegt von:

Dr. med. Marvin Petersen
aus Hofgeismar

Hamburg 2024

(wird von der Medizinischen Fakultät ausgefüllt)

Angenommen von der
Medizinischen Fakultät der Universität Hamburg am: 20.06.2025

Veröffentlicht mit Genehmigung der
Medizinischen Fakultät der Universität Hamburg.

Prüfungsausschuss, der/die Vorsitzende: Prof. Dr. Götz Thomalla

Prüfungsausschuss, zweite/r Gutachter/in: Prof. Dr. Simone Kühn

Prüfungsausschuss, dritte/r Gutachter/in: Prof. Dr. Petra Ritter

Table of contents

1 Synopsis

1.1 Thesis background and objectives

Vascular cognitive impairment (VCI) describes the spectrum of cognitive impairment due to vascular brain damage, ranging from subtle subclinical cognitive changes to manifest dementia.[1] This spectrum not only encompasses pure vascular disorders, such as vascular dementia due to cerebral small vessel disease and stroke, but also mixed forms involving coincident Alzheimer's disease or other pathologies.[2] VCI is driven by cerebrovascular and metabolic risk factors including obesity, arterial hypertension, dyslipidemia and insulin resistance.[1] How these risk factors contribute to VCI is intricate and remains not fully understood.

The most common clinical manifestations of VCI are impairment of executive functioning (e.g., in planning, organizing and monitoring behavior), reduced information processing speed as well as memory issues.[3] The symptom profile and severity of VCI are theorized to be shaped by the nature, size, and site of brain damage induced by vasculopathy.[4] Given that lifestyle and medical interventions can alter the progression of VCI, comprehending its impact on the brain is vital for effective prevention and management of related cognitive sequelae.

The development of reliable disease biomarkers is a key priority within the VCI research field as they are crucial for translating scientific advances into effective prevention and treatment strategies.[5,6] Magnetic resonance imaging (MRI) has been instrumental in this development, enabling the characterization of VCI-related structural brain changes including white matter hyperintensities of presumed vascular origin (WMH) visible on T2-weighted imaging, gray matter morphological changes quantifiable via brain morphometry, and the disruption of tissue microstructure which can be measured in diffusion-weighted imaging.[7] Despite this progress, considerable gaps in understanding persist. The role of brain structural changes in mediating the link between primary vascular damage and cognition remains to be understood.[8] Additionally, individual-level symptom prediction in VCI is still imprecise.[4] Moreover, since the onset of the pandemic, COVID-19 has been repeatedly associated with cerebrovascular disease as well as the development of cognitive impairment and dementia.[9] Still, it remains uncertain whether SARS-CoV-2 contributes to VCI pathophysiology.

Advanced neuroimaging targeting brain network macro- and microstructure provides a means to bridge these knowledge gaps. It represents a promising avenue towards biomarkers improving pathomechanistic understanding, as well as informing diagnostics and treatment strategies.[5] Therefore, this thesis encompasses three research projects that investigate macro-

and microstructural aspects of VCI leveraging multimodal neuroimaging, network neuroscience, and advanced statistical analyses.

Figure 1. Vascular cognitive impairment.

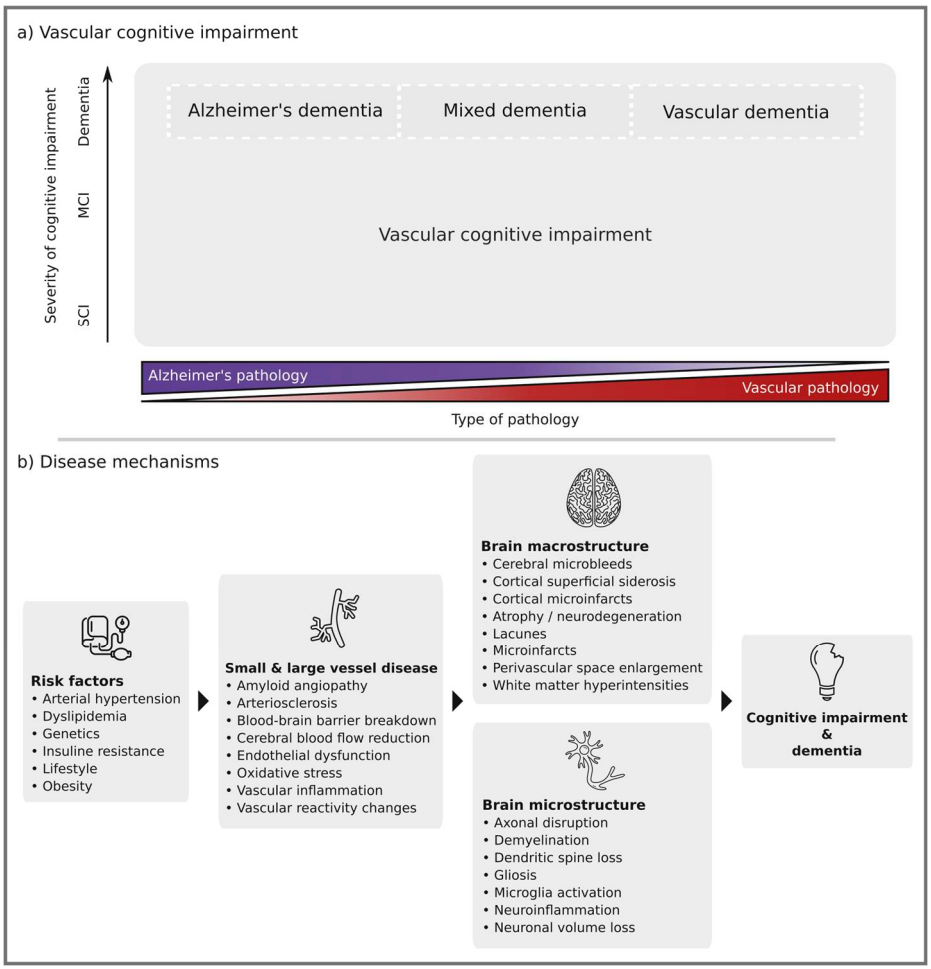

a) VCI encompasses a range of cognitive deficits linked to varying degrees of vascular pathology, including subjective cognitive impairment, mild cognitive impairment, and dementia. VCI can refer to a clinical syndrome caused solely by cerebrovascular pathology, known as vascular dementia, or a condition where cerebrovascular pathology contributes to cognitive decline to any extent, e.g., mixed dementia with joint vascular and Alzheimer's pathology. b) Disease mechanism model of VCI. Of note, the listed mechanisms are considered to interact relevantly, and the displayed order of cause and effect is tentative. Modified with permission from van der Flier et al.[2] *Abbreviations*: MCI – mild cognitive impairment, SCI – subjective cognitive impairment, VCI – vascular cognitive impairment.

Study A.[10] Brain atrophy is recognized as an imaging surrogate for VCI, but the specific morphological changes connecting vascular risk factors with cognition are unclear. The first presented study titled "A latent clinical-anatomical dimension relating metabolic syndrome to brain structure and cognition," published in *eLife* on December 7, 2023, investigated this issue.[10] We analyzed the relationship between metabolic syndrome (i.e., a joint vascular risk profile composed of obesity, arterial hypertension, dyslipidemia and insulin resistance), brain morphology, and cognitive function in 40,087 individuals from the UK Biobank and Hamburg City Health Study (HCHS), using multivariate statistics, imaging transcriptomics, and connectomics.

Study B.[11] WMH are key imaging indicators of VCI. However, the correlation between WMH volume and symptom severity is not consistent across individuals, with some exhibiting fewer symptoms despite extensive WMH and vice versa. Because of this clinical-radiological paradox, current individual-level predictions of cognitive impairment in VCI remain inaccurate. In our project "Enhancing Cognitive Performance Prediction through White Matter Hyperintensity Disconnectivity Assessment: A Multicenter Lesion Network Mapping Analysis of 3,485 Memory Clinic Patients" we posit that analyzing the regional network disconnection caused by WMH may provide biomarkers with superior predictive power than WMH volumes alone. Based on this hypothesis, we investigated lesion and cognitive data of 3,485 patients of 10 memory clinic cohorts within the Meta VCI Map Consortium, aiming to refine cognitive impairment predictions in VCI. The project has been published as a preprint at *medRxiv* and is under review at *BRAIN*.

Study C.[12] In April 2021, as this thesis commenced, the COVID-19 pandemic was profoundly impacting global societies. In response, we decided to examine long-term effects of SARS-CoV-2 on brain structure and cognition. This decision was particularly motivated by evidence that the virus adversely affects brain health through vasculopathy, which directly aligns with the focus of this thesis. Therefore, we examined neuroimaging and cognitive data of 223 individuals on average 10 months after their SARS-CoV-2 infection from the HCHS COVID Program. This work has been published in *PNAS* on May 23, 2023 and is titled "Brain imaging and neuropsychological assessment of individuals recovered from a mild to moderate SARS-CoV-2 infection".

The thesis is structured as follows: 1) a general overview over the investigated cohorts, MR preprocessing and applied analysis techniques; 2) background, methods, and results of the individual studies; 3) a general discussion section that interprets and contextualizes the collective findings of the thesis.

1.2 Methods overview

1.2.1 Study samples

The presented thesis examined demographic, cognitive and MRI data of four large-scale datasets, including the UK Biobank, HCHS (both study A), the Meta VCI Map Consortium (study B), and the HCHS COVID Program (study C). The participants of these studies cover the full severity spectrum of cognitive impairment from healthy, over subclinical changes and mild cognitive impairment to manifest dementia (***figure 2a***).

The UK Biobank study is a large-scale, prospective, population-based cohort study examining adults aged 45-80 to enhance the prevention, diagnosis, and treatment of various

serious illnesses.[13] It collects detailed lifestyle and clinical data, complemented by multimodal brain MRI and a computerized battery of cognitive tests covering domains of attention, executive function, processing speed, memory, and reasoning.[14] Neuroimaging is performed using Siemens Skyra 3T MRI scanners across four centers with identical software and hardware setups.

The HCHS is a prospective, population-based, single-center cohort study based in Hamburg, Germany, investigating adults aged 45-75 to enhance the detection of major chronic disease risks through extensive clinical and imaging phenotyping.[15] Cognitive functions are evaluated using an extended version of the Consortium to Establish a Registry for Alzheimer's Disease Neuropsychological Assessment Battery (CERAD-NP/Plus), which includes tests for general cognitive status, attention and executive function, processing speed, memory, reasoning and verbal fluency. A subset of participants, chosen partly at random and partly due to elevated vascular risk, receive multimodal brain MRI scans using a 3T Siemens Skyra.

The Meta VCI Map Consortium is a collaborative, multicenter initiative focused on studying vascular contributions to cognitive impairment through advanced neuroimaging and meta-analyses of lesion topography.[16] It pools data from patients of multiple memory clinic cohorts, spanning different stages of cognitive disease from subjective cognitive impairment to manifest dementia.[17] The cohorts consist of patients assessed at outpatient memory clinics for cognitive symptoms, undergoing MRI and cognitive evaluations. Patients with cognitive issues from non-vascular or non-neurodegenerative causes (e.g., alcohol abuse) or monogenic disorders (e.g., CADASIL) were excluded. Cognitive assessments, covering tests for attention and executive function, processing speed, memory and reasoning, were harmonized across cohorts.[17]

The HCHS COVID Program is a substudy of the HCHS. It enrolled individuals after a SARS-CoV-2 infection to study multi-organ, long-term effects of COVID-19 at the start of the pandemic.[18] Recruitment occurred between March 1 to December 31, 2020 with inclusion criteria being (1) a positive polymerase chain reaction (PCR) test for SARS-CoV-2 and (2) age between 45 and 74 at inclusion. Participants received the HCHS assessment, including cognitive testing and brain MRI, alongside a questionnaire on COVID-19-related information.

1.2.2 MRI preprocessing (all studies)

To mitigate the effects of acquisition artifacts, movement and physiological responses, MR images require preprocessing and quality assessment procedures. For the presented studies, we developed a software framework for MRI preprocessing implementing the latest advancements in neuroimaging. This framework unifies reproducible neuroimaging, facilitated data management and high-performance computing to meet the demands of the large-scale data analyses presented in this project. The corresponding code and pipeline documentation

can be found on GitHub (https://github.com/csi-hamburg/CSIframe). MR images were processed with this framework leveraging pre-configured and containerized pipelines. T1-weighted MR images were processed based on the Computational Anatomy Toolbox (CAT, version 12.7).[19] Diffusion-weighted MR images were preprocessed via QSIprep (version 0.14.2).[20]

1.2.3. Analysis techniques

We capitalized on a broad range of advanced neuroimaging and statistical techniques in this thesis. The following sections provide an overview about the analysis concepts to provide enough context for understanding the study summaries in the subsequent sections. The techniques are depicted in ***figure 2b***.

Brain morphometry (study A and C)

Brain morphometry refers to the quantitative study of macroscopic brain features. Morphometric measurements cover volume and cortical thickness, surface area, and the shape of various brain regions. These markers can provide insights into macrostructural disease effects like atrophy and neurodegenerative processes.[19]

Connectomics (study A and B)

The field of connectomics focuses on mapping and understanding the complex networks of neural connections within the brain.[21] It utilizes functional and structural neuroimaging methods to reconstruct wiring diagrams of the brain network, so called connectomes. Functional connectomes, commonly obtained from resting-state fMRI, map connections between brain regions by identifying correlated fluctuations of the blood oxygen level dependency (BOLD) signal. Structural connectomes are reconstructions of anatomical pathways, specifically white matter fiber tracts, based on streamline tractography from diffusion-weighted imaging.

Lesion network mapping (study B)

Lesion network mapping is a technique for identifying the brain circuits affected by lesions.[22] It involves overlaying lesion segmentations onto connectomes to measure the connection strength between brain regions and the lesion, thereby inferring the resulting disconnectivity. The employed connectomes are commonly derived from supplementary datasets of healthy adults to reduce bias by disease effects. There are two main types of lesion network mapping: functional lesion network mapping, using functional connectomes based on resting-state fMRI to quantify connections between regions and the lesion, and structural lesion network mapping, using structural connectomes based on streamline tractography from diffusion MRI.

Figure 2: Cohorts and applied analysis techniques.

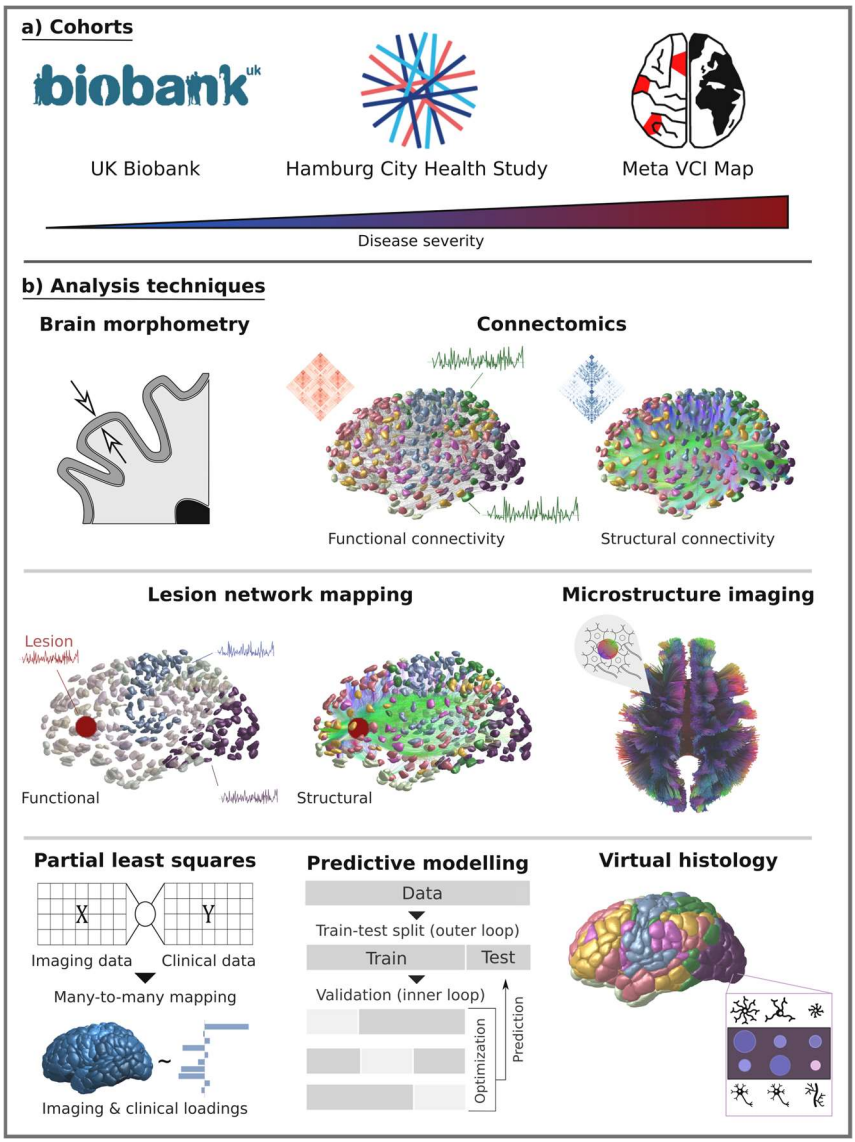

The thesis is based on data from the UK Biobank, the Hamburg City Health Study and the Meta VCI Map Consortium, which cover different parts of the severity spectrum in vascular cognitive impairment: normal population, normal population with elevated vascular risk, and memory clinic patients. Employed analysis techniques include brain morphometry, connectomics, lesion network mapping, microstructure imaging, partial least squares correlation analysis, predictive modelling and virtual histology.

Imaging of tissue microstructure: diffusion-tensor imaging, free-water imaging and fixel-based analysis (study C)

Beyond streamline tractography, diffusion MRI allows to assess microstructural integrity, i.e., microscale cellular and extracellular tissue organization. This thesis harnessed diffusion tensor imaging (DTI), free-water imaging, and fixel-based analysis to analyze the tissue microstructure of the white matter.[23–25] DTI leverages diffusion information to compute the mean diffusivity (MD) and fractional anisotropy (FA), reflecting water diffusion extent and directionality in neural tissue, respectively. Free-water imaging complements metrics on extracellular volume and tissue-specific diffusion directionality. Fixel-based analysis, employing a more complex diffusion model, provides insights into fiber-bundle density and cross-section at a sub-voxel level. Together, these approaches aid in detecting abnormalities in tissue microarchitecture such as demyelination, axonal damage, dendritic alterations, and inflammation.

Partial least squares correlation analysis (study A)

Partial least squares correlation analysis (PLS) is a data-driven, multivariate statistical technique designed to model and analyze the relationship between two sets of multivariable data domains, e.g., imaging data and clinical metrics.[26] This technique uncovers latent variables — i.e., unobservable underlying factors — that represent a many-to-many mapping between the input data domains. By identifying these latent variables, it reduces the dimensionality of the data while preserving the core information, making it easier to understand and interpret the relationship between two large and complex datasets.

Predictive modelling analysis (study B and C)

In neuroimaging research, predictive modelling is instrumental for assessing the predictive power of imaging biomarkers for unseen outcomes, a key property for improving diagnostic and therapeutic approaches.[27] To ensure robustness and generalizability, predictive models are trained through nested cross-validation on labelled data. Specifically, the dataset is split into multiple folds to enable training and validation across distinct segments resulting in reliable performance metrics. The splitting regimen involves an external loop for assessing model performance and an internal loop dedicated to choosing the optimal model and adjusting hyperparameters, thereby reducing overfitting and data leakage.[28]

Virtual histology (study A)

Virtual histology analysis represents a recently developed neuroimaging technique, combining high-resolution imaging transcriptomics data, such as that from the Allen Human Brain Atlas, with gene-cell assignments derived from single-cell sequencing techniques.[29] This integration enables the inference of regional cellular densities and distributions within the brain complementing traditional histological methods.

1.3. Study A: A latent clinical-anatomical dimension relating metabolic syndrome to brain structure and cognition

1.3.1 Background and aims

Metabolic syndrome (MetS), characterized by the joint presence of obesity, arterial hypertension, dyslipidemia, and insulin resistance, is a major etiological factor in VCI.[30] Recognizing that MetS is modifiable through lifestyle and pharmacological interventions highlights the importance of understanding its pathophysiological impact on brain structure to inform risk reduction and treatment strategies.

Despite previous structural neuroimaging studies suggesting altered gray matter morphology in MetS, several research gaps persist.[31] It is unclear if there is a specific pattern of brain

morphological differences in those at vascular risk, particularly whether MetS affects some brain regions more than others. The potential mediatory role of such brain structural differences in the link between MetS and cognitive performance is yet to be clarified. Additionally, the determinants of the interaction between MetS and brain structure remain incompletely understood. These uncertainties are compounded by the limitations of prior studies, such as small sample sizes, a focus on global rather than regional brain morphology, and the isolated examination of singular risk factors.[31,32]

Our study capitalized on cortical thickness and subcortical volume data from 40,087 participants of the UK Biobank and HCHS to investigate the relationship of MetS and brain morphology. We modelled the multivariable relationship between clinical risk factor measures and regional brain morphological measures using multivariate, data-driven statistics. Integrating cognitive assessments, we further investigated the mediation effect of brain structure on the relationship between MetS and cognitive function. Additionally, we explored cellular and brain network topological characteristics associated with MetS-related brain morphological abnormalities, aiming to deepen the understanding of the neurobiological underpinnings of MetS.

1.3.2 Methods and results

We analyzed cross-sectional clinical and imaging data from 40,087 individuals (mean age 63.55 ± 7.59; 46.47% female) of the UK Biobank and HCHS, free from neurological or psychiatric conditions. We processed T1-weighted MR images with the CAT12 pipeline, yielding measures of cortical thickness and subcortical volumes for regions defined by the Schaefer400x7 atlas and Melbourne Subcortical Atlas.[19,33,34] Regarding MetS-defining risk factors, clinical measurements included waist and hip circumferences, waist-hip ratio, body mass index (for obesity); systolic and diastolic blood pressures (for arterial hypertension); high-density lipoprotein, low-density lipoprotein, total cholesterol, triglycerides (for dyslipidemia); and HbA1c, non-fasting blood glucose (for insulin resistance). Investigated cognitive tests covered executive function and processing speed (Reaction Time, Symbol Digit Substitution, Tower Rearranging, Trail Making Test A and B), memory (Numeric Memory, Paired Associate Learning, Prospective Memory, Word List Recall), reasoning (Fluid Intelligence, Matrix Pattern Completion, Multiple Choice Vocabulary B), verbal fluency (Animal Naming), and visuospatial ability (Clock Drawing Test).[14] The analysis design is illustrated in ***figure A1***.

In our study, we addressed the data complexity of vascular risk factors and regional brain morphology by using partial least squares correlation analysis (PLS; ***figure A1a***), a statistical method well-suited for relating high-dimensional data of two domains.[26] Simplified, PLS acts

as a dual regression that yields interpretable loadings (like β coefficients in regression) for all input variables. The resulting two sets of loadings represent covariance profiles that capture the multivariate associative effects between the data domains. Put differently, the two sets of loadings provide a many-to-many mapping, capturing how the input data domains are linked, contrasting the many-to-one mapping provided by β coefficients in multiple regression. This approach facilitates the investigation of the link between MetS and brain structure within a unified model. The PLS was adjusted for age, sex, education, and cohort effects.

Figure A1: Methodology.[10]

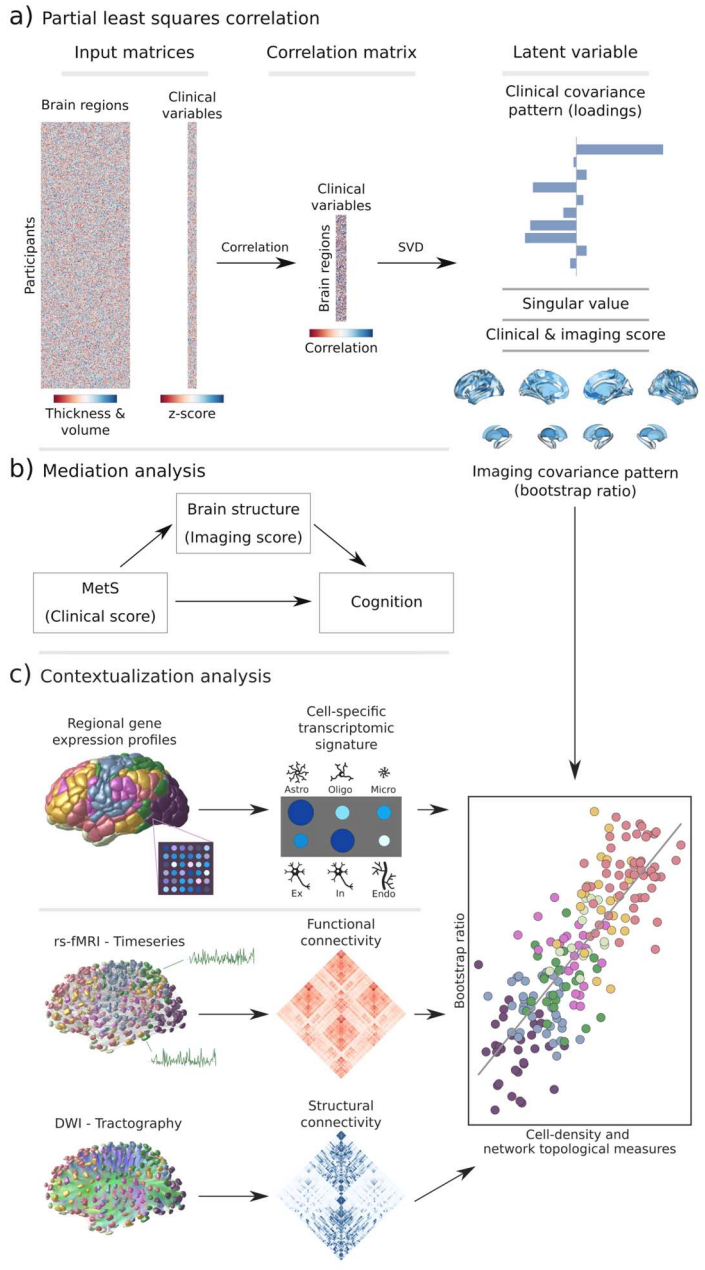

a) PLS was employed to relate multivariable datasets of MetS-defining vascular risk factors and regional brain morphology. PLS results in latent variables that represent clinical and imaging covariance profiles representing the multivariate associative effects within the input data. b) Mediation analysis was performed to investigate whether the imaging PLS score – capturing how strongly an individual expresses MetS-related brain morphological abnormalities – mediates the relationship between the clinical PLS score – representing MetS severity – and cognitive test outcomes. c) To explore pathomechanistic pathways linking MetS to brain structure, a contextualization analysis was performed. Spatial correlations between the PLS-derived imaging covariance profile (i.e., bootstrap ratio) and regional information on cell densities and brain network topology were performed. Adapted from Petersen et al.[35] *Abbreviations*: Astro – astrocytes, DWI – diffusion-weighted magnetic resonance imaging, Endo – endothelial cells, Ex – excitatory neuron populations (Ex1-8), In – inhibitory neuron populations (In1-8), Micro – microglia; Oligo – oligodendrocytes, PLS – partial least squares correlation analysis, rs-fMRI – resting-state functional MRI, SVD – singular value decomposition.

PLS revealed 8 significant latent variables capturing the multivariable associative effects between MetS and regional brain morphology. As the first latent variable explained the major

share of covariance (71%, ***figure A2a***), it was further investigated. The first latent variable encoded a positive link between MetS severity and brain morphological differences: higher MetS severity, i.e., higher degrees of obesity, hypertension, dyslipidemia, and insulin resistance (***figure A2d***), was associated to widespread brain morphological abnormalities (***figure A2d***). Specifically, higher MetS severity was linked to lower thickness and volume in the orbitofrontal, lateral prefrontal, insular, cingulate, temporal cortices and subcortical areas, alongside higher thickness in the superior frontal, parietal, and occipital regions. Among vascular risk factors, obesity measures contributed strongest to this relationship.

Figure A2: Partial least squares (PLS) correlation analysis results.[10]

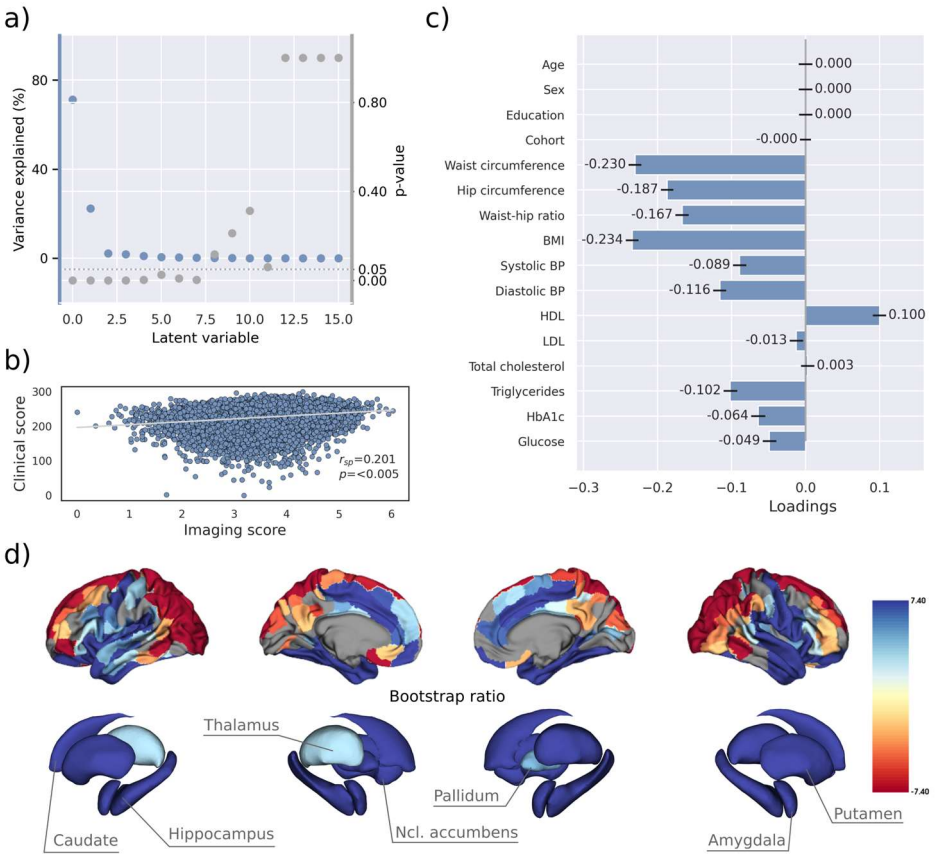

a) Explained shared variance (blue dots) and *p*-values (gray dots) of latent variables. b) Scatter plot illustrating the relationship between clinical and imaging PLS scores per subject, where higher scores reflect greater alignment with the respective identified covariance profile. c) Clinical covariance profile represented by clinical loadings, with 95% confidence intervals determined through bootstrap resampling. Prior adjustments for age, sex, education, and cohort differences were made. d) Imaging covariance profile represented by bootstrap ratio of imaging loadings. A high positive or negative bootstrap ratio indicates high contribution of a brain region to the overall covariance profile. Regions with a significant bootstrap ratio (> 1.96 or < -1.96) are highlighted by colors (blue - positive, red - negative). Abbreviations: r_{sp} - Spearman correlation coefficient.

Subsequently, we computed subject-specific PLS scores to quantify individual-level expression of the identified covariance profiles, with higher scores indicating stronger alignment with these profiles. Hence, PLS scores can be understood as factor scores in factor or principal component analysis. In our analysis, lower clinical scores denoted higher MetS severity, while lower imaging scores suggested stronger expression of the abovementioned brain morphological abnormalities. The scores were correlated (***figure A2b***), indicating that,

on the subject level, higher adherence to the imaging covariance profile (less brain morphological abnormalities) coincided with higher adherence to the clinical covariance profile (lower MetS severity), and vice versa. To investigate if brain structural differences mediate the link between MetS and cognitive function, we performed a mediation analysis. Therefore, we tested if the imaging PLS scores, reflecting expression of MetS-related brain morphological abnormalities, mediate the link between the clinical PLS score – capturing MetS severity – and cognitive performance. Our findings, detailed in ***figure A3***, revealed that imaging PLS scores fully mediated the link of clinical PLS scores on the performance of the Fluid Intelligence Test, Matrix Pattern Completion Test, and Trail Making Test B. Additionally, the associations between clinical PLS scores and the results of the Numeric Memory, Paired Associate Learning and Symbol Digit Substitution Tests were partially mediated.

To explore potential pathomechanisms linking MetS to brain structural changes, we integrated our findings with normative data on imaging transcriptomics and connectomics.[36,37] Specifically, we investigated whether MetS-associated brain morphological abnormalities, identified through PLS, spatially correlated with the regional density of certain cell populations and markers of brain network topology (***figure A1c***). Spatial correlations were performed via Spearman correlation of the respective brain maps. Significance was tested via null models accounting for the spatial autocorrelation between brain maps.[38–41]

Figure A3: Mediation analysis results.[10]

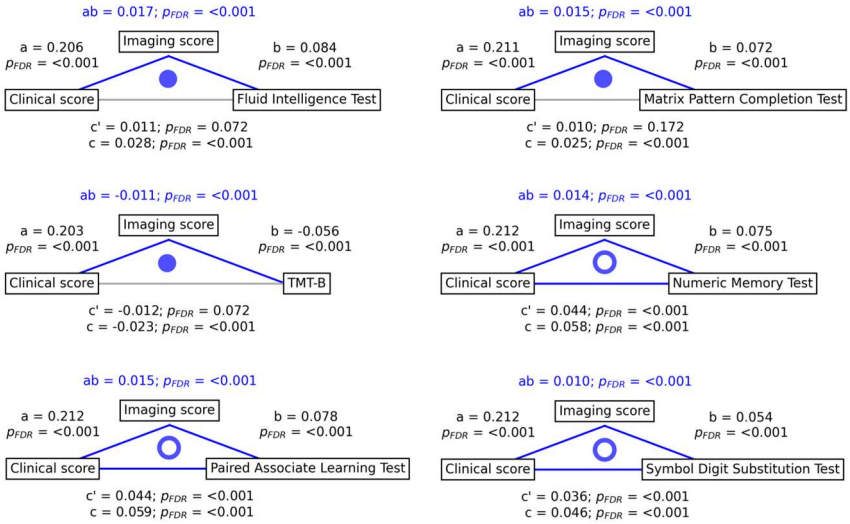

Path plots display the statistical relationships between clinical PLS scores, imaging PLS scores and cognitive test results. Presented are standardized effects and *p*-values for: (a) clinical to imaging scores, (b) imaging to cognitive test scores, (ab) the indirect effect, (c') the direct effect, and (c) the total effect. Significant pathways are marked in blue, with non-significant ones in light gray. A blue highlight on the text for ab signifies a significant indirect effect. A blue dot signifies mediation (significant indirect effect ab with a reduced or non-significant direct effect c' compared to the total effect c), with an empty dot representing partial mediation and a full dot full mediation. *Abbreviations*: p_{FDR} - false discovery rate-corrected *p*-values, PLS – partial least squares correlation, TMT-A – Trail Making Test A, TMT-B – Trail Making Test B.

First, we implemented a virtual histology approach to correlate the PLS-derived pattern of brain morphological abnormalities (i.e., bootstrap ratio map) with cell-type specific gene expression from the Allen Human Brain Atlas.[36] This technique allows to infer the regional density of specific cell populations by quantifying corresponding transcriptomic signatures. Our analysis showed significant positive correlations between the imaging covariance profile and the densities of endothelial cells, microglia, and excitatory neurons type 8, with these findings being consistent in sensitivity analyses. Thus, MetS-related brain morphological abnormalities were strongest in regions rich in these cell types (***figure A4a)***.

Second, we explored the relationship between the imaging covariance profile and brain network topology metrics, focusing, among others, on neighborhood abnormality measures derived from group consensus functional and structural connectomes of the Human Connectome Project. Neighborhood abnormality reflects the average of a cortical feature across a region's network neighborhood. We found a moderate positive correlation with functional neighborhood abnormality and a strong positive correlation with structural neighborhood abnormality, indicating that areas with similar MetS-related brain morphological abnormalities are highly functionally and structurally interconnected (***figure A4b)***.

Figure A4: Virtual histology and network contextualization analysis.[10]

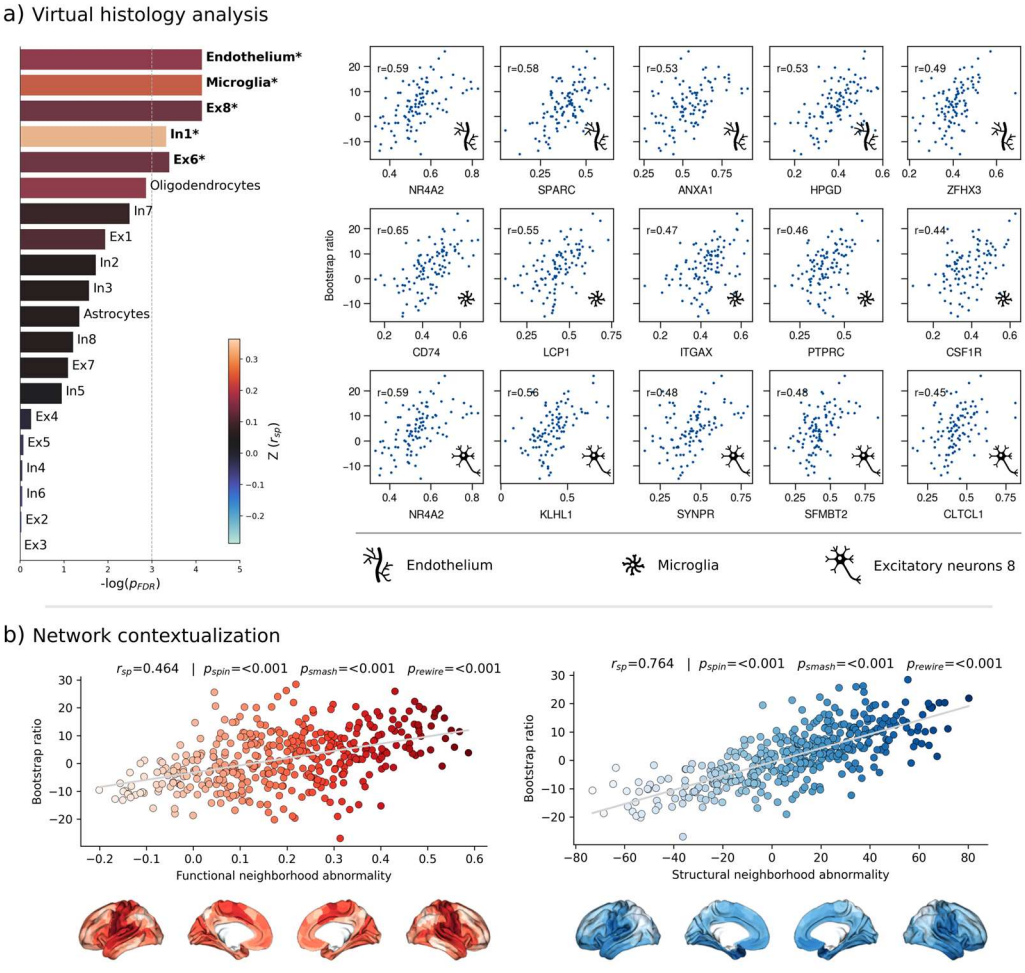

a) Virtual histology analysis. The regional correspondence between MetS-related brain morphological abnormalities (bootstrap ratio) and cell type-specific gene expression profiles was examined. Left: barplot displaying spatial correlation results. The bar width displays the significance level. Colors encode the aggregate z-transformed Spearman correlation coefficient relating the Schaefer-parcellated bootstrap ratio map and respective cell population densities. Asterisks indicate statistical significance. The significance threshold of p_{FDR}<.05 is highlighted by a vertical dashed line. Scatter plots show spatial correlations between MetS-related morphological abnormalities and specific cortical gene expressions in the endothelium, microglia, and excitatory neurons type 8, highlighting the top 5 correlating genes per cell type; cell types are identified by icons. b) Network contextualization analysis. Spatial correlation results derived from relating Schaefer-parcellated maps of MetS-related brain morphological abnormalities (bootstrap ratio) to the functional (red) and structural (blue) neighborhood abnormality. Scatter plots that illustrate the spatial relationship are supplemented by surface plots for anatomical localization. *Abbreviations*: $-log(p_{FDR})$ – negative logarithm of the false discovery rate-corrected *p*-value derived from spatial lag models[38], r_{sp} - Spearman correlation coefficient, p_{rewire} - *p*-value derived from network rewiring[40], p_{smash} - *p*-value derived from brainSMASH surrogates[41], p_{spin} - *p*-value derived from spin permutation results[39], $Z(r_{sp})$ – aggregate z-transformed Spearman correlation coefficient.

1.4. Study B: Enhancing Cognitive Performance Prediction through White Matter Hyperintensity Disconnectivity Assessment: A Multicenter Lesion Network Mapping Analysis of 3,485 Memory Clinic Patients

1.4.1 Background and aims

White matter hyperintensities of presumed vascular origin (WMH) are the signature imaging correlate of cerebral small vessel disease, and mark sites of white matter disconnection caused by microangiopathic axonal loss and demyelination.[42,43] Cerebral small vessel disease is considered the most frequent cause of VCI and relevantly contributes to mixed-type dementia.[1] Nonetheless, the pathomechanistic pathways connecting small vessel injury to clinical symptoms are not fully understood. Although considered a key imaging marker for evaluating cognitive health in at risk populations, WMH volume is not consistently linked to symptom severity across individuals: some individuals with extensive WMH exhibit few symptoms and vice versa.[4] Successful individual prediction of clinical impairment is, however, essential to patient care and for designing individualized therapeutic interventions in VCI.

Recent lesion-symptom inference analyses demonstrated an association between cognitive impairments and WMH located in strategic white matter regions, independent of total WMH volume.[17,44] Yet, these insights may not capture the full complexity of small vessel pathology-related cognitive impairment, which is thought to result from disruptions in the interactions of large-scale brain networks interconnecting cortical and subcortical gray matter areas through white matter tracts.[45] In recent years, advanced imaging analysis models have been developed to capture lesion impacts on brain circuitry.[46] Specifically, lesion network mapping (LNM) techniques map lesions onto brain network reconstructions to quantify a lesion's connectivity to different brain regions.[47] By that, it allows to infer which brain regions are disconnected by

the lesion. LNM has been shown to enhance symptom prediction in neurological disorders viewed as “disconnection syndromes”, including stroke and multiple sclerosis.[48,49]

In this study, we argued that clinical impairment due to WMH in VCI is relevantly explained by the strategic location of WMH and their impact on brain connectivity rather than their size. Therefore, we integrated LNM with WMH segmentations and cognitive data from 3485 memory clinic patients of the Meta VCI Map Consortium to test the following hypotheses: (1) LNM-informed markers surpass WMH volume-based metrics in predicting cognitive performance, and (2) WMH that contribute to cognitive impairment map to specific brain networks that determine their symptom profile.[16,17]

1.4.2 Methods and results

The methodological approach is illustrated in ***figure B1***. We analyzed cross-sectional data of 3,485 patients from 10 memory clinic cohorts in the Meta VCI Map Consortium (mean age 71.71 ± 8.87; 49.8% female), using WMH segmentations as well harmonized cognitive domain scores (z-scores) for attention / executive function, information processing speed, language and memory (***figure B1a)***. WMH segmentations were registered to the Montreal Neurological Institute standard space and integrated with normative functional and structural brain connectome data to perform LNM.[50,51] Employing LNM we quantified WMH disconnectivity across 480 atlas-based anatomical gray and white matter brain regions, resulting in regional functional LNM (fLNM) and structural LNM (sLNM) scores (***figure B1b)***.[52] A higher fLNM or sLNM score of a region suggests higher WMH-related disconnectivity of the region. A predictive modelling analysis was performed to compare the performance of demographic confounds (age, sex and education), WMH volume-based metrics, and LNM scores to predict cognitive domain scores. Subsequently, to investigate whether WMH-related disconnectivity of specific brain circuits links to cognitive performance, we performed a region of interest-level analysis linking cognitive domain scores to the regional LNM scores in a general linear model (***figure B1c***).

In the predictive modelling analysis, ridge regression models were optimized using repeated nested cross-validation (10 repetitions, 10 folds) to predict cognitive domain scores, evaluating model performance via Pearson correlation between predicted and actual scores. Models included age, sex, and education as baseline predictors. Prediction performance was compared via machine learning-adjusted t-tests of Pearson correlations.[53] The analysis compared six feature sets: (1) demographic confounds (age, sex, education), (2) total WMH volume with confounds, (3) regional WMH volumes within 64 white matter tracts of the HCP1065 atlas with confounds, (4) regional fLNM scores with confounds, (5) regional sLNM scores with confounds, and (6) combined regional fLNM and sLNM scores with confounds.

Figure B1. Methodology.[11]

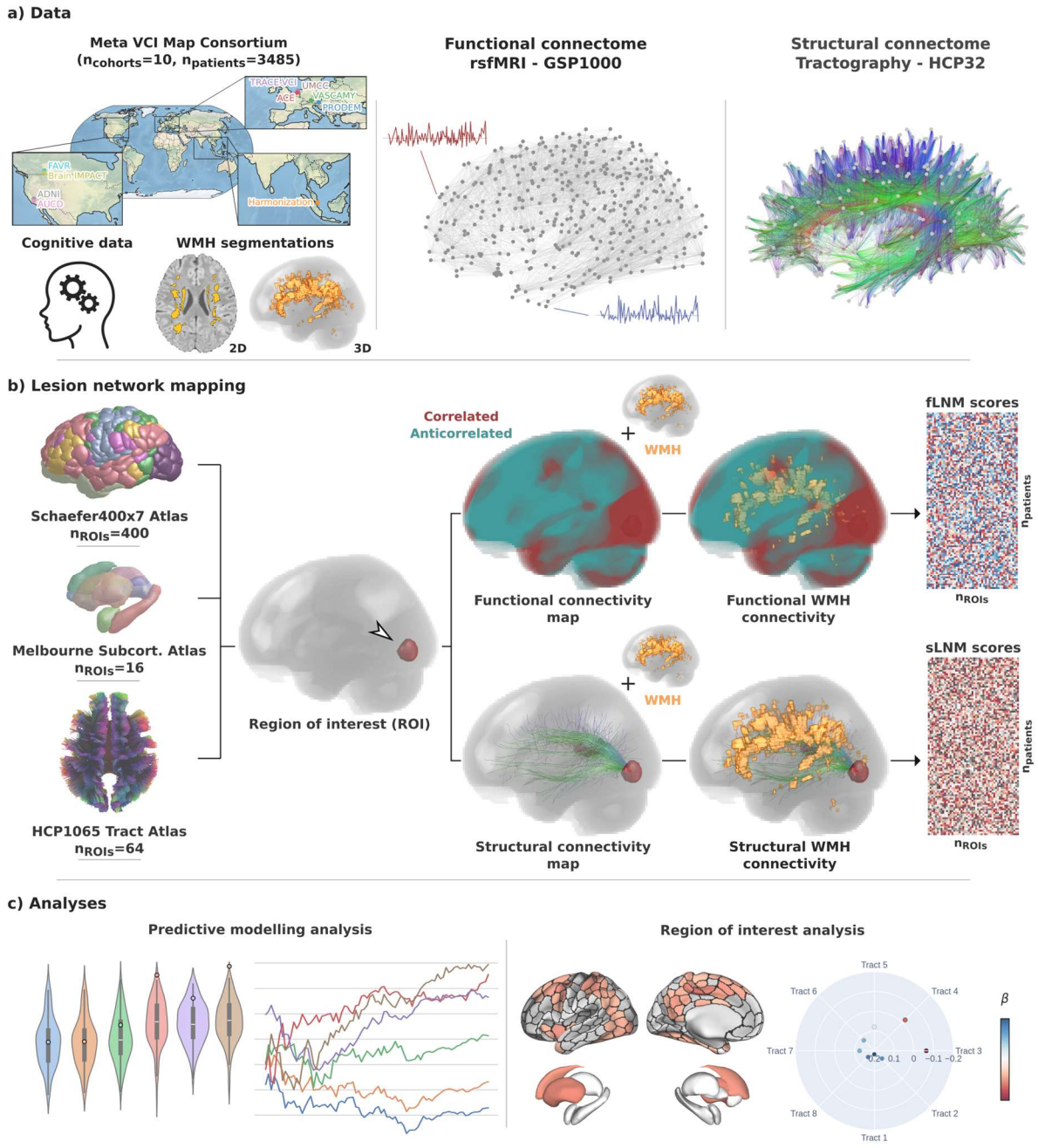

a) Harmonized cognitive domain scores and WMH segmentations from 10 memory clinic cohorts of the Meta VCI Map Consortium were used. To perform functional lesion network mapping, we used the GSP1000 normative functional connectome, which includes resting-state fMRI data from 1,000 healthy participants of the Genomic Superstruct Project.[50] For structural lesion network mapping, the HCP32 normative structural connectome was employed, based on diffusion-weighted imaging from 32 healthy Human Connectome Project participants, representing fibre-bundle architecture.[51] b) We conducted LNM to assess both functional and structural connections of WMHs to multiple ROIs, including the cortical Schaefer400x7 atlas, the Melbourne Subcortical Atlas, and the HCP1065 atlas of predefined white matter tracts. First, voxel-level connectivity maps were generated for each ROI, based on resting-state BOLD correlations or anatomical connections through tractography, respectively. These maps encoded in each voxel the functional or structural connectivity to the respective region of interest, i.e., the Pearson correlation between the resting-state BOLD timeseries of voxel and ROI or the number of streamlines connecting the voxel and the ROI. Next, ROI-specific lesion network mapping scores were

calculated by averaging voxel-level functional or structural connectivity indices within WMH masks. For the functional lesion network mapping scores, only positive Pearson correlations were considered. This resulted in matrices of functional and structural lesion network mapping (fLNM and sLNM) scores for each patient across ROIs (n_{ROIs} x $n_{patients}$). The matrices shown in the figure contain only random data for illustration purposes. c) In a predictive modelling analysis, the LNM scores were used to predict cognitive domain scores. In addition, a region of interest analysis was performed to identify regions in which LNM scores and cognitive domain performance were significantly associated. *Abbreviations*: fLNM – functional lesion network mapping, GSP – Genomic Superstruct Project, HCP – Human Connectome Project, ROI – region of interest, rsfMRI – resting-state functional magnetic resonance imaging, sLNM – structural lesion network mapping, WMH – white matter hyperintensities of presumed vascular origin.

The corresponding results are visualized in ***figure B2***. LNM-based models significantly surpassed the performance of those based on WMH volume measures and confounds for predicting attention/executive function, information processing speed, and verbal memory (***figure B2a***). As this analysis implements current best practices of predictive modelling in neuroimaging, our findings represent evidence for a true prediction of cognitive performance by LNM.[54] Comparing the improvement from the confounds-based model to the model informed by total WMH volume with the improvement to the model based on both LNM modalities, the usage of fLNM and sLNM scores amounted to a 3- to 7-fold increase in added predictive performance across the three cognitive domains. For language scores, LNM measures did not significantly surpass prediction performance of WMH volume measures.

To evaluate the stability of our predictive modelling results, we conducted the analysis across subsamples of increasing sizes (***figure B2b***). For the cognitive domains of attention/executive function and verbal memory, models informed by LNM began to surpass those based on WMH volume when the subsample size reached about 50% (attention / executive function: n=1723, verbal memory: n=1712, note variations in data availability across cognitive domains). In the case of information processing speed, LNM-based models exceeded WMH volume models at a subsample size of roughly 25% (n=604). For language abilities, LNM-based models matched the performance of WMH volume models as sample sizes increased. Across all cognitive domains, predictive accuracy showed high consistency and minimal improvement within the 80-100% sample size range, suggesting a plateau in performance gains.

Figure B2. Predictive modelling analysis.[11]

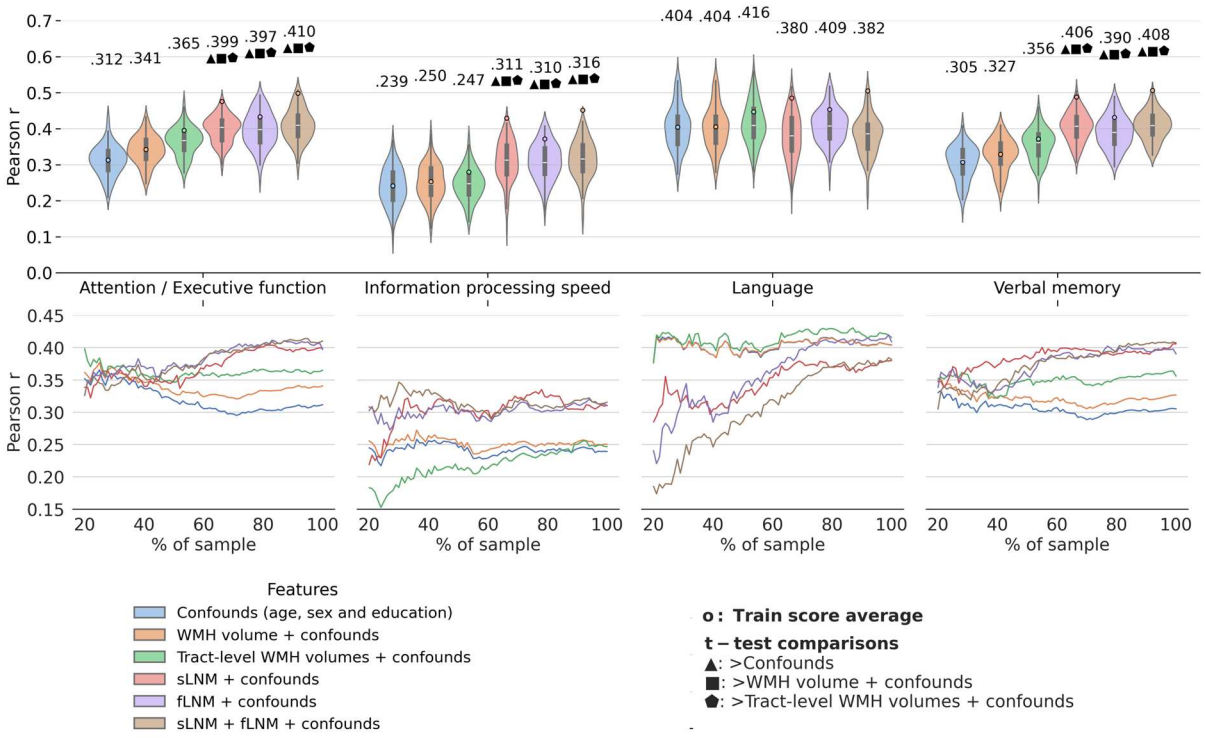

a) Violin plots display the distribution of prediction scores (Pearson correlations) across cognitive domains (100 Pearson correlations for 100 folds from 10-fold cross-validation repeated 10 times). Colors represent different feature sets: blue for demographic confounds (age, sex, education), orange for total WMH volume with confounds, green for tract-level WMH volumes with confounds, red for sLNM scores with confounds, purple for fLNM scores with confounds, and brown for combined sLNM and fLNM scores with confounds. Average Pearson correlations are shown above each violin. Training score averages are represented by colored dots on the violin. Machine learning adjusted t-test results comparing LNM-based models to confound- and WMH volume-based models are indicated by geometric symbols: ▲ for significantly higher correlation than confounds, ■ for significantly higher than total WMH volume with confounds, and ⬟ for significantly higher than tract-level WMH volumes with confounds. b) Performance curves illustrate average Pearson correlations across folds for different sample subsets, increasing in size. Line colors correspond to those in the violin plots of panel a). *Abbreviations*: fLNM – functional lesion network mapping, sLNM – structural lesion network mapping, WMH – white matter hyperintensities of presumed vascular origin.

To investigate the link between WMH disconnectivity in specific brain circuits and cognitive performance, we related regional LNM scores and cognitive domain scores. Associations of cortical and subcortical regions are displayed in ***figure B3***. Higher fLNM scores in cortical regions of the dorsal and ventral attention networks were associated with lower scores in attention/executive function, information processing speed and verbal memory (***figure B3a-c***). Association between cognition and structural lesion connectivity showed a similar spatial pattern: sLNM scores in the dorsal attention network correlated negatively with attention/executive function and information processing speed (***figure B3d-f***). The link of sLNM and verbal memory showed a distinct spatial distribution: higher sLNM scores in the ventral attention, frontoparietal, and default mode network were significantly associated with

lower verbal memory. No significant association was found between LNM scores and language abilities. The spatial effect patterns, represented by the reported β-coefficient maps, demonstrated significant overlap, with 26 out of 28 effect pattern pairs showing significant correlation.

Figure B3. Region of interest-level statistics for cortical and subcortical gray matter.[11]

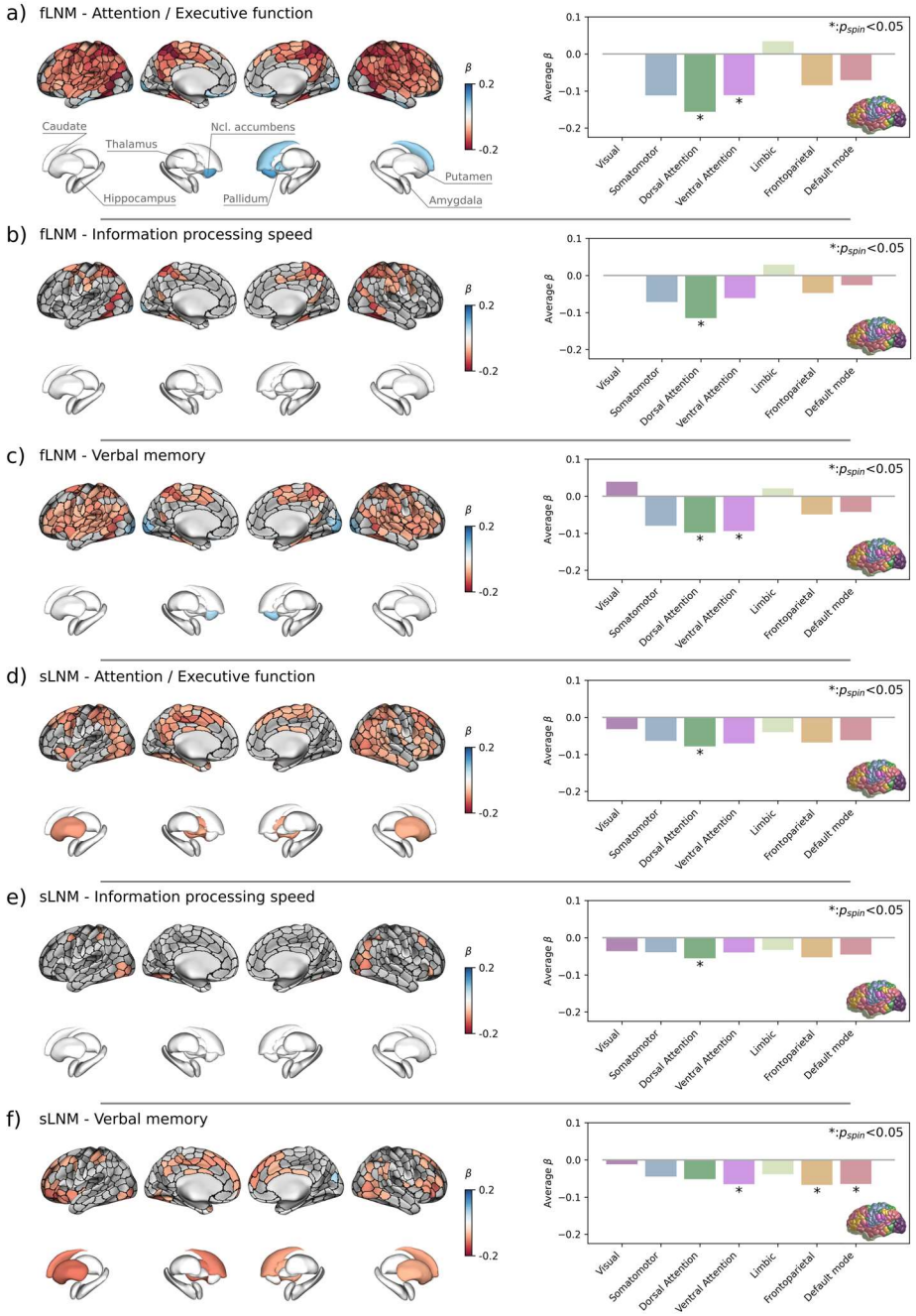

Left panels depict anatomical maps with β-coefficients from general linear models, where red indicates negative β-coefficients (higher regional LNM scores associated with lower cognitive performance) and blue indicates positive β-coefficients (higher cognitive performance with higher LNM scores). Right panels display bar plots of these β-coefficients averaged across Yeo's canonical resting-state networks,[55] with a color-coded network distribution illustration in the lower right. Statistical significance was assessed via spin permutations. Rows represent different LNM-cognitive domain pairs: a) fLNM – attention/executive, b) fLNM – processing speed, c) fLNM – verbal memory, d) sLNM – attention/executive, e) sLNM – processing speed, f) sLNM – verbal memory. *Abbreviations*: fLNM – functional lesion network mapping, p_{spin} – *p*-value derived from spin permutations, sLNM – structural lesion network mapping.

Further regional analysis of predefined white matter tracts showed that lower cognitive performance in attention/executive function, information processing speed, and verbal memory was associated with higher LNM scores in tracts connecting the frontal as well as parietal cortex. This included, among others, the bilateral superior longitudinal fascicles, cingulate tracts, the anterior thalamic radiation, corticostriatal and corticopontine tracts. There was no significant association between tract-level LNM scores and language function.

1.5 Study C: Brain imaging and neuropsychological assessment of individuals recovered from a mild to moderate SARS-CoV-2 infection

1.5.1 Background and aims

By February 11, 2024, over 750 million COVID-19 cases were reported globally by the World Health Organization (https://data.who.int/dashboards/covid19/cases). The pandemic has highlighted that severe acute respiratory syndrome coronavirus 2 (SARS-CoV-2) not only induces respiratory dysfunction but can also affect multiple organ systems.[18] Importantly, SARS-CoV-2 infections can have profound impacts on the central nervous system, leading to a range of neurological symptoms including, but not limited to, deficits of attention and executive function, memory impairment, headaches, and fatigue.[56] These issues can last for months or years, then commonly referred to as long COVID, and severely challenge individual recovery and overall well-being.[57] Comprehending the pathological underpinnings of these long-term consequences is essential for meeting ensuing health care needs.

Histopathological studies on patients deceased from COVID-19 suggest that vascular damage and neuroinflammation may relevantly contribute to COVID-19's neuropsychiatric effects.[58] However, these post-mortem studies cannot directly investigate the disease-symptom relationship. In vivo brain imaging allows to link brain structural changes to clinical outcomes and could help to identify reliable biomarkers of long-term effects of COVID-19, enhancing diagnostics and prognostication. But studies jointly investigating brain imaging and neurological as well as psychiatric symptoms are scarce, highlighting the need for further investigations.

Our study aimed to address this issue by examining the long-term neuropsychological and neuroanatomical outcomes associated with COVID-19, focusing on individuals with mild to moderate disease course. We analyzed 223 non-vaccinated individuals at a median of 10 months post-recovery, using multimodal MRI to detect signs of neurodegeneration, neuroinflammation, and vasculopathy, coupled with broad neuropsychological assessments.

1.5.2 Methods and results

In this cross-sectional case-control study, we analyzed 223 participants of the HCHS COVID Program (mean age 55.54 ± 7.07; 44.8% female) who had recovered from a SARS-CoV-2 infection confirmed by PCR tests.[18] These participants completed cranial MRI, neuropsychological testing, and symptom questionnaires, following HCHS protocols. We matched a healthy control group assessed pre-pandemic from the original HCHS for age, sex, education, and vascular risk factors (age: 55.54 ± 7.07, 41.7% female). We processed T1-weighted, FLAIR, and diffusion-weighted MRI scans to assess measures of brain tissue integrity, including cortical thickness, white matter microstructure (via diffusion tensor imaging, free-water imaging, and fixel-based analysis), and cerebral small vessel disease markers (WMH load and peak width of skeletonized mean diffusivity, PSMD). The individual measures are described in ***figure C1***. We analyzed imaging markers at three different scales: globally, by regions of interest (cortical regions defined by the Desikan-Kiliany atlas, white matter tracts derived via TractSeg), and at vertex- or voxel-levels. Cognitive and neuropsychiatric assessments included the Animal Naming Test, Clock Drawing Test, Mini-Mental State Exam, Trail Making Test, Word List Recall, GAD-7, and PHQ-9, plus self-reported neurological symptoms from the PHQ-15. Statistical group comparisons were adjusted for age, sex, education and vascular risk factors.

Figure C1. Schematic illustration of the investigated imaging markers.[12]

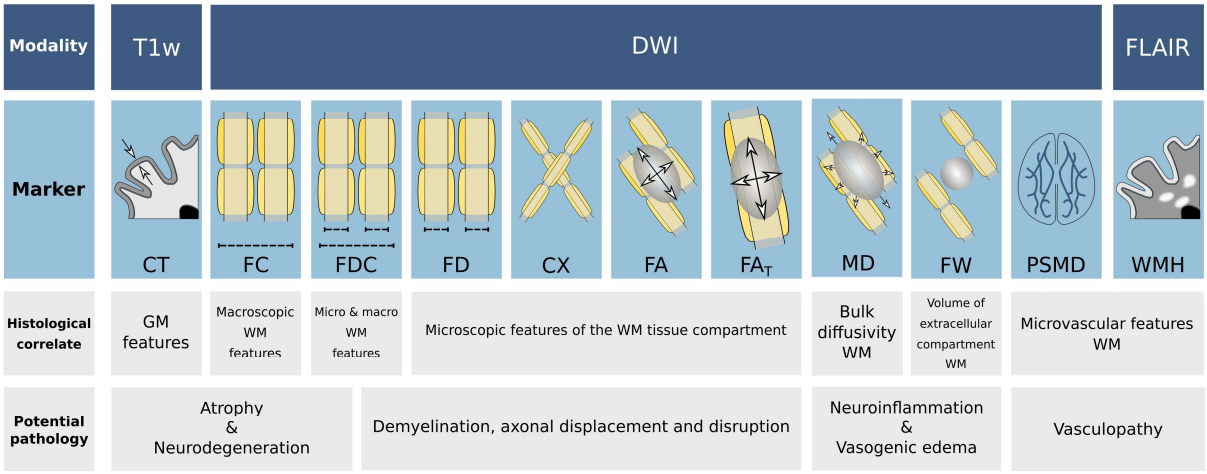

This figure outlines the derivation and interpretation of cerebral gray and white matter imaging markers. The first row details the imaging sequences used, while the second row illustrates the markers: cortical thickness (CT) as the distance from the pial surface to the gray/white matter boundary; fiber cross-section (FC) indicating white matter bundle diameter; fiber density (FD) reflecting intraaxonal volume; fiber density and cross-section (FDC) assessing both micro- and macroscopic white matter alterations; complexity (CX) of fiber configurations; fractional anisotropy (FA) for diffusion directionality; mean diffusivity (MD) for diffusion rate; fractional anisotropy of the tissue (FA_T); free-water (FW) quantifying the volume of the extracellular compartment; peak width of skeletonized mean diffusivity (PSMD) as the mean diffusivity 95th and 5th percentile difference; and white matter hyperintensity volume normalized by intracranial volume (WMH load). The third and fourth rows provide histological interpretations and information on sensitivity to pathologies of these markers.

Recovered SARS-CoV-2 individuals showed increased global MD and extracellular free-water in the cerebral white matter compared to controls (***figure C2***). The remaining global imaging markers showed no statistically significant group differences including cerebral small vessel disease markers, fractional anisotropy, cortical thickness and fixel-based analysis indices. For biological interpretability, we translated mean differences in MD and free-water between groups into "years of healthy aging" based on linear regression of the imaging markers with control group age. The observed differences corresponded to 7 years of healthy aging for MD and 6.67 years for free-water. For spatial localization we performed tract-based spatial statistics (TBSS) which represents a voxel-level analysis across the white matter skeleton. TBSS revealed widespread differences, with significantly higher free-water and MD across all brain lobes in post-SARS-CoV-2 individuals.

Figure C2. Group comparison of mean diffusivity and extracellular free-water.[12]

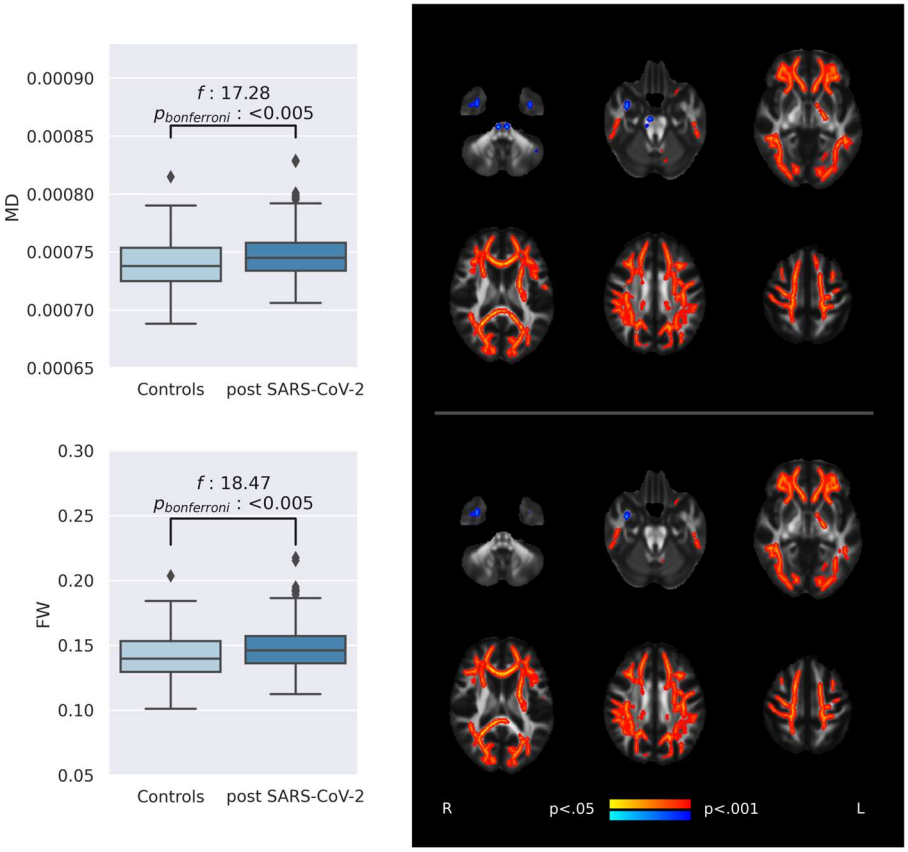

Left: boxplots of averaged imaging measures and the corresponding statistical results (F-statistics and Bonferroni-corrected *p*-values) from the ANCOVAs comparing matched controls with post-SARS-CoV-2 individuals adjusted for age, sex, and years of education. Right: tract-based spatial statistics results showing group comparisons of skeletonized diffusion indices. Skeleton voxels that significantly differed between groups are highlighted by colors: post-SARS-CoV-2 individuals > matched controls, red; post-SARS-CoV-2 individuals < matched controls, blue. *Abbreviations*: FW – free-water, p – family-wise error corrected *p*-values, MD – mean diffusivity, post-SARS-CoV-2 – individuals who recovered from a severe acute respiratory coronavirus type 2 infection.

Furthermore, we assessed the predictive power of imaging markers in a supervised predictive modelling analysis, specifically logistic regression with ElasticNet penalties. Models were scored with prediction accuracy (*accuracy* = $n_{correct\ predictions}$ / $n_{total\ predictions}$). Based on this, we aimed to predict SARS-CoV-2 infection status based on regional imaging data, i.e., cortical

thickness in Desikan Kiliany regions and white matter indices in anatomically predefined white matter tracts derived via TractSeg. Free-water and MD emerged as the most accurate predictors, with median accuracies of 80.21% and 79.38%, respectively (***figure C3***). Except for cortical thickness, all metrics significantly outperformed null models which were based on randomized group assignments.

Figure C3. Predicting past SARS-CoV-2 infection with imaging markers.[12]

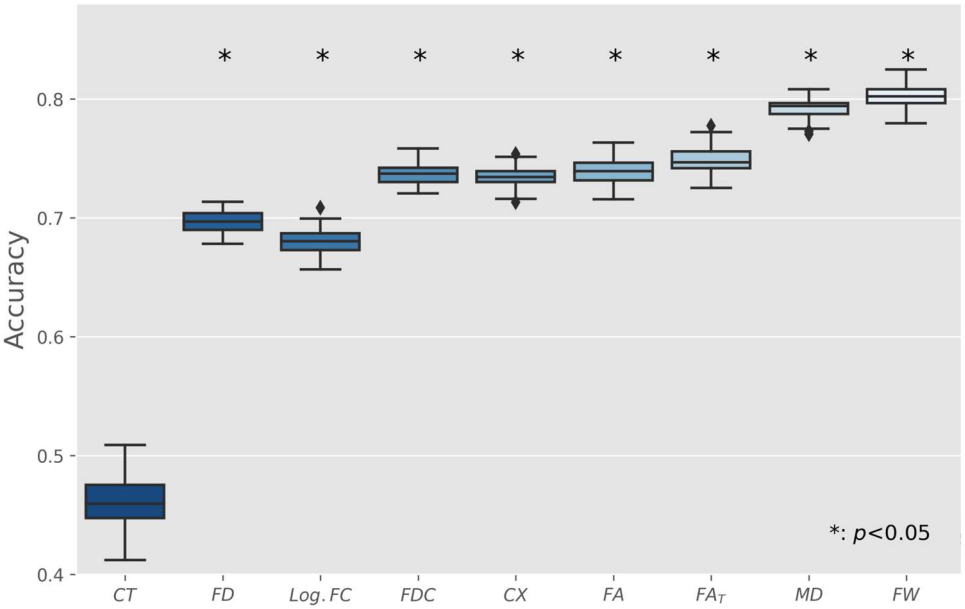

A supervised machine learning analysis was conducted to evaluate the diagnostic capacity of brain imaging markers. The boxplot illustrates the accuracy for predicting a past SARS-CoV-2 infection via logistic regression models informed by regional brain imaging markers. Models were trained using 10-fold nested cross-validation, repeated 100 times per marker with varied random splits. Asterisks denote models significantly outperforming null predictions based on permuted group labels. *Abbreviations*: CT – cortical thickness, CX – complexity, FA – fractional anisotropy, FA_T – FA of the tissue, FD – fiber density, FDC – fiber density and cross-section, FW – free-water, Log. FC – logarithm of fiber cross-section, MD – mean diffusivity, PSMD – peak width of skeletonized mean diffusivity, WMH – white matter hyperintensity

Clinical test results showed no significant differences between groups, including assessments of cognition, psychosocial and neurological symptom burden (***table C4***). However, exploratory regression analyses with an interaction term (imaging x group) for free-water and MD revealed significant interactions. Specifically, we found significant interactions for the association of free-water with the Animal Naming Test, Clock Drawing Test, Mini-Mental State Exam and Word List Recall Test, indicating more pronounced effects in post-SARS-CoV-2 individuals. Similar patterns were observed for MD, indicating significant interactions for the Animal Naming Test, Clock Drawing Test, Mini-Mental State Exam, Trail Making Test A, Word List Recall.

Table C4. Results of clinical and neuropsychological assessments of post-SARS-CoV-2 individuals compared to matched controls[12]

Clinical measure[a]	Post-SARS-CoV-2	Matched controls	P_{uncorr}[b]	P_{bonf}[c]	*F*
Neurocognition					
Animal Naming Test	28.03 ± 6.04 (212)	26.43 ± 7.15 (212)	.02	.14	5.94
Clock Drawing Test	6.75 ± 0.78 (212)	6.57 ± 1.03 (214)	.04	.37	4.20
MMSE	28.37 ± 1.26 (211)	28.02 ± 1.72 (210)	.02	.19	5.34
TMT-A in seconds	31.89 ± 10.60 (212)	33.71 ± 11.67 (190)	.12	>.99	2.40
TMT-B in seconds	68.50 ± 22.69 (212)	70.89 ± 25.57 (187)	.37	>.99	.81
Word List Recall	8.52 ± 1.63 (210)	8.32 ± 1.61 (204)	.25	>.99	1.33
Psychosocial symptom burden					
PHQ-9	3.94 ± 3.74 (212)	3.91 ± 3.77 (215)	.97	>.99	<.01
GAD-7	2.94 ± 3.28 (212)	2.80 ± 3.06 (215)	.67	>.99	.18
Neurological symptom burden					
PHQ-15[d]	2.13 ± 1.83 (212)	1.83 ± 1.73 (215)	.09	.82	2.86

Abbreviations: GAD – General Anxiety Disorder, MMSE – Mini-Mental State Examination, PHQ – Patient Health Questionnaire, post-SARS-CoV-2 individuals – individuals who recovered from a severe acute respiratory coronavirus type 2 infection, SD – standard deviation, TMT-A – Trail Making Test A, TMT-B – Trail Making Test B

[a]Presented as mean ± SD (N)
[b]Uncorrected P values of analyses of covariance, adjusted for age, sex and years of education
[c]Bonferroni-corrected P values of analyses of covariance, adjusted for age, sex and years of education (considering 9 comparisons)
[d]PHQ-15 items: headache, dizziness, fatigue, sleep disturbances

1.6 General discussion

Research in cognitive disorders of vascular origin is hampered by the lack of disease biomarkers, i.e., objectively measurable indicators that are specific to pathogenic processes. The presented thesis summarizes original research from three projects addressing this issue by investigating imaging biomarkers of brain network macro- and microstructure in the context of VCI. Our goal with this body of work was to improve the understanding of disease pathways that link primary vascular pathology to cognitive sequelae. Furthermore, we sought to explore ways in how these associations might be harnessed to predict symptoms at the individual level, which would have tangible implications for diagnostics and treatment. These aims were achieved by the development of a complementary set of analyses to integrate clinical data with advanced neuroimaging biomarkers at scale. The implemented workflows have since been

used beyond this thesis to investigate macrostructural and microstructural brain abnormalities in stroke, nutrition, periodontitis, COVID-19, aging and cerebral small vessel disease.[18,35,59–67]

1.6.1 Vascular risk links to widespread brain morphological abnormalities

Brain atrophy is considered a key imaging surrogate of VCI.[8] However, the specific processes by which vascular pathology leads to brain structural changes are not well understood, partly due to the varied causes and severity levels of VCI. Multiple factors, including chronic alterations from cerebral small vessel disease and both direct and indirect damage caused by acute ischemic stroke, can drive brain atrophy. In study A (presented in ***section 1.3***), we addressed this heterogeneity by narrowing our focus to cognitively healthy or subclinically affected individuals in two population-based cohorts, deliberately excluding participants with neurological diagnoses. This approach allowed us to concentrate on brain morphological abnormalities in the normal population at vascular risk, i.e., exhibiting obesity, arterial hypertension, dyslipidemia, and insulin resistance.

By integrating vascular risk factors and brain imaging data via multivariate, data-driven statistics, we could demonstrate that composite vascular risk, commonly referred to as MetS, is associated with a specific pattern of brain morphological abnormalities, independent of age, sex and education status (***figure A2***). Although all risk factor measures contributed significantly to the observed associative effects, obesity measures were most strongly associated, which indicates that obesity might be the strongest driver of brain morphological abnormalities among MetS components. Contributing to the understanding of brain health in individuals at vascular risk in general, this finding points to potential clinical utilization by highlighting that future studies could focus on the investigation of weight-reducing interventions to examine their effects on brain structure and cognitive outcomes.

Higher vascular risk was related to widespread brain morphological abnormalities across multiple regions, including the lower thickness in orbitofrontal and lateral frontal, insular, cingulate and temporal cortices as well as lower volume in subcortical regions. Strikingly, this morphological pattern mediated the association between vascular risk severity and cognitive performance in multiple cognitive tests of attention / executive function, information processing speed, memory and reasoning (***figure A3***). This underscores the role of macrostructural brain changes as a key pathway connecting vascular and cognitive health in individuals at risk. It aligns with prior evidence on the mediating role of brain structure in a pediatric sample at vascular risk.[68] Considering its association with cognitive performance, we propose that the detected associative effects reflect a disease continuum, ranging from minor cognitive impairments associated with vascular risk to severe cognitive decline seen in cerebral small

vessel disease-related mild cognitive impairment and vascular dementia, as well as Alzheimer's disease.[69–71] This theory is supported by the similarity between the observed morphological profile and the atrophy patterns found in these conditions. Future studies capitalizing on longitudinal data of participants on the full severity spectrum of VCI should follow up on these findings.

By integrating our *in-vivo* imaging findings with *post-mortem* transcriptomic data in a virtual histology analysis, we demonstrated that vascular risk-related brain morphological abnormalities were strongest in regions with higher density of endothelial cells, microglia and neurons entertaining long-range connectivity (***figure A4a***). These results affirm the roles of these cell types in vascular risk pathophysiology. Endothelial dysfunction has been shown to impact tissue integrity by promoting chronic inflammation and impairing blood supply.[72] In addition, endothelial cell density indicates the level of overall tissue vascularization, with highly vascularized areas being more prone to effects of vascular pathology. Although our indirect approach has methodological limitations, the results are supported by animal studies linking vascular risk-related microglial activation to brain structural damage through inflammatory and oxidative mechanisms.[73,74] Given the strengthening evidence, therapeutic approaches targeting pathways involving endothelial cells and microglia hold potential for preserving brain health in individuals at risk. We also discovered an association with the density of excitatory neurons of subtype 8 in cortical layer 6, which form long-range connections rendering them susceptible to the effects of VCI-related white matter disease.[75,76] Collectively, these results provide a foundation for research that unifies brain imaging and histopathological data to deepen our understanding of cellular-level contributions to VCI.

Leveraging normative brain network topological information from group-consensus connectomes, we showed that morphological brain abnormalities coincided within macroscale functional and structural brain networks (***figure A4b***), indicating that regions with similar thickness or volume effects were highly interconnected. Hence, the observed brain morphological abnormalities localize to large-scale brain networks rather than isolated regions. A potential mechanism linking connectivity to vascular risk-related morphological abnormalities is the impairment of white matter tracts through microvascular pathology, leading to concurrent degeneration in connected yet distant cortical areas. This implies that morphological abnormalities in highly connected regions may stem from their shared disconnectivity profiles.[77] The demonstrated connection between brain morphology and network topology in individuals at vascular risk offers insights that could benefit research on patients with severe VCI stages, such as those experiencing cognitive impairment from ischemic stroke. While the localization of stroke-induced atrophy varies greatly depending on stroke location, contributing

to individual heterogeneity, the stroke-related brain morphological changes linked to cognitive effects may be more consistent and traceable to specific regions or networks.[78] Future research should further investigate this hypothesis integrating lesion and brain morphometry data in stroke-related cognitive impairment.

Taken together, study A covers a comprehensive analysis of brain health in individuals at vascular risk, highlighting widespread morphological abnormalities and their connection to cognitive function. In addition, these findings lent important insights into vascular risk-related pathophysiology at multiple scales: the observed brain structural differences were associated with microscale tissue composition and macroscale brain network organization. These findings were generalizable over the UK Biobank and HCHS subsamples as well as robust across sensitivity analyses.

1.6.2 Lesion network mapping improves cognitive performance prediction in memory clinic patients

Attributing cognitive symptoms to VCI is challenging. Clinically, the diagnosis of cognitive symptoms due to vascular causes often depends on the assessment of WMH. However, the considerable variance in the link between WMH burden and cognition complicates diagnostics and hinders accurate individual predictions. In study B (presented in ***section 1.4***), we aimed to improve individual-level prediction of cognitive performance. Therefore, we investigated cognitive and imaging data of a large sample of memory clinic patients with varying degrees of VCI excluding individuals with a history of stroke. In this sample, we used LNM to assess the connectivity between predefined gray and white matter regions and WMH, thereby estimating the extent of disconnection due to WMH.

Our analysis showed that models incorporating measures of regional WMH disconnectivity, i.e., fLNM and sLNM scores, surpassed those based on total or tract-level WMH volumes in predicting cognitive performance in three of four cognitive domains (***figure B2***). Comparing the improvement over models only informed by demographic confounds (age, sex and education), LNM-informed models surpassed the improvement of models informed by total WMH volume 3- to 7-fold. Additionally, our findings highlighted that the predictive capacity of total WMH volume was only marginally better than demographic factors. This questions the established reliance on WMH extent for assessing VCI and stresses the importance of including demographic confounds in models using WMH data. Collectively, these results underscore the significance of WMH-related “covert” network effects, confirming earlier results from smaller clinical or population-based studies.[45,79–81]

To localize these network effects, we analyzed the relationship between WMH disconnectivity and cognitive domain scores at the regional level. Our analysis revealed that higher WMH disconnectivity within gray and white matter regions of the dorsal and ventral attention networks were associated with lower attention / executive function, processing speed, and verbal memory (***figure B3***). This suggests that WMH impair cognitive function by disrupting brain circuits involved in attention control. Prior studies showing changes in functional connectivity and task activation within the attention control networks in VCI corroborate our results.[82–84] Expanding on the results presented in study A, these findings reinforce the conceptualization of VCI as a network disorder.

The dorsal attention network regulates top-down attention control, i.e., the voluntary and goal-directed allocation of attention.[85,86] The ventral attention network governs bottom-up attention control, i.e., the process of detecting and orienting to unexpected, salient stimuli in the environment.[85,87] The observation that WMH-related disconnectivity in the attention control networks contributes to cognitive variance aligns with observations of attention and executive function deficits being prominent symptoms in VCI in general.[1] As the investigation of different cognitive domains largely converged on the attention control networks, WMH may also influence other cognitive domains by affecting the attentional resources required by various tasks: e.g., VCI might contribute to variance in memory by affecting attention rather than the memory demands of corresponding tests. Future analyses should further explore this theory. Here, multivariate, data-driven techniques – e.g., PLS as used in study A – could be of help as they can resolve the potentially covarying associative effects of regional WMH disconnectivity and multi-domain cognitive performance in VCI.

Intriguingly, the regions highlighted in this analysis, i.e., attention control networks, and the pattern of vascular risk-associated morphological abnormalities identified in study A, did not completely align. As VCI is a spectrum unified by vascular pathophysiology rather than a homogeneous condition, we speculate that brain morphometry and LNM may reveal different yet complementary pathological processes: morphometric indices capture local pathologies with macrostructural impact, whereas LNM scores specifically indicate a region's connectivity to WMH, potentially highlighting remote effects. Although a region's connectivity to WMH is linked to lower cortical thickness, the observed statistical effects are small, suggesting that WMH disconnectivity is just one of several factors shaping morphological abnormalities in VCI.[77] Other complementary pathologies, involving local cellular level pathways as well as network topological aspects beyond WMH connectivity as discussed in study A, should be considered.

Taken together, our study demonstrates that WMH disconnectivity metrics reveal disease-specific signatures useful for predicting cognitive outcomes, while their computation was feasible in multiple large cohorts. Therefore, WMH disconnectivity is a viable candidate biomarker for a more robust identification of VCI pathophysiology in clinical research. Future studies should evaluate whether WMH disconnectivity information can contribute to streamlining the process of selecting participants who are most likely to experience cognitive deterioration due to vascular issues. By that, WMH disconnectivity measures could not only improve diagnostics but also treatment calibration.

1.6.3 Mild COVID-19 is associated with long-term white matter abnormalities

As in VCI, characterizing the pathophysiology and identifying disease biomarkers of COVID-19 is crucial for advancing diagnosis, prognosis, and treatment stratification for individuals with long-term effects of the disease. Tapping into these research needs, we investigated if individuals recovered from a mild to moderate SARS-CoV-2 infection exhibit long-term brain structural differences and clinical sequelae in study C (presented in ***section 1.5***). Therefore, we analyzed a broad range of macro- and microstructural neuroimaging markers alongside clinical assessments in a large cohort of COVID-19 convalescents on average 10 months after the acute infection and matched healthy controls.

Our study found significantly higher global extracellular free-water and MD in post-SARS-CoV-2 individuals indicative of higher amounts of water in the extracellular compartment and higher bulk diffusivity (***figure C2***). Similar microstructural differences have been demonstrated in hospitalized as well as cognitively impaired COVID-19 cases.[88,89] Results from complementary analyses refined these insights: the observed effects were comparable to approximately 7 "years of healthy aging," signifying a biologically significant effect. In addition, voxel-level analyses revealed that the group differences were widespread, i.e., involved the cerebral white matter of all brain lobes. Lastly, tract-level measurements of free-water and MD could be leveraged to predict a past SARS-CoV-2 infection with ~80% accuracy surpassing all other regional imaging markers under study (***figure C3***), further underscoring the diagnostic relevance of these markers. The remaining global imaging markers showed no statistically significant differences including cortical thickness, other microstructural markers based on diffusion MRI, as well as the WMH load.

The response of the intrathecal immune system to the virus is thought to be a fundamental component of COVID-19 neuropathology.[56] There is histopathological and clinical evidence on neuroinflammation including the activation of glial cells, a cytokine response in the cerebrospinal fluid as well as immune-mediated vasculopathy including endothelial injury and

blood brain barrier disruption.[56,90,91] Both free-water and MD are sensitive to immune activation and accompanying vascular damage increasing extracellular free-water and thus diffusivity.[24] More specifically, activated microglia and astrocytes release cytokines, leading to osmosis of water from the blood into the extracellular space.[92] Moreover, more pronounced neuroinflammation damages the neurovascular unit, exacerbating blood brain barrier leakage.[93] Taken together, the observed increase in free-water and MD is suggestive of a prolonged neuroinflammatory reaction to a SARS-CoV-2 infection.

Within the scope of this thesis, COVID-19-related vasculopathy was a pathway of particular interest, as vascular pathology might be a relevant intermediary in the link between SARS-CoV-2 infection and long-term cognitive outcomes. There is evidence for this connection from other studies suggesting that long COVID-related cognitive impairment could be integrated into the VCI spectrum.[93,94] Elevated free-water and MD are compatible with vascular involvement being demonstrably elevated in cerebral small vessel disease.[95] Yet, WMH load and PSMD – biomarkers of more established vascular injury – did not significantly differ in post-SARS-CoV-2 individuals. More specifically, PSMD values were nominally higher in the post-SARS-CoV-2 cases, but the differences were not statistically significant after adjusting for multiple comparisons. Taken together, this may indicate that, within our primarily mildly affected cohort, vasculopathy is less pronounced, manifesting more as subtle alterations in tissue microstructure rather than detectable lesions in anatomical imaging. Future imaging studies focusing on more severely affected individuals could provide deeper insights into the nuanced relationship of vascular brain imaging markers and cognitive performance in COVID-19 convalescents.

Placing the observed microstructural white matter abnormalities in a clinical context is essential. Commonly reported long-term sequelae of COVID-19 include impairment of attention / executive function and memory, anxiety, depression, fatigue, headache and sleep impairment.[96–98] Contrasting these reports, our findings showed no significant differences for any cognitive domain, depression, anxiety, or neurological symptoms between groups. Possible reasons for these findings could be the mild severity of symptoms in our subjects, the extended follow-up duration, a potential selection bias towards highly motivated participants in the HCHS COVID Program, and the impact of varying levels of social deprivation due to country-specific pandemic measures. Our exploration of interaction effects of the imaging-behavior correlations with post-SARS-CoV-2 status revealed that associations between higher free-water and MD with lower executive function and information processing speed (Trail Making Test A and B), working memory (Word List Recall Test), and verbal fluency (Animal Naming Test) were stronger in post-SARS-CoV-2 individuals. These findings suggest a

pathophysiological connection between neurocognitive impairments and structural brain abnormalities in those recovered from COVID-19. This underscores the necessity for further research to elucidate the complex relationship between COVID-19 and long-term impact on brain health.

Currently, the HCHS is enlisting participants who were examined in the study pre-pandemic and have since developed long COVID symptoms. Recruited long COVID cases will undergo a comprehensive assessment, including the standard HCHS protocol and additional evaluations focused on long COVID symptoms. This approach will enable us to examine a more severely affected cohort adopting a longitudinal analysis design. Consequently, we plan to build upon the findings discussed here, analyzing the forthcoming dataset to characterize biomarkers of long COVID, understand its progression over time, and assess its impact on cognitive and physical health.

In summary, our research suggests that individuals recovering from COVID-19 show imaging evidence of a prolonged neuroinflammatory response, as demonstrated by subtle yet widespread higher extracellular free-water and MD across white matter regions. Additionally, these findings are compatible with a potential involvement of vascular pathology, despite macrostructural evidence for vascular damage like WMH being absent. Notably, while this distinct imaging profile was identified, the study cohort displayed no marked neuropsychological symptoms 10 months after the SARS-CoV-2 infection. Further research in individuals with long COVID will help to clarify the connection between SARS-CoV-2 infection, brain structure and cognition.

1.6.4 Strengths and limitations

The studies presented in this thesis exhibit multiple strengths involving the investigation of over 40,000 individuals covering different segments of the VCI spectrum, broad behavioral phenotyping, and reproducible advanced neuroimaging enabling a comprehensive characterization of brain structure and connectivity. However, it is important to acknowledge certain limitations that need to be considered when interpreting our results. Firstly, the recruitment of selected participant samples in specific cohorts might limit the generalizability of our results to the broader population. For instance, as the participants were predominantly of European ancestry, the generalizability of our findings to other ethnicities remains to be established. Additionally, while efforts were made to harmonize cognitive and imaging data across cohorts, as well as to statistically adjust for site differences, the potential for biases due to variations in data collection and processing methods across the studied cohorts may have impacted our results. Furthermore, the cross-sectional nature of the study data limits our ability

to infer causality. Longitudinal assessment of the examined relationships would provide stronger evidence, suggesting this as a direction for future research.

1.6.5 Conclusion

This thesis leveraged advanced multimodal and multiscale neuroimaging approaches to improve our understanding of VCI as a complex heterogeneous spectrum of pathology and provides a foundation to translate this knowledge in clinical research. The presented studies are centered around the concept of VCI as a network disorder affecting brain macro- and microstructure and describe comprehensive analysis workflows to contextualize neuroimaging findings across different neurobiological domains. Through these advances, we were able to integrate gray matter morphology, white matter microstructure, cell-specific regional gene expression, connectomic properties and WMH network topology to characterize VCI-related brain network abnormalities. Based on this, three key findings emerged: 1) Composite vascular risk is associated with a distinct profile of brain morphological abnormalities that is linked to cognitive function, microscale tissue composition, and macroscale brain network architecture. 2) Lesion network mapping techniques improve individual-level prediction of cognitive performance in memory clinic patients, highlighting the WMH-related disruption of attention control networks in VCI. 3) Individuals recovered from mild-to-moderate COVID-19 exhibit long-term widespread white matter microstructural alterations without cognitive deficits. Moving forward, the conceptual frameworks discussed here lay the groundwork for applying these findings to clinical management in the long-term to advance imaging-informed diagnosis, prognosis and patient-tailored therapeutic intervention in VCI.

2 Abbreviations

COVID-19 – Coronavirus disease 2019
DTI – Diffusion tensor imaging
FA – Fractional anisotropy
fLNM – Functional lesion network mapping
rsfMRI – Resting-state functional magnetic resonance imaging
LNM – Lesion network mapping
MD – Mean diffusivity
MetS – Metabolic syndrome
MRI – Magnetic resonance imaging
PLS – Partial least squares correlation analysis
ROI – Region of interest
SARS-CoV-2 – Severe acute respiratory syndrome coronavirus 2
sLNM – Structural lesion network mapping
TBSS – Tract-based spatial statistics
VCI – Vascular cognitive impairment
WMH – White matter hyperintensities of presumed vascular origin

3 References

1. Dichgans Martin, Leys Didier. Vascular Cognitive Impairment. *Circulation Research*. 2017;120(3):573-591. doi:10.1161/CIRCRESAHA.116.308426
2. van der Flier WM, Skoog I, Schneider JA, et al. Vascular cognitive impairment. *Nat Rev Dis Primers*. 2018;4(1):1-16. doi:10.1038/nrdp.2018.3
3. Gorelick PB, Scuteri A, Black SE, et al. Vascular contributions to cognitive impairment and dementia: a statement for healthcare professionals from the american heart association/american stroke association. *Stroke*. 2011;42(9):2672-2713. doi:10.1161/STR.0b013e3182299496
4. Biesbroek JM, Biessels GJ. Diagnosing vascular cognitive impairment: Current challenges and future perspectives. *International Journal of Stroke*. 2023;18(1):36-43. doi:10.1177/17474930211073387
5. Wilcock D, Jicha G, Blacker D, et al. MarkVCID cerebral small vessel consortium: I. Enrollment, clinical, fluid protocols. *Alzheimers Dement*. 2021;17(4):704-715. doi:10.1002/alz.12215
6. Lu H, Kashani AH, Arfanakis K, et al. MarkVCID cerebral small vessel consortium: II. Neuroimaging protocols. *Alzheimer's & Dementia*. 2021;17(4):716-725. doi:10.1002/alz.12216
7. Duering M, Biessels GJ, Brodtmann A, et al. Neuroimaging standards for research into small vessel disease—advances since 2013. *The Lancet Neurology*. Published online May 23, 2023. doi:10.1016/S1474-4422(23)00131-X
8. De Guio F, Duering M, Fazekas F, et al. Brain atrophy in cerebral small vessel diseases: Extent, consequences, technical limitations and perspectives: The HARNESS initiative. *Journal of Cerebral Blood Flow & Metabolism*. 2020;40(2):231-245. doi:10.1177/0271678X19888967
9. Teuwen LA, Geldhof V, Pasut A, Carmeliet P. COVID-19: the vasculature unleashed. *Nat Rev Immunol*. 2020;20(7):389-391. doi:10.1038/s41577-020-0343-0
10. Petersen M, Hoffstaedter F, Nägele FL, et al. A latent clinical-anatomical dimension relating metabolic syndrome to brain structure and cognition. Lerch JP, Roiser J, eds. *eLife*. 2024;12:RP93246. doi:10.7554/eLife.93246
11. Petersen M, Coenen M, DeCarli C, et al. Enhancing Cognitive Performance Prediction through White Matter Hyperintensity Disconnectivity Assessment: A Multicenter Lesion Network Mapping Analysis of 3,485 Memory Clinic Patients. *medRxiv*. Published online 2024.
12. Petersen M, Nägele FL, Mayer C, et al. Brain imaging and neuropsychological assessment of individuals recovered from a mild to moderate SARS-CoV-2 infection. *Proceedings of the National Academy of Sciences*. 2023;120(22):e2217232120. doi:10.1073/pnas.2217232120
13. Miller KL, Alfaro-Almagro F, Bangerter NK, et al. Multimodal population brain imaging in the UK Biobank prospective epidemiological study. *Nat Neurosci*. 2016;19(11):1523-1536. doi:10.1038/nn.4393
14. Fawns-Ritchie C, Deary IJ. Reliability and validity of the UK Biobank cognitive tests. *PLoS One*. 2020;15(4):e0231627. doi:10.1371/journal.pone.0231627
15. Jagodzinski A, Koch-gromus U, Adam G, Anders S, Augustin M. Rationale and Design of the Hamburg City Health Study. *European Journal of Epidemiology*. Published online 2019. doi:10.1007/s10654-019-00577-4
16. Weaver NA, Zhao L, Biesbroek JM, et al. The Meta VCI Map consortium for meta-analyses on strategic lesion locations for vascular cognitive impairment using lesion-symptom mapping: Design and multicenter pilot study. *Alzheimers Dement (Amst)*. 2019;11:310-326. doi:10.1016/j.dadm.2019.02.007
17. Coenen M, Kuijf HJ, Huenges Wajer IMC, et al. Strategic white matter hyperintensity locations for cognitive impairment: A multicenter lesion-symptom mapping study in 3525 memory clinic patients. *Alzheimer's & Dementia*. Published online December 12, 2022:alz.12827. doi:10.1002/alz.12827
18. Petersen EL, Goßling A, Adam G, et al. Multi-organ assessment in mainly non-hospitalized individuals after SARS-CoV-2 infection: The Hamburg City Health Study COVID programme. *European Heart Journal*. Published online January 6, 2022:ehab914. doi:10.1093/eurheartj/ehab914
19. Gaser C, Dahnke R, Thompson PM, Kurth F, Luders E, Initiative ADN. CAT – A Computational Anatomy Toolbox for the Analysis of Structural MRI Data. Published online June 13, 2022:2022.06.11.495736. doi:10.1101/2022.06.11.495736
20. Cieslak M, Cook PA, He X, et al. QSIPrep: an integrative platform for preprocessing and reconstructing diffusion MRI data. *Nat Methods*. 2021;18(7):775-778. doi:10.1038/s41592-021-01185-5
21. Fornito A, Bullmore ET. Connectomics : A new paradigm for understanding brain disease. Published online 2015:733-748. doi:10.1016/j.euroneuro.2014.02.011
22. Fox MD. Mapping Symptoms to Brain Networks with the Human Connectome. *New England Journal of Medicine*. 2018;379(23):2237-2245. doi:10.1056/NEJMra1706158
23. Assaf Y, Pasternak O. Diffusion Tensor Imaging (DTI)-based White Matter Mapping in Brain Research: A Review. *J Mol Neurosci*. 2008;34(1):51-61. doi:10.1007/s12031-007-0029-0
24. Pasternak O, Sochen N, Gur Y, Intrator N, Assaf Y. Free water elimination and mapping from diffusion MRI. *Magnetic Resonance in Medicine*. 2009;62(3):717-730. doi:10.1002/mrm.22055
25. Raffelt DA, Tournier JD, Smith RE, et al. Investigating white matter fibre density and morphology using fixel-based analysis. *Neuroimage*. 2017;144(Pt A):58-73. doi:10.1016/j.neuroimage.2016.09.029
26. Mihalik A, Chapman J, Adams RA, et al. Canonical Correlation Analysis and Partial Least Squares for identifying brain-behaviour associations: a tutorial and a comparative study. *Biological Psychiatry: Cognitive Neuroscience and Neuroimaging*. Published online August 8, 2022. doi:10.1016/j.bpsc.2022.07.012
27. Abraham A, Pedregosa F, Eickenberg M, et al. Machine learning for neuroimaging with scikit-learn. *Frontiers in Neuroinformatics*. 2014;8. Accessed March 28, 2022. https://www.frontiersin.org/article/10.3389/fninf.2014.00014

28. Varoquaux G, Raamana PR, Engemann DA, Hoyos-Idrobo A, Schwartz Y, Thirion B. Assessing and tuning brain decoders: Cross-validation, caveats, and guidelines. *NeuroImage*. 2017;145:166-179. doi:10.1016/j.neuroimage.2016.10.038
29. Seidlitz J, Nadig A, Liu S, et al. Transcriptomic and cellular decoding of regional brain vulnerability to neurogenetic disorders. *Nat Commun*. 2020;11(1):3358. doi:10.1038/s41467-020-17051-5
30. Alberti KGMM, Zimmet P, Shaw J. Metabolic syndrome--a new world-wide definition. A Consensus Statement from the International Diabetes Federation. *Diabet Med*. 2006;23(5):469-480. doi:10.1111/j.1464-5491.2006.01858.x
31. Schwarz NF, Nordstrom LK, Pagen LHG, et al. Differential associations of metabolic risk factors on cortical thickness in metabolic syndrome. *Neuroimage Clin*. 2018;17:98-108. doi:10.1016/j.nicl.2017.09.022
32. Krishnadas R, McLean J, Batty DG, et al. Cardio-metabolic risk factors and cortical thickness in a neurologically healthy male population: Results from the psychological, social and biological determinants of ill health (pSoBid) study. *NeuroImage: Clinical*. 2013;2:646-657. doi:10.1016/j.nicl.2013.04.012
33. Schaefer A, Kong R, Gordon EM, et al. Local-Global Parcellation of the Human Cerebral Cortex from Intrinsic Functional Connectivity MRI. *Cerebral Cortex*. 2018;28(9):3095-3114. doi:10.1093/cercor/bhx179
34. Tian Y, Margulies DS, Breakspear M, Zalesky A. Topographic organization of the human subcortex unveiled with functional connectivity gradients. *Nat Neurosci*. 2020;23(11):1421-1432. doi:10.1038/s41593-020-00711-6
35. Petersen M, Nägele FL, Mayer C, et al. Brain network architecture constrains age-related cortical thinning. *NeuroImage*. 2022;264:119721. doi:10.1016/j.neuroimage.2022.119721
36. Lotter LD, Kohl SH, Gerloff C, et al. Revealing the neurobiology underlying interpersonal neural synchronization with multimodal data fusion. *Neuroscience & Biobehavioral Reviews*. 2023;146:105042. doi:10.1016/j.neubiorev.2023.105042
37. Larivière S, Paquola C, Park B yong, et al. The ENIGMA Toolbox: multiscale neural contextualization of multisite neuroimaging datasets. *Nat Methods*. 2021;18(7):698-700. doi:10.1038/s41592-021-01186-4
38. Burt JB, Demirtaş M, Eckner WJ, et al. Hierarchy of transcriptomic specialization across human cortex captured by structural neuroimaging topography. *Nat Neurosci*. 2018;21(9):1251-1259. doi:10.1038/s41593-018-0195-0
39. Alexander-Bloch AF, Shou H, Liu S, et al. On testing for spatial correspondence between maps of human brain structure and function. *NeuroImage*. 2018;178:540-551. doi:10.1016/j.neuroimage.2018.05.070
40. Maslov S, Sneppen K, Zaliznyak A. Pattern Detection in Complex Networks: Correlation Profile of the Internet. *Physica A: Statistical Mechanics and its Applications*. 2004;333:529-540. doi:10.1016/j.physa.2003.06.002
41. Burt JB, Helmer M, Shinn M, Anticevic A, Murray JD. Generative modeling of brain maps with spatial autocorrelation. *NeuroImage*. 2020;220:117038. doi:10.1016/j.neuroimage.2020.117038
42. Wardlaw JM, Smith EE, Biessels GJ, et al. Neuroimaging standards for research into small vessel disease and its contribution to ageing and neurodegeneration. *The Lancet Neurology*. 2013;12(8):822-838. doi:10.1016/S1474-4422(13)70124-8
43. Wardlaw JM, Valdés Hernández MC, Muñoz-Maniega S. What are White Matter Hyperintensities Made of? *J Am Heart Assoc*. 2015;4(6). doi:10.1161/JAHA.114.001140
44. Biesbroek JM, Weaver NA, Hilal S, et al. Impact of Strategically Located White Matter Hyperintensities on Cognition in Memory Clinic Patients with Small Vessel Disease. *PLOS ONE*. 2016;11(11):e0166261. doi:10.1371/journal.pone.0166261
45. ter Telgte A, van Leijsen EMC, Wiegertjes K, Klijn CJM, Tuladhar AM, de Leeuw FE. Cerebral small vessel disease: from a focal to a global perspective. *Nature Reviews Neurology*. 2018;14(7):387-398. doi:10.1038/s41582-018-0014-y
46. Salvalaggio A, De Filippo De Grazia M, Zorzi M, Thiebaut de Schotten M, Corbetta M. Post-stroke deficit prediction from lesion and indirect structural and functional disconnection. *Brain*. 2020;143(7):2173-2188. doi:10.1093/brain/awaa156
47. Foulon C, Cerliani L, Kinkingnéhun S, et al. Advanced lesion symptom mapping analyses and implementation as BCBtoolkit. *Gigascience*. 2018;7(3):1-17. doi:10.1093/gigascience/giy004
48. Talozzi L, Forkel SJ, Pacella V, et al. Latent disconnectome prediction of long-term cognitive-behavioural symptoms in stroke. *Brain*. Published online March 16, 2023:awad013. doi:10.1093/brain/awad013
49. Siddiqi SH, Kletenik I, Anderson MC, et al. Lesion network localization of depression in multiple sclerosis. *Nat Mental Health*. 2023;1(1):36-44. doi:10.1038/s44220-022-00002-y
50. Cohen A, Al-Fatly B, Horn A. GSP1000 Preprocessed Connectome for Lead DBS. Published online February 2, 2024. doi:10.7910/DVN/KKTJQC
51. Horn A, Reich M, Vorwerk J, et al. Connectivity Predicts deep brain stimulation outcome in Parkinson disease. *Annals of Neurology*. 2017;82(1):67-78. doi:10.1002/ana.24974
52. Jiang J, Bruss J, Lee WT, Tranel D, Boes AD. White matter disconnection of left multiple demand network is associated with post-lesion deficits in cognitive control. *Nat Commun*. 2023;14(1):1740. doi:10.1038/s41467-023-37330-1
53. Nadeau C, Bengio Y. Inference for the Generalization Error. *Machine Learning*. 2003;52(3):239-281. doi:10.1023/A:1024068626366
54. Poldrack RA, Huckins G, Varoquaux G. Establishment of Best Practices for Evidence for Prediction: A Review. *JAMA Psychiatry*. 2020;77(5):534-540. doi:10.1001/jamapsychiatry.2019.3671
55. Yeo BTT, Krienen FM, Sepulcre J, et al. The organization of the human cerebral cortex estimated by intrinsic functional connectivity. *J Neurophysiol*. 2011;106(3):1125-1165. doi:10.1152/jn.00338.2011

56. Monje M, Iwasaki A. The neurobiology of long COVID. *Neuron*. 2022;110(21):3484-3496. doi:10.1016/j.neuron.2022.10.006
57. Davis HE, McCorkell L, Vogel JM, Topol EJ. Long COVID: major findings, mechanisms and recommendations. *Nat Rev Microbiol*. 2023;21(3):133-146. doi:10.1038/s41579-022-00846-2
58. Owens CD, Pinto CB, Detwiler S, et al. Cerebral small vessel disease pathology in COVID-19 patients: A systematic review. *Ageing Research Reviews*. 2023;88:101962. doi:10.1016/j.arr.2023.101962
59. Schulz M, Mayer C, Schlemm E, et al. Association of Age and Structural Brain Changes With Functional Connectivity and Executive Function in a Middle-Aged to Older Population-Based Cohort. *Front Aging Neurosci*. 2022;14:782738. doi:10.3389/fnagi.2022.782738
60. Petersen M, Frey BM, Mayer C, et al. Fixel based analysis of white matter alterations in early stage cerebral small vessel disease. *Sci Rep*. 2022;12(1):1581. doi:10.1038/s41598-022-05665-2
61. Nägele FL, Petersen M, Mayer C, et al. Longitudinal alterations in brain microstructure surrounding subcortical ischemic stroke lesions detected by free-water imaging. Published online April 17, 2023:2023.04.14.23288593. doi:10.1101/2023.04.14.23288593
62. Mayer C, Nägele FL, Petersen M, et al. Association between Coffee Consumption and Brain MRI Parameters in the Hamburg City Health Study. *Nutrients*. 2023;15(3):674. doi:10.3390/nu15030674
63. Mayer C, Walther C, Borof K, et al. Association between periodontal disease and microstructural brain alterations in the Hamburg City Health Study. *Journal of Clinical Periodontology*. 2023;n/a(n/a). doi:10.1111/jcpe.13828
64. Rimmele DL, Petersen EL, Schlemm E, et al. Association of Carotid Plaque and Flow Velocity With White Matter Integrity in a Middle-aged to Elderly Population. *Neurology*. Published online September 19, 2022. doi:10.1212/WNL.0000000000201297
65. Schulz M, Petersen M, Cheng B, Thomalla G. Association of structural connectivity with functional brain network segregation in a middle-aged to elderly population. *Front Aging Neurosci*. 2024;16. doi:10.3389/fnagi.2024.1291162
66. Ingwersen T, Mayer C, Petersen M, et al. Functional MRI brain state occupancy in the presence of cerebral small vessel disease— a pre-registered replication analysis of the Hamburg City Health Study. *Imaging Neuroscience*. Published online March 18, 2024. doi:10.1162/imag_a_00122
67. Cheng B, Petersen M, Schulz R, et al. White matter degeneration revealed by fiber-specific analysis relates to recovery of hand function after stroke. *Hum Brain Mapp*. 2021;42(16):5423-5432. doi:10.1002/hbm.25632
68. Laurent JS, Watts R, Adise S, et al. Associations Among Body Mass Index, Cortical Thickness, and Executive Function in Children. *JAMA Pediatrics*. 2020;174(2):170-177. doi:10.1001/jamapediatrics.2019.4708
69. Seo SW, Ahn J, Yoon U, et al. Cortical Thinning in Vascular Mild Cognitive Impairment and Vascular Dementia of Subcortical Type. *Journal of Neuroimaging*. 2010;20(1):37-45. doi:10.1111/j.1552-6569.2008.00293.x
70. Kim HJ, Ye BS, Yoon CW, et al. Cortical thickness and hippocampal shape in pure vascular mild cognitive impairment and dementia of subcortical type. *Eur J Neurol*. 2014;21(5):744-751. doi:10.1111/ene.12376
71. Morys F, Potvin O, Zeighami Y, et al. Obesity-Associated Neurodegeneration Pattern Mimics Alzheimer's Disease in an Observational Cohort Study. *J Alzheimers Dis*. 91(3):1059-1071. doi:10.3233/JAD-220535
72. Lind L. Endothelium-dependent vasodilation, insulin resistance and the metabolic syndrome in an elderly cohort: The Prospective Investigation of the Vasculature in Uppsala Seniors (PIVUS) study. *Atherosclerosis*. 2008;196(2):795-802. doi:10.1016/j.atherosclerosis.2007.01.014
73. Denes A, Drake C, Stordy J, et al. Interleukin-1 Mediates Neuroinflammatory Changes Associated With Diet-Induced Atherosclerosis. *Journal of the American Heart Association*. 1(3):e002006. doi:10.1161/JAHA.112.002006
74. Tucsek Z, Toth P, Sosnowska D, et al. Obesity in Aging Exacerbates Blood–Brain Barrier Disruption, Neuroinflammation, and Oxidative Stress in the Mouse Hippocampus: Effects on Expression of Genes Involved in Beta-Amyloid Generation and Alzheimer's Disease. *The Journals of Gerontology: Series A*. 2014;69(10):1212-1226. doi:10.1093/gerona/glt177
75. Lake BB, Ai R, Kaeser GE, et al. Neuronal subtypes and diversity revealed by single-nucleus RNA sequencing of the human brain. *Science*. 2016;352(6293):1586-1590. doi:10.1126/science.aaf1204
76. Petersen M, Frey BM, Schlemm E, et al. Network Localisation of White Matter Damage in Cerebral Small Vessel Disease. *Scientific Reports*. 2020;10(1):9210. doi:10.1038/s41598-020-66013-w
77. Mayer C, Frey BM, Schlemm E, et al. Linking cortical atrophy to white matter hyperintensities of presumed vascular origin: *Journal of Cerebral Blood Flow & Metabolism*. Published online December 1, 2020. doi:10.1177/0271678X20974170
78. Cheng B, Dietzmann P, Schulz R, et al. Cortical atrophy and transcallosal diaschisis following isolated subcortical stroke. *Journal of Cerebral Blood Flow & Metabolism*. Published online February 2019:0271678X1983158. doi:10.1177/0271678X19831583
79. De Luca A, Kuijf H, Exalto L, Thiebaut de Schotten M, Biessels GJ. Multimodal tract-based MRI metrics outperform whole brain markers in determining cognitive impact of small vessel disease-related brain injury. *Brain Struct Funct*. 2022;227(7):2553-2567. doi:10.1007/s00429-022-02546-2
80. Frey BM, Petersen M, Schlemm E, et al. White matter integrity and structural brain network topology in cerebral small vessel disease: The Hamburg city health study. *Hum Brain Mapp*. 2021;42(5):1406-1415. doi:10.1002/hbm.25301
81. Schlemm E, Frey BM, Mayer C, et al. Equalization of Brain State Occupancy Accompanies Cognitive Impairment in Cerebral Small Vessel Disease. *Biological Psychiatry*. 2022;92(7):592-602. doi:10.1016/j.biopsych.2022.03.019

82. Schulz M, Malherbe C, Cheng B, Thomalla G, Schlemm E. Functional connectivity changes in cerebral small vessel disease - a systematic review of the resting-state MRI literature. *BMC Med*. 2021;19:103. doi:10.1186/s12916-021-01962-1
83. Ding JR, Ding X, Hua B, et al. Altered connectivity patterns among resting state networks in patients with ischemic white matter lesions. *Brain Imaging Behav*. 2018;12(5):1239-1250. doi:10.1007/s11682-017-9793-9
84. Dey AK, Stamenova V, Turner G, Black SE, Levine B. Pathoconnectomics of cognitive impairment in small vessel disease: A systematic review. *Alzheimer's & Dementia*. 2016;12(7):831-845. doi:10.1016/j.jalz.2016.01.007
85. Corbetta M, Kincade JM, Ollinger JM, McAvoy MP, Shulman GL. Voluntary orienting is dissociated from target detection in human posterior parietal cortex. *Nat Neurosci*. 2000;3(3):292-297. doi:10.1038/73009
86. Shulman GL, McAvoy MP, Cowan MC, et al. Quantitative analysis of attention and detection signals during visual search. *J Neurophysiol*. 2003;90(5):3384-3397. doi:10.1152/jn.00343.2003
87. Astafiev SV, Shulman GL, Stanley CM, Snyder AZ, Van Essen DC, Corbetta M. Functional organization of human intraparietal and frontal cortex for attending, looking, and pointing. *J Neurosci*. 2003;23(11):4689-4699. doi:10.1523/JNEUROSCI.23-11-04689.2003
88. Rau A, Schroeter N, Blazhenets G, et al. Widespread white matter oedema in subacute COVID-19 patients with neurological symptoms. *Brain*. 2022;145(9):3203-3213. doi:10.1093/brain/awac045
89. Lu Y, Li X, Geng D, et al. Cerebral Micro-Structural Changes in COVID-19 Patients - An MRI-based 3-month Follow-up Study. *EClinicalMedicine*. 2020;25:100484. doi:10.1016/j.eclinm.2020.100484
90. Matschke J, Lütgehetmann M, Hagel C, et al. Neuropathology of patients with COVID-19 in Germany: a post-mortem case series. *The Lancet Neurology*. 2020;19(11):919-929. doi:10.1016/S1474-4422(20)30308-2
91. Espíndola OM, Gomes YCP, Brandão CO, et al. Inflammatory Cytokine Patterns Associated with Neurological Diseases in Coronavirus Disease 2019. *Ann Neurol*. 2021;89(5):1041-1045. doi:10.1002/ana.26041
92. Schwartz M, Butovsky O, Brück W, Hanisch UK. Microglial phenotype: is the commitment reversible? *Trends Neurosci*. 2006;29(2):68-74. doi:10.1016/j.tins.2005.12.005
93. Greene C, Connolly R, Brennan D, et al. Blood–brain barrier disruption and sustained systemic inflammation in individuals with long COVID-associated cognitive impairment. *Nat Neurosci*. 2024;27(3):421-432. doi:10.1038/s41593-024-01576-9
94. Owens CD, Bonin Pinto C, Mukli P, et al. Vascular mechanisms leading to progression of mild cognitive impairment to dementia after COVID-19: Protocol and methodology of a prospective longitudinal observational study. *PLoS One*. 2023;18(8):e0289508. doi:10.1371/journal.pone.0289508
95. Mayer C, Nägele FL, Petersen M, et al. Free-water diffusion MRI detects structural alterations surrounding white matter hyperintensities in the early stage of cerebral small vessel disease. *J Cereb Blood Flow Metab*. 2022;42(9):1707-1718. doi:10.1177/0271678X221093579
96. Douaud G, Lee S, Alfaro-Almagro F, et al. SARS-CoV-2 is associated with changes in brain structure in UK Biobank. *Nature*. Published online March 7, 2022:1-17. doi:10.1038/s41586-022-04569-5
97. Carfì A, Bernabei R, Landi F, for the Gemelli Against COVID-19 Post-Acute Care Study Group. Persistent Symptoms in Patients After Acute COVID-19. *JAMA*. 2020;324(6):603-605. doi:10.1001/jama.2020.12603
98. Al-Aly Z, Xie Y, Bowe B. High-dimensional characterization of post-acute sequelae of COVID-19. *Nature*. 2021;594(7862):259-264. doi:10.1038/s41586-021-03553-9

4 List of publications and declaration of personal contribution

Study A - **Petersen, M.**, Hoffstaedter, F., Nägele, F. L., Mayer, C., Schell, M., Rimmele, D. L., Zyriax, B.-C., Zeller, T., Kühn, S., Gallinat, J., Fiehler, J., Twerenbold, R., Omidvarnia, A., Patil, K. R., Eickhoff, S. B., Thomalla, G., & Cheng, B. (2024). A latent clinical-anatomical dimension relating metabolic syndrome to brain structure and cognition. *eLife*, *12*, RP93246. https://doi.org/10.7554/eLife.93246

As the lead author of this study, I was responsible for conceptualizing the project, securing data usage permissions, conducting preprocessing and quality assurance for both MRI and cognitive datasets, implementing and conducting the statistical analysis, interpreting results, and drafting the original manuscript.

Study B – **Petersen, M.**, Coenen, M., DeCarli, C., De Luca, A., van der Lelij, E., Alzheimer's Disease Neuroimaging Initiative, Barkhof, F., Benke, T., Chen, C. P. L. H., Dal Bianco, P., Dewenter, A., Duering, M., Enzinger, C., Ewers, M., Koek, H. L., Maier, A. B., Maillard, P. M., McCreary, C. R., Papma, J. M., … Cheng, B. (2024). Enhancing Cognitive Performance Prediction through White Matter Hyperintensity Disconnectivity Assessment: A Multicenter Lesion Network Mapping Analysis of 3,485 Memory Clinic Patients. *medRxiv*.

As the lead author of this study, I was responsible for conceptualizing the project, securing data usage permissions, conducting preprocessing and quality assurance for the MRI dataset, implementing and conducting the statistical analysis, interpreting results, and drafting the original manuscript.

Study C - **Petersen, M.**, Nägele, F. L., Mayer, C., Schell, M., Petersen, E., Kühn, S., Gallinat, J., Fiehler, J., Pasternak, O., Matschke, J., Glatzel, M., Twerenbold, R., Gerloff, C., Thomalla, G., & Cheng, B. (2023). Brain imaging and neuropsychological assessment of individuals recovered from a mild to moderate SARS-CoV-2 infection. *Proceedings of the National Academy of Sciences*, *120*(22), e2217232120. https://doi.org/10.1073/pnas.2217232120

I shared the first authorship for this project with Felix L. Nägele. Together, we were equally responsible for conceptualizing the project, securing data usage permissions, conducting preprocessing and quality assurance for both MRI and cognitive datasets, implementing and conducting the statistical analysis, interpreting results, and drafting the original manuscript.

5 Summaries

5.1 Summary in English

Vascular cognitive impairment (VCI) describes the spectrum of cognitive deficits due to vascular brain pathology, ranging in severity from subtle changes to pronounced dementia. As lifestyle and medical interventions can modify the progression of VCI, a better comprehension of how vascular damage links to cognitive decline is crucial for enhanced prevention and treatment strategies. This thesis presents three studies aimed at deepening our understanding of VCI by examining its effects on brain network macro- and microstructure integrating advanced neuroimaging and broad cognitive phenotyping of multiple large-scale cohorts.

The first study identified a distinct pattern of brain morphological abnormalities, i.e., regional differences in cortical thickness and subcortical volumes, in individuals at vascular risk. This pattern not only mediated the relationship between vascular risk severity and cognitive function but also correlated with both microscale tissue composition and macroscale brain network organization. Together, these insights unravel the complex relationship between brain structure and VCI.

Capitalizing on pooled imaging and cognitive data of 10 memory clinic cohorts, the second study demonstrated that integrating white matter hyperintensity (WMH) data with brain connectivity information to obtain biomarkers capturing the regional WMH-related disconnectivity improves individual-level prediction of cognitive function in VCI. This study further clarified the pathophysiological role of WMH in VCI, particularly by highlighting their disruptive impact on attention-related brain regions.

The third study provided imaging evidence of long-term microstructural abnormalities in the cerebral white matter of individuals post a mild-to-moderate SARS-CoV-2 infection. Despite the absence of WMH, these results could suggest a possible link to vascular pathology. Importantly, even though this imaging profile was identified, the cohort exhibited no significant neuropsychological symptoms 10 months post-infection.

Collectively, these studies integrate advanced neuroimaging with clinical data to offer a comprehensive view of VCI-related brain network abnormalities. By laying down conceptual frameworks for understanding VCI, this thesis provides the basis for future translational and clinical research aimed at improving imaging-based diagnostics, prognosis, and tailored therapeutic interventions for VCI.

5.1 Summary in German

Vaskuläre kognitive Beeinträchtigung (*engl.*, vascular cognitive impairment, VCI) beschreibt das Spektrum kognitiver Defizite aufgrund vaskulärer Hirnpathologien, die in ihrer Schwere von subtilen Veränderungen bis hin zu ausgeprägter Demenz reichen. Lebensstil- und medizinische Maßnahmen können helfen, das Fortschreiten von VCI zu verlangsamen.

Deshalb ist es wichtig zu verstehen, wie vaskuläre Schäden und kognitive Veränderungen zusammenhängen, um Prävention und Behandlung zu verbessern. Diese Dissertation stellt drei Studien vor, die mittels moderner bildgebender Verfahren unser Verständnis davon vertieften, wie VCI die Makro- und Mikrostruktur des Gehirnnetzwerks beeinflusst.

Die erste Studie identifizierte ein spezifisches Muster morphologischer Gehirnveränderungen bei Personen mit vaskulärem Risiko, d.h. regionale Unterschiede in der kortikalen Dicke und subkortikaler Volumina. Dieses Muster mediierte nicht nur die Beziehung zwischen dem Schweregrad des vaskulären Risikos und der kognitiven Funktion, sondern korrelierte auch sowohl mit der zellulären Zusammensetzung des Gewebes als auch mit der Makroarchitektur des Gehirnnetzwerks. Gemeinsam liefern diese Resultate ein verbessertes Verständnis der komplexen Beziehung zwischen Gehirnstruktur und VCI.

Durch die Untersuchung gepoolter bildgebender und kognitiver Daten von 10 Gedächtnisklinik-Kohorten demonstrierte die zweite Studie, dass Daten über Hyperintensitäten der weißen Substanz (*engl.*, white matter hyperintensities of presumed vascular origin, WMH) mit Informationen zur Gehirnkonnektivität integriert werden können, um die regionale WMH-bezogene Diskonnektivität zu erfassen. Diese Biomarker der WMH Netzwerktopologie ermöglichten eine verbesserte individuelle Vorhersage der kognitiven Funktion bei VCI gegenüber WMH Volumina. Diese Studie beleuchtete zudem die pathophysiologische Rolle von WMH bei VCI, insbesondere indem sie deren störenden Einfluss auf aufmerksamkeitsbezogene Gehirnregionen hervorhebt.

Die dritte Studie lieferte bildgebende Evidenz für langfristige mikrostrukturelle Veränderungen in der weißen Substanz des Gehirns von Personen, die sich von einer milden SARS-CoV-2-Infektion genesen sind. Trotzdass keine Unterschiede bezüglich WMH nachweisbar waren, könnten diese Ergebnisse auf einen möglichen Zusammenhang mit vaskulärer Pathologie hinweisen. Wichtig ist, dass trotz der Identifizierung dieses bildgebenden Profils die Kohorte 10 Monate nach der Infektion keine signifikanten neuropsychologischen Symptome aufwies.

Zusammenfassend integrieren diese Studien fortgeschrittene bildgebende Verfahren mit klinischen Daten, um einen umfassenden Blick auf VCI-bezogene Gehirnnetzwerkabnormalitäten zu bieten. Durch die Etablierung konzeptueller Modelle zur Erklärung von VCI schafft diese Dissertation die Grundlage für zukünftige translationale und klinische Forschungen, deren Ziel es ist, bildbasierte Diagnostik, Prognostik und individuell angepasste Therapieansätze für VCI zu optimieren.

6 Acknowledgements / Danksagung

The content of this doctoral thesis reflects my development as a scientist over the three years of my PhD. Much of my personal and professional journey is due to outstanding supervision and a long list of special people who deserve to be mentioned here.

Firstly, I would like to thank my supervisors and mentors Götz Thomalla and Bastian Cheng for all the impulses, support, and wisdom. I came to your lab to learn about brain imaging in cerebrovascular diseases, and you generously shared your knowledge, time and passion with me. I highly appreciate all the opportunities I have received thanks to you.

Thank you to the CSI Lab family: Felix Nägele, Carola Mayer, Maximilian Schell, Moritz Link, Märit Jensen, Caroline Malherbe, Max Schulz, Rafael Bourry, Marlene Heinze, Eckhard Schlemm, Thies Ingwersen and Leander Rimmele. I am thankful for all the insightful discussions, encouragement, and camaraderie.

Furthermore, I would like to highlight my collaborators Geert Jan Biessels, Matthijs Biesbroek, Felix Hoffstaedter, Kaustubh Patil, and Simon Eickhoff. Thank you for your invaluable insights and guidance over the course of my thesis. Also, thanks to the members of the VCI Lab for making the time during my PhD rotation in Utrecht such a valuable experience. My thanks also go to all other collaborators around the world with whom I had the opportunity to work, especially the colleagues in the Meta VCI Map Consortium.

Ich möchte meiner Familie und meinen Freunden für ihre große Unterstützung danken – insbesondere meinen Eltern, meinem Bruder und meinen Großeltern. Ihr habt mir abseits der Hektik der Großstadt viele Momente der Entspannung, immer ein offenes Ohr und viele gute Ratschläge geschenkt. Ein besonderer Dank gilt meiner Freundin Caroline, die mich mit viel Verständnis durch die Höhen und Tiefen meiner Promotion begleitet hat. Nichts relativiert die täglichen Herausforderungen einer Doktorarbeit mehr als ein Tag in der Natur mit dir.

7 Curriculum vitae

Personal Data

Name	Dr. med. Marvin Petersen
Born	01/12/1994, Hofgeismar, Germany
Address	Robert-Koch-Stieg 2, 20249 Hamburg, Germany
Current position	Research fellow and junior doctor (Assistenzarzt)
Current institution	University Medical Center Hamburg-Eppendorf, Germany
ORCID	0000-0001-6426-7167

Qualifications and Career

Medical degree	*10/2013 - 11/2020, University of Hamburg, Germany*
Medical doctorate	*13/04/2021, supervised by Prof. Dr. Götz Thomalla, Network Topological Aspects of Cerebral Small Vessel Disease, University Medical Center Hamburg-Eppendorf, Graduate Research Center 936, Germany*
Residency	*Since 01/04/2021, Department of Neurology, University Medical Center Hamburg-Eppendorf, Germany*
Philosophical Doctorate (PhD)	*Since 01/04/2021, supervised by Prof. Dr. Götz Thomalla, "Alterations of Brain Network Micro- and Macrostructure in Vascular Cognitive Impairment", Hamburg Brain School, University Medical Center Hamburg-Eppendorf, Germany*

Academic Distinctions

- Young Investigator Award – European Stroke Organization Conference (ESOC) 2024 for "Enhancing Cognitive Performance Prediction through White Matter Hyperintensity Disconnectivity Assessment: A Multicenter Lesion Network Mapping Analysis of 3,485 Memory Clinic Patients" (Study B)
- Best Poster Award – European Stroke Organization Conference (ESOC) 2023 for „A latent clinical-anatomical dimension relating metabolic syndrome to brain structure and cognition" (Study A)
- Egon-Bücheler-Award 2021, University of Hamburg

Scholarships

- Doctoral Fellowship, Graduate Research Center 936
- HamburGlobal, University of Hamburg
- Erasmus+, University of Hamburg

8 Eidesstattliche Versicherung *[als letztes Blatt in die Dissertation einzubinden]*

Ich versichere ausdrücklich, dass ich die Arbeit selbständig und ohne fremde Hilfe verfasst, andere als die von mir angegebenen Quellen und Hilfsmittel nicht benutzt und die aus den benutzten Werken wörtlich oder inhaltlich entnommenen Stellen einzeln nach Ausgabe (Auflage und Jahr des Erscheinens), Band und Seite des benutzten Werkes kenntlich gemacht habe.
Ferner versichere ich, dass ich die Dissertation bisher nicht einem Fachvertreter an einer anderen Hochschule zur Überprüfung vorgelegt oder mich anderweitig um Zulassung zur Promotion beworben habe.
Ich erkläre mich einverstanden, dass meine Dissertation vom Dekanat der Medizinischen Fakultät mit einer gängigen Software zur Erkennung von Plagiaten überprüft werden kann.

Unterschrift: .....

RESEARCH ARTICLE

A latent clinical-anatomical dimension relating metabolic syndrome to brain structure and cognition

Marvin Petersen[1]*, Felix Hoffstaedter[2,3], Felix L Nägele[1], Carola Mayer[1], Maximilian Schell[1], D Leander Rimmele[1], Birgit-Christiane Zyriax[4], Tanja Zeller[5,6,7], Simone Kühn[8], Jürgen Gallinat[8], Jens Fiehler[9], Raphael Twerenbold[5,6,7,10], Amir Omidvarnia[2,3], Kaustubh R Patil[2,3], Simon B Eickhoff[2,3], Goetz Thomalla[1], Bastian Cheng[1]

[1]Department of Neurology, University Medical Center Hamburg-Eppendorf, Hamburg, Germany; [2]Institute for Systems Neuroscience, Medical Faculty, Heinrich-Heine University Düsseldorf, Düsseldorf, Germany; [3]Institute of Neuroscience and Medicine, Brain and Behaviour (INM-7), Research Center Jülich, Jülich, Germany; [4]Midwifery Science-Health Services Research and Prevention, Institute for Health Services Research in Dermatology and Nursing (IVDP), University Medical Center Hamburg-Eppendorf, Hamburg, Germany; [5]Department of Cardiology, University Heart and Vascular Center, Hamburg, Germany; [6]German Center for Cardiovascular Research (DZHK), partner site Hamburg/Kiel/Luebeck, Hamburg, Germany; [7]University Center of Cardiovascular Science, University Heart and Vascular Center, Hamburg, Germany; [8]Department of Psychiatry and Psychotherapy, University Medical Center Hamburg-Eppendorf, Hamburg, Germany; [9]Department of Diagnostic and Interventional Neuroradiology, University Medical Center Hamburg-Eppendorf, Hamburg, Germany; [10]Epidemiological Study Center, University Medical Center Hamburg-Eppendorf, Hamburg, Germany

***For correspondence:** mar.petersen@uke.de

Competing interest: See page 19

Funding: See page 20

Preprint posted
12 October 2023
Sent for Review
12 October 2023
Reviewed preprint posted
07 December 2023
Reviewed preprint revised
28 February 2024
Version of Record published
21 March 2024

Reviewing Editor: Jason P Lerch, University of Oxford, United Kingdom

Abstract The link between metabolic syndrome (MetS) and neurodegenerative as well as cerebrovascular conditions holds substantial implications for brain health in at-risk populations. This study elucidates the complex relationship between MetS and brain health by conducting a comprehensive examination of cardiometabolic risk factors, brain morphology, and cognitive function in 40,087 individuals. Multivariate, data-driven statistics identified a latent dimension linking more severe MetS to widespread brain morphological abnormalities, accounting for up to 71% of shared variance in the data. This dimension was replicable across sub-samples. In a mediation analysis, we could demonstrate that MetS-related brain morphological abnormalities mediated the link between MetS severity and cognitive performance in multiple domains. Employing imaging transcriptomics and connectomics, our results also suggest that MetS-related morphological abnormalities are linked to the regional cellular composition and macroscopic brain network organization. By leveraging extensive, multi-domain data combined with a dimensional stratification approach, our analysis provides profound insights into the association of MetS and brain health. These findings can inform effective therapeutic and risk mitigation strategies aimed at maintaining brain integrity.

eLife assessment

This **important** work contributes to our understanding of the combined effects of metabolic syndrome on fronto-temporal gray matter morphology from two large-scale datasets. The evidence

based on state-of-the art multivariate imaging analysis and detailed micro- and macrostructural contextualization analyses is **convincing** and provides an understanding of the neurological correlates of metabolic syndrome, although the study would have benefitted from the inclusion of longitudinal data.

Introduction

Metabolic syndrome (MetS) represents a cluster of cardiometabolic risk factors, including abdominal obesity, arterial hypertension, dyslipidemia, and insulin resistance (***Alberti et al., 2006***). With a prevalence of 23–35% in Western societies, it poses a considerable health challenge, promoting neurodegenerative, and cerebrovascular diseases such as cognitive decline, dementia, and stroke (***Aguilar et al., 2015***; ***Scuteri et al., 2015***; ***Beltrán-Sánchez et al., 2013***; ***Boden-Albala et al., 2008***; ***Atti et al., 2019***). As lifestyle and pharmacological interventions can modify the trajectory of MetS, advancing our understanding of its pathophysiological effects on brain structure and function as potential mediators of MetS-related neurological diseases is crucial to inform and motivate risk reduction strategies (***Eckel et al., 2005***).

Magnetic resonance imaging (MRI) is a powerful non-invasive tool for examining the intricacies of neurological conditions in vivo. Among studies exploring MetS and brain structure, one of the most consistent findings has been alterations in cortical gray matter morphology (***Yates et al., 2012***). Still, our understanding of the relationship between MetS and brain structure is constrained by several factors. To date, there have been only a few studies on MetS effects on gray matter integrity that are well-powered (***Beyer et al., 2019***; ***Lu et al., 2021***; ***Wolf et al., 2016***; ***Tiehuis et al., 2014***). The majority of analyses are based on small sample sizes and report effects only on global measures of brain morphology or a priori-defined regions of interest, limiting their scope (***Tiehuis et al., 2014***; ***McIntosh et al., 2017***; ***Sala et al., 2014***). As a result, reported effects are heterogeneous and most likely difficult to reproduce (***Marek et al., 2022***). Existing large-scale analyses on the isolated effects of individual risk factors (such as hypertension or obesity) do not account for the high covariance of MetS components driven by interacting pathophysiological effects, which may prevent them from capturing the whole picture of MetS as a risk factor composite (***Hamer and Batty, 2019***; ***Opel et al., 2021***; ***Schaare et al., 2019***; ***Borshchev et al., 2019***). In addition, analyses addressing the complex interrelationship of MetS, brain structure, and cognitive functioning by investigating them in conjunction are scarce (***Yates et al., 2012***). Lastly, while previous studies adopted a case-control design treating MetS as a broad diagnostic category (***Lu et al., 2021***; ***Wolf et al., 2016***; ***Tiehuis et al., 2014***), a dimensional approach viewing MetS as a continuum could offer a more nuanced representation of the multivariate, continuous nature of the risk factor composite.

Despite reports on MetS effects on brain structure, the determinants and spatial effect patterns remain unclear. A growing body of evidence shows that spatial patterns of brain pathology are shaped by multi-scale neurobiological processes, ranging from the cellular level to regional dynamics to large-scale brain networks (***Fornito et al., 2015***). Accordingly, disease effects can not only be driven by local properties, when local patterns of tissue composition predispose individual regions to pathology, but also by topological properties of structural and functional brain networks (***Fornito et al., 2015***; ***Seidlitz et al., 2020***). Guided by these concepts, multi-modal and multi-scale analysis approaches could advance our understanding of the mechanisms influencing MetS effects on brain morphology.

We argue that further research leveraging extensive clinical and brain imaging data is required to explore MetS effects on brain morphology. These examinations should integrate (1) a research methodology that strikes a balance between resolving the multivariate connection of MetS and brain structure while accounting for the high covariance of MetS components; (2) the recognition of impaired cognitive function as a pertinent consequence of MetS; and (3) the analysis of the spatial effect pattern of MetS and its possible determinants.

To meet these research needs, we investigated cortical thickness and subcortical volumetric measurements in a pooled sample of two large-scale population-based cohorts from the UK Biobank (UKB) and Hamburg City Health Study (HCHS) comprising in total 40,087 participants. Partial least squares correlation analysis (PLS) was employed to characterize MetS effects on regional brain morphology. PLS is especially suitable for this research task as it identifies overarching latent relationships by establishing a data-driven multivariate mapping between MetS components and brain

morphometric indices. Furthermore, capitalizing on the cognitive phenotyping of both investigated cohorts, we examined the interrelation between MetS, cognitive function, and brain structure in a mediation analysis. Finally, to uncover factors associated with brain region-specific MetS effects, we mapped local cellular as well as network topological attributes to observed MetS-associated cortical abnormalities. With this work, we aimed to advance the understanding of the fundamental principles underlying the neurobiology of MetS.

Results

Sample characteristics

Application of exclusion criteria and quality assessment ruled out 2188 UKB subjects and 30 HCHS subjects resulting in a final analysis sample of 40,087 individuals. For a flowchart providing details on the sample selection procedure please refer to ***Appendix 1—figure 1***. Descriptive statistics are listed in ***Table 1***. To sensitivity analyze our results, as well as to facilitate the comparison with previous reports which primarily rely on a case-control design, we supplemented group statistics comparing individuals with clinically defined MetS and matched controls, where applicable. Corresponding group analysis results are described in more detail in *appendix 2*.

Partial least squares correlation analysis

We investigated the relationship between brain morphological and clinical measures of MetS (abdominal obesity, arterial hypertension, dyslipidemia, insulin resistance) in a PLS considering all individuals from both studies (n=40,087) (***Figure 1***). By this, we aimed to detect the continuous effect of any MetS component independent from a formal binary classification of MetS (present/not present). A correlation matrix relating all considered MetS component measures is displayed in ***Appendix 1—figure 2***. Before conducting the PLS, brain morphological and clinical data were deconfounded for age, sex, education, and cohort effects.

PLS identified eight significant latent variables which represent clinical-anatomical dimensions relating MetS components to brain morphology (***Appendix 1—table 1***). The first latent variable explained 71.20% of the shared variance and was thus further investigated (***Figure 2a***). Specifically, the first latent variable corresponded with a covariance profile of lower severity of MetS (***Figure 2c***; loadings [95% confidence interval]; waist circumference: –0.230 [–0.239, –0.221], hip circumference: –0.187 [–0.195, –0.178], waist-hip ratio: –0.167 [–0.176, –0.158], body mass index: –0.234 [–0.243, –0.226], systolic blood pressure: –0.089 [–0.098, –0.080], diastolic blood pressure: –0.116 [–0.125, –0.107], high-density lipoprotein: 0.099 [0.090, 0.108], low-density lipoprotein: –0.013 [–0.022, –0.004], total cholesterol: 0.003 [–0.006, 0.012], triglycerides: –0.102 [–0.111, –0.092], HbA1c: –0.064 [–0.073, –0.54], glucose: –0.049 [–0.058, –0.039]). Notably, the obesity-related measures showed the strongest contribution to the covariance profile as indicated by the highest loading to the latent variable. Age (<0.001 [–0.009, 0.009]), sex (<0.001 [–0.009, 0.009]), education (<0.001 [–0.009, 0.009]), and cohort (<–0.001 [–0.008, 0.007]) did not significantly contribute to the latent variable, which is compatible with sufficient effects of deconfounding. Details on the second latent variable which explained 22.33% of shared variance are provided in ***Figure 2—figure supplement 1***. In brief, it predominantly related lower HbA1c and blood glucose to higher thickness and volume in lateral frontal, posterior temporal, parietal, and occipital regions and vice versa.

Bootstrap ratios ($= \frac{singular\ vector\ weight}{bootstrap-estimated\ standard\ error}$) were computed to identify brain regions with a significant contribution to the covariance profile (see Methods). Cortical thickness in orbitofrontal, lateral prefrontal, insular, anterior cingulate, and temporal areas as well as volumes of all investigated subcortical regions contributed positively to the covariance profile as indicated by a positive bootstrap ratio (***Figure 2d***). Thus, a higher cortical thickness and subcortical volume in these areas corresponded with less obesity, hypertension, dyslipidemia, and insulin resistance and vice versa, i.e., lower cortical thickness and subcortical volumes with increased severity of MetS. A negative bootstrap ratio was found in superior frontal, parietal, and occipital regions indicating that a higher cortical thickness in these regions corresponded with more severe MetS. This overall pattern was confirmed via conventional, vertex-wise group comparisons of cortical thickness measurements based on the binary classification of individuals with MetS and matched controls (***Appendix 2—figure 4***) as well as subsample analyses considering the UKB and HCHS participants independently (***Figure 2—figure supplements***

Table 1. Descriptive statistics UKB and HCHS.

Metric	Stat*
Age (years)	63.55±7.59 (40087)
Sex (% female)	46.47 (40087)
Education (ISCED)	2.62±0.73 (39944)
Metabolic syndrome components	
Waist circumference (cm)	88.47±12.71 (38800)
Hip circumference (cm)	100.90±8.79 (38801)
Waist-hip ratio	0.88±0.09 (38800)
Body mass index	26.47±4.37 (38701)
$RR_{systolic}$ (mmHg)	138.30±18.57 (31234)
$RR_{diastolic}$ (mmHg)	78.88±10.09 (31238)
Antihypertensive therapy (%)	6.96 (39976)
HDL (mg/dL)	61.76±23.69 (34468)
LDL (mg/dL)	137.38±36.29 (37456)
Cholesterol (mg/dL)	211.29±56.42 (37531)
Triglycerides (mg/dL)	148.90±83.84 (37510)
Lipid lowering therapy (%)	14.44 (39976)
HbA1c (%)	5.37±0.48 (37284)
Blood glucose (mg/dL)	90.29±17.58 (34432)
Antidiabetic therapy (%)	0.45 (39976)
Imaging	
Mean cortical thickness (mm)	2.40±0.09 (40087)
Cognitive variables of the UK Biobank	
Fluid Intelligence	6.63±2.06 (36510)
Matrix Pattern Completion	7.99±2.13 (25771)
Numeric Memory Test	6.69±1.52 (26780)
Paired Associate Learning	6.92±2.63 (26048)
Prospective Memory	1.07±0.39 (37192)
Reaction Time (sec)	594.16±109.08 (37015)
Symbol Digit Substitution	18.96±5.25 (25810)
Tower Rearranging Test	9.91±3.23 (25555)
Trail Making Test A (sec)	223.03±86.51 (26048)
Trail Making Test B (sec)	550.01±270.09 (26048)
Cognitive variables of the Hamburg City Health Study	
Animal Naming Test	24.78±6.92 (2416)
Clock Drawing Test	6.43±1.12 (2479)

Table 1 continued on next page

Table 1 continued

Metric	Stat*
Trail Making Test A (sec)	40.09±14.33 (2290)
Trail Making Test B (sec)	90.05±37.30 (2264)
Multiple-Choice Vocabulary Intelligence Test	31.27±3.58 (2026)
Word List Recall	7.75±1.84 (2342)

*Presented as mean ± SD (N).

2 and 3). The correlation matrix of all spatial effect maps investigated in this study (bootstrap ratio and Schaefer 400-parcellated t-statistic from group comparisons) is visualized in ***Figure 2—figure supplement 4***. All derived effect size maps were significantly correlated (r_{sp} =0.67−0.99, p_{FDR} < 0.05) (***Schaefer et al., 2018***).

Subject-specific imaging and clinical scores for the first latent variable were computed. These scores indicate to which degree an individual expresses the corresponding covariance profiles. By definition, the scores are correlated (r_{sp} = 0.201, p<0.005, ***Figure 2b***) indicating that individuals exhibiting the clinical covariance profile (severity of MetS components) also express the brain morphological pattern. This relationship was robust across a 10-fold cross-validation (avg. r_{sp} = 0.19, ***Appendix 1—table 2***).

These results were consistent in separate PLS analyses for both the UKB and HCHS samples, as displayed in ***Figure 2—figure supplements 2 and 3***. In these subset-specific analyses, cognitive test performances significantly contributed to the first latent variable when included in the PLS. Consequently, the first latent variable associated more severe MetS with both brain morphological abnormalities and poorer cognitive performance.

Mediation analysis of cognitive outcomes

To gain a better understanding of the link between MetS, brain morphology, and cognitive function, we performed a mediation analysis on cognitive test results and subject-specific PLS scores. Therefore, we investigated whether the imaging PLS score (representing MetS-related brain structural abnormalities) acts as a mediator in the relationship between the clinical PLS score (representing MetS severity) and cognitive test performances. Importantly, scores of the main PLS analysis, which did not include cognitive measures, were considered. The corresponding path plots are shown in ***Figure 3***. The imaging score was found to fully mediate the relationship of the clinical score and results of the Trail Making Test B (ab = –0.011, P_{FDR} <0.001; c'=–0.012, P_{FDR} = 0.072; c=–0.023, P_{FDR} <0.001), Fluid Intelligence Test (ab = 0.017, P_{FDR} <0.001; c'=0.011, P_{FDR} = 0.072; c=0.028, P_{FDR} <0.001) as well as Matrix Pattern Completion Test (ab = 0.015, P_{FDR} <0.001; c'=0.010, P_{FDR} = 0.172; c=0.025, P_{FDR} <0.001). Further, the imaging score partially mediated the relationship of the clinical score and results of the Symbol Digit Substitution Test (ab = 0.010, P_{FDR} <0.001; c'=0.036, P_{FDR} <0.001; c=0.046, P_{FDR} <0.001), Numeric Memory Test (ab = 0.014, P_{FDR} <0.001; c'=0.044, P_{FDR} <0.001; c=0.058, P_{FDR} <0.001) and Paired Associate Learning Test (ab = 0.015, P_{FDR} <0.001; c'=0.044, P_{FDR} <0.001; c=0.059, P_{FDR} <0.001). For the remaining cognitive tests, no significant mediation was found.

Contextualization of MetS-associated brain morphological abnormalities

We investigated whether the pattern of MetS effects on cortical structure is linked to the regional density of specific cell populations and global brain network topology in a surface-based contextualization analysis (see Methods).

Therefore, we first used a virtual histology approach to relate the bootstrap ratio from PLS to the differential expression of cell-type specific genes based on microarray data from the Allen Human Brain Atlas (***Hawrylycz et al., 2012***). The results are illustrated in ***Figure 4***. The bootstrap ratio was significantly positively correlated with the density of endothelial cells ($Z_{r_{sp}}$ = 0.190, p_{FDR} = 0.016), microglia ($Z_{r_{sp}}$ = 0.271, p_{FDR} = 0.016), excitatory neurons type 8 ($Z_{r_{sp}}$ = 0.165, p_{FDR} = 0.016), inhibitory neurons type 1 ($Z_{r_{sp}}$ = 0.363, p_{FDR} = 0.036) and excitatory neurons type 6 ($Z_{r_{sp}}$ = 0.146, p_{FDR} = 0.034) indicating that MetS-related brain morphological abnormalities are strongest in regions of the

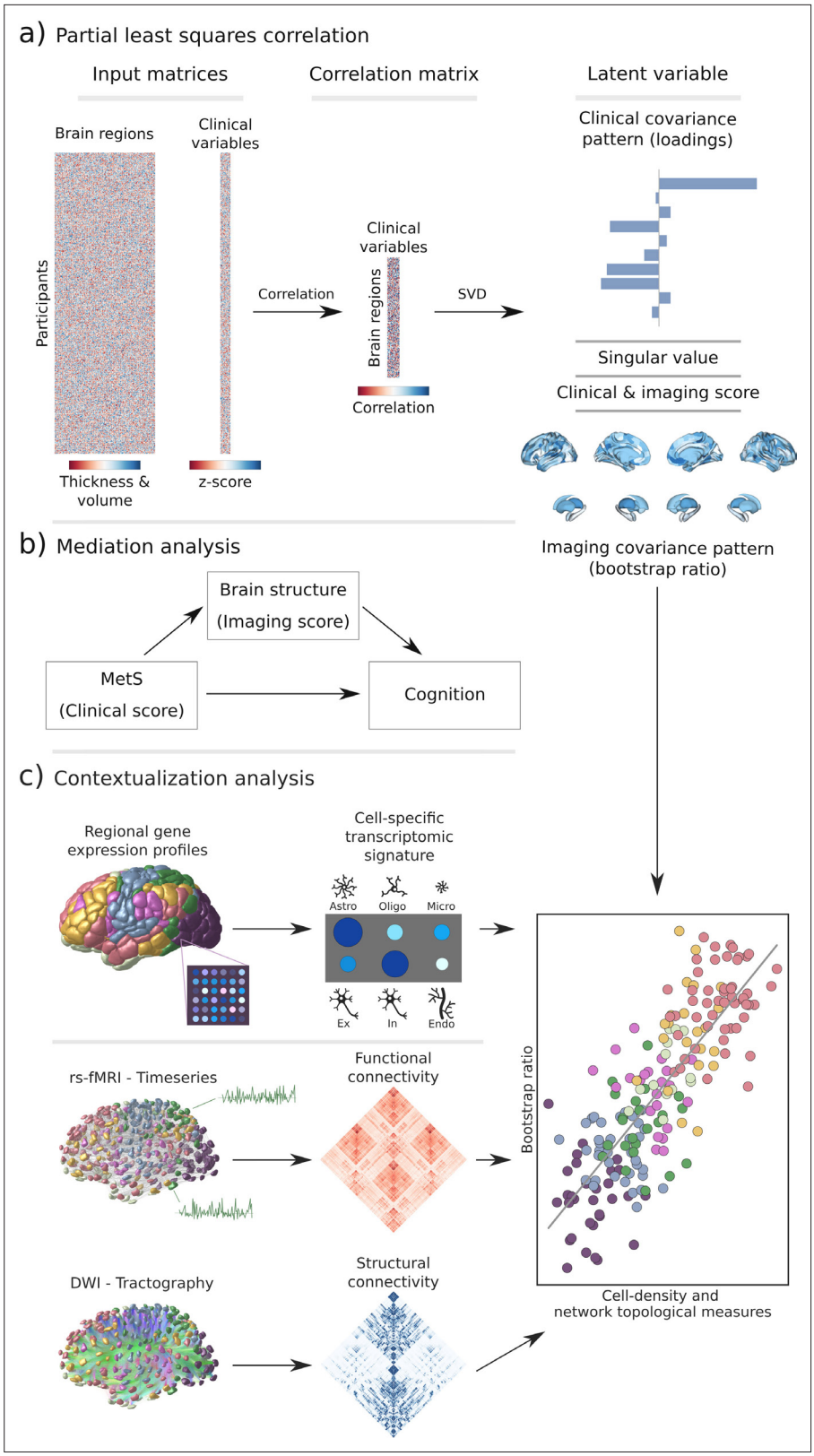

Figure 1. Methodology. (**a**) Illustration of the partial least squares correlation analysis. Starting from two input matrices containing per-subject information of regional morphological measures as well as clinical data (demographic and metabolic syndrome (MetS)-related risk factors) a correlation matrix is computed. This matrix is subsequently subjected to singular value decomposition resulting in a set of mutually orthogonal latent

Figure 1 continued on next page

Figure 1 continued

variables. Latent variables each consist of a left singular vector (here, clinical covariance profile), singular value, and right singular vector (here, imaging covariance profile). In addition, subject-specific clinical and imaging scores are computed. (**b**) The interplay between MetS, brain structure, and cognition was investigated in a post-hoc mediation analysis. We tested whether the relationship between the clinical score, representing MetS severity, and different cognitive test performances was statistically mediated by the imaging score. (**c**) Contextualization analysis. Upper row: based on microarray gene expression data, the densities of different cell populations across the cortex were quantified. Middle and lower row: based on functional and structural group-consensus connectomes based on data from the Human Connectome Project, metrics of functional and structural brain network topology were derived. Cell density as well as connectomic measures were related to the bootstrap ratio via spatial correlations. Modified from ***Petersen et al., 2022b***; ***Zeighami et al., 2019***. Abbreviations: Astro – astrocytes; DWI – diffusion-weighted magnetic resonance imaging; Endo – endothelial cells; Ex – excitatory neuron populations (Ex1-8); In – inhibitory neuron populations (In1-8); Micro – microglia; Oligo – oligodendrocytes; rs-fMRI – resting-state functional magnetic resonance imaging; SVD – singular value decomposition.

highest density of these cell types. No significant associations were found regarding the remaining excitatory neuron types (Ex1-Ex5, Ex7), inhibitory neurons (In2-In8), astrocytes, and oligodendrocytes (***Appendix 1—table 3***). Virtual histology analysis results for bootstrap ratios corresponding with latent variables 2 and 3 are shown in ***Figure 4—figure supplement 1***. As a sensitivity analysis, we contextualized the t-statistic map derived from group statistics. The results remained stable except for excitatory neurons type 6 ($Z_{r_{sp}}$ = 0.145, p_{FDR} = 0.123) and inhibitory neurons type 1 ($Z_{r_{sp}}$ = 0.432, p_{FDR} = 0.108), which no longer showed a significant association (***Figure 4—figure supplement 2***, ***Appendix 1—table 4***).

Second, we associated the bootstrap ratio with three pre-selected measures of brain network topology derived from group consensus functional and structural connectomes of the Human Connectome Project (HCP) (***Figure 5***): weighted degree centrality (marking brain network hubs), neighborhood abnormality, and macroscale functional connectivity gradients (***Petersen et al., 2022b***). The bootstrap ratio showed a medium positive correlation with the functional neighborhood abnormality (r_{sp} = 0.464, p_{spin} < 0.001, p_{smash} < 0.001, p_{rewire} < 0.001) and a strong positive correlation with the structural neighborhood abnormality (r_{sp} = 0.764, p_{spin} = <0.001, p_{smash} < 0.001, p_{rewire} < 0.001) indicating functional and structural interconnectedness of areas exhibiting similar MetS effects. These results remained significant when the t-statistic map was contextualized instead of the bootstrap ratio as well as when neighborhood abnormality measures were derived from consensus connectomes of the HCHS instead of the HCP (***Figure 5—figure supplements 1 and 2***). We found no significant associations for the remaining indices of network topology, i.e., functional degree centrality (r_{sp} = 0.163, p_{spin} = 0 .365, p_{smash} = 0.406, p_{rewire} = 0.870), structural degree centrality (r_{sp} = 0.029, p_{spin} = 0.423, p_{smash} = 0.814, p_{rewire} = 0.103) as well as functional cortical gradient 1 (r_{sp} = 0.152, p_{spin} = 0.313, p_{smash} = 0.406, p_{rewire} = 0.030) and gradient 2 (r_{sp} = –0.177, p_{spin} = 0.313, p_{smash} = 0.406, p_{rewire} < 0.001).

Discussion

We investigated the impact of MetS on brain morphology and cognitive function in a large sample of individuals from two population-based neuroimaging studies. We report three main findings: (1) multivariate, data-driven statistics revealed a latent variable relating MetS and brain health: participants were distributed along a clinical-anatomical dimension of interindividual variability, linking more severe MetS to widespread brain morphological abnormalities. Negative MetS-related brain morphological abnormalities were strongest in orbitofrontal, lateral prefrontal, insular, cingulate, and temporal cortices as well as subcortical areas. Positive MetS-related brain morphological abnormalities were strongest in superior frontal, parietal, and occipital regions. (2) The severity of MetS was associated with executive function and processing speed, memory, and reasoning test performances, and was found to be statistically mediated by MetS-related brain morphological abnormalities. (3) The pattern of MetS-related brain morphological abnormalities appeared to be linked to regional cell composition as well as functional and structural connectivity. These findings were robust across sensitivity analyses. In sum, our study provides an in-depth examination of the intricate relationship between MetS, brain morphology, and cognition. A graphical abstract summarizing the results is included as ***Figure 6***.

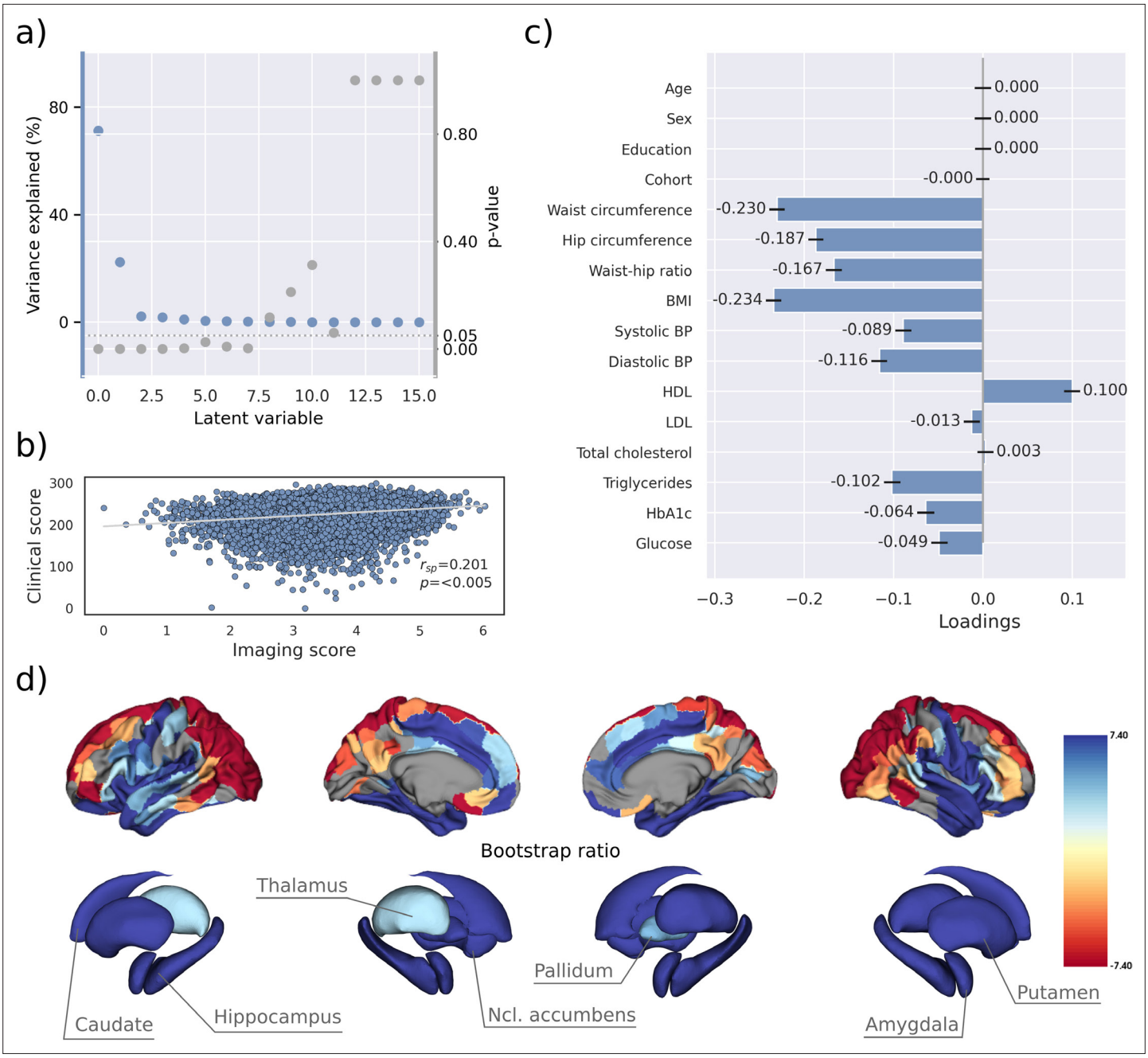

Figure 2. Partial least squares correlation analysis (PLS). (**a**) Explained variance and p-values of latent variables. (**b**) Scatter plot relating subject-specific clinical and imaging PLS scores. Higher scores indicate higher adherence to the respective covariance profile. (**c**) Clinical covariance profile. 95% confidence intervals were calculated via bootstrap resampling. Note that confound removal for age, sex, education, and cohort was performed prior to the PLS. (**d**) Imaging covariance profile represented by bootstrap ratio. A high positive or negative bootstrap ratio indicates high contribution of a brain region to the overall covariance profile. Regions with a significant bootstrap ratio (>1.96 or <–1.96) are highlighted by colors. Abbreviations: BMI – Body mass index, HDL – high-density lipoprotein, LDL – low-density lipoprotein, r_{sp} - Spearman correlation coefficient.

The online version of this article includes the following figure supplement(s) for figure 2:

Figure supplement 1. Partial least squares correlation analysis – Latent variable 2.

Figure supplement 2. Partial least squares correlation analysis – UK Biobank (including cognitive test results).

Figure supplement 3. Partial least squares correlation analysis – Hamburg City Health Study (HCHS) (including cognitive test results).

Figure supplement 4. Spatial correlation of effect size maps.

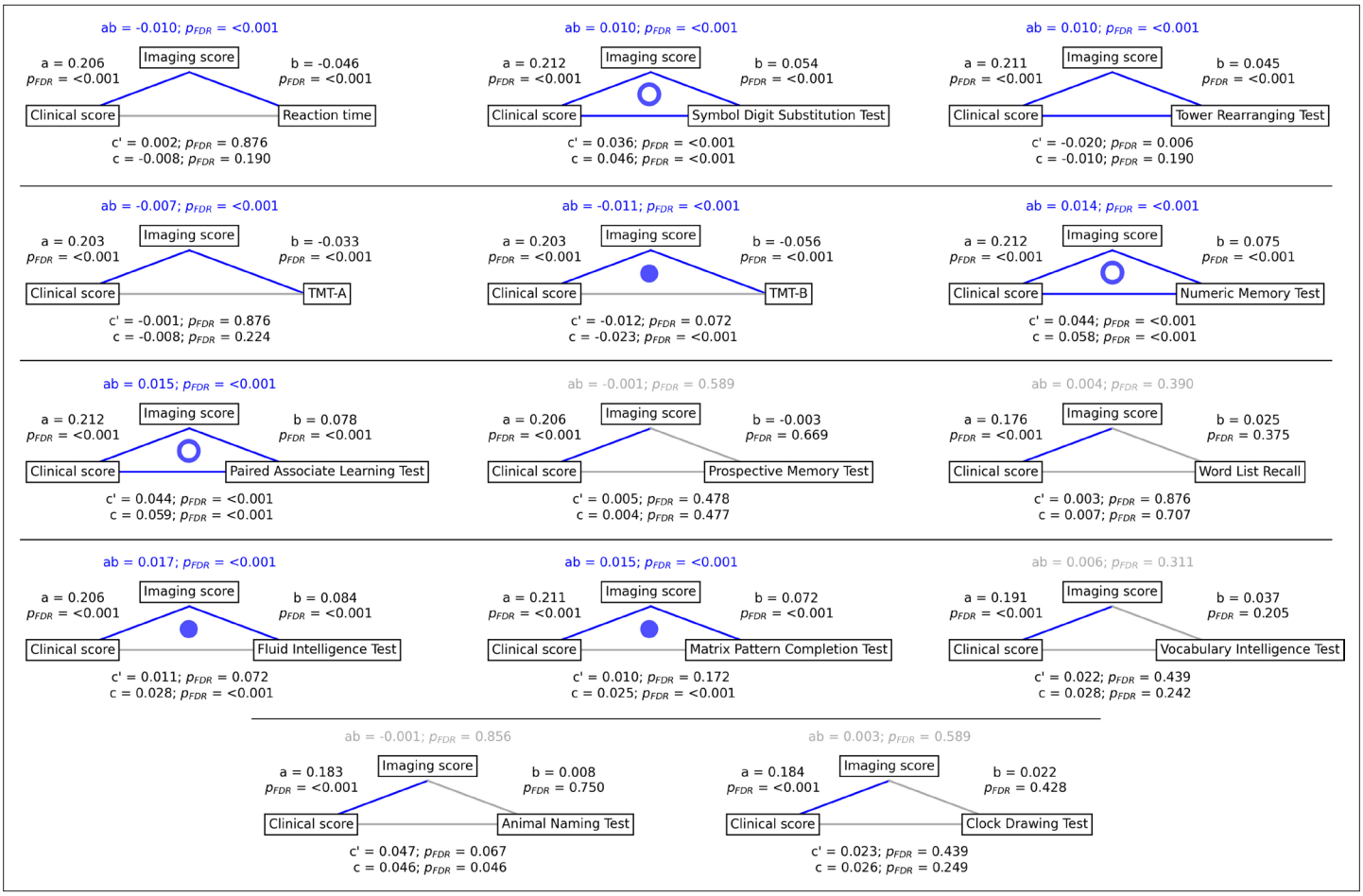

Figure 3. Mediation analysis results. Mediation effects of subject-specific imaging PLS scores on the relationship between metabolic syndrome (MetS) represented by the clinical PLS score and cognitive test performances. Path plots display standardized effects and p-values: (**a**) clinical score to imaging score, (**b**) imaging score to cognitive score, (ab) indirect effect (**c'**) direct effect, and (**c**) total effect. Significant paths are highlighted in blue; non-significant in light gray. If the indirect effect ab was significant, the text for ab is highlighted in blue. A blue dot in the path plot indicates if a relationship is significantly mediated, i.e., the indirect effect ab was significant and the direct effect c' was reduced or non-significant compared to the total effect c. An empty dot indicates a partial mediation, and a full dot indicates a full mediation. Abbreviations: p_{FDR} - false discovery rate-corrected p-values; PLS – partial least squares correlation; TMT-A – Trail Making Test A; TMT-B – Trail Making Test B.

PLS reveals a latent clinical-anatomical dimension relating MetS and brain health

MetS adversely impacts brain health through complex, interacting effects on the cerebral vasculature and parenchyma as shown by histopathological and imaging studies (***Borshchev et al., 2019***). The pathophysiology of MetS involves atherosclerosis, which affects blood supply and triggers inflammation (***Libby et al., 2002***; ***Birdsill et al., 2013***); endothelial dysfunction reducing cerebral vasoreactivity ***Lind, 2008***; breakdown of the blood-brain barrier inciting an inflammatory response ***Hussain et al., 2021***; oxidative stress causing neuronal and mitochondrial dysfunction ***Mullins et al., 2020***; and small vessel injury leading to various pathologies including white matter damage, microinfarcts, and cerebral microbleeds (***Frey et al., 2019***).

To address these interacting effects, we harnessed multivariate, data-driven statistics in the form of a PLS in two large-scale population-based studies to probe for covariance profiles relating the full range of MetS components (such as obesity or arterial hypertension) to regional brain morphological information in a single analysis. PLS identified eight significant latent variables with the first variable explaining the majority (71.20%) of shared variance within the imaging and clinical data (***Figure 2a***). This finding indicates a relatively uniform connection between MetS and brain morphology, implying

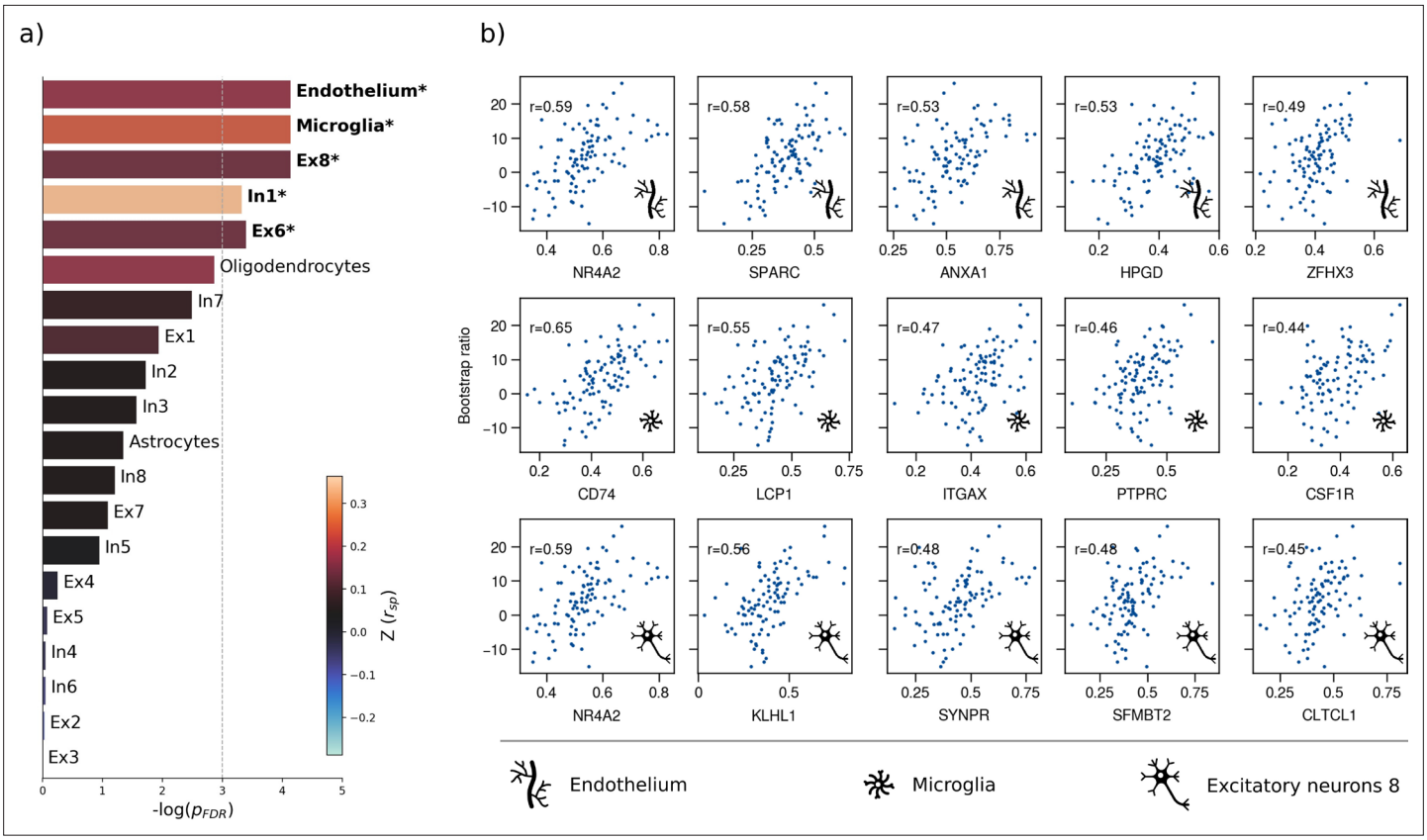

Figure 4. Virtual histology analysis. The regional correspondence between metabolic syndrome (MetS) effects (bootstrap ratio) and cell type-specific gene expression profiles was examined via an ensemble-based gene category enrichment analysis. (**a**) Barplot displaying spatial correlation results. The bar height displays the significance level. Colors encode the aggregate z-transformed Spearman correlation coefficient relating the Schaefer100-parcellated bootstrap ratio and respective cell population densities. Asterisks indicate statistical significance. The significance threshold of p_{FDR} <0.05 is highlighted by a vertical dashed line. (**b**) Scatter plots illustrating spatial correlations between MetS effects and exemplary cortical gene expression profiles per cell population significantly associated across analyses – i.e., endothelium, microglia, and excitatory neurons type 8. Top 5 genes most strongly correlating with the bootstrap ratio map were visualized for each of these cell populations. Icons in the bottom right of each scatter plot indicate the corresponding cell type. A legend explaining the icons is provided at the bottom. First row: endothelium; second row: microglia; third row: excitatory neurons type 8. Virtual histology analysis results for the bootstrap ratios of latent variables 2 and 3 are shown in ***Figure 4—figure supplement 1***. A corresponding plot illustrating the contextualization of the t-statistic derived from group statistics is shown in ***Figure 4—figure supplement 2***. Abbreviations: $-log\left(p_{FDR}\right)$ – negative logarithm of the false discovery rate-corrected p-value derived from spatial lag models (***Dukart et al., 2021***; ***Burt et al., 2018***); r – Spearman correlation coeffient. $Z\left(r_{sp}\right)$ – aggregate z-transformed Spearman correlation coefficient.

The online version of this article includes the following figure supplement(s) for figure 4:

Figure supplement 1. Virtual histology analysis of latent variables 2 and 3.

Figure supplement 2. Sensitivity virtual histology analysis based on t-statistic map from group comparison.

that the associative effects of various MetS components on brain structure are comparatively similar, despite the distinct pathomechanisms each component entails.

PLS revealed that all MetS components were contributing to this latent signature. However, waist circumference, hip circumference, waist-hip ratio, and body mass index consistently contributed higher than the remaining variables across conducted analyses which highlights obesity as the strongest driver of MetS-related brain morphological abnormalities.

We interpret these findings as evidence that MetS-associated conditions jointly contribute to the harmful effects on brain structure rather than affecting it in a strictly individual manner. This notion is supported by previous work in the UKB demonstrating overlapping effects of individual risk factors on brain morphology (***Cox et al., 2019***). Specifically, the first latent variable related to increased severity of obesity, dyslipidemia, arterial hypertension, and insulin resistance with lower thickness in orbitofrontal, lateral prefrontal, insular, cingulate, and temporal cortices as well as lower volume

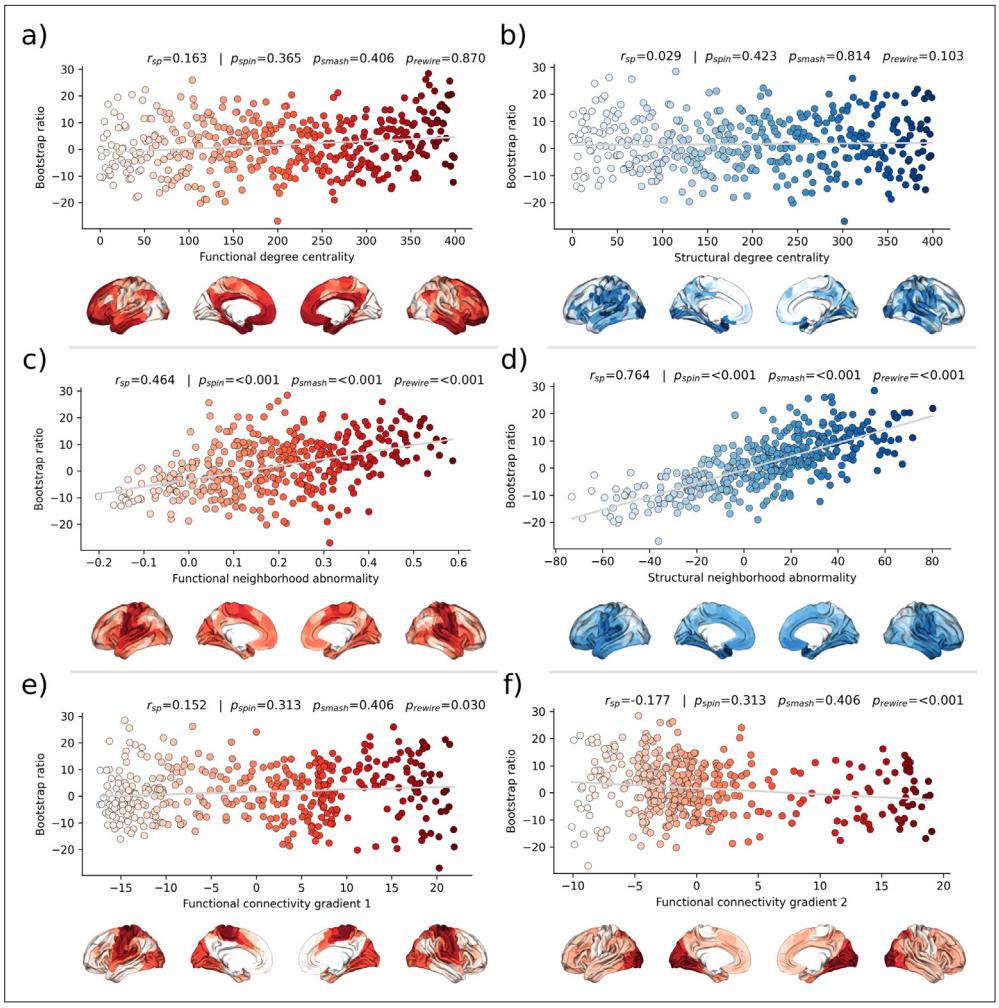

Figure 5. Brain network contextualization. Spatial correlation results derived from relating Schaefer 400×7-parcellated maps of metabolic syndrome (MetS) effects (bootstrap ratio) to network topological indices (red: functional connectivity, blue: structural connectivity). Scatter plots that illustrate the spatial relationship are supplemented by surface plots for anatomical localization. The color coding of cortical regions and associated dots corresponds. (**a and b**) Functional and structural degree centrality rank. (**c and d**) Functional and structural neighborhood abnormality. (**e and f**) Intrinsic functional network hierarchy represented by functional connectivity gradients 1 and 2. Complementary results concerning t-statistic maps derived from group comparisons between MetS subjects and controls are presented in ***Figure 5—figure supplement 1***. Corresponding results after reperforming the analysis with HCHS-derived group-consensus connectomes are presented in ***Figure 5—figure supplement 2***. Abbreviations: HCHS – Hamburg City Health Study; p_{rewire} - p-value derived from network rewiring (***Maslov et al., 2004***); p_{smash} - p-value derived from brainSMASH surrogates (***Burt et al., 2020***); p_{spin} - p-value derived from spin permutation results (***Alexander-Bloch et al., 2018***); r_{sp} - Spearman correlation coefficient.

The online version of this article includes the following figure supplement(s) for figure 5:

Figure supplement 1. Sensitivity network contextualization analysis based on t-statistic map derived from group comparison.

Figure supplement 2. Sensitivity network contextualization analysis based on group-consensus connectomes from the Hamburg City Health Study.

across subcortical regions (***Figure 2c and d***). This profile was consistent in separate PLS analyses of UKB and HCHS participants as well as group comparisons (***Figure 2—figure supplement 4***). Previous research aligns with our detection of a MetS-associated frontotemporal morphometric abnormality pattern (***Beyer et al., 2019***; ***McIntosh et al., 2017***; ***Kotkowski et al., 2019***). As a speculative causative pathway, human and animal studies have related the orbitofrontal, insular, and anterior cingulate cortex to food-related reward processing, taste, and impulse regulation (***Tuulari et al., 2015***; ***Rolls,***

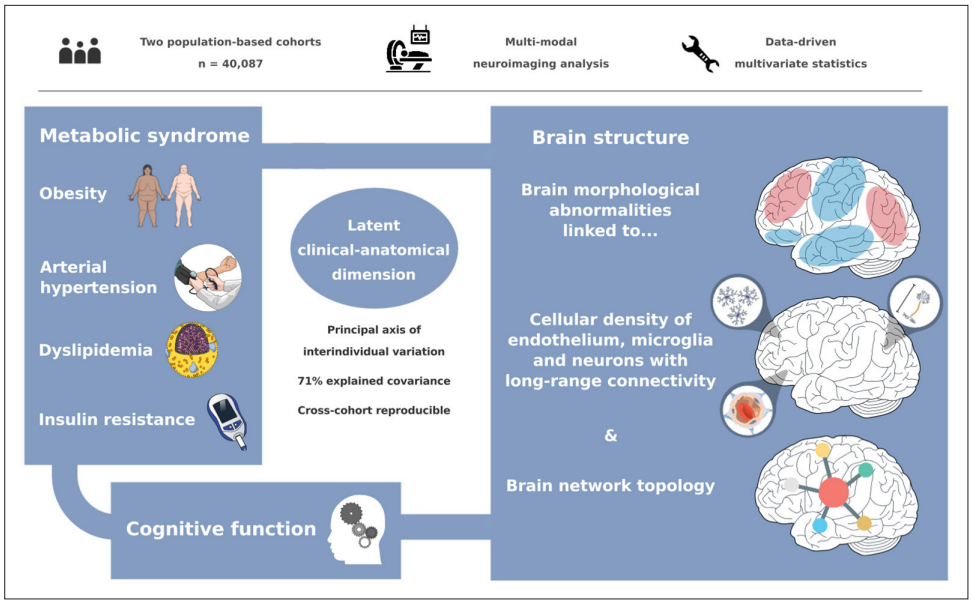

Figure 6. Graphical abstract.

2016). Conceivably, structural alterations of these brain regions are linked to brain functions and behaviors that exacerbate the risk profile leading to MetS (*Rolls, 2023*; *Price et al., 2019*). We also noted a positive MetS-cortical thickness association in superior frontal, parietal, and occipital lobes, a less intuitive finding that has been previously reported (*Krishnadas et al., 2013*; *Leritz et al., 2011*). Although speculative, the positive effects might be due to MetS compensating cholesterol disruptions associated with neurodegenerative processes (*Qin et al., 2021*).

The second latent variable accounted for 22.33% of the shared variance and linked higher markers of insulin resistance and lower dyslipidemia to lower thickness and volume in lateral frontal, posterior temporal, parietal, and occipital regions. The distinct covariance profile of this latent variable, compared to the first, likely indicates a separate pathomechanistic connection between MetS components and brain morphology. Given that HbA1c and blood glucose were the most significant contributors to this variable, insulin resistance might drive the observed clinical-anatomical relationship.

Brain morphological abnormalities mediate the relationship between MetS and cognitive deficits

Cognitive performance has been consistently linked to cardiometabolic risk factors in health and disease (*Genon et al., 2022*). Yet, the pathomechanistic correlates of this relationship remain to be understood. Our mediation analysis revealed that increased MetS severity correlates with worse performance in executive function and processing speed (Symbol Digit Substitution Test, Trail Making Test B), memory (Numeric Memory Test, Paired Associate Learning Test), and reasoning (Fluid intelligence, Matrix Pattern Completion Test), with brain morphological abnormalities statistically mediating these relationships. Additionally, group comparisons indicated poorer cognitive performance in MetS subjects (*Appendix 2—tables 1 and 2*) and including cognitive outcomes in the PLS as clinical variables revealed a significant contribution to the first latent variable (*Figure 2—figure supplements 2 and 3*). These results suggest that MetS is significantly associated with cognitive deficits across various domains, and brain morphological abnormalities are a crucial pathomechanistic link in this relationship. In support of this, previous studies have shown that brain structure mediates the relationship between MetS and cognitive performance in a pediatric sample and elderly patients with vascular cognitive impairment (*Laurent et al., 2020*; *Seo et al., 2010*; *Kim et al., 2014*). The detected latent variable might represent a continuous disease spectrum spanning from minor cognitive deficits due to a cardiometabolic risk profile to severe cognitive deficits due to dementia. In support of this hypothesis, the determined brain morphological abnormality pattern is consistent with the atrophy pattern

found in vascular mild cognitive impairment, vascular dementia, and Alzheimer's dementia (***Seo et al., 2010***; ***Kim et al., 2014***; ***Morys et al., 2023***).

Collectively, these findings highlight the role of MetS in cognitive impairment and underscore the potential impact of therapies targeting cardiometabolic risk factors. Although the definitive role of such therapies in preventing cognitive decline is not yet fully established, emerging evidence suggests that these interventions can mitigate the adverse cognitive effects of MetS (***Veronese et al., 2017***; ***Lennon et al., 2023***; ***Gelber et al., 2013***). As our results highlight obesity as a key factor in the observed clinical-anatomical relationship, we think that future studies should further investigate weight-reducing interventions to examine their effects on cognitive outcomes. Advanced neuroimaging techniques promise to refine these therapeutic approaches by enabling to identify MetS patients at risk of cognitive decline that would benefit the most from targeted interventions for cognitive health protection.

MetS-related brain morphological abnormalities link to cellular tissue composition and network topology

To better understand the emergence of the spatial pattern of MetS-related brain morphological abnormalities, we conducted two contextualization analyses leveraging reference datasets of local gene expression data as well as properties of brain network topology.

Using a virtual histology approach based on regional gene expression data, we investigated MetS effects in relation to cell population densities (***Figure 4***). As the main finding, we report that higher MetS-related brain morphological abnormalities coincide with a higher regional density of endothelial cells. This aligns with the known role of endothelial dysfunction in MetS compromising tissues via chronic vascular inflammation, increased thrombosis risk, and hypoperfusion due to altered vasoreactivity and vascular remodeling (***Lind, 2008***). As endothelial density also indicates the degree of general tissue vascularization, well-vascularized regions are also likely more exposed to cardiometabolic risk factor effects in general (***Libby et al., 2002***). Our results furthermore indicate that microglial density determines a brain region's susceptibility to MetS effects. Microglia are resident macrophages of the central nervous system that sustain neuronal integrity by maintaining a healthy microenvironment. Animal studies have linked microglial activation mediated by blood-brain barrier leakage and systemic inflammation to cardiometabolic risk (***Denes et al., 2012***; ***Tucsek et al., 2014***). Activated microglia can harm the brain structure by releasing reactive oxygen species, proinflammatory cytokines, and proteinases (***Dheen et al., 2007***). Lastly, we found an association with the density of excitatory neurons of subtype 8. These neurons reside in cortical layer 6 and their axons mainly entertain long-range cortico-cortical and cortico-thalamic connections (***Lake et al., 2016***; ***Thomson, 2010***). Consequently, layer 6 neurons might be particularly susceptible to MetS effects due to their exposition to MetS-related white matter disease (***Petersen et al., 2022a***; ***Petersen et al., 2020***). Taken together, the virtual histology analysis indicates that MetS-related brain morphological abnormalities are associated with local cellular fingerprints. Our findings emphasize the involvement of endothelial cells and microglia in brain structural abnormalities due to cardiometabolic risk, marking them as potential targets for therapies aimed at mitigating MetS effects on brain health.

For the second approach, we contextualized MetS-related brain morphological abnormalities using principal topological properties of functional and structural brain networks. We found that regional MetS effects and those of functionally and structurally connected neighbors were correlated (***Figure 5c and d***) – i.e., areas with similar MetS effects tended to be disproportionately interconnected. Put differently, MetS effects coincided within functional and structural brain networks. Therefore, our findings can be interpreted as evidence that a region's functional and structural network embedding – i.e., its individual profile of functional interactions as well as white matter fiber tract connections – are associated with its susceptibility to morphological MetS effects. Multiple mechanisms might explain how connectivity might be associated with MetS-related morphological alterations. For example, microvascular pathology might impair white matter fiber tracts leading to joint degeneration in interconnected cortical brain areas: that is, the occurrence of shared MetS effects within functionally and structurally connected neighborhoods is explained by their shared (dis-)connectivity profile (***Mayer et al., 2021***). In support of this, previous work using diffusion tensor imaging suggests that MetS-related microstructural white matter alterations preferentially occur in the frontal and temporal lobe, which spatially matches the frontotemporal morphometric differences observed in our work (***Segura***

et al., 2009). Furthermore, we speculate on an interplay between local and network-topological susceptibility in MetS: functional and structural connectivity may provide a scaffold for propagating MetS-related perturbation across the network in the sense of a spreading phenomenon – i.e., a region might be influenced by network-driven exposure to regions with higher local susceptibility. Observed degeneration of a region might be aggravated by malfunctional communication to other vulnerable regions including mechanisms of excitotoxicity, diminished excitation and metabolic stress (*Saxena and Caroni, 2011*). These findings underscore the relevance of brain network organization in understanding the pathomechanistic link of MetS and brain morphology.

While this work's strengths lie in a large sample size, high-quality MRI and clinical data, robust image processing, and a comprehensive methodology for examining the link of MetS and brain health, it also has limitations. First, the virtual histology analysis relies on post-mortem brain samples, potentially different from in-vivo profiles. In addition, the predominance of UKB subjects may bias the results, and potential reliability issues of the cognitive assessment in the UKB need to be acknowledged (*Gell et al., 2023*). Lastly, the cross-sectional design restricts the ability for demonstrating causative effects. Longitudinal assessment of the surveyed relationships would provide more robust evidence and therefore, future studies should move in this direction.

Conclusion

Our analysis revealed associative effects of MetS, structural brain integrity, and cognition, complementing existing efforts to motivate and inform strategies for cardiometabolic risk reduction. In conjunction, a characteristic and reproducible structural imaging fingerprint associated with MetS was identified. This pattern of MetS-related brain morphological abnormalities was linked to local histological as well as global network topological features. Collectively, our results highlight how an integrative, multi-modal, and multi-scale analysis approach can lead to a more holistic understanding of the neural underpinnings of MetS and its risk components. As research in this field advances, leveraging neuroimaging may improve personalized cardiometabolic risk mitigation approaches.

Materials and methods

Study population – the UK Biobank and Hamburg City Health Study

Here, we investigated cross-sectional clinical and imaging data from two large-scale population-based cohort studies: (1) the UK Biobank (UKB, n=39,668, age 45–80 years; application number 41655) and (2) the Hamburg City Health Study (HCHS, n=2637, age 45–74 years) (*Miller et al., 2016*; *Jagodzinski et al., 2020*). Both studies recruit large study samples with neuroimaging data alongside a detailed demographic and clinical assessment. Respectively, data for the first visit including a neuroimaging assessment were included. Individuals were excluded if they had a history or a current diagnosis of neurological or psychiatric disease. Field IDs of the used UKB variables are presented in *Appendix 1—table 5*. UKB individuals were excluded based on the non-cancer illnesses codes (http://biobank.ndph.ox.ac.uk/showcase/coding.cgi?id=6). Excluded conditions were Alzheimer's disease; alcohol, opioid, and other dependencies; amyotrophic lateral sclerosis; brain injury; brain abscess; chronic neurological problem; encephalitis; epilepsy; hemorrhage; head injury; meningitis; multiple sclerosis; Parkinson's disease; skull fracture. Same criteria were applied to HCHS individuals based on the neuroradiological evaluation and self-reported diagnoses variables. To enhance comparability to previous studies we supplemented a case-control analysis enabling to complement continuous multivariate statistical analyses by group statistics. Therefore, a MetS sample was identified based on the consensus definition of the International Diabetes Federation (*Appendix 1—table 6*) and matched to a control cohort.

Ethics approval

The UKB was ethically approved by the North West Multi-Centre Research Ethics Committee (MREC). Details on the UKB Ethics and Governance framework are provided online (https://www.ukbiobank.ac.uk/media/0xsbmfmw/egf.pdf). The HCHS was approved by the local ethics committee of the Landesärztekammer Hamburg (State of Hamburg Chamber of Medical Practitioners, PV5131). Good Clinical Practice (GCP), Good Epidemiological Practice (GEP), and the Declaration of Helsinki were the

ethical guidelines that governed the conduct of the HCHS (**Petersen et al., 2020**). Written informed consent was obtained from all participants investigated in this work.

Clinical assessment

In the UK Biobank, a battery of cognitive tests is administered, most of which represent shortened and computerized versions of established tests aiming for a comprehensive and concise assessment of cognition (**Sudlow et al., 2015**). From this battery, we investigated tests for executive function and processing speed (Reaction Time Test, Symbol Digit Substitution Test, Tower Rearranging Test, Trail Making Tests A and B), memory (Numeric Memory Test, Paired Associate Learning Test, Prospective Memory Test), and reasoning (Fluid Intelligence Test, Matrix Pattern Completion Test). Detailed descriptions of the individual tests can be found elsewhere (**Fawns-Ritchie and Deary, 2020**). Furthermore, some tests (Matrix Pattern Completion Test, Numeric Memory Test, Paired Associate Learning Test, Symbol Digit Substitution Test, Trail Making Test, and Tower Rearranging Test) are only administered to a subsample of the UKB imaging cohort explaining the missing test results for a subgroup of participants.

In the HCHS, cognitive testing was administered by a trained study nurse and included the Animal Naming Test, Trail Making Test A and B, Multiple Choice Vocabulary Intelligence Test B, and Word List Recall subtests of the Consortium to Establish a Registry for Alzheimer's Disease Neuropsychological Assessment Battery (CERAD-Plus), as well as the Clock Drawing Test (**Morris et al., 1989**; **Shulman, 2000**).

MRI acquisition

The full UKB neuroimaging protocol can be found online (https://biobank.ctsu.ox.ac.uk/crystal/crystal/docs/brain_mri.pdf; **Miller et al., 2016**). MR images were acquired on a 3 T Siemens Skyra MRI scanner (Siemens, Erlangen, Germany). T1-weighted MRI used a 3D MPRAGE sequence with 1 mm isotropic resolution with the following sequence parameters: repetition time = 2000 ms, echo time = 2.01 ms, 256 axial slices, slice thickness = 1 mm, and in-plane resolution = 1 × 1 mm. In the HCHS, MR images were acquired as well on a 3 T Siemens Skyra MRI scanner. Measurements were performed with a protocol as described in previous work (**Petersen et al., 2020**). In detail, for 3D T1-weighted anatomical images, rapid acquisition gradient-echo sequence (MPRAGE) was used with the following sequence parameters: repetition time = 2500 ms, echo time = 2.12 ms, 256 axial slices, slice thickness = 0.94 mm, and in-plane resolution = 0.83 × 0.83 mm.

Estimation of brain morphological measures

To achieve comparability and reproducibility, the preconfigured and containerized CAT12 pipeline (CAT12.7 r1743; https://github.com/m-wierzba/cat-container; **Wierzba and Hoffstaedter, 2022**) was employed for surface reconstruction and cortical thickness measurement building upon a projection-based thickness estimation method as well as computation of subcortical volumes (**Gaser et al., 2022**). Cortical thickness measures were normalized from individual to 32 k fsLR surface space (conte69) to ensure vertex correspondence across subjects. Subcortical volumes were computed for the Melbourne Subcortex Atlas parcellation resolution 1 (**Tian et al., 2020**). Volumetric measures for the anterior and posterior thalamus parcels were averaged to obtain a single measure for the thalamus. Individuals with a CAT12 image quality rating lower than 75% were excluded during the quality assessment. To facilitate large-scale data management while ensuring provenance tracking and reproducibility, we employed the DataLad-based FAIRly big workflow for image data processing (**Wagner et al., 2022**).

Statistical analysis

Statistical computations and plotting were performed in python 3.9.7 leveraging bctpy (v. 0.6.0), brainstat (v. 0.3.6), brainSMASH (v. 0.11.0), and the ENIGMA toolbox (v. 1.1.3). matplotlib (v. 3.5.1), neuromaps (v. 0.0.1), numpy (v. 1.22.3), pandas (v. 1.4.2), pingouin (v. 0.5.1), pyls (v. 0.0.1), scikit-learn (v. 1.0.2), scipy (v. 1.7.3), seaborn (v. 0.11.2) as well as in matlab (v. 2021b) using ABAnnotate (v. 0.1.1).

Partial least squares correlation analysis

To relate MetS components and brain morphology, we performed a PLS using pyls (https://github.com/rmarkello/pyls; **Markello, 2021**). PLS identifies covariance profiles that relate to two sets of variables in a data-driven multivariate analysis (**Krishnan et al., 2011**). Here, we related regional cortical

thickness and subcortical volumes to clinical measurements of MetS components, i.e., obesity (waist circumference, hip circumference, waist-hip ratio, body mass index), arterial hypertension (systolic blood pressure, diastolic blood pressure), dyslipidemia (high-density lipoprotein, low-density lipoprotein, total cholesterol, triglycerides) and insulin resistance (HbA1c, non-fasting blood glucose). Before conducting the PLS, missing values were imputed via k-nearest neighbor imputation ($n_{neighbor}$ = 4) with imputation only taking into account variables of the same group, i.e., MetS component variables were imputed based on the remaining MetS component data only and not based on demographic variables. To account for age, sex, education, and cohort (UKB/HCHS) as potential confounds, they were regressed out of brain morphological and MetS component data.

We then performed PLS as described in previous work (***Petersen et al., 2022b***). Methodological details are covered in ***Figure 1a*** and ***Box 1***. Brain morphological measures were randomly permuted ($n_{permute}$ = 5000) to assess the statistical significance of derived latent variables and their corresponding covariance profiles. Subject-specific PLS scores, including a clinical score and an imaging score, were computed. Higher scores indicate stronger adherence to the respective covariance profiles: a high clinical score signifies pronounced expression of the clinical profile, and a high imaging score reflects marked adherence to the brain morphological profile. Bootstrap resampling ($n_{bootstrap}$ = 5000) was performed to assess the contribution of individual variables to the imaging-clinical relationship. Confidence intervals (95%) of singular vector weights were computed for clinical variables to assess the significance of their contribution. To estimate the contributions of brain regions, bootstrap ratios were computed as the singular vector weight divided by the bootstrap-estimated standard error. A high bootstrap ratio is indicative of a region's contribution, as a relevant region shows a high singular vector weight alongside a small standard error implying stability across bootstraps. The bootstrap ratio equals a z-score in the case of a normally distributed bootstrap. Hence, brain region contributions were considered significant if the bootstrap ratio was >1.96 or <−1.96 (95% confidence interval). Overall model robustness was assessed via a 10-fold cross-validation by correlating out-of-sample PLS scores within each fold.

Mediation analysis

In a post-hoc mediation analysis, we investigated how the subject-specific clinical PLS score of the first latent variable, reflecting the degree of an individual's expression of the identified MetS risk profile, relates to cognitive test outcomes, and whether this relationship is influenced by the imaging PLS score of the first latent variable, which represents the degree of brain morphological differences (***Figure 1b***). This analysis allows to separate the total effect of the clinical PLS score on cognitive performance into: (1) a direct effect (the immediate link of clinical scores and cognition), and (2) an indirect effect (the portion influenced by the imaging PLS score). This approach helps to disentangle the complex interplay between MetS and cognitive function by examining the role of brain structural effects as a potential intermediary. We considered an indirect effect as mediating if there was a significant association between the clinical and imaging PLS scores, the imaging PLS score was significantly associated with the cognitive outcome, and if the link between clinical scores and cognitive outcomes weakened (partial mediation) or became insignificant (full mediation) after accounting for imaging scores. The significance of mediation was assessed using bootstrapping ($n_{bootstrap}$ = 5000), with models adjusted for age, sex, and education. To obtain standardized estimates, mediation analysis inputs were z-scored beforehand. Given the variation in cognitive test batteries between the UKB and HCHS cohorts, only individuals with results from the respective tests were considered in each mediation analysis. To account for the different versions of the Trail Making Tests A and B used in both cohorts, test results were harmonized through z-scoring within the individual subsamples before a pooled z-scoring step.

Contextualization analysis

We investigated the link of MetS and regional brain morphological measurements in the context of cell-specific gene expression profiles and structural and functional brain network characteristics (***Figure 1c***). Therefore, we used the Schaefer-parcellated (400×7 and 100×7, v.1) bootstrap ratio map and related it to indices representing different gene expression and network topological properties of the human cortex via spatial correlations (Spearman correlation, r_{sp}) on a group-level (***Schaefer et al., 2018***).

Box 1. Partial least squares correlation analysis explained.

Regional morphometric information (Schaefer 400- and Melbourne Subcortical Atlas-parcellated) and clinical data (age sex, education, and MetS component data) were arranged in two matrices $X_{n_{participants} \times n_{brain\ regions}}$ and $Y_{n_{participants} \times n_{clinical\ variables}}$ and then z-scored. Subsequently, a clinical-anatomical correlation matrix was calculated. Singular value decomposition was performed on the correlation matrix which resulted in a set of mutually orthogonal latent variables. The smaller dimension of the correlation matrix – its rank – equals the latent variable count. In our case, this was the number of clinical variables. Singular value decomposition results in a left singular vector matrix ($U_{n_{brain\ regions} \times n_{latent\ variables}}$), right singular vector matrix ($V_{n_{clinical\ variables} \times n_{latent\ variables}}$) and a diagonal matrix of singular values ($\Delta_{n_{latent\ variables} \times n_{latent\ variables}}$). Together, these represent a set of latent variables with a latent variable being composed of a left and right singular vector and a corresponding singular value. Each latent variable represents a specific covariance profile within the input data. A singular vector weights the corresponding original variables to maximize their covariance, i.e., the weighted regional values of a singular vector $U_{\text{brain regions, latent variable j}}$ can be interpreted as a maximally covarying brain morphology pattern and its corresponding clinical substrate ($V_{\text{clinical variables, latent variable j}}$). The explained variance of a latent variable was calculated as the ratio of its corresponding squared singular value to the sum of the remaining squared singular values. Significance of a latent variable was assessed by comparing the observed explained variance to a non-parametric distribution of permuted values acquired by permuting the subject order in *X* ($n_{permute}$ = 5000).

Subject-specific PLS scores measure to which extent an individual expresses a covariance profile represented by a latent variable. Thus, scores can be thought of as factor weightings in factor analysis. A high score describes the high agreement of a participant with the identified pattern. They were calculated by projecting *U* on *X* for an imaging score

$$Imaging\ score = UX$$

and *V* on *Y* for a clinical score

$$Clinical\ score = VY$$

Bootstrap resampling was performed to identify brain regions and clinical variables with a high and robust contribution to the clinical-anatomical association. Individuals were randomly sampled from *X* and *Y* with replacement (n=5000) which resulted in a set of resampled correlation matrices propagated to singular value decomposition resulting in a sampling distribution of singular vector weights for each input variable. This enabled the computation of 95% confidence intervals for the clinical variables and a bootstrap ratio for the brain regions.

$$Bootstrap\ ratio = \frac{Singular\ vector\ weight\ U_{\text{brain region i, latent variable j}}}{Standard\ error\ estimated\ from\ bootstrapping}$$

The bootstrap ratio measures a brain region's contribution to the observed covariance profile of a respective latent variable, as a relevant region shows a high singular vector weight alongside a small standard error implying stability across bootstraps.

Virtual histology analysis. We performed a virtual histology analysis leveraging gene transcription information to quantify the density of different cell populations across the cortex employing the ABAnnotate toolbox (***Lotter, 2022***; ***Dukart et al., 2021***). Genes corresponding with specific cell populations of the central nervous system were identified based on a classification derived from single nucleus-RNA sequencing data (***Lake et al., 2016***). The gene-cell type mapping is provided by the

PsychENCODE database (http://resource.psychencode.org/Datasets/Derived/SC_Decomp/DER-19_Single_cell_markergenes_TPM.xlsx; **Wang et al., 2018**). The abagen toolbox (v. 0.1.3) was used to obtain regional microarray expression data of these genes for Schaefer 100×7 parcels based on the Allen Human Brain Atlas (AHBA) (**Markello et al., 2021**). The Schaefer 100×7 atlas was used as it better matches the sampling density of the AHBA eventually resulting in no parcels with missing values. Regional expression patterns of genes corresponding to astrocytes, endothelial cells, excitatory neuron populations (Ex1-8), inhibitory neuron populations (In1-8), microglia, and oligodendrocytes were extracted. Instead of assessing the correspondence between MetS effects and the expression pattern of each gene directly, we employed ensemble-based gene category enrichment analysis (GCEA) (**Fulcher et al., 2021**). This approach represents a modification to customary GCEA addressing the issues of gene-gene dependency through within-category co-expression which is caused by shared spatial embedding as well as spatial autocorrelation of cortical transcriptomics data. In brief, gene transcription indices were averaged within categories (here cell populations) and spatially correlated with the bootstrap ratio map. Statistical significance was assessed by comparing the empirical correlation coefficients against a null distribution derived from surrogate maps with preserved spatial embedding and autocorrelation computed via a spatial lag model (**Burt et al., 2018**). Further details on the processing steps covered by ABAnnotate can be found elsewhere (https://osf.io/gcxun; **Lotter et al., 2023**).

Brain network topology. To investigate the cortical MetS effects pattern in the context of brain network topology, three connectivity metrics were leveraged based on data from structural and functional brain imaging: weighted degree centrality, neighborhood abnormality as well as macroscale functional connectivity gradients as described previously (**Petersen et al., 2022b**). These were computed based on functional and structural consensus connectomes at group-level derived from the Human Connectome Project Young Adults dataset comprised in the ENIGMA toolbox (**Larivière et al., 2021**; **Larivière et al., 2020**). The preprocessing of these connectomes is described elsewhere (**Larivière et al., 2020**).

Weighted degree centrality. Weighted degree centrality is a measure of a brain region's topological relevance and is commonly used for the identification of brain network hubs (**van den Heuvel and Sporns, 2013**). The degree centrality of a node i was computed as the sum of its functional or structural connection weights (**Rubinov and Sporns, 2010**). The resulting values were ranked before further analysis.

Neighborhood abnormality. Neighborhood abnormality represents a summary measure of a cortical property in the node neighborhood defined by functional or structural brain network connectivity (**Shafiei et al., 2020**). In this work, the MetS-related morphological abnormalities (bootstrap ratio or t-statistic) in nodes j connected to node i were averaged and weighted by their respective functional or structural seed connectivity (w_{ij}):

$$A_i = \frac{1}{N_i}\sum_{j \in N_i} C_j w_{ij}$$

where j is one of the connected nodes N_i , C_j is the measure of MetS-related effects on cortical thickness and the corresponding connection weight w_{ij} . The term $\frac{1}{Ni}$ corrects for the nodal degree by normalizing the number of connections. For example, a high positive or negative A_i represents strong connectivity to nodes of pronounced MetS effects (**Petersen et al., 2022b**).

Functional connectivity gradients. To contextualize the MetS-related morphological abnormalities with the functional network hierarchy, we derived macroscale functional connectivity gradients as a proxy of the canonical sensorimotor-association axis, which determines the distribution of manifold cortical properties (**Margulies et al., 2016**; **Sydnor et al., 2021**). Functional connectivity gradients were derived by applying diffusion map embedding on the HCP functional connectivity matrix using BrainSpace (**Vos de Wael et al., 2020**). A functional connectivity gradient can be interpreted as a spatial axis of connectivity variation spanning the cortical surface, as nodes of similar connectivity profiles are closely located on these axes.

For this analysis, the statistical significance of spatial correlations was assessed via spin permutations (n=1000) which represent a null model preserving the inherent spatial autocorrelation of cortical information (**Alexander-Bloch et al., 2018**). Spin permutations are performed by projecting parcel-wise data onto a sphere which then is randomly rotated. After rotation, information is projected back

on the surface, and a permuted r_{sp} is computed. A p-value is computed comparing the empirical correlation coefficient to the permuted distribution. To assure that our results do not depend on null model choice, we additionally tested our results against a variogram-based null model implemented in the brainSMASH toolbox (https://github.com/murraylab/brainsmash; ***Burt and Murray, 2020***) as well as a network rewiring null model with preserved density and degree sequence (***Burt et al., 2020***; ***Maslov et al., 2004***).

All p-values resulting from both contextualization analyses were FDR-corrected for multiple comparisons. As we conducted this study mindful of the reuse of our resources, the MetS effect maps are provided as separate supplementary files to enable further analyses (***Supplementary files 1-3***).

Sensitivity analyses

For a sensitivity analysis, we reperformed the PLS separately within the UKB and HCHS cohorts. In contrast to the PLS main analysis, in these subset-specific PLS analyses cognitive test performances were also incorporated as clinical variables as cognitive batteries were subset-specific. This approach was employed to evaluate the stability of the results and to determine if cognitive tests contribute to the latent variables.

To test whether the PLS indeed captures the link of MetS and brain morphology, we conducted a group comparison as in previous studies of MetS. Besides descriptive group statistics, the cortical thickness of individuals with MetS and matched controls was compared on a surface vertex-level leveraging the BrainStat toolbox (v 0.3.6, https://brainstat.readthedocs.io/) (***Larivière et al., 2023***). A general linear model was applied correcting for age, sex, education, and cohort effects. Vertex-wise p-values were FDR-corrected for multiple comparisons. To demonstrate the correspondence between the t-statistic and cortical bootstrap ratio maps, we related them via spatial correlation analyses. The t-statistic map was also used for sensitivity analysis of the virtual histology analysis and brain network contextualization.

To ensure that the brain network contextualization results were not biased by the connectome choice, we reperformed the analysis with structural and functional group consensus connectomes based on resting-state functional and diffusion-weighted MRI data from the HCHS. The corresponding connectome reconstruction approaches were described elsewhere (***Petersen et al., 2022b***).

Acknowledgements

German Research Foundation, Schwerpunktprogramm (SPP) 2041, (grant number 454012190) to SBE, GT; German Research Foundation, Sonderforschungsbereich (SFB) 936 (grant number 178316478) project C2 - MP, CM, JF, GT and BC and C7 - SK, JG; German Research Foundation, SFB 1451 & IRTG 2150 to SBE; National Institute of Health, R01 (grant number MH074457) to SBE; European Union's Horizon 2020 Research and Innovation Program (grant number 945539, 826421) to SBE; German Center for Cardiovascular Research (FKZ 81Z1710101 and FKZ 81Z0710102); the Hamburg City Health Study is also supported by Amgen, Astra Zeneca, Bayer, BASF, Deutsche Gesetzliche Unfallversicherung (DGUV), Deutsches Institut für Ernährungsforschung, the Innovative medicine initiative (IMI) under grant number No. 116074, the Fondation Leducq under grant number 16 CVD 03., the euCanSHare grant agreement under grant number 825903-euCanSHare H2020, Novartis, Pfizer, Schiller, Siemens, Unilever, and 'Förderverein zur Förderung der HCHS e.V.'

Additional information

Competing interests

Tanja Zeller: TZ is listed as co-inventor of an international patent on the use of a computing device to estimate the probability of myocardial infarction (PCT/EP2021/073193, International Publication Number WO2022043229A1). TZ is shareholder of the company ART-EMIS GmbH Hamburg. Jürgen Gallinat: JG has received speaker fees from Lundbeck, Janssen-Cilag, Lilly, Otsuka and Boehringer outside the submitted work. Jens Fiehler: JF reported receiving personal fees from Acandis, Cerenovus, Microvention, Medtronic, Phenox, and Penumbra; receiving grants from Stryker and Route 92; being managing director of eppdata; and owning shares in Tegus and Vastrax; all outside the

submitted work. Raphael Twerenbold: RT is listed as co-inventor of an international patent on the use of a computing device to estimate the probability of myocardial infarction (PCT/EP2021/073193, International Publication Number WO2022043229A1). RT is shareholder of the company ART-EMIS GmbH Hamburg. Goetz Thomalla: GT has received fees as consultant or lecturer from Acandis, Alexion, Amarin, Bayer, Boehringer Ingelheim, BristolMyersSquibb/Pfizer, Daichi Sankyo, Portola, and Stryker outside the submitted work. The other authors declare that no competing interests exist.

Funding

Funder	Grant reference number	Author
German Research Foundation	454012190	Simon B Eickhoff Goetz Thomalla
German Research Foundation	178316478	Bastian Cheng
National Institutes of Health	MH074457	Simon B Eickhoff
Horizon 2020 - Research and Innovation Framework Programme	945539	Simon B Eickhoff
Horizon 2020 - Research and Innovation Framework Programme	826421	Simon B Eickhoff

The funders had no role in study design, data collection and interpretation, or the decision to submit the work for publication.

Author contributions

Marvin Petersen, Conceptualization, Resources, Data curation, Software, Formal analysis, Investigation, Visualization, Methodology, Writing - original draft, Project administration, Writing – review and editing; Felix Hoffstaedter, Conceptualization, Resources, Data curation, Software, Writing – review and editing; Felix L Nägele, Carola Mayer, Maximilian Schell, Data curation, Writing – review and editing; D Leander Rimmele, Birgit-Christiane Zyriax, Tanja Zeller, Simone Kühn, Jürgen Gallinat, Jens Fiehler, Raphael Twerenbold, Amir Omidvarnia, Kaustubh R Patil, Writing – review and editing; Simon B Eickhoff, Resources, Funding acquisition, Writing – review and editing; Goetz Thomalla, Supervision, Funding acquisition, Writing – review and editing; Bastian Cheng, Conceptualization, Resources, Supervision, Funding acquisition, Writing – review and editing

Author ORCIDs

Marvin Petersen http://orcid.org/0000-0001-6426-7167
Felix Hoffstaedter https://orcid.org/0000-0001-7163-3110
Carola Mayer http://orcid.org/0000-0002-8065-8683
Raphael Twerenbold https://orcid.org/0000-0003-3814-6542
Amir Omidvarnia http://orcid.org/0000-0002-4744-8721

Ethics

The UKB was ethically approved by the North West Multi-Centre Research Ethics Committee (MREC). Details on the UKB Ethics and Governance framework are provided online (https://www.ukbiobank.ac.uk/media/0xsbmfmw/egf.pdf). The HCHS was approved by the local ethics committee of the Landesärztekammer Hamburg (State of Hamburg Chamber of Medical Practitioners, PV5131). Good Clinical Practice (GCP), Good Epidemiological Practice (GEP) and the Declaration of Helsinki were the ethical guidelines that governed the conduct of the HCHS (Petersen et al., 2020). Written informed consent was obtained from all participants investigated in this work.

Peer review material

Reviewer #1 (Public Review): https://doi.org/10.7554/eLife.93246.3.sa1
Reviewer #2 (Public Review): https://doi.org/10.7554/eLife.93246.3.sa2
Author Response https://doi.org/10.7554/eLife.93246.3.sa3

Additional files

Supplementary files

- Supplementary file 1. Schaefer 400×7-parcellated maps of metabolic syndrome (MetS)-related brain morphological abnormalities (bootstrap ratio from PLS, t-statistic from group comparison).
- Supplementary file 2. Schaefer 100×7-parcellated bootstrap ratio map.
- Supplementary file 3. t-statistic from group comparison on fsLR.
- MDAR checklist

Data availability

UK Biobank data can be obtained via its standardized data access procedure (https://www.ukbiobank.ac.uk/). HCHS participant data used in this analysis is not publicly available for privacy reasons, but access can be established via request to the HCHS steering committee. The analysis code is publicly available on GitHub (https://github.com/csi-hamburg/2023_petersen_mets_brain_morphology (copy archived at ***Petersen, 2023***) and https://github.com/csi-hamburg/CSIframe/wiki/Structural-processing-with-CAT).

References

Aguilar M, Bhuket T, Torres S, Liu B, Wong RJ. 2015. Prevalence of the metabolic syndrome in the United States, 2003-2012. *JAMA* **313**:1973–1974. DOI: https://doi.org/10.1001/jama.2015.4260, PMID: 25988468

Alberti K, Zimmet P, Shaw J. 2006. Metabolic syndrome--a new world-wide definition. A consensus statement from the international diabetes federation. *Diabetic Medicine* **23**:469–480. DOI: https://doi.org/10.1111/j.1464-5491.2006.01858.x, PMID: 16681555

Alexander-Bloch AF, Shou H, Liu S, Satterthwaite TD, Glahn DC, Shinohara RT, Vandekar SN, Raznahan A. 2018. On testing for spatial correspondence between maps of human brain structure and function. *NeuroImage* **178**:540–551. DOI: https://doi.org/10.1016/j.neuroimage.2018.05.070, PMID: 29860082

Atti AR, Valente S, Iodice A, Caramella I, Ferrari B, Albert U, Mandelli L, De Ronchi D. 2019. Metabolic syndrome, mild cognitive impairment, and dementia: A meta-analysis of longitudinal studies. *The American Journal of Geriatric Psychiatry* **27**:625–637. DOI: https://doi.org/10.1016/j.jagp.2019.01.214, PMID: 30917904

Beltrán-Sánchez H, Harhay MO, Harhay MM, McElligott S. 2013. Prevalence and trends of metabolic syndrome in the adult U.S. population, 1999-2010. *Journal of the American College of Cardiology* **62**:697–703. DOI: https://doi.org/10.1016/j.jacc.2013.05.064, PMID: 23810877

Beyer F, Kharabian Masouleh S, Kratzsch J, Schroeter ML, Röhr S, Riedel-Heller SG, Villringer A, Witte AV. 2019. A metabolic obesity profile is associated with decreased gray matter volume in cognitively healthy older adults. *Frontiers in Aging Neuroscience* **11**:202. DOI: https://doi.org/10.3389/fnagi.2019.00202, PMID: 31427957

Birdsill AC, Carlsson CM, Willette AA, Okonkwo OC, Johnson SC, Xu G, Oh JM, Gallagher CL, Koscik RL, Jonaitis EM, Hermann BP, LaRue A, Rowley HA, Asthana S, Sager MA, Bendlin BB. 2013. Low cerebral blood flow is associated with lower memory function in metabolic syndrome. *Obesity* **21**:1313–1320. DOI: https://doi.org/10.1002/oby.20170, PMID: 23687103

Boden-Albala B, Sacco RL, Lee HS, Grahame-Clarke C, Rundek T, Elkind MV, Wright C, Giardina EGV, DiTullio MR, Homma S, Paik MC. 2008. Metabolic syndrome and ischemic stroke risk. *Stroke* **39**:30–35. DOI: https://doi.org/10.1161/STROKEAHA.107.496588

Borshchev Yy, Uspensky YP, Galagudza MM. 2019. Pathogenetic pathways of cognitive dysfunction and dementia in metabolic syndrome. *Life Sciences* **237**:116932. DOI: https://doi.org/10.1016/j.lfs.2019.116932

Burt JB, Demirtaş M, Eckner WJ, Navejar NM, Ji JL, Martin WJ, Bernacchia A, Anticevic A, Murray JD. 2018. Hierarchy of transcriptomic specialization across human cortex captured by structural neuroimaging topography. *Nature Neuroscience* **21**:1251–1259. DOI: https://doi.org/10.1038/s41593-018-0195-0, PMID: 30082915

Burt JB, Helmer M, Shinn M, Anticevic A, Murray JD. 2020. Generative modeling of brain maps with spatial autocorrelation. *NeuroImage* **220**:117038. DOI: https://doi.org/10.1016/j.neuroimage.2020.117038, PMID: 32585343

Burt JB, Murray JD. 2020. brainSMASH. 0.11. Github. https://github.com/murraylab/brainsmash

Cox SR, Lyall DM, Ritchie SJ, Bastin ME, Harris MA, Buchanan CR, Fawns-Ritchie C, Barbu MC, de Nooij L, Reus LM, Alloza C, Shen X, Neilson E, Alderson HL, Hunter S, Liewald DC, Whalley HC, McIntosh AM, Lawrie SM, Pell JP, et al. 2019. Associations between vascular risk factors and brain MRI indices in UK Biobank. *European Heart Journal* **40**:2290–2300. DOI: https://doi.org/10.1093/eurheartj/ehz100

Denes A, Drake C, Stordy J, Chamberlain J, McColl BW, Gram H, Crossman D, Francis S, Allan SM, Rothwell NJ. 2012. Interleukin-1 mediates neuroinflammatory changes associated with diet-induced atherosclerosis. *Journal of the American Heart Association* **1**:e002006. DOI: https://doi.org/10.1161/JAHA.112.002006, PMID: 23130147

Dheen ST, Kaur C, Ling EA. 2007. Microglial activation and its implications in the brain diseases. *Current Medicinal Chemistry* **14**:1189–1197. DOI: https://doi.org/10.2174/092986707780597961, PMID: 17504139

Dukart J, Holiga S, Rullmann M, Lanzenberger R, Hawkins PCT, Mehta MA, Hesse S, Barthel H, Sabri O, Jech R, Eickhoff SB. 2021. JuSpace: A tool for spatial correlation analyses of magnetic resonance imaging data with nuclear imaging derived neurotransmitter maps. *Human Brain Mapping* **42**:555–566. DOI: https://doi.org/10.1002/hbm.25244, PMID: 33079453

Eckel RH, Grundy SM, Zimmet PZ. 2005. The metabolic syndrome. *The Lancet* **365**:1415–1428. DOI: https://doi.org/10.1016/S0140-6736(05)66378-7

Fawns-Ritchie C, Deary IJ. 2020. Reliability and validity of the UK Biobank cognitive tests. *PLOS ONE* **15**:e0231627. DOI: https://doi.org/10.1371/journal.pone.0231627, PMID: 32310977

Fornito A, Zalesky A, Breakspear M. 2015. The connectomics of brain disorders. *Nature Reviews. Neuroscience* **16**:159–172. DOI: https://doi.org/10.1038/nrn3901, PMID: 25697159

Frey BM, Petersen M, Mayer C, Schulz M, Cheng B, Thomalla G. 2019. Characterization of white matter hyperintensities in large-scale MRI-studies. *Frontiers in Neurology* **10**:238. DOI: https://doi.org/10.3389/fneur.2019.00238, PMID: 30972001

Fulcher BD, Arnatkeviciute A, Fornito A. 2021. Overcoming false-positive gene-category enrichment in the analysis of spatially resolved transcriptomic brain atlas data. *Nature Communications* **12**:2669. DOI: https://doi.org/10.1038/s41467-021-22862-1, PMID: 33976144

Gaser C, Dahnke R, Thompson PM, Kurth F, Luders E, Alzheimer's Disease Neuroimaging Initiative. 2022. CAT – A Computational Anatomy Toolbox for the Analysis of Structural MRI Data. *bioRxiv*. DOI: https://doi.org/10.1101/2022.06.11.495736

Gelber RP, Ross GW, Petrovitch H, Masaki KH, Launer LJ, White LR. 2013. Antihypertensive medication use and risk of cognitive impairment: the Honolulu-Asia Aging Study. *Neurology* **81**:888–895. DOI: https://doi.org/10.1212/WNL.0b013e3182a351d4, PMID: 23911753

Gell M, Eickhoff SB, Omidvarnia A, Küppers V, Patil KR, Satterthwaite TD. 2023. The Burden of Reliability: How Measurement Noise Limits Brain-Behaviour Predictions. *bioRxiv*. DOI: https://doi.org/10.1101/2023.02.09.527898

Genon S, Eickhoff SB, Kharabian S. 2022. Linking interindividual variability in brain structure to behaviour. *Nature Reviews. Neuroscience* **23**:307–318. DOI: https://doi.org/10.1038/s41583-022-00584-7, PMID: 35365814

Hamer M, Batty GD. 2019. Association of body mass index and waist-to-hip ratio with brain structure: UK Biobank study. *Neurology* **92**:e594–e600. DOI: https://doi.org/10.1212/WNL.0000000000006879, PMID: 30626649

Hawrylycz MJ, Lein ES, Guillozet-Bongaarts AL, Shen EH, Ng L, Miller JA, van de Lagemaat LN, Smith KA, Ebbert A, Riley ZL, Abajian C, Beckmann CF, Bernard A, Bertagnolli D, Boe AF, Cartagena PM, Chakravarty MM, Chapin M, Chong J, Dalley RA, et al. 2012. An anatomically comprehensive atlas of the adult human brain transcriptome. *Nature* **489**:391–399. DOI: https://doi.org/10.1038/nature11405, PMID: 22996553

Hussain B, Fang C, Chang J. 2021. Blood-brain barrier breakdown: An emerging biomarker of cognitive impairment in normal aging and dementia. *Frontiers in Neuroscience* **15**:688090. DOI: https://doi.org/10.3389/fnins.2021.688090, PMID: 34489623

Jagodzinski A, Johansen C, Koch-Gromus U, Aarabi G, Adam G, Anders S, Augustin M, der Kellen RB, Beikler T, Behrendt C-A, Betz CS, Bokemeyer C, Borof K, Briken P, Busch C-J, Büchel C, Brassen S, Debus ES, Eggers L, Fiehler J, et al. 2020. Rationale and design of the hamburg city health study. *European Journal of Epidemiology* **35**:169–181. DOI: https://doi.org/10.1007/s10654-019-00577-4, PMID: 31705407

Kim HJ, Ye BS, Yoon CW, Noh Y, Kim GH, Cho H, Jeon S, Lee JM, Kim J-H, Seong J-K, Kim C-H, Choe YS, Lee KH, Kim ST, Kim JS, Park SE, Kim J-H, Chin J, Cho J, Kim C, et al. 2014. Cortical thickness and hippocampal shape in pure vascular mild cognitive impairment and dementia of subcortical type. *European Journal of Neurology* **21**:744–751. DOI: https://doi.org/10.1111/ene.12376, PMID: 24495089

Kotkowski E, Price LR, Franklin C, Salazar M, Woolsey M, DeFronzo RA, Blangero J, Glahn DC, Fox PT. 2019. A neural signature of metabolic syndrome. *Human Brain Mapping* **40**:3575–3588. DOI: https://doi.org/10.1002/hbm.24617, PMID: 31062906

Krishnadas R, McLean J, Batty GD, Burns H, Deans KA, Ford I, McConnachie A, McGinty A, McLean JS, Millar K, Sattar N, Shiels PG, Velupillai YN, Packard CJ, Cavanagh J. 2013. Cardio-metabolic risk factors and cortical thickness in a neurologically healthy male population: Results from the psychological, social and biological determinants of ill health (pSoBid) study. *NeuroImage. Clinical* **2**:646–657. DOI: https://doi.org/10.1016/j.nicl.2013.04.012, PMID: 24179815

Krishnan A, Williams LJ, McIntosh AR, Abdi H. 2011. Partial Least Squares (PLS) methods for neuroimaging: A tutorial and review. *NeuroImage* **56**:455–475. DOI: https://doi.org/10.1016/j.neuroimage.2010.07.034, PMID: 20656037

Lake BB, Ai R, Kaeser GE, Salathia NS, Yung YC, Liu R, Wildberg A, Gao D, Fung H-L, Chen S, Vijayaraghavan R, Wong J, Chen A, Sheng X, Kaper F, Shen R, Ronaghi M, Fan J-B, Wang W, Chun J, et al. 2016. Neuronal subtypes and diversity revealed by single-nucleus RNA sequencing of the human brain. *Science* **352**:1586–1590. DOI: https://doi.org/10.1126/science.aaf1204, PMID: 27339989

Larivière S, Rodríguez-Cruces R, Royer J, Caligiuri ME, Gambardella A, Concha L, Keller SS, Cendes F, Yasuda C, Bonilha L, Gleichgerrcht E, Focke NK, Domin M, von Podewills F, Langner S, Rummel C, Wiest R, Martin P, Kotikalapudi R, O'Brien TJ, et al. 2020. Network-based atrophy modeling in the common epilepsies: A worldwide ENIGMA study. *Science Advances* **6**:eabc6457. DOI: https://doi.org/10.1126/sciadv.abc6457, PMID: 33208365

Larivière S, Paquola C, Park B-Y, Royer J, Wang Y, Benkarim O, Vos de Wael R, Valk SL, Thomopoulos SI, Kirschner M, Lewis LB, Evans AC, Sisodiya SM, McDonald CR, Thompson PM, Bernhardt BC. 2021. The

ENIGMA Toolbox: multiscale neural contextualization of multisite neuroimaging datasets. *Nature Methods* **18**:698–700. DOI: https://doi.org/10.1038/s41592-021-01186-4, PMID: 34194050

Larivière S, Bayrak Ş, Vos de Wael R, Benkarim O, Herholz P, Rodriguez-Cruces R, Paquola C, Hong SJ, Misic B, Evans AC, Valk SL, Bernhardt BC. 2023. BrainStat: A toolbox for brain-wide statistics and multimodal feature associations. *NeuroImage* **266**:119807. DOI: https://doi.org/10.1016/j.neuroimage.2022.119807, PMID: 36513290

Laurent JS, Watts R, Adise S, Allgaier N, Chaarani B, Garavan H, Potter A, Mackey S. 2020. Associations among body mass index, cortical thickness, and executive function in children. *JAMA Pediatrics* **174**:170–177. DOI: https://doi.org/10.1001/jamapediatrics.2019.4708, PMID: 31816020

Lennon MJ, Lam BCP, Lipnicki DM, Crawford JD, Peters R, Schutte AE, Brodaty H, Thalamuthu A, Rydberg-Sterner T, Najar J, Skoog I, Riedel-Heller SG, Röhr S, Pabst A, Lobo A, De-la-Cámara C, Lobo E, Bello T, Gureje O, Ojagbemi A, et al. 2023. Use of antihypertensives, blood pressure, and estimated risk of dementia in late life. *JAMA Network Open* **6**:e2333353. DOI: https://doi.org/10.1001/jamanetworkopen.2023.33353

Leritz EC, Salat DH, Williams VJ, Schnyer DM, Rudolph JL, Lipsitz L, Fischl B, McGlinchey RE, Milberg WP. 2011. Thickness of the human cerebral cortex is associated with metrics of cerebrovascular health in a normative sample of community dwelling older adults. *NeuroImage* **54**:2659–2671. DOI: https://doi.org/10.1016/j.neuroimage.2010.10.050, PMID: 21035552

Libby P, Ridker PM, Maseri A. 2002. Inflammation and atherosclerosis. *Circulation* **105**:1135–1143. DOI: https://doi.org/10.1161/hc0902.104353, PMID: 11877368

Lind L. 2008. Endothelium-dependent vasodilation, insulin resistance and the metabolic syndrome in an elderly cohort: the Prospective Investigation of the Vasculature in Uppsala Seniors (PIVUS) study. *Atherosclerosis* **196**:795–802. DOI: https://doi.org/10.1016/j.atherosclerosis.2007.01.014, PMID: 17335830

Lotter L. 2022. Leondlotter/Abannotate: 0.1.1. Version v0.1.1. Zenodo. https://doi.org/10.5281/zenodo.6640855

Lotter LD, Saberi A, Hansen JY, Misic B, Paquola C, Barker GJ, Bokde ALW, Desrivières S, Flor H, Grigis A, Garavan H, Gowland P, Heinz A, Brühl R, Martinot JL, Paillère ML, Artiges E, Orfanos DP, Paus T, Poustka L, et al. 2023. Human Cortex Development Is Shaped by Molecular and Cellular Brain Systems. *bioRxiv*. DOI: https://doi.org/10.1101/2023.05.05.539537

Lu R, Aziz NA, Diers K, Stöcker T, Reuter M, Breteler MMB. 2021. Insulin resistance accounts for metabolic syndrome-related alterations in brain structure. *Human Brain Mapping* **42**:2434–2444. DOI: https://doi.org/10.1002/hbm.25377, PMID: 33769661

Marek S, Tervo-Clemmens B, Calabro FJ, Montez DF, Kay BP, Hatoum AS, Donohue MR, Foran W, Miller RL, Hendrickson TJ, Malone SM, Kandala S, Feczko E, Miranda-Dominguez O, Graham AM, Earl EA, Perrone AJ, Cordova M, Doyle O, Moore LA, et al. 2022. Reproducible brain-wide association studies require thousands of individuals. *Nature* **603**:654–660. DOI: https://doi.org/10.1038/s41586-022-04492-9, PMID: 35296861

Margulies DS, Ghosh SS, Goulas A, Falkiewicz M, Huntenburg JM, Langs G, Bezgin G, Eickhoff SB, Castellanos FX, Petrides M, Jefferies E, Smallwood J. 2016. Situating the default-mode network along a principal gradient of macroscale cortical organization. *PNAS* **113**:12574–12579. DOI: https://doi.org/10.1073/pnas.1608282113, PMID: 27791099

Markello R. 2021. Pylsversion. 0.0.1. Github. https://github.com/rmarkello/pyls

Markello RD, Arnatkeviciute A, Poline JB, Fulcher BD, Fornito A, Misic B. 2021. Standardizing workflows in imaging transcriptomics with the abagen toolbox. *eLife* **10**:e72129. DOI: https://doi.org/10.7554/eLife.72129, PMID: 34783653

Maslov S, Sneppen K, Zaliznyak A. 2004. Detection of topological patterns in complex networks: correlation profile of the internet. *Physica A* **333**:529–540. DOI: https://doi.org/10.1016/j.physa.2003.06.002

Mayer C, Frey BM, Schlemm E, Petersen M, Engelke K, Hanning U, Jagodzinski A, Borof K, Fiehler J, Gerloff C, Thomalla G, Cheng B. 2021. Linking cortical atrophy to white matter hyperintensities of presumed vascular origin. *Journal of Cerebral Blood Flow & Metabolism* **41**:1682–1691. DOI: https://doi.org/10.1177/0271678X20974170

McIntosh EC, Jacobson A, Kemmotsu N, Pongpipat E, Green E, Haase L, Murphy C. 2017. Does medial temporal lobe thickness mediate the association between risk factor burden and memory performance in middle-aged or older adults with metabolic syndrome? *Neuroscience Letters* **636**:225–232. DOI: https://doi.org/10.1016/j.neulet.2016.10.010, PMID: 27717834

Miller KL, Alfaro-Almagro F, Bangerter NK, Thomas DL, Yacoub E, Xu J, Bartsch AJ, Jbabdi S, Sotiropoulos SN, Andersson JLR, Griffanti L, Douaud G, Okell TW, Weale P, Dragonu I, Garratt S, Hudson S, Collins R, Jenkinson M, Matthews PM, et al. 2016. Multimodal population brain imaging in the UK Biobank prospective epidemiological study. *Nature Neuroscience* **19**:1523–1536. DOI: https://doi.org/10.1038/nn.4393, PMID: 27643430

Morris JC, Heyman A, Mohs RC, Hughes JP, van Belle G, Fillenbaum G, Mellits ED, Clark C. 1989. The Consortium to Establish a Registry for Alzheimer's Disease (CERAD). Part I. Clinical and neuropsychological assessment of Alzheimer's disease. *Neurology* **39**:1159–1165. DOI: https://doi.org/10.1212/wnl.39.9.1159, PMID: 2771064

Morys F, Potvin O, Zeighami Y, Vogel J, Lamontagne-Caron R, Duchesne S, Dagher A, Alzheimer's Disease Neuroimaging Initiative. 2023. Obesity-associated neurodegeneration pattern mimics alzheimer's disease in an observational cohort study. *Journal of Alzheimer's Disease* **91**:1059–1071. DOI: https://doi.org/10.3233/JAD-220535, PMID: 36565111

Mullins CA, Gannaban RB, Khan MS, Shah H, Siddik MAB, Hegde VK, Reddy PH, Shin AC. 2020. Neural underpinnings of obesity: The role of oxidative stress and inflammation in the brain. *Antioxidants* **9**:1018. DOI: https://doi.org/10.3390/antiox9101018, PMID: 33092099

Opel N, Thalamuthu A, Milaneschi Y, Grotegerd D, Flint C, Leenings R, Goltermann J, Richter M, Hahn T, Woditsch G, Berger K, Hermesdorf M, McIntosh A, Whalley HC, Harris MA, MacMaster FP, Walter H, Veer IM, Frodl T, Carballedo A, et al. 2021. Brain structural abnormalities in obesity: relation to age, genetic risk, and common psychiatric disorders. *Molecular Psychiatry* **26**:4839–4852. DOI: https://doi.org/10.1038/s41380-020-0774-9, PMID: 32467648

Petersen M, Frey BM, Schlemm E, Mayer C, Hanning U, Engelke K, Fiehler J, Borof K, Jagodzinski A, Gerloff C, Thomalla G, Cheng B. 2020. Network localisation of white matter damage in cerebral small vessel disease. *Scientific Reports* **10**:9210. DOI: https://doi.org/10.1038/s41598-020-66013-w, PMID: 32514044

Petersen M, Frey BM, Mayer C, Kühn S, Gallinat J, Hanning U, Fiehler J, Borof K, Jagodzinski A, Gerloff C, Thomalla G, Cheng B. 2022a. Fixel based analysis of white matter alterations in early stage cerebral small vessel disease. *Scientific Reports* **12**:1581. DOI: https://doi.org/10.1038/s41598-022-05665-2, PMID: 35091684

Petersen M, Nägele FL, Mayer C, Schell M, Rimmele DL, Petersen E, Kühn S, Gallinat J, Hanning U, Fiehler J, Twerenbold R, Gerloff C, Thomalla G, Cheng B. 2022b. Brain network architecture constrains age-related cortical thinning. *NeuroImage* **264**:119721. DOI: https://doi.org/10.1016/j.neuroimage.2022.119721, PMID: 36341953

Petersen M. 2023. 2023_Petersen_Mets_Brain_Morphology. swh:1:rev:e2d655a401fb8da036ba2dc2d8495619f2d223f6. Software Heritage. https://archive.softwareheritage.org/swh:1:dir:363e6d203e471a16d0edc269281eb10c4e165fbd;origin=https://github.com/csi-hamburg/2023_petersen_mets_brain_morphology;visit=swh:1:snp:b531e1fb70dae65f218043a270ce04dfb0192195;anchor=swh:1:rev:e2d655a401fb8da036ba2dc2d8495619f2d223f6

Price AE, Stutz SJ, Hommel JD, Anastasio NC, Cunningham KA. 2019. Anterior insula activity regulates the associated behaviors of high fat food binge intake and cue reactivity in male rats. *Appetite* **133**:231–239. DOI: https://doi.org/10.1016/j.appet.2018.11.011, PMID: 30447231

Qin Q, Yin Y, Xing Y, Wang X, Wang Y, Wang F, Tang Y. 2021. Lipid metabolism in the development and progression of vascular cognitive impairment: A systematic review. *Frontiers in Neurology* **12**:709134. DOI: https://doi.org/10.3389/fneur.2021.709134, PMID: 34867708

Rolls ET. 2016. Reward systems in the brain and nutrition. *Annual Review of Nutrition* **36**:435–470. DOI: https://doi.org/10.1146/annurev-nutr-071715-050725, PMID: 27146018

Rolls ET. 2023. The orbitofrontal cortex, food reward, body weight and obesity. *Social Cognitive and Affective Neuroscience* **18**:nsab044. DOI: https://doi.org/10.1093/scan/nsab044, PMID: 33830272

Rubinov M, Sporns O. 2010. Complex network measures of brain connectivity: uses and interpretations. *NeuroImage* **52**:1059–1069. DOI: https://doi.org/10.1016/j.neuroimage.2009.10.003, PMID: 19819337

Sala M, de Roos A, van den Berg A, Altmann-Schneider I, Slagboom PE, Westendorp RG, van Buchem MA, de Craen AJM, van der Grond J. 2014. Microstructural brain tissue damage in metabolic syndrome. *Diabetes Care* **37**:493–500. DOI: https://doi.org/10.2337/dc13-1160, PMID: 24089543

Saxena S, Caroni P. 2011. Selective neuronal vulnerability in neurodegenerative diseases: from stressor thresholds to degeneration. *Neuron* **71**:35–48. DOI: https://doi.org/10.1016/j.neuron.2011.06.031, PMID: 21745636

Schaare HL, Kharabian Masouleh S, Beyer F, Kumral D, Uhlig M, Reinelt JD, Reiter AMF, Lampe L, Babayan A, Erbey M, Roebbig J, Schroeter ML, Okon-Singer H, Müller K, Mendes N, Margulies DS, Witte AV, Gaebler M, Villringer A. 2019. Association of peripheral blood pressure with gray matter volume in 19- to 40-year-old adults. *Neurology* **92**:e758–e773. DOI: https://doi.org/10.1212/WNL.0000000000006947, PMID: 30674602

Schaefer A, Kong R, Gordon EM, Laumann TO, Zuo X-N, Holmes AJ, Eickhoff SB, Yeo BTT. 2018. Local-global parcellation of the human cerebral cortex from intrinsic functional connectivity MRI. *Cerebral Cortex* **28**:3095–3114. DOI: https://doi.org/10.1093/cercor/bhx179, PMID: 28981612

Scuteri A, Laurent S, Cucca F, Cockcroft J, Cunha PG, Mañas LR, Mattace Raso FU, Muiesan ML, Ryliškytė L, Rietzschel E, Strait J, Vlachopoulos C, Völzke H, Lakatta EG, Nilsson PM, Metabolic Syndrome and Arteries Research Consortium. 2015. Metabolic syndrome across Europe: different clusters of risk factors. *European Journal of Preventive Cardiology* **22**:486–491. DOI: https://doi.org/10.1177/2047487314525529, PMID: 24647805

Segura B, Jurado MA, Freixenet N, Falcón C, Junqué C, Arboix A. 2009. Microstructural white matter changes in metabolic syndrome: a diffusion tensor imaging study. *Neurology* **73**:438–444. DOI: https://doi.org/10.1212/WNL.0b013e3181b163cd, PMID: 19667318

Seidlitz J, Nadig A, Liu S, Bethlehem RAI, Vértes PE, Morgan SE, Váša F, Romero-Garcia R, Lalonde FM, Clasen LS, Blumenthal JD, Paquola C, Bernhardt B, Wagstyl K, Polioudakis D, de la Torre-Ubieta L, Geschwind DH, Han JC, Lee NR, Murphy DG, et al. 2020. Transcriptomic and cellular decoding of regional brain vulnerability to neurogenetic disorders. *Nature Communications* **11**:3358. DOI: https://doi.org/10.1038/s41467-020-17051-5, PMID: 32620757

Seo SW, Ahn J, Yoon U, Im K, Lee JM, Tae Kim S, Ahn HJ, Chin J, Jeong Y, Na DL. 2010. Cortical thinning in vascular mild cognitive impairment and vascular dementia of subcortical type. *Journal of Neuroimaging* **20**:37–45. DOI: https://doi.org/10.1111/j.1552-6569.2008.00293.x, PMID: 19220710

Shafiei G, Markello RD, Makowski C, Talpalaru A, Kirschner M, Devenyi GA, Guma E, Hagmann P, Cashman NR, Lepage M, Chakravarty MM, Dagher A, Mišić B. 2020. Spatial patterning of tissue volume loss in schizophrenia

reflects brain network architecture. *Biological Psychiatry* **87**:727–735. DOI: https://doi.org/10.1016/j.biopsych.2019.09.031, PMID: 31837746

Shulman KI. 2000. Clock-drawing: is it the ideal cognitive screening test? *International Journal of Geriatric Psychiatry* **15**:548–561. DOI: https://doi.org/10.1002/1099-1166(200006)15:6<548::aid-gps242>3.0.co;2-u, PMID: 10861923

Sudlow C, Gallacher J, Allen N, Beral V, Burton P, Danesh J, Downey P, Elliott P, Green J, Landray M, Liu B, Matthews P, Ong G, Pell J, Silman A, Young A, Sprosen T, Peakman T, Collins R. 2015. UK biobank: an open access resource for identifying the causes of a wide range of complex diseases of middle and old age. *PLOS Medicine* **12**:e1001779. DOI: https://doi.org/10.1371/journal.pmed.1001779, PMID: 25826379

Sydnor VJ, Larsen B, Bassett DS, Alexander-Bloch A, Fair DA, Liston C, Mackey AP, Milham MP, Pines A, Roalf DR, Seidlitz J, Xu T, Raznahan A, Satterthwaite TD. 2021. Neurodevelopment of the association cortices: Patterns, mechanisms, and implications for psychopathology. *Neuron* **109**:2820–2846. DOI: https://doi.org/10.1016/j.neuron.2021.06.016, PMID: 34270921

Thomson A. 2010. Neocortical layer 6, a review. *Frontiers in Neuroanatomy* **4**:13. DOI: https://doi.org/10.3389/fnana.2010.00013

Tian Y, Margulies DS, Breakspear M, Zalesky A. 2020. Topographic organization of the human subcortex unveiled with functional connectivity gradients. *Nature Neuroscience* **23**:1421–1432. DOI: https://doi.org/10.1038/s41593-020-00711-6, PMID: 32989295

Tiehuis AM, van der Graaf Y, Mali WPTM, Vincken K, Muller M, Geerlings MI, SMART Study Group. 2014. Metabolic syndrome, prediabetes, and brain abnormalities on MRI in patients with manifest arterial disease: the SMART-MR study. *Diabetes Care* **37**:2515–2521. DOI: https://doi.org/10.2337/dc14-0154, PMID: 24947788

Tucsek Z, Toth P, Sosnowska D, Gautam T, Mitschelen M, Koller A, Szalai G, Sonntag WE, Ungvari Z, Csiszar A. 2014. Obesity in aging exacerbates blood-brain barrier disruption, neuroinflammation, and oxidative stress in the mouse hippocampus: Effects on expression of genes involved in beta-amyloid generation and alzheimer's disease. *The Journals of Gerontology Series A* **69**:1212–1226. DOI: https://doi.org/10.1093/gerona/glt177

Tuulari JJ, Karlsson HK, Hirvonen J, Salminen P, Nuutila P, Nummenmaa L. 2015. Neural circuits for cognitive appetite control in healthy and obese individuals: an fMRI study. *PLOS ONE* **10**:e0116640. DOI: https://doi.org/10.1371/journal.pone.0116640, PMID: 25658479

van den Heuvel MP, Sporns O. 2013. Network hubs in the human brain. *Trends in Cognitive Sciences* **17**:683–696. DOI: https://doi.org/10.1016/j.tics.2013.09.012

Veronese N, Facchini S, Stubbs B, Luchini C, Solmi M, Manzato E, Sergi G, Maggi S, Cosco T, Fontana L. 2017. Weight loss is associated with improvements in cognitive function among overweight and obese people: A systematic review and meta-analysis. *Neuroscience & Biobehavioral Reviews* **72**:87–94. DOI: https://doi.org/10.1016/j.neubiorev.2016.11.017

Vos de Wael R, Benkarim O, Paquola C, Lariviere S, Royer J, Tavakol S, Xu T, Hong S-J, Langs G, Valk S, Misic B, Milham M, Margulies D, Smallwood J, Bernhardt BC. 2020. BrainSpace: a toolbox for the analysis of macroscale gradients in neuroimaging and connectomics datasets. *Communications Biology* **3**:103. DOI: https://doi.org/10.1038/s42003-020-0794-7, PMID: 32139786

Wagner AS, Waite LK, Wierzba M, Hoffstaedter F, Waite AQ, Poldrack B, Eickhoff SB, Hanke M. 2022. FAIRly big: A framework for computationally reproducible processing of large-scale data. *Scientific Data* **9**:80. DOI: https://doi.org/10.1038/s41597-022-01163-2, PMID: 35277501

Wang D, Liu S, Warrell J, Won H, Shi X, Navarro FCP, Clarke D, Gu M, Emani P, Yang YT, Xu M, Gandal MJ, Lou S, Zhang J, Park JJ, Yan C, Rhie SK, Manakongtreecheep K, Zhou H, Nathan A, et al. 2018. Comprehensive functional genomic resource and integrative model for the human brain. *Science* **362**:eaat8464. DOI: https://doi.org/10.1126/science.aat8464, PMID: 30545857

Wierzba M, Hoffstaedter F. 2022. CAT - computational anatomy Toolbox. 12.7. Github. https://github.com/m-wierzba/cat-container

Wolf EJ, Sadeh N, Leritz EC, Logue MW, Stoop TB, McGlinchey R, Milberg W, Miller MW. 2016. Posttraumatic stress disorder as a catalyst for the association between metabolic syndrome and reduced cortical thickness. *Biological Psychiatry* **80**:363–371. DOI: https://doi.org/10.1016/j.biopsych.2015.11.023, PMID: 26826875

Yates KF, Sweat V, Yau PL, Turchiano MM, Convit A. 2012. Impact of metabolic syndrome on cognition and brain: A selected review of the literature. *Arteriosclerosis, Thrombosis, and Vascular Biology* **32**:2060–2067. DOI: https://doi.org/10.1161/ATVBAHA.112.252759, PMID: 22895667

Zeighami Y, Fereshtehnejad S-M, Dadar M, Collins DL, Postuma RB, Mišić B, Dagher A. 2019. A clinical-anatomical signature of Parkinson's disease identified with partial least squares and magnetic resonance imaging. *NeuroImage* **190**:69–78. DOI: https://doi.org/10.1016/j.neuroimage.2017.12.050, PMID: 29277406

Zhu AH, Salminen LE, Thompson PM, Jahanshad N. 2019. UK Biobank data parser. Github. https://github.com/USC-IGC/ukbb_parser

Appendix 1

General appendix

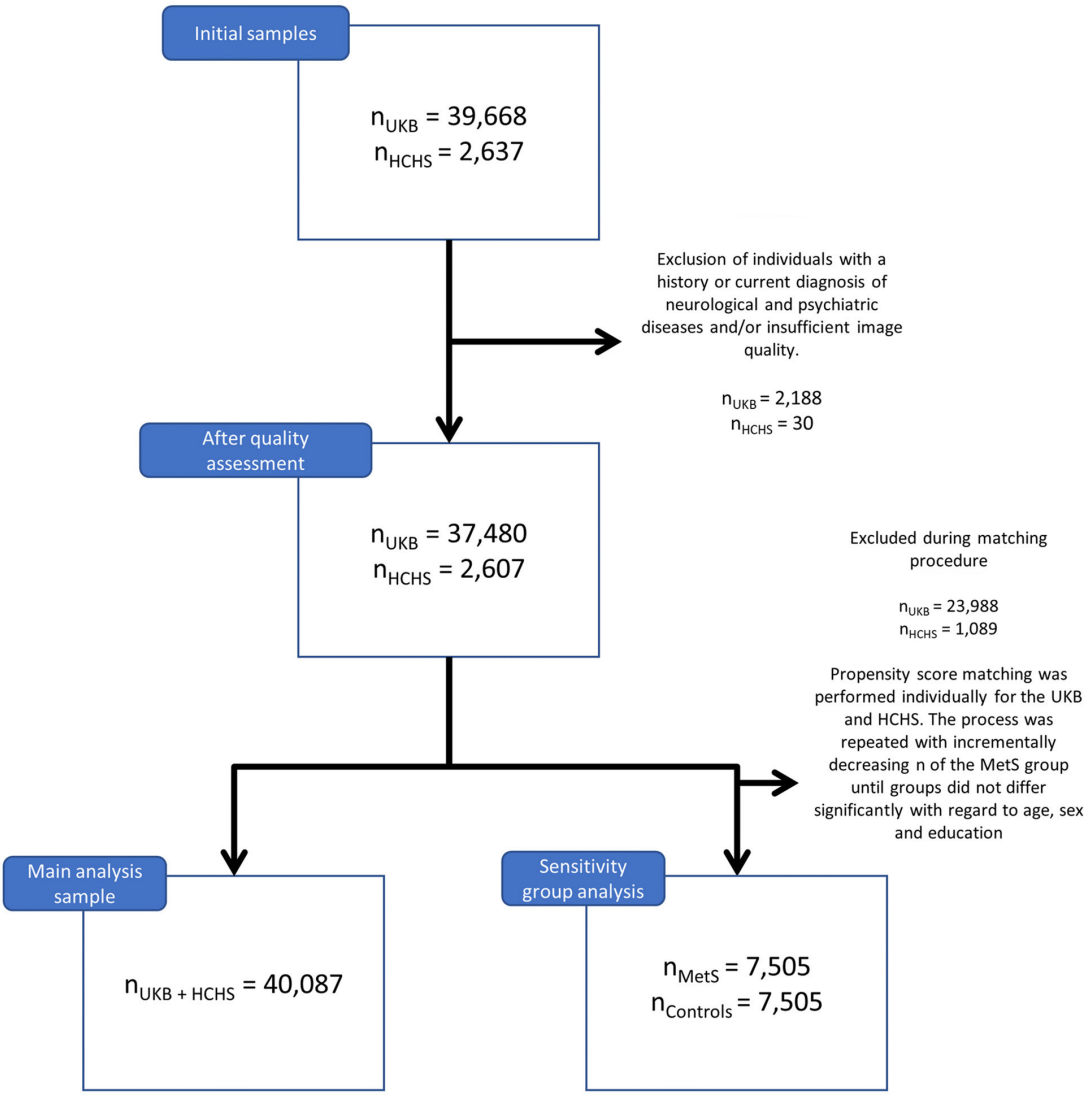

Appendix 1—figure 1. Flowchart sample selection procedure.

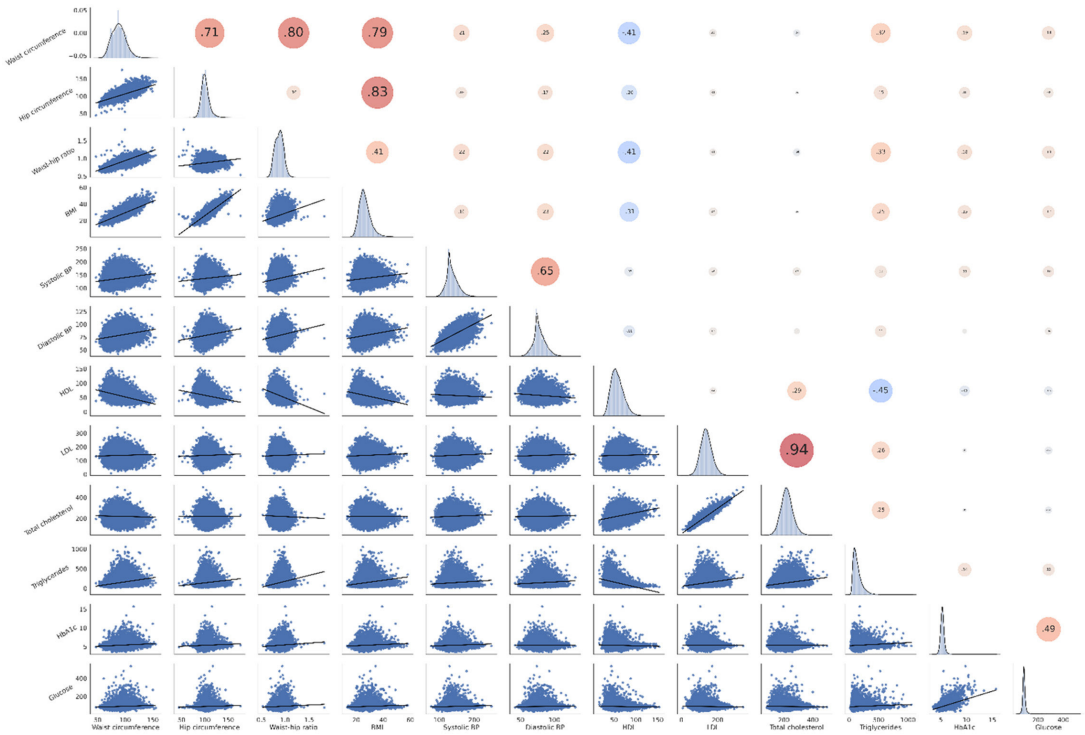

Appendix 1—figure 2. Correlation matrix of metabolic syndrome-related risk factors. The upper triangle of the matrix displays Pearson correlations with dot size and color representing the magnitude of the coefficients. The diagonal shows kernel density plots. The lower triangle illustrates the variables' linear relationships via regression plots. Of note, non fasting plasma glucose was investigated in this analysis. Abbreviations: BP – blood pressure.

Appendix 1—table 1. Partial least squares analysis - latent variables.

Latent variable	Explained variance (%)	p-value
0	71.20	0.0002
1	22.33	0.0002
2	2.12	0.0002
3	1.84	0.0006
4	1.03	0.0026
5	0.52	0.0266
6	0.38	0.0100
7	0.23	0.0032
8	0.18	0.1178
9	0.16	0.2122
10	0.00	0.3137
11	0.00	0.0608
12	0.00	1
13	0.00	1
14	0.00	1
15	0.00	1

Appendix 1—table 2. Partial least squares analysis-Cross-validation.

CV fold	r_{sp}
0	0.17
1	0.21
2	0.22
3	0.16
4	0.15
5	0.18
6	0.23
7	0.13
8	0.20
9	0.22

Appendix 1—table 3. Virtual histology analysis - Bootstrap ratio (partial least squares, PLS).

Cell type	Zr_{sp}	p_{FDR}
Endo	0.190	0.016
Micro	0.271	0.016
Ex8	0.165	0.016
In1	0.363	0.036
Ex6	0.146	0.034
Oligo	0.207	0.057
In7	0.079	0.083
Ex1	0.122	0.144
In2	0.058	0.179
In3	0.047	0.208
Astro	0.071	0.259
In8	0.055	0.299
Ex7	0.044	0.336
In5	0.037	0.388
Ex4	–0.020	0.776
Ex5	–0.055	0.924
In4	–0.056	0.949
In6	–0.099	0.949
Ex2	–0.102	0.967
Ex3	–0.289	0.999

Appendix 1—table 4. Virtual histology analysis - t-statistic (group comparison).

Cell type	Zr_{sp}	p_{FDR}
Endo	0.208	0.020
Micro	0.321	0.040
Ex8	0.208	0.040
Oligo	0.233	0.055

Appendix 1—table 4 Continued on next page

Appendix 1—table 4 Continued

Cell type	Zr_{sp}	p_{FDR}
In1	0.432	0.108
Ex6	0.145	0.123
Ex1	0.156	0.229
In3	0.058	0.233
Astro	0.120	0.233
In7	0.059	0.233
In2	0.063	0.233
Ex7	0.089	0.263
In5	0.063	0.300
In8	0.066	0.317
Ex4	0.015	0.585
Ex5	–0.007	0.690
In6	–0.078	0.861
Ex2	–0.070	0.861
In4	–0.087	0.901
Ex3	–0.341	0.997

Appendix 1—table 5. UK Biobank field IDs.

Age	**21003**
Sex	31
Education	6133*
Waist circumference	48
Hip circumference	49
Body mass index	21001
$RR_{systolic}$	4080
$RR_{diastolic}$	4079
HDL	30760
LDL	30780
Cholesterol	30690
Triglycerides	30870
HbA1c	30750
Blood glucose	30740
Medication for cholesterol, blood pressure, diabetes	6153
Fluid Intelligence	20191
Matrix Pattern Completion	6373
Numeric Memory Test	20240
Paired Associate Learning	20197
Prospective Memory	20018
Reaction Time	20023

Appendix 1—table 5 Continued on next page

Appendix 1—table 5 Continued

Age	21003
Symbol Digit Substitution	20159
Tower Rearranging Test	21004
Trail Making Test A	6348
Trail Making Test B	6350

Abbreviations: RR = blood pressure.

*Converted to International Standard Classification of Education (ISCED) via the UKBB parser (https://github.com/USC-IGC/ukbb_parser; ***Zhu et al., 2019***).

Appendix 1—table 6. Metabolic syndrome Criteria of the International Diabetes Federation (IDF) (***Alberti et al., 2006***).

Metabolic syndrome = obesity + two further criteria	
Obesity	waist circumference ♀:≥80 cm; ♂:≥94 cm
Dyslipidemia (raised triglycerides)	≥150 mg/dL (1.7 mmol/L) or lipid lowering medication
Dyslipidemia (reduced HDL cholesterol)	♀:<50 mg/dL (1.29 mmol/L); ♂:<40 mg/dL (1.03 mmol/L) in males
Arterial hypertension (raised blood pressure)	systolic BP ≥130 or diastolic BP ≥85 mm Hg or antihypertensive medication or diagnosis of hypertension
Insuline resistance	Fasting plasma glucose ≥100 mg/dL (5.6 mmol/L) or antidiabetic therapy or diagnosis of diabetes mellitus type 2*

*Measurements of fasting plasma glucose were not available for the study sample. Consequently, the criterion of insulin resistance was only based on the diagnosis of diabetes mellitus and administration of antidiabetic therapy.

Appendix 2

Case-control analysis

As a sensitivity analysis and to facilitate the comparison with previous reports which mainly rely on group statistics, we supplemented the continuous partial least squares correlation analysis with a group analysis based on a case-control design.

Matching procedure

After quality assessment, individuals with metabolic syndrome were identified based on the consensus criteria of the *International Diabetes Federation* (n_{UKB} = 6746, n_{HCHS} = 759). An individual was considered to exhibit MetS in case of obesity (increased waist circumference) and two further criteria being raised plasma triglycerides, reduced HDL cholesterol, arterial hypertension or insulin resistance. Of note, measurements of fasting plasma glucose were not available for the study sample. Consequently, the criterion of insulin resistance was only based on the diagnosis of diabetes mellitus and administration of antidiabetic therapy. Within each cohort, an equally sized control cohort was sampled which was matched for age, sex and education (International Standard Classification of Education) using propensity score matching as implemented in the matchit (v4.3.3) R package. MetS and control samples from both cohorts were pooled yielding an analysis sample of 15,010 individuals (n_{MetS} = 7505,, $n_{controls}$ = 7505). For detailed matching results refer to ***Appendix 2—figures 1 and 2*** shown below.

Group comparison of clinical data

Sample characteristics were compared between participants with MetS and controls using χ^2 -tests for binary and two-sample t-tests for continuous data. Cognitive variables were compared within UKB and HCHS subgroups via analyses of covariance (ANCOVA) adjusting for age, sex and education. Resulting test statistics were converted to Cohen's d which quantifies the group difference in standard deviations. P-values were false-discovery rate (FDR)-corrected for multiple comparisons. Separate group statistics of demographic, risk and cognitive variables for the UKB and HCHS are shown in ***Appendix 1—table 1–2***. Individuals with MetS exhibited a more severe risk profile indicating that the group definitions captured considerable differences in the MetS components profile. Group differences regarding MetS criteria proportions are visualized in ***Appendix 2—figure 3***. As the cognitive assessment of the UKB and HCHS differed, cognitive scores were compared between groups within the individual studies. UKB subjects with MetS performed significantly worse in the Fluid Intelligence Test (6.66±2.10 vs 6.82±2.09, Cohen's d=0.08, $p_{FDR} < 0.001$), Numeric Memory Test (6.64±1.61 vs 6.84±1.53, Cohen's d=.12, $p_{FDR} < 0.001$), Paired Associate Learning Test (6.45±2.60 vs 6.73±2.61, Cohen's d=0.10, $p_{FDR} < 0.001$) and Symbol Digit Substitution Test (18.47±5.12 vs 19.00±5.16, Cohen's d=0.10, $p_{FDR} < 0.001$). HCHS subjects exhibiting MetS showed worse cognitive performance in the Animal Naming Test (23.71±6.46 vs 24.77±6.75, Cohen's d=0.16, $p_{FDR} < 0.009$) and Multiple-choice Vocabulary Intelligence Test (31.18±3.43 vs 31.71±3.22, Cohen's d=0.16, $p_{FDR} < 0.034$).

Vertex-wise cortical thickness analysis

The cortical thickness of individuals with MetS and matched controls were compared on a surface vertex-level leveraging the BrainStat toolbox (v 0.3.6, https://brainstat.readthedocs.io/). Corresponding results are shown in ***Appendix 2—figure 4***. The vertex-wise t-statistic, which captures the differential MetS effects across the cortical surface, was Schaefer 400 and Schaefer 100-parcellated and propagated to further analyses. The t-statistic map strongly correlated with the bootstrap ratio maps derived from the PLS analyses. Furthermore, the t-statistic map was significantly associated with density of endothelial cells ($Z_{r_{sp}}$ = 0.208, p_{FDR} = 0.040), microglia ($Z_{r_{sp}}$ = 0.321, p_{FDR} = 0.040), excitatory neurons type 8 ($Z_{r_{sp}}$ = 0.208, p_{FDR} = 0.004) and also correlated significantly with the functional neighborhood abnormality (r_{sp} = 0.313, p_{spin} = 0.024, p_{smash} = 0.018, $p_{rewire} < 0.001$) and structural neighborhood abnormality (r_{sp} = 0.775, p_{spin} = <0.001, $p_{smash} < 0.001$, $p_{rewire} < 0.001$).

Appendix 2—table 1. Descriptive group statistics - UK Biobank.

Metric*	Individuals with MetS	Matched controls	P_{uncorr}	P_{FDR}	Stat†
Age (years)	64.73±7.42 (6746)	64.51±7.27 (6746)	0.095	0.154	–0.03
Sex (% female)	18.81 (6746)	18.81 (6746)	>0.99	>0.99	0
Education (ISCED)	2.63±0.73 (6746)	2.67±0.71 (6746)	0.036	0.069	0.04
Metabolic syndrome criteria					
Waist circumference (cm)	97.39±10.21 (6726)	88.22±10.59 (6595)	<0.001	<0.001 ‡	–0.88
$RR_{systolic}$ (mmHg)	146.41±15.38 (6213)	135.57±17.71 (5397)	<0.001	<0.001 ‡	–0.66
$RR_{diastolic}$ (mmHg)	82.26±9.39 (6214)	77.58±9.79 (5397)	<0.001	<0.001 ‡	–0.49
Antihypertensive therapy (%)	9.96 (6746)	9.68 (6746)	<0.001	<0.001 ‡	7.07
HDL (mmol/L)	1.18±0.26 (6225)	1.49±0.32 (6332)	<0.001	<0.001 ‡	1.08
Triglycerides (mmol/L)	2.43±1.13 (6617)	1.30±0.59 (6543)	<0.001	<0.001 ‡	–1.25
Lipid-lowering therapy (%)	39.05 (6746)	7.07 (6746)	<0.001	<.001 ‡	2446.5
Blood glucose (mmol/L)	5.18±1.41 (6219)	4.92±0.68 (6325)	<0.001	<.001 ‡	–0.23
Antidiabetic therapy (%)	0.06 (6746)	0.19 (6746)	0.052	0.097	3.77
Cognitive scores					
Fluid Intelligence	6.66±2.10 (6221)	6.82±2.09 (6241)	<0.001	<0.001 ‡	0.08
Matrix Pattern Completion	8.02±2.13 (4283)	8.14±2.06 (4355)	0.055	0.096	0.06
Numeric Memory Test	6.64±1.61 (4419)	6.84±1.53 (4505)	<0.001	<0.001 ‡	0.12
Paired Associate Learning	6.45±2.60 (4337)	6.73±2.61 (4392)	<0.001	<0.001 ‡	0.10
Prospective Memory	1.05±0.40 (6362)	1.06±0.39 (6349)	0.221	0.339	0.02
Reaction Time	590.75±108.27 (6331)	590.15±111.13 (6325)	0.792	0.858	–0.005

Appendix 2—table 1 continued on next page

Appendix 2—table 1 continued

Metric*	Individuals with MetS	Matched controls	P_{uncorr}	P_{FDR}	Stat†
Symbol Digit Substitution	18.47±5.12 (4292)	19.00±5.16 (4353)	<0.001	<0.001 ‡	0.10
Tower Rearranging Test	10.00±3.28 (4255)	10.08±3.20 (4325)	0.747	0.845	0.02
Trail Making Test A (sec)	226.83±86.26 (4337)	224.06±83.06 (4392)	0.643	0.836	–0.03
Trail Making Test B (sec)	561.81±271.39 (4337)	553.62±282.55 (4392)	0.611	0.756	–0.03
Imaging					
Mean cortical thickness (mm)	2.392±0.09 (6746)	2.397±0.09 (6746)	0.035	0.071	0.05

Abbreviations: cm = centimeter, dL = deciliter, HDL = high-density lipoprotein, ISCED = International Standard Classification of Education, MetS = metabolic syndrome, mg = milligram, mm = millimeter, mmHg = millimeters of mercury, mmol/L = millimole perliter, PC = principal component, Puncor = uncorrected p-values, PFDR = false-discovery rate-corrected p-values, RR = Blood pressure, sec = seconds.

*Presented as mean ± SD (N).

†Presented as $\chi 2$ for categorical and Cohen's d for continuous data.

‡Denotes statistical significance at FDR-corrected p<0.001

Appendix 2—table 2. Descriptive group statistics Hamburg City Health Study (HCHS).

Metric*	Individuals with MetS	Matched controls	P_{uncorr}	P_{FDR}	Stat
Age (years)	65.77±7.40 (759)	65.97±7.52 (759)	0.613	0.647	0.03
Sex (% female)	33.47	36.50	0.236	0.281	1.4
Education (ISCED)	2.37±0.58 (759)	2.42±0.60 (759)	0.09	0.114	0.09
Metabolic syndrome criteria					
Waist circumference (cm)	103.38±11.23 (754)	91.45±11.36 (747)	<0.001	<0.001†	–1.06
$RR_{systolic}$ (mmHg)	145.66±18.54 (740)	140.17±21.10 (746)	<0.001	<0.001†	–.28
$RR_{diastolic}$ (mmHg)	83.75±10.11 (740)	82.00±10.40 (746)	0.001	0.002	–.17
Antihypertensive therapy (%)	52.60%	26.22%	<0.001	<0.001†	108.89
HDL (mg/dL)	54.60±16.13 (751)	67.63±17.46 (759)	<0.001	<0.001†	0.78
Triglycerides (mg/dL)	161.53±92.61 (751)	91.23±30.62 (759)	<0.001	<0.001†	–1.02
Lipid lowering therapy (%)	40.85%	7.64%	<0.001	<0.001†	225.29
Blood glucose (mg/dL)	107.47±28.59 (742)	90.99±10.87 (753)	<0.001	<0.001†	–0.76
Antidiabetic therapy (%)	14.42%	1.45%	<0.001	<0.001†	85.47
Cognitive scores					
Animal Naming Test	23.71±6.46 (712)	24.77±6.75 (711)	0.005	0.009	0.16
Clock Drawing Test	6.36±1.17 (730)	6.39±1.16 (733)	0.774	0.774	0.02
Trail Making Test A (sec)	41.26±14.28 (685)	40.42±14.54 (675)	0.321	0.359	–0.06
Trail Making Test B (sec)	93.74±37.30 (675)	89.89±37.69 (671)	0.086	0.114	–0.10
Multiple-Choice Vocabulary Intelligence Test	31.18±3.43 (603)	31.71±3.22 (619)	0.019	0.034	0.16
Word List Recall	7.42±1.89 (691)	7.64±1.84 (673)	0.057	0.083	0.12

Appendix 2—table 2 continued on next page

Appendix 2—table 2 continued

Metric*	Individuals with MetS	Matched controls	P_{uncorr}	P_{FDR}	*Stat*
Imaging					
Mean cortical thickness (mm)	2.327±0.08 (759)	2.334±0.08 (757)	0.045	0.071	0.1

Abbreviations: cm = centimeter, dL = deciliter, HDL = high-density lipoprotein, ISCED = International Standard Classification of Education, MetS = metabolic syndrome, mg = milligram, mm = millimeter, mmHg = millimeters of mercury, Puncor = uncorrected p-values, PFDR = false-discovery rate-corrected p-values, RR = Blood pressure, sec = seconds.

*Presented as mean ± SD (N).

†Denotes statistical significance at FDR-corrected p<0.001.

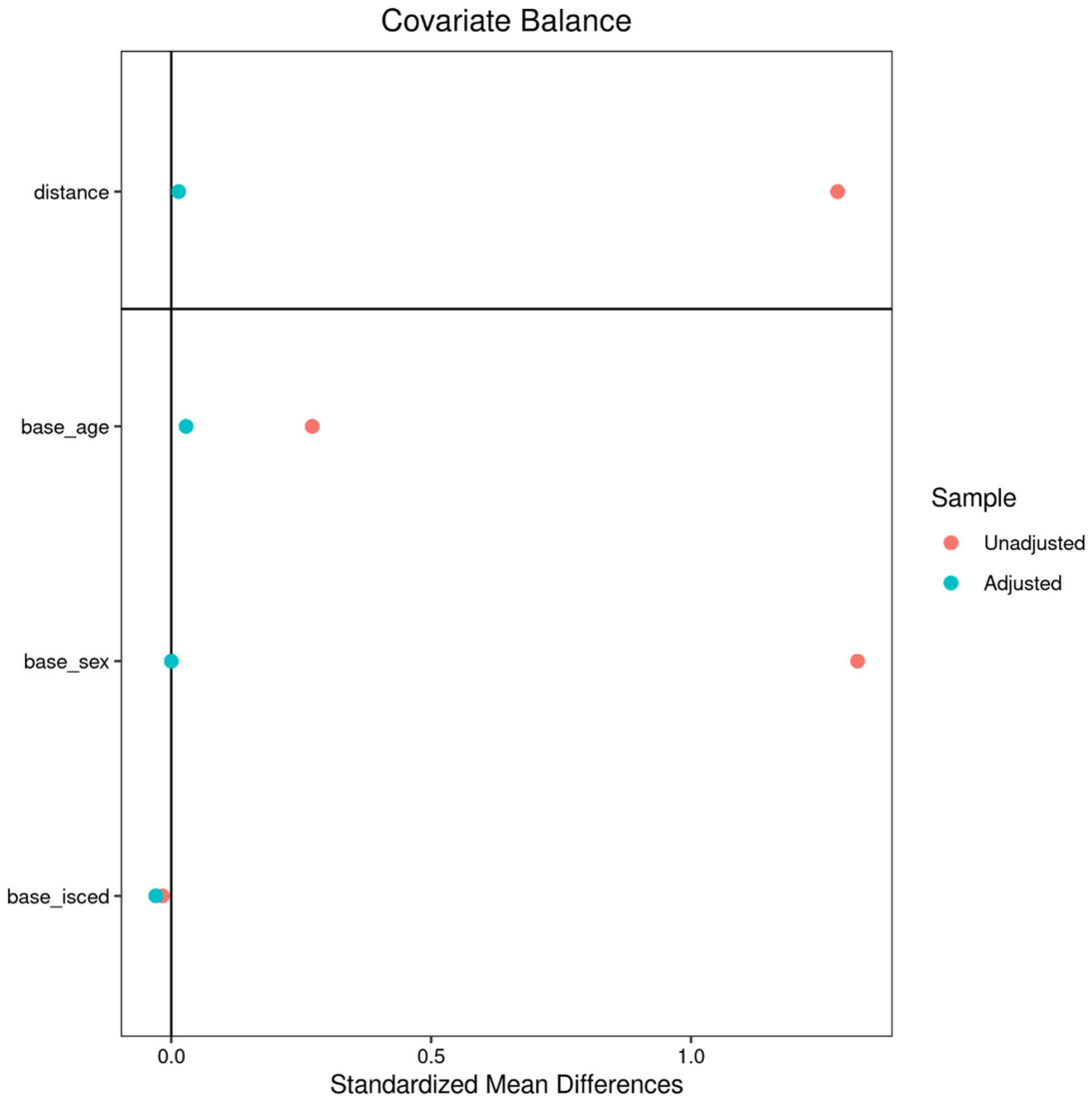

Appendix 2—figure 1. Matching - UK Biobank.

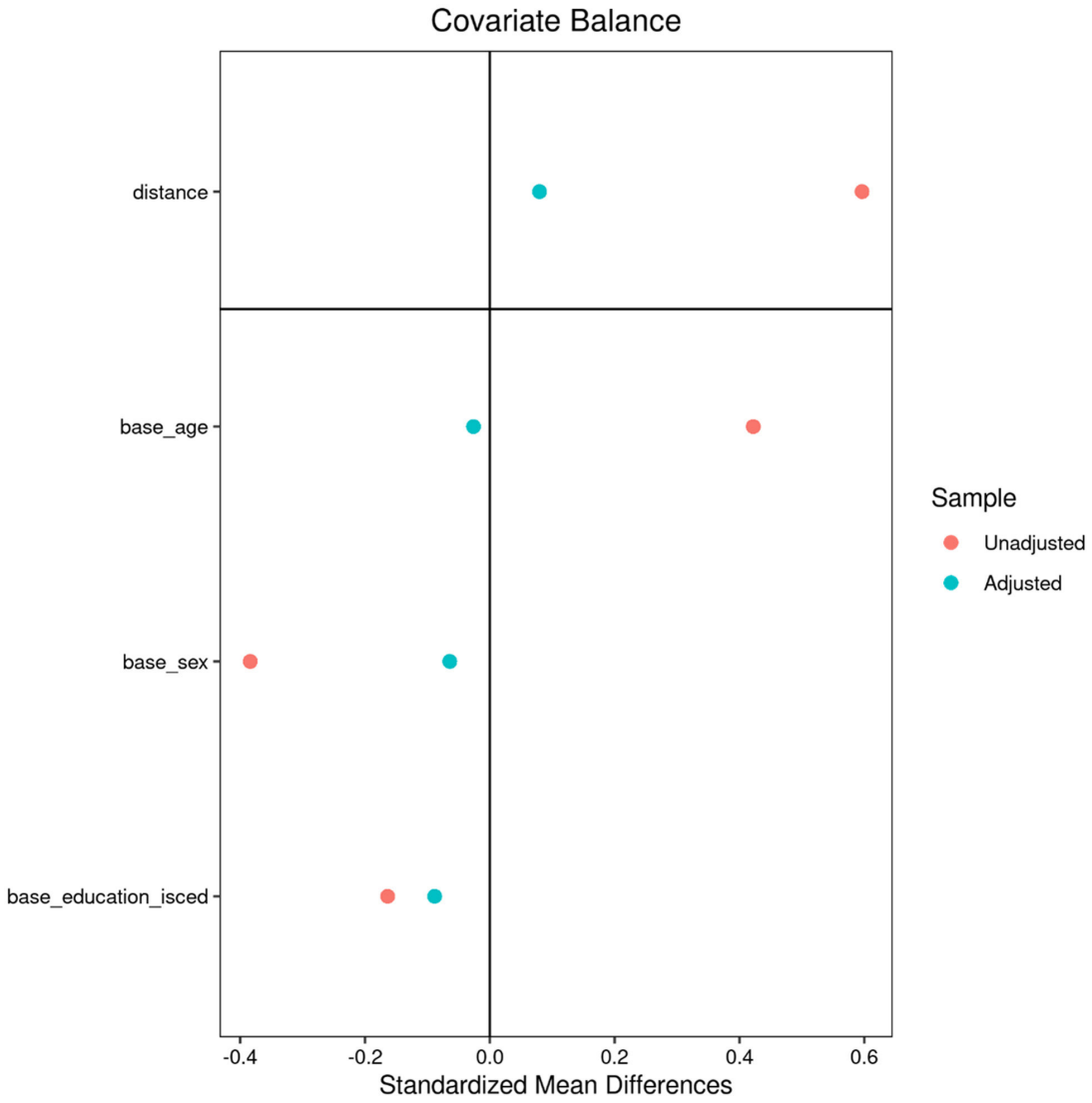

Appendix 2—figure 2. Matching – Hamburg City Health Study.

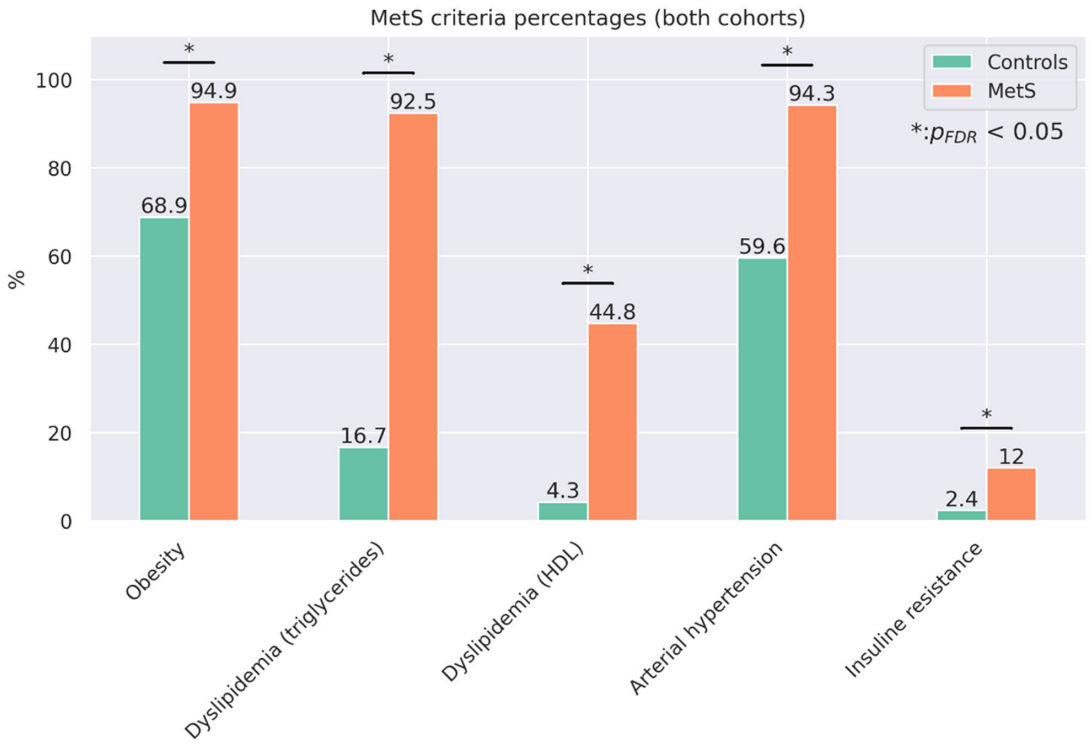

Appendix 2—figure 3. Proportion of metabolic syndrome criteria. Barplots indicate the percentage amount of metabolic syndrome (MetS) criteria that apply by group for the pooled sample. Significant group differences in χ 2-tests are highlighted by asterisks.

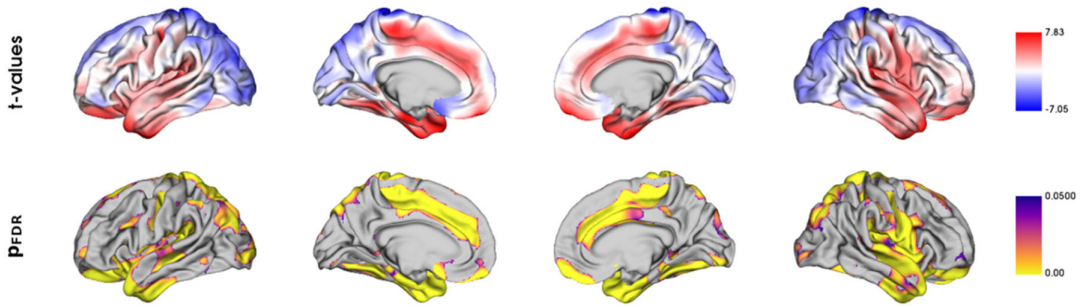

Appendix 2—figure 4. Vertix-wise group comparison of cortical thickness. Vertex-level group comparison between individuals with metabolic syndrome and matched controls. Resulting surface maps of standardized *t*-statistic estimates encode the group-differences between patients and controls, with lower cortical thickness in the metabolic syndrome (MetS) group being represented by a positive *t* and lower by a negative *t*. The vertex-wise t-statistic map was Schaefer-parcellated for the downstream analyses.

medRxiv

Enhancing Cognitive Performance Prediction through White Matter Hyperintensity Connectivity Assessment: A Multicenter Lesion Network Mapping Analysis of 3,485 Memory Clinic Patients

Marvin Petersen[1*], Mirthe Coenen[2], Charles DeCarli[3], Alberto De Luca[2,4], Ewoud van der Lelij[2], Alzheimer's Disease Neuroimaging Initiative, Frederik Barkhof[5,6], Thomas Benke[7], Christopher P. L. H. Chen[8,9], Peter Dal-Bianco[10], Anna Dewenter[11], Marco Duering[11,12], Christian Enzinger[13,14], Michael Ewers[11], Lieza G. Exalto[2], Evan F. Fletcher[3], Nicolai Franzmeier[11], Saima Hilal[9,15], Edith Hofer[16,17], Huiberdina L. Koek[2,18], Andrea B. Maier[8,9], Pauline M. Maillard[3], Cheryl R. McCreary[19], Janne M. Papma[20,21,22], Yolande A. L. Pijnenburg[23], Reinhold Schmidt[16,17], Eric E. Smith[19], Rebecca M. E. Steketee[23,24], Esther van den Berg[20,21], Wiesje M. van der Flier[23,24], Vikram Venkatraghavan[23,24], Narayanaswamy Venketasubramanian[9,26], Meike W. Vernooij[20,25,27], Frank J. Wolters[25,27], Xin Xu[9,28], Andreas Horn[29,30], Kaustubh R. Patil[31,32], Simon B. Eickhoff[31,32], Götz Thomalla[1], J. Matthijs Biesbroek[2,33], Geert Jan Biessels[2], Bastian Cheng[1]

1 Department of Neurology, University Medical Center Hamburg-Eppendorf, Hamburg, Germany
2 University Medical Center Utrecht Brain Center, Utrecht, The Netherlands
3 University of California at Davis, USA
4 Image Sciences Institute, Division Imaging and Oncology, UMC Utrecht
5 Department of Radiology & Nuclear Medicine, Amsterdam UMC, Vrije Universiteit, the Netherlands
6 Queen Square Institute of Neurology and Centre for Medical Image Computing, University College London, UK
7 Clinic of Neurology, Medical University Innsbruck, Austria
8 Departments of Pharmacology and Psychological Medicine, Yong Loo Lin School of Medicine, National University of Singapore, Singapore
9 Memory, Aging and Cognition Center, National University Health System, Singapore
10 Medical University Vienna, Austria
11 Institute for Stroke and Dementia Research (ISD), LMU University Hospital, LMU Munich, Munich, Germany
12 Medical Image Analysis Center (MIAC) and Department of Biomedical Engineering, University of Basel, Basel, Switzerland
13 Division of General Neurology, Department of Neurology, Medical University Graz, Austria
14 Division of Neuroradiology, Interventional and Vascular Radiology, Department of Radiology, Medical University of Graz, Austria
15 Saw Swee Hock School of Public Health, National University of Singapore and National University Health System, Singapore
16 Division of Neurogeriatrics, Department of Neurology, Medical University of Graz, Austria
17 Institute for Medical Informatics, Statistics and Documentation, Medical University of Graz, Austria
18 Department of Geriatric Medicine, University Medical Center Utrecht, Utrecht University, Utrecht, The Netherlands
19 Department of Clinical Neurosciences and Radiology and Hotchkiss Brain Institute, University of Calgary, Calgary, Alberta, Canada
20 Alzheimer Center Erasmus MC, Erasmus MC University Medical Center, Rotterdam, The Netherlands
21 Department of Neurology, Erasmus MC University Medical Center, Rotterdam, The Netherlands
22 Department of Internal Medicine, Erasmus MC University Medical Center, Rotterdam, The Netherlands
23 Alzheimer Center Amsterdam, Department of Neurology, Amsterdam Neuroscience, Vrije Universiteit Amsterdam, Amsterdam UMC, Amsterdam, The Netherlands.
24 Amsterdam Neuroscience, Neurodegeneration, Amsterdam, The Netherlands
25 Department of Radiology & Nuclear Medicine, Erasmus MC University Medical Center, Rotterdam, The Netherlands
26 Raffles Neuroscience Center, Raffles Hospital, Singapore, Singapore
27 Department of Epidemiology, Erasmus MC University Medical Center, Rotterdam, The Netherlands.
28 School of Public Health and the Second Affiliated Hospital of School of Medicine, Zhejiang University, China
29 Charité - Universitätsmedizin Berlin, Movement Disorders and Neuromodulation Unit, Department of Neurology with Experimental Neurology, 10117 Berlin, Germany.
30 Center for Brain Circuit Therapeutics, Department of Neurology, Psychiatry, and Radiology, Brigham and Women's Hospital, Harvard Medical School, Boston, USA.
31 Institute for Systems Neuroscience, Medical Faculty, Heinrich-Heine University Düsseldorf, Düsseldorf, Germany
32 Institute of Neuroscience and Medicine, Brain and Behaviour (INM-7), Research Center Jülich, Germany
33 Department of Neurology, Diakonessenhuis Hospital, Utrecht, The Netherlands
*Correspondence should be addressed to M.P. (mar.petersen@uke.de)

Abstract. Introduction: White matter hyperintensities of presumed vascular origin (WMH) are associated with cognitive impairment and are a key imaging marker in evaluating cognitive health. However, WMH volume alone does not fully account for the extent of cognitive deficits and the mechanisms linking WMH to these deficits remain unclear. We propose that lesion network mapping (LNM), enables to infer if brain networks are connected to lesions, and could be a promising technique for enhancing our understanding of the role of WMH in cognitive disorders. Our study employed this approach to test the following hypotheses: (1) LNM-informed markers surpass WMH volumes in predicting cognitive performance, and (2) WMH contributing to cognitive impairment map to specific brain networks. **Methods & results:** We analyzed cross-sectional data of 3,485 patients from 10 memory clinic cohorts within the Meta VCI Map Consortium, using harmonized test results in 4 cognitive domains and WMH segmentations. WMH segmentations were registered to a standard space and mapped onto existing normative structural and functional brain connectome data. We employed LNM to quantify WMH connectivity across 480 atlas-based gray and white matter regions of interest (ROI), resulting in ROI-level structural and functional LNM scores. The capacity of total and regional WMH volumes and LNM scores in predicting cognitive function was compared using ridge regression models in a nested cross-validation. LNM scores predicted performance in three cognitive domains (attention and executive function, information processing speed, and verbal memory) significantly better than WMH volumes. LNM scores did not improve prediction for language functions. ROI-level analysis revealed that higher LNM scores, representing greater disruptive effects of WMH on regional connectivity, in gray and white matter regions of the dorsal and ventral attention networks were associated with lower cognitive performance. **Conclusion:** Measures of WMH-related brain network connectivity significantly improve the prediction of current cognitive performance in memory clinic patients compared to WMH volume as a traditional imaging marker of cerebrovascular disease. This highlights the crucial role of network effects, particularly in attention-related brain regions, improving our understanding of vascular contributions to cognitive impairment. Moving forward, refining WMH information with connectivity data could contribute to patient-tailored therapeutic interventions and facilitate the identification of subgroups at risk of cognitive disorders.

Introduction

Cerebral small vessel disease (CSVD) is a major driver of vascular cognitive impairment (VCI) and often also contributes to dementia with a primary neurodegenerative or mixed pathology.[1] White matter hyperintensities (WMH) are the signature imaging marker of CSVD, and mark sites of white matter disintegration caused by microangiopathic axonal loss and demyelination.[2,3] However, a comprehensive understanding of mechanisms linking WMH to their broad range of clinical manifestations, specifically cognitive impairment, is still lacking.

Although there is a well-documented association between WMH volumes and cognitive functions at the group-level, the association between WMH volume and symptom severity demonstrates considerable variability with some individuals exhibiting fewer symptoms despite high WMH burden and vice versa.[4] The apparent complexity of this relationship underscores the need for improved techniques for disease quantification to more accurately predict individual cognitive impairment for effective diagnostics and ultimately targeted treatment of CSVD patients.[5] For example, lesion-symptom inference techniques have linked cognitive impairment to WMH located in strategic white matter regions, independent of total WMH volume.[4,6,7]

However, these recent findings might not fully reflect the complexity of CSVD-related cognitive impairment, which is thought to emerge from disturbances in the interplay of large-scale brain networks involving cortical and subcortical gray matter areas, interconnected by white matter tracts.[8] In recent years, advanced imaging analysis models have been developed to comprehensively capture lesion effects on brain circuitry.[9] Specifically, lesion network mapping (LNM) techniques capitalize on advanced neuroimaging to map lesions on reconstructions of the human brain network.[10] By that, a lesion's impact on connectivity to different brain regions can be quantified – i.e., the lesion's network embedding is measured – allowing to infer which regions are disconnected. Application of LNM has been shown to predict clinical symptoms in a variety of neurological disorders that can be understood as "disconnection syndromes", such as stroke or multiple sclerosis.[11,12]

Here, we propose LNM as a technique to quantify WMH-related, strategic neuronal disconnectivity for improved prediction of cognitive performance in CSVD. We employ LNM on a large-scale, multicenter dataset, integrating cognitive test results and MRI-based WMH segmentations from 3485 patients of 10 memory clinic cohorts through the Meta VCI Map Consortium.[6,13] Our hypotheses are twofold: (1) LNM-based measures of WMH connectivity surpass WMH volumes in predicting cognitive performance, and (2) WMH contributing to cognitive deficits map to specific brain networks that functionally determine their symptom profile.

Materials and methods

Study population

Methodological details are illustrated in *figure 1*. We examined previously harmonized, cross-sectional clinical and imaging data of 3485 patients from 10 memory clinic cohorts of the Meta VCI Map Consortium.[6,13] Meta VCI Map is a multi-site collaboration for conducting meta-analyses of strategic lesion topography in vascular cognitive impairment. The memory clinic cohorts included in this study comprise the Erasmus MC Memory Clinic Cohort (ACE, n=52, Netherlands), Alzheimer's Disease Neuroimaging Initiative (ADNI, n=994, USA)[14], UC Davis Alzheimer's Disease Center Diversity Cohort (AUCD, n=641, USA)[15], BrainIMPACT (n=53, Canada)[16], Functional Assessment of Vascular Reactivity (FAVR, n=47, Canada)[16], Harmonization (n=207, Singapore)[4], Prospective Dementia Registry (PRODEM, n=367, Austria)[17], TRACE-VCI (n=821, Netherlands)[18], Utrecht Memory Clinic Cohort (UMCC, n=227, Netherlands) and VASCAMY (n=76, Germany). All cohorts include patients assessed at outpatient memory clinics for cognitive symptoms, undergoing structural MRI alongside neuropsychological tests of cognitive performance.

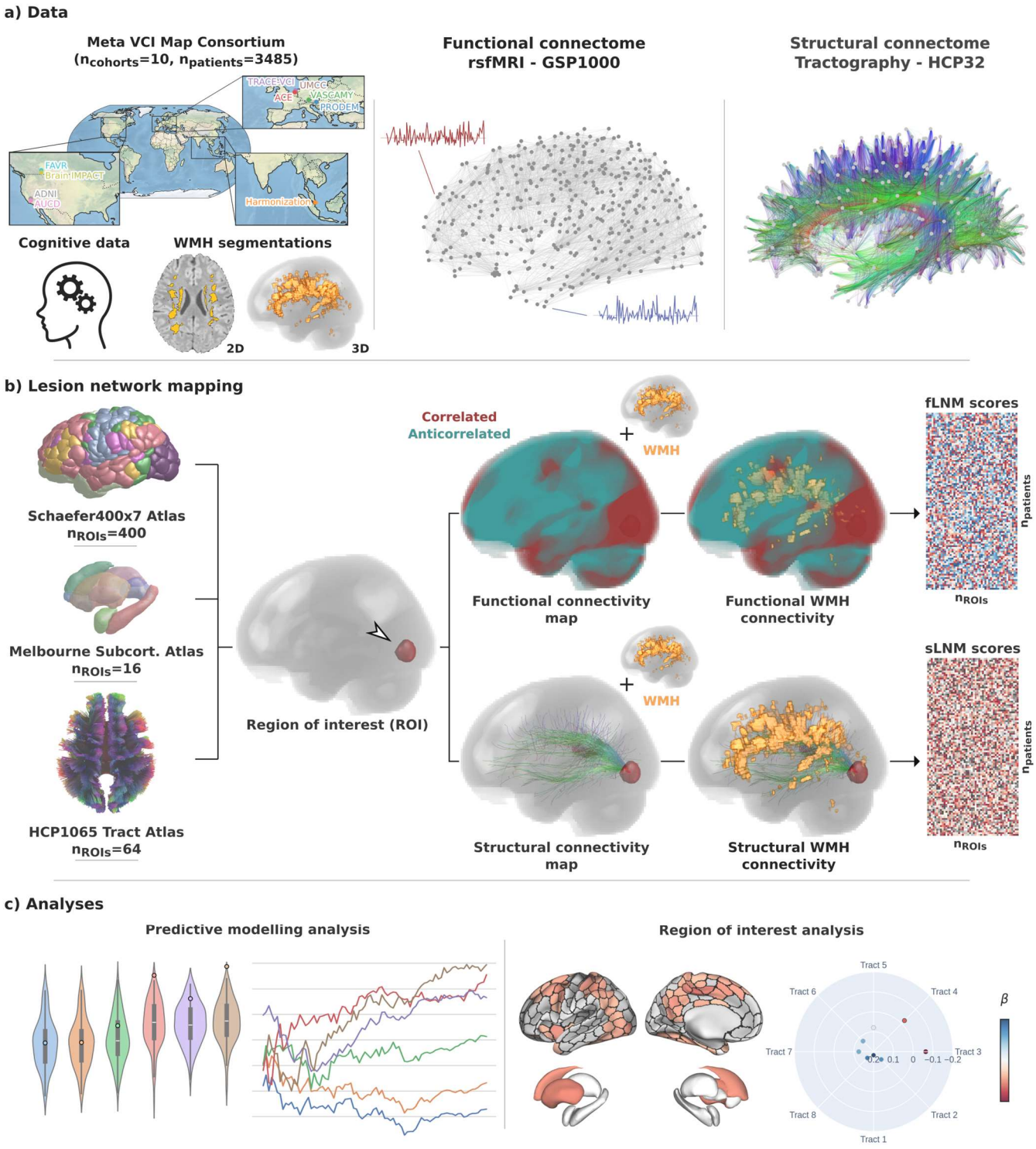

Figure 1. Methodology. a) Data from 10 memory clinic cohorts of the Meta VCI Map Consortium were used including harmonized cognitive scores and WMH segmentations in MNI space. For functional LNM we employed the GSP1000 normative functional connectome comprising resting-state fMRI data from 1000 healthy GSP participants. For structural lesion network mapping, we used the HCP32 normative structural connectome based on diffusion-weighted imaging data from 32 healthy HCP participants, detailing the fiber bundle architecture. b) LNM was performed to quantify the functional and structural connectivity of WMH to multiple ROIs (Schaefer400x7 cortical, Melbourne Subcortical Atlas subcortical, HCP1065 white matter areas). For this, voxel-level functional and structural connectivity maps were computed for each ROI, reflecting resting-state BOLD correlations or anatomical connection strength via tractography streamlines, respectively. ROIwise LNM scores were derived by averaging voxel-level connectivity indices within the normalized WMH masks, considering only positive correlation coefficients for functional mapping. This resulted in a matrix for both fLNM and sLNM scores per ROI per patient (n_{ROIs} x $n_{patients}$). The matrices shown in the figure are populated with random data only serving as a visual aid. c) The fLNM and sLNM scores across patients were used in predictive models to estimate cognitive domain scores (predictive modelling analysis) and analyzed in permutation-based general linear models to identify regions significantly influencing the cognitive domain-WMH disconnectivity relationship at the ROI level (ROI-level inferential statistics). *Abbreviations*: fLNM = functional lesion network mapping, GSP = Genomic Superstruct Project, HCP = Human Connectome Project, ROI = region of interest, rsfMRI = resting-state functional magnetic resonance imaging, sLNM = structural lesion network mapping, WMH = white matter hyperintensities of presumed vascular origin.

Patients with cognitive impairment due to non-vascular, non-neurodegenerative causes (e.g., excessive alcohol use disorder, cerebral malignancies, multiple sclerosis) or monogenic disorders (e.g., CADASIL) were excluded. Further details on each cohort including sample-specific inclusion and exclusion criteria were reported previously.[6]

Ethics approval

All cohorts received the requisite ethical and institutional approval in accordance with local regulations, which included informed consent, to allow data acquisition and sharing.[6]

Cognitive assessments

Detailed harmonization procedures, including specific test-to-domain assignments, were reported previously.[19] Neuropsychological tests from participating cohorts were norm-referenced against local norms or a healthy control group, and adjusted on the individual subject level for age, sex, and education. These tests were categorized into four cognitive domains: attention/executive function, information processing speed, language, and verbal memory. Within these domains, norm-referenced neuropsychological test scores were z-scored and averaged to obtain cognitive domain scores (z-scores), which capture individual-level cognitive domain performance relative to healthy controls.

White matter hyperintensity segmentation

WMH segmentations were provided by the participating centers or performed at the UMC Utrecht (ACE cohort). Segmentation masks were obtained applying established automated neuroimaging software on fluid-attenuated inversion recovery (FLAIR) MRI.[20] WMH segmentations were spatially normalized to the Montreal Neurological Institute (MNI)-152 template.[21] To ensure registration quality, the normalized WMH masks were visually inspected and patients with failed registrations were excluded. Furthermore, random subsamples of normalized WMH segmentations were returned to the respective participating institutions to confirm the data quality. WMH segmentation masks were used to compute the total WMH volume as well as tract-level WMH volumes for each of the 64 white matter fiber tracts of the HCP1065 Tract Atlas.[22] Details on cohort-specific segmentation and registration procedures were reported previously.[6,23]

Lesion network mapping

LNM was performed to quantify the functional and structural connectivity of WMH to cortical, subcortical and white matter regions of interest (ROIs).[24] ROIs were defined in MNI space according to the Schaefer400x7 Atlas (n_{ROIs}=400), the Melbourne Subcortical Atlas (n_{ROIs}=16) and the HCP1065 Tract Atlas (n_{ROIs}=64) (*figure 1b*).[22,25,26] For visualization of the investigated HCP1065 tracts, see *supplementary figure S1*.

Functional lesion network mapping (fLNM) was conducted using a normative functional connectome, derived from resting-state fMRI scans of 1,000 healthy individuals from the Genomic Superstruct Project (GSP1000).[27] Preprocessing included global signal regression and spatial smoothing at a 6mm full width at half maximum kernel as previously detailed.[28] For each ROI, we averaged blood oxygen level-dependent (BOLD) signal fluctuations across voxels within the ROI and correlated this aggregate time series with BOLD signals of all brain voxels. This process generated 1,000 Pearson correlation coefficients per voxel, i.e., one for each GSP1000 subject, which were then Fischer z-transformed and averaged across subjects to create a functional connectivity map per ROI. Functional connectivity map computations were performed using the ROI masks as seeds in the *connectome mapper* function of Lead-DBS (lead-dbs.org).[29] Subsequently, ROI-level fLNM scores were calculated by averaging positive Pearson correlation coefficients within the WMH mask, reflecting each ROI's functional connectivity to WMH.

Structural lesion network mapping (sLNM) was performed employing a normative structural connectome of 32 subjects of the Human Connectome Project (HCP32).[30] The structural connectome was reconstructed by applying DSI Studio on multi-shell diffusion MRI data acquired on a MRI scanner specifically designed for high-fidelity connectome reconstruction. Streamlines resulting from whole brain tractography were normalized to MNI and aggregated across subjects.[31] Employing Lead-DBS, voxel-wise structural connectivity maps were computed per atlas ROI, quantifying per voxel the number of streamlines connecting the voxel to the ROI.[29] ROI-level sLNM scores, reflecting structural connectivity between WMH and individual ROI, were determined by averaging the voxel values (representing streamline counts to the ROI) within the WMH mask.

Summarized, LNM yielded both a fLNM and sLNM score for each ROI per subject, indicating the functional and structural connectivity between WMH and ROI, respectively.

Predictive modelling analysis

To evaluate the predictive capacity of fLNM and sLNM scores, we performed a predictive modelling analysis leveraging scikit-learn (v. 1.0.2, scikit-learn.org) and julearn (v. 0.3.0, juaml.github.io/julearn).[32,33] This work defines 'prediction' in accordance with previous studies as the estimation of target variables using a trained statistical model on new unseen data – emphasizing the crucial aspect of model generalizability.[9,34,35] We note that this definition varies from those indicating longitudinal study designs used in epidemiological contexts.[36] In the analysis, six different feature sets were compared: (1) demographics (age, sex and education), (2) total WMH volume + demographics, (3) tract-level WMH volumes + demographics, (4) ROI-level fLNM scores + demographics, (5) ROI-level sLNM scores + demographics, (6) ROI-level fLNM and sLNM scores + demographics.

For each cognitive domain, multivariable ridge regression models were trained using the abovementioned feature sets to predict cognitive domain scores. Ridge regression models include a L2 penalty that reduces coefficients to mitigate overfitting and address multicollinearity. We optimized the L2 penalties through a 10-fold nested cross-validation, tuning α values ranging from 0.001 to 1000 (α = 0.001, 0.01, 0.1, 1, 10, 100, 1000). The model performance was scored by the Pearson correlation between actual and predicted cognitive domain scores,

supplemented with explained variance (R^2, coefficient of determination) and negative mean squared error as additional measures of performance. In line with best practices, explained variance was calculated via sum-of-squares formulation (using scikit-learn's *r2_score*) instead of squaring Pearson correlations.[34] Before model fitting, continuous input features were z-scored in a cross-validation consistent manner to avoid data leakage.[37] To maintain a consistent distribution of the target variable across training and test sets, we employed julearn's *ContinuousStratifiedKFold* function for creating the folds. Cross-validations were repeated 10 times with varied random splits to minimize bias from any single split.[38] This approach yielded 100 scores for each feature-target set combination which were compared between feature sets using a machine learning-adjusted t-test.[39] We repeated the predictive modelling analysis for different sample sizes (20%-100%, 1% steps, randomly sampled) to examine the robustness and sample size dependency of predictive performances. As a whole, this analysis follows current best practices of predictive modelling in neuroimaging.[34]

Region of interest-level inferential statistics

To investigate whether WMH-related connectivity of specific brain circuits links to impaired cognitive performance, we conducted permutation-based testing for linear associations between regional LNM scores and cognitive domain scores in a general linear model. All statistical analyses were conducted in FSL's Permutation Analysis of Linear Models (PALM) based on MATLAB (v. 2021b) and Python 3.9.1 leveraging neuromaps (v. 0.0.5).[40–42] Statistical tests were two-sided ($n_{permutation}$=5000), with a $p<0.05$ as the significance threshold. To account for multiple comparisons, p-values were adjusted for family-wise error. General linear models were adjusted for age, sex and education. To obtain standardized β-coefficients, input variables were z-scored beforehand. As a result, β-coefficients and p-values were obtained for each cortical, subcortical, and white matter ROI (n_{ROIs}=480) indicating the strength and significance of the LNM score's linear association with cognitive domain scores for each ROI. To aid in interpreting the spatial effect patterns, we averaged the β-coefficients representing cortical effects in the 7 intrinsic resting-state networks (Yeo networks), which reflect the cerebral cortex's intrinsic functional organization.[28] The Schaefer400x7 Atlas assigns ROIs to these networks: visual, somatomotor, dorsal attention, ventral attention (salience), limbic, frontoparietal control, and default mode network.[25] Significance was tested via spin permutations (n_{spins}=1000) which represent a null model preserving the inherent spatial autocorrelation of cortical information.

Sensitivity analyses

During computations of fLNM scores, we decided to only consider positive Pearson correlations of resting-state BOLD signal within WMH masks following previous approaches as the role of negative correlations is controversial.[43] However, some studies suggest biological meaning in anticorrelations of BOLD signal fluctuations.[44,45] Hence, we conducted a sensitivity analysis based on fLNM scores computed by averaging only the negative Pearson correlations in the WMH masks. We reconducted the predictive modelling analysis and ROI-level inferential statistics using these negative fLNM scores.

Moreover, previous work employs thresholding to discard potentially noisy connectivity information. To further examine the effect of thresholding on our results we repeated the predictive modelling analysis comparing the main analysis results to fLNM and sLNM scores computed based on 25% and 50% highest voxel intensities in the WMH mask. For negative fLNM scores, the lowest 25% and 50% voxel intensities in the WMH mask were considered.

Exploratory analyses

Further exploratory analyses including investigations of voxel-level lesion network maps and structure-function coupling of LNM scores are described in *supplementary text S2.*

Data availability

Analysis code can be accessed on GitHub (https://github.com/csi-hamburg/2024_petersen_wmh_disconnectivity_memory_clinic). The data that support the findings of this study are available from the corresponding author/project leads on reasonable request (https://metavcimap.org/group/become-a-member/). Restrictions related to privacy and personal data sharing regulations and informed consent may apply.

Results

Sample characteristics

The pooled study sample of 3485 patients had a mean age of 71.7 ± 8.9 years and 49.8% were female. Among patients, 777 (22.3%) had subjective cognitive impairment, 1389 (39.9%) had mild cognitive impairment, and 1319 (37.9%) had dementia. Further details on the sample characteristics can be found in *table 1*. A heatmap of WMH distribution can be found in *supplementary figure S3.*

Predictive modelling analysis

To evaluate if information on WMH network connectivity exceeds the predictive capacity of volumetric WMH metrics for cognitive performance, we first computed regional fLNM and sLNM scores, that capture the structural and functional connectivity profile of WMH. We then employed ridge regression for predictive modelling. Model performance was assessed via Pearson correlation (r) of predicted and actual cognitive domain scores averaged across folds. All models incorporated age, sex, and education (demographics) as features to establish a performance baseline. The corresponding results are visualized in *figure 2a*. In summary, LNM scores significantly improved cognitive function prediction in all domains, except language, over WMH volumes. In detail, the predictive performance achieved by the demographics-only model was r = 0.312 for attention / executive function, r = 0.239 for information processing speed, r = 0.404 for language, and r = 0.305 for verbal memory. Models informed by total or tract-wise WMH volumes achieved a predictive performance of r = 0.341 - 0.365 for attention /

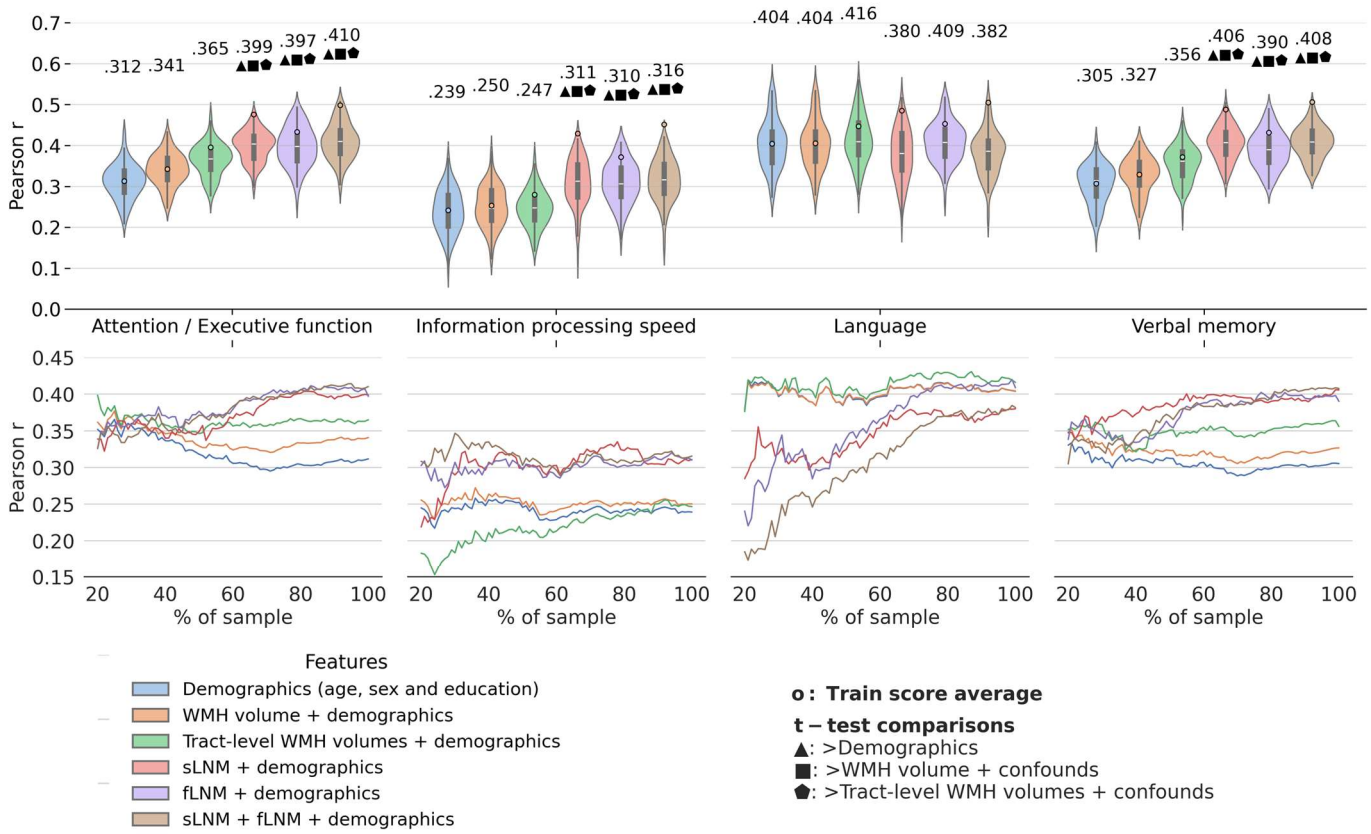

Figure 2. Predictive modelling analysis. Violin plots illustrate prediction outcomes across cognitive domains. Each violin displays the distribution of Pearson correlations (between actual and predicted cognitive domain performance; 10-fold cross-validation × 10 repeats = 100 folds → 100 Pearson correlations) for a model informed by a different feature set. The higher the Pearson correlation, the higher the prediction performance. blue: demographics (age, sex and education); orange: total WMH volume + demographics; green: tract-level WMH volumes + demographics; red: sLNM scores + demographics; purple: fLNM scores + demographics; brown: sLNM scores + fLNM scores + demographics. Average Pearson correlations are indicated above each violin, with colored dots showing training score averages. Geometric symbols denote t-test results comparing LNM-based models against demographics- and WMH volume-based models: ▲ indicates higher Pearson correlation than demographics, ■ than WMH volume + demographics, ⬟ than tract-level WMH volume + demographics. Below the violin plots, performance curves display the average Pearson correlations across folds, for subsets randomly sampled in sizes ranging from 20% to 100% of the entire dataset. Line colors match the corresponding violin plots in panel a) which display predictive modelling results for the full sample size. Again, higher Pearson correlation indicates higher prediction performance. *Abbreviations*: fLNM = functional lesion network mapping, sLNM = structural lesion network mapping, WMH = white matter hyperintensities of presumed vascular origin.

executive function, r = 0.247 – 0.250 for information processing speed, r = 0.404 – 0.416 for language, and r = 0.327 – 0.356 for verbal memory. For the prediction of attention / executive function, models informed by LNM scores exhibited a significantly higher predictive performance than models informed by volumetric WMH measures (LNM: r = 0.399 - 0.410 vs. WMH volume: r = 0.341 – 0.365; adjusted t-test, all $p < 0.05$). LNM-informed models also better predicted information processing speed (LNM: r = 0.310 - 0.316 vs. WMH volume: r = 0.247 – 0.250, adjusted t-test, all $p < 0.05$) as well as verbal memory (LNM: r = 0.390 - 0.408 vs. WMH volume: r = 0.327 – 0.356; adjusted t-test, all $p < 0.05$). Across these domains, the best prediction was achieved by models incorporating both structural and functional LNM scores. For attention / executive function, comparing the improvement from the demographics-based model to the model informed by total WMH volume (0.341 – 0.312 = 0.029) with the improvement to the model based on both LNM modalities (0.410 – 0.312 = 0.098), the usage of fLNM and sLNM scores amounts to a 3.38-fold increase (0.098 / 0.029 = 3.38) in added predictive performance. Considering both LNM modalities for predicting information processing speed and verbal memory amounted to 7.00-fold and 4.68-fold increase in predictive performance, respectively. For the prediction of language domain scores, performance between LNM-informed models and WMH volume measures did not differ significantly (LNM: r = 0.380 - 0.409 vs. WMH volume: r = 0.404 – 0.416, all $p > 0.05$). See *supplementary materials S4* and *S5* for predictive modelling results using explained variance and negative mean squared error as scoring methods. Details on regional averages of LNM scores are shown *supplementary figure S6*.

To test the robustness of prediction results, we repeated the analysis in randomly chosen subsamples of increasing sizes (*figure 2b*). For attention / executive function and verbal memory, LNM-informed models started to consistently exceed WMH volume-based models at approximately 50% (attention / executive function: n=1723, verbal memory: n=1712; note that data availability differed between cognitive domain scores) of the sample size.

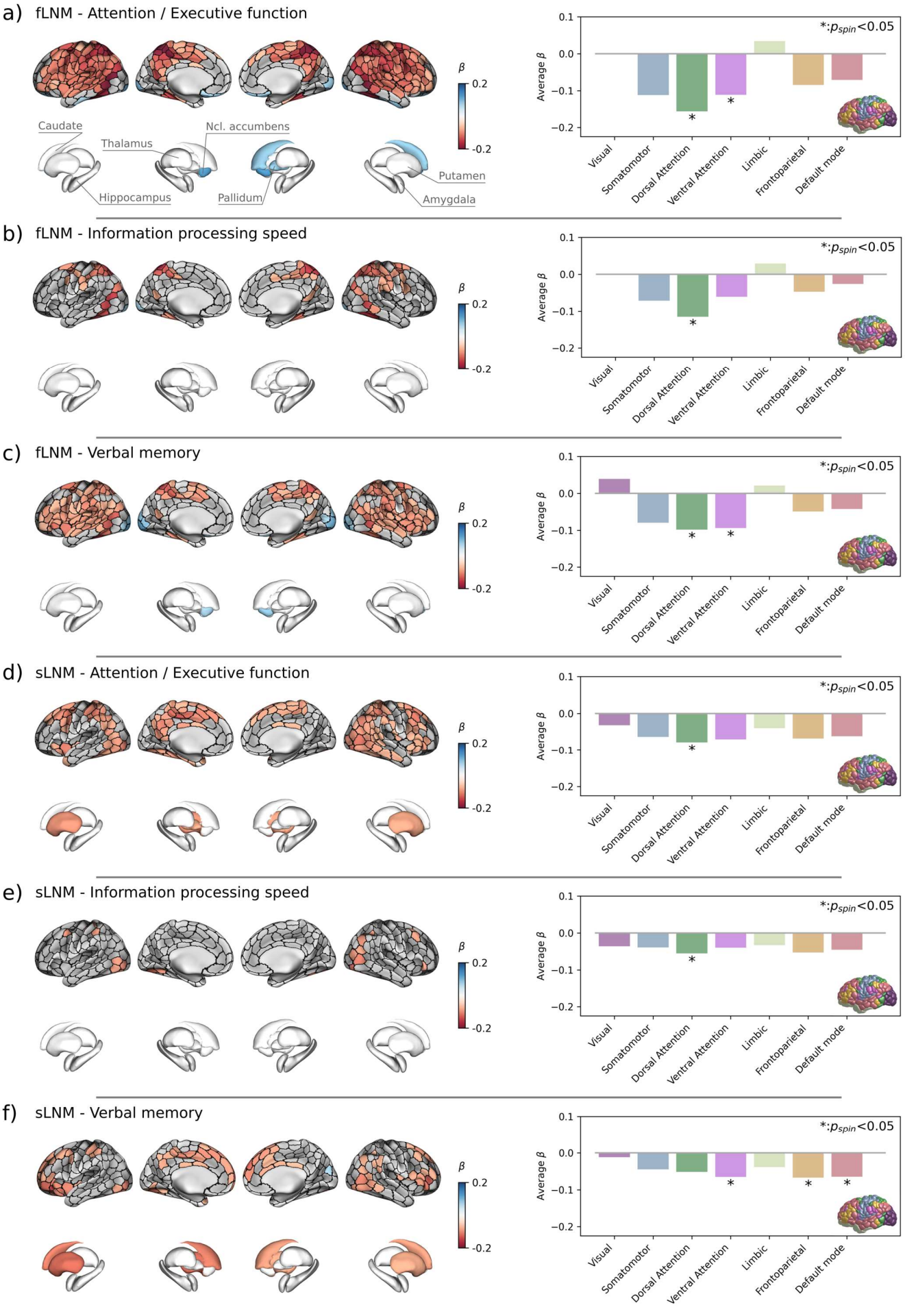
a) fLNM - Attention / Executive function
b) fLNM - Information processing speed
c) fLNM - Verbal memory
d) sLNM - Attention / Executive function
e) sLNM - Information processing speed
f) sLNM - Verbal memory
Caudate
Thalamus
Ncl. accumbens
Hippocampus
Pallidum
Putamen
Amygdala
β
0.2
-0.2
*:p_{spin}<0.05
Average β
0.1
0.0
−0.1
−0.2
Visual
Somatomotor
Dorsal Attention
Ventral Attention
Limbic
Frontoparietal
Default mode

Figure 3. Inferential statistics results of cortical and subcortical gray matter. Anatomical plots on the left side display the regional relationship between LNM scores and cognitive domain scores. ROIs in which LNM scores across participants were significantly associated with cognitive domain scores after family-wise error-correction are highlighted by colors encoding β-coefficients from general linear models: a negative β (red) denotes that a higher regional LNM score, i.e., higher WMH connectivity, is associated to a lower performance in individual cognitive domains; a positive β (blue) indicates that a higher regional LNM score is linked to a higher cognitive domain performance. Barplots on the right side display the corresponding β coefficients averaged in the canonical (Yeo) resting-state functional connectivity networks. The brain in the lower right corner indicates the regional distribution of the canonical resting-state networks with colors corresponding to the bars. Statistical significance was assessed using spin permutations. Each row corresponds with a different combination of lesion network mapping modality and cognitive domain: a) fLNM – attention / executive function, b) fLNM – information processing speed, c) fLNM – verbal memory, d) sLNM – attention / executive function, e) sLNM – information processing speed, f) sLNM – verbal memory. *Abbreviations*: fLNM = functional lesion network mapping, p_{spin} = p-value derived from spin permutations, ROIs = regions of interest, sLNM = structural lesion network mapping.

For information processing speed, LNM-informed models surpassed WMH volume-based models at approximately 25% (n=604) of the sample size. Regarding language, LNM-informed models approximated the performance of WMH volume-based models with increasing sample sizes. For all cognitive domain scores, predictive performance in the sample size range 80-100% showed high stability and only minor increases indicating saturation.

Contextualization of WMH connectivity: Region of interest analysis

We tested if WMH connectivity of specific brain circuits links to cognitive performance by quantifying the association between *regional* LNM scores (cortical brain regions and white matter tracts) and cognitive domain scores adjusting for age, sex and education.

Results of the general linear model linking LNM scores in cortical and subcortical gray matter regions to cognitive domain scores are shown in *figure 3*. Higher fLNM scores (i. e. increased WMH connectivity) in cortical regions of the dorsal attention and ventral attention networks were linked to lower attention / executive function and verbal memory (*figure 3a* and *c*). Regarding information processing speed, the extent of the effect was limited to several cortical brain areas mapping to the dorsal attention network (*figure 3b*). In terms of sLNM, higher scores in the dorsal attention network were significantly associated with lower attention / executive function and information processing speed (*figure 3d* and *e*). Again, information processing speed showed a spatially more limited effect pattern. The relationship of regional sLNM and verbal memory scores showed a different spatial distribution mapping to the ventral attention, frontoparietal and default mode network (*figure 3f*). The cortical and subcortical LNM scores showed no significant association with the language domain score.

The results for anatomically predefined white matter tracts are shown in *figure* 4. For tract-level fLNM, lower cognitive performance in attention / executive function, information processing speed and verbal memory was most strongly linked to higher fLNM scores in association and projection tracts connecting the parietal cortex (*figure 4b*): the middle longitudinal fasciculus (MdLF), parietal corticopontine tract (CPT), dorsal, medial and ventral sections of the superior longitudinal fasciculus (SLF 1-3), the parietoparahippocampal cingulate (C parietoparahipp.). For attention / executive function, a strong negative effect was also evident for the right arcuate fasciculus (AF). For verbal memory, significant negative effects were additionally found for the corticobulbar tract (CBT) and frontal aslant tract (FAT).

Regarding tract-level sLNM, lower attention / executive function and verbal memory were significantly associated with higher sLNM scores in association and projection tracts connecting frontal regions (*figure 4c*): the frontoparahippocampal cingulate (C parietoparahipp.), parolfactory cingulate (C parolfactory), the superior longitudinal fasciculus (SLF 1-3), frontoparietal cingulate (C frontoparietal), anterior thalamic radiation, anterior corticostriatal pathways (CS anterior), uncinate fascicle, frontal corticopontine tract (CPT frontal). For attention / executive function, a strong negative effect was also evident for the right arcuate fasciculus (AF). Furthermore, higher verbal memory scores were significantly linked to higher sLNM scores in the fornices. Information processing speed showed a significant negative association with sLNM scores in the right medial superior longitudinal fasciculus (SLF 2) and frontoparahippocampal cingulate (C frontoparahipp.). Tract-level LNM scores showed no significant association with language function. For plots displaying all tract-level associations refer to *supplementary figures S7* and *S8*.

The spatial effect patterns, i.e., β-coefficient maps, showed significant overlap with 26 of 28 effect pattern pairs being significantly correlated (see *supplementary figure S9* for a correlation matrix).

Sensitivity analyses

Predictive modelling results were stable when using negative fLNM scores (based on anti-correlations in resting-state fMRI measures) and when including a 25% or 50% thresholding step (*supplementary figure S10*). Exploratory ROI-level inferential statistics based on negative fLNM scores indicated that lower attention / executive function and information processing speed were more significantly associated with more negative fLNM scores in the default mode network (*supplementary figure S11 & S12*).

Exploratory analyses

Exploratory analyses are detailed in *supplementary text S2*. Functional and structural LNM scores were significantly correlated across ROIs and across subjects (*supplementary figure S13*). Voxel-level lesion network maps indicating white matter regions that contribute to variance in cognitive domain function are shown in *supplementary figure S14 & S15*.

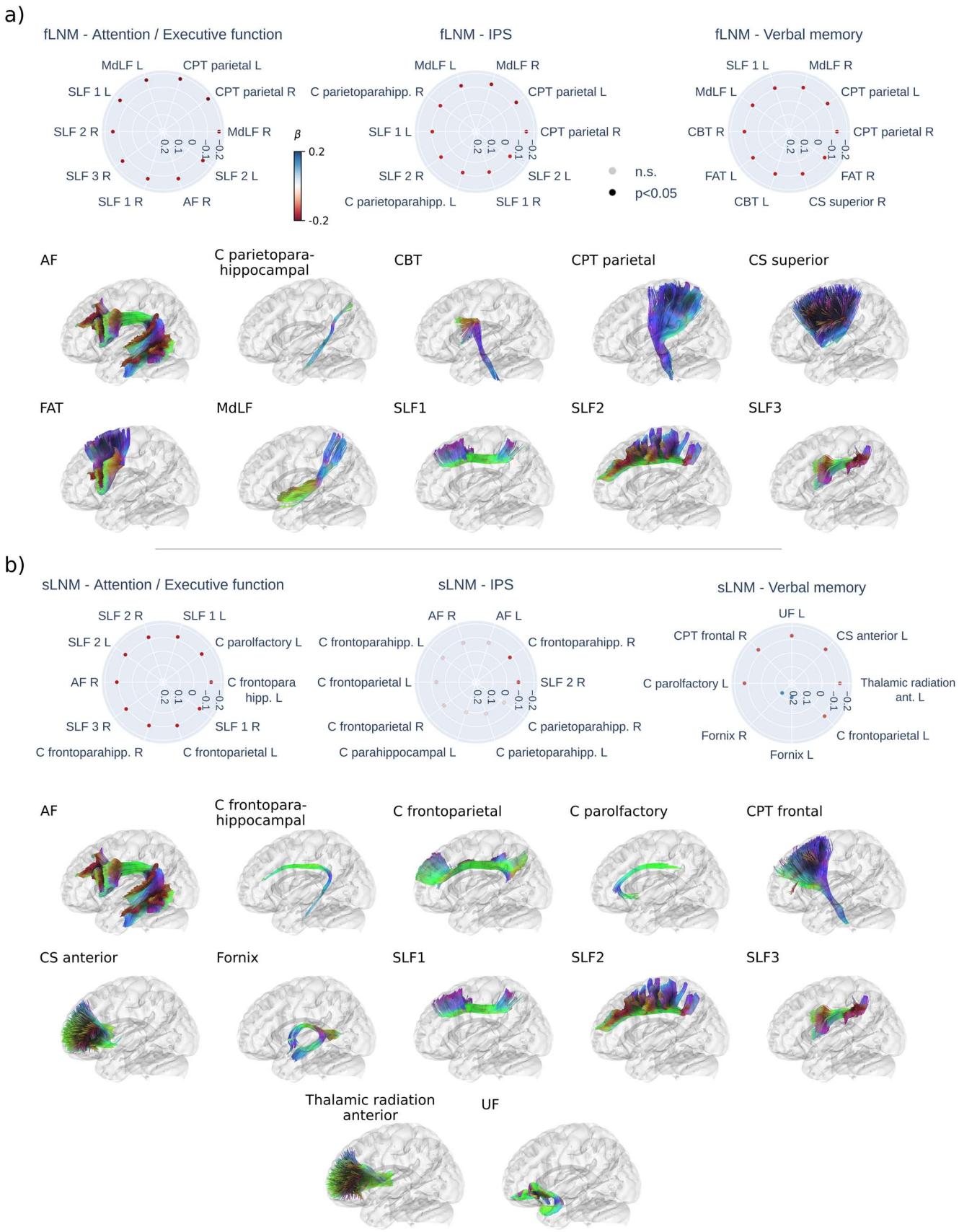
a)
fLNM - Attention / Executive function
MdLF L
CPT parietal L
SLF 1 L
CPT parietal R
SLF 2 R
MdLF R
SLF 3 R
SLF 2 L
SLF 1 R
AF R
β
0.2
-0.2
fLNM - IPS
MdLF L
MdLF R
C parietoparahipp. R
CPT parietal L
SLF 1 L
CPT parietal R
SLF 2 R
SLF 2 L
C parietoparahipp. L
SLF 1 R
n.s.
p<0.05
fLNM - Verbal memory
SLF 1 L
MdLF R
MdLF L
CPT parietal L
CBT R
CPT parietal R
FAT L
FAT R
CBT L
CS superior R
AF
C parietopara-hippocampal
CBT
CPT parietal
CS superior
FAT
MdLF
SLF1
SLF2
SLF3
b)
sLNM - Attention / Executive function
SLF 2 R
SLF 1 L
SLF 2 L
C parolfactory L
AF R
C frontopara hipp. L
SLF 3 R
SLF 1 R
C frontoparahipp. R
C frontoparietal L
sLNM - IPS
AF R
AF L
C frontoparahipp. L
C frontoparahipp. R
C frontoparietal L
SLF 2 R
C frontoparietal R
C parietoparahipp. R
C parahippocampal L
C parietoparahipp. L
sLNM - Verbal memory
UF L
CPT frontal R
CS anterior L
C parolfactory L
Thalamic radiation ant. L
Fornix R
C frontoparietal L
Fornix L
AF
C frontopara-hippocampal
C frontoparietal
C parolfactory
CPT frontal
CS anterior
Fornix
SLF1
SLF2
SLF3
Thalamic radiation anterior
UF

Figure 4. Inferential statistics results of white matter tracts. Radar plots displaying the top 10 of strongest linear associations (standardized β) for the functional (a) and structural (b) lesion network mapping scores in each tract in association with cognitive domain scores. Strongest associations are shown at the 3 o'clock position, decreasing in strength counterclockwise. Red dots indicate a negative association (higher LNM score – lower cognitive domain score) and blue dots indicate a positive association (higher LNM score – higher cognitive domain score). Faintly colored dots indicate non-significant associations. Tracts with a significant association are displayed below the radar plots in alphabetical order. For paired tracts only left side examples are visualized. *Tract abbreviations*: AF = arcuate fascicle, C = cingulate, CBT = corticobulbar tract, CPT = corticopontine tract, CS = corticostriatal pathway, F = fornix, FAT = frontal aslant tract, MdLF = middle longitudinal fasciculus, SLF = superior longitudinal fasciculus, UF = uncinate fasciculus; *Abbreviations*: fLNM = functional lesion network mapping, IPS – information processing speed, n.s. = non-significant, p = p-value, sLNM = structural lesion network mapping.

Discussion

In a large multicentric sample of memory clinic patients, we conducted an in-depth examination of the link between functional and structural LNM scores and cognitive performance. We report two main findings: (1) both structural and functional LNM scores, capturing WMH-related connectivity, significantly improved the prediction of cognitive performance compared to WMH volume; (2) WMH connectivity associated with lower cognitive performance, predominantly mapped to the dorsal and ventral attention networks.

LNM scores surpass WMH volumes in predicting cognitive performance

In current clinical practice, vascular cognitive impairment in individual patients is often attributed to total WMH burden, but interindividual variance in this relationship can lead to diagnostic dilemmas. Previous research has demonstrated that strategic WMH locations, specifically in commissural and association tracts are statistically more likely to be associated with lower cognitive performance.[4,6,7] Our approach adds to this perspective, not only considering the localization of WMH but also integrating them with network connectivity information to capture the WMH network embedding. In our analysis, statistical models capitalizing on LNM scores demonstrated superior performance over those relying on total or tract-level WMH volume in predicting cognitive performance in almost all cognitive domains. As this analysis implements current best practices of predictive modelling in neuroimaging, our findings represent evidence for a true prediction of cognitive performance by LNM.[34] Comparing the improvement from the demographics-based model to the model informed by total WMH volume with the improvement to the model based on both LNM modalities, the usage of fLNM and sLNM scores yielded to a 3- to 7-fold increase in added predictive performance across the three cognitive domains. Moreover, our findings highlighted that total WMH volumes only marginally surpass age, sex, and education in predictive accuracy, stressing the importance of including demographic information as a baseline in predictive models to assess the added value of WMH volume. Collectively, these findings are important, given the longstanding reliance on WMH extent as a primary imaging surrogate marker for cognitive impairment in CSVD. We provide evidence for the considerable role of WMH-related "covert" network effects as indicated previously in studies from smaller clinical or population-based studies.[8,46–48]

Improved prediction of cognitive performance was achieved irrespective of the applied LNM modality. Contrasting prior studies suggesting the inferiority of functional LNM compared to structural approaches for predicting cognitive performance post-stroke,[9,49] our contrary findings might arise from differences in the LNM approach as well as our focus on WMH rather than ischemic stroke lesions. The ROI-based functional LNM method we used may be more suitable to detect the widespread network disturbances induced by WMH, as opposed to the localized disruptions from stroke lesions. Notably, fLNM and sLNM scores were positively correlated, suggesting some degree of structure-function coupling that could account for their comparable predictive performance. However, the correlation strength was mostly moderate and prediction performance of fLNM and sLNM differed noticeably across sample sizes. In addition, among LNM-informed models, those incorporating both fLNM and sLNM modalities yielded the strongest results. This suggests that both LNM approaches are equally valuable for achieving a high predictive accuracy in general but might also offer complementary information.

Although prediction of almost all cognitive domains was improved by LNM scores, predictive performance for language functions did not exceed that of WMH volumes and demographics. From a network perspective, we argue that this finding can be explained by the relatively confined network of left-lateralized brain regions involved in language functions which might present lower vulnerability to WMH disconnectivity compared to cognitive functions such as information processing speed, that rely on a widely distributed network of brain regions.[50] In general, the minor improvement of WMH-based measures over the predictive performance attributed to demographics in the whole sample suggests that in this patient population, WMH contribute minimally to the variance in language function.

WMH related to cognitive impairment map to attention control networks

WMH compromise cognitive performance by impacting the function of specific brain networks. To localize these effects, we investigated *regional* associations between functional and structural LNM scores to cognitive performance. We found that higher LNM scores in cortical areas of the dorsal and ventral attention networks were linked to lower attention and executive function, information processing speed and verbal memory (figure 3). Therefore, higher WMH connectivity in these networks is associated with reduced cognitive performance indicating that WMH impair cognitive function by disrupting the respective connecting white matter fiber tracts.

The dorsal attention network – including the frontal eye field, the superior parietal lobule, the intraparietal sulcus and caudal areas of the medial temporal gyrus – governs top-down attention control by enabling voluntary orientation, with increased activity in response to cues indicating the focus location, timing, or subject.[51,52] The ventral attention network comprises the frontal and parietal operculum in the inferior frontal gyrus, medial areas of the

superior frontal cortex and the temporoparietal junction.[44,53] This system exhibits activity increases during bottom-up attention control, i.e., upon detection and orientation to salient targets, especially when they appear in unexpected locations.[51,54] As the effect patterns largely converged on these networks (*supplementary figure S9*), we argue that WMH affect the cognitive functions emerging from these networks, specifically top-down and bottom-up attention control. This aligns with the observation that deficits in attention and executive function are among the most prominent symptoms in CSVD and VCI in general.[1] Furthermore, prior work demonstrates altered resting-state functional connectivity as well as task activation in attention control networks related to CSVD.[55–57] Given the covariance of the identified effect patterns, we speculate that WMH contribute to variance in the performance of other cognitive domains, e.g., information processing speed by affecting the attention demands posited by the corresponding tests.

WMH contribute to cognitive impairment by disrupting frontal and parietal white matter tracts

Regional findings in gray matter areas of the attention control networks are further complemented by white matter tract-level results (figure 4). Functional and structural LNM converged on a significant involvement of tracts connecting frontal and parietal areas involved in attention: the dorsal, medial and ventral section of the superior longitudinal fasciculus – which are known to connect the anterior and posterior parts of the dorsal and ventral attention networks, the medial longitudinal fasciculus, the corticopontine tract, frontoparietal sections of the cingulate, the anterior thalamic radiation, the frontal aslant tract and the arcuate fascicle. Although there were some differences in highlighted tracts between functional and structural LNM, this possibly reflects that both approaches capture different aspects of the same anatomy, with sLNM possibly being more sensitive to direct WMH-induced disruption of axonal connections and functional LNM also reflecting effects mediated via polysynaptic brain circuitry.

Strikingly, in the context of verbal memory, structural WMH connectivity pinpointed a distinct set of memory-relevant tracts: the uncinate fascicle, cingulate, and fornix. Intriguingly, disruptions in fornix connectivity due to WMH were associated with improved verbal memory in patients, a finding that appears counterintuitive given the fornix's involvement in maintaining memory function. This paradox may be attributable to WMH disrupting inhibitory fibers. For further discussion covering negative fLNM scores/anticorrelations see *supplementary text S16*.

A unifying hypothesis of WMH disconnectivity

Drawing upon a comprehensive LNM analysis in a memory clinic sample of patients with differing extent and etiology of cognitive impairment, our research converges on a unifying hypothesis: WMH contribute to variance in cognitive functions by disrupting brain circuitry involved in attention control. Our findings not only shed light on the intricate relationships between CSVD, neuroanatomy and cognitive impairment, but they also hint at potential avenues of clinical utilization. The definitive role of CSVD treatments, particularly in precluding cognitive sequelae, is yet to be firmly established. Although there have been promising outcomes related to risk factor modification, particularly blood pressure control,[58,59] pointing towards enhanced cognitive trajectories, clinical trials in VCI require biomarkers to robustly identify vascular contributions to cognitive impairment and vulnerable individuals. Moving forward, leveraging connectivity information could address this gap contributing to patient-tailored therapeutic interventions and facilitating the identification of subgroups at risk of cognitive disorders through vascular lesions likely to reap the most substantial benefits from medical interventions.

Strengths and limitations

This study's strength lies in its integration of innovative analytical techniques with a large, multicentric dataset.[60] However, we acknowledge several limitations that warrant consideration when interpreting our findings. The inclusion of selected patient samples in several cohorts may limit generalizability to the broader memory clinic population. Additionally, with most patients being of European ancestry, the generalizability of our findings to other ethnicities remains to be established. Furthermore, despite the harmonization of cognitive and imaging data, biases stemming from variations in data acquisition and processing protocols across sites may have impacted our results. On a technical note, while computing fLNM scores, we sampled resting-state BOLD signals in the white matter, typically regarded as noisy and often dismissed as an artifact. However, by integrating it with WMH data, we successfully predicted cognitive performance and demonstrated correlations with structural connectivity information. This challenges the traditional view of the white matter BOLD signal as a mere artefact and supports recent studies – including LNM analyses of white matter lesions in multiple sclerosis – demonstrating that it contains biologically meaningful information.[61–63]

Conclusion

WMH-related brain network connectivity measures significantly improve the prediction of current cognitive performance in memory clinic patients compared to WMH volume or epidemiological factors. Our findings highlight the contribution of WMH disconnectivity, particularly in attention-related brain regions, to vascular cognitive impairment. As this research field progresses, harnessing neuroimaging markers of WMH connectivity in CSVD has the potential to aid individualized diagnostic and therapeutic strategies.

Acknowledgements

The authors wish to acknowledge all participants of the Meta VCI Map Consortium. We thank Lei Zhao for his contribution to imaging data harmonization of the Meta VCI Map project data. We thank Guido Cammà and Charlotte M. Verhagen for their contribution to the processing of the imaging data. We thank Olivia K.L. Hamilton, Irene M.C. Huenges Wajer, Bonnie Y.K. Lam, Adrian Wong and Xu Xin as members of the Meta VCI Map neuropsychology working group for their advice on neuropsychological data harmonization.

ADNI data used in preparation of this article were obtained from the Alzheimer's Disease Neuroimaging

Initiative (ADNI) database (adni.loni.usc.edu). As such, the investigators within the ADNI contributed to the design and implementation of ADNI and/or provided data but did not participate in analysis or writing of this report. A complete listing of ADNI investigators can be found at: https://adni.loni.usc.edu/wp-content/uploads/how_to_apply/ADNI_Acknowledgement_List.pdf

Funding

This work was funded by the Deutsche Forschungsgemeinschaft (DFG, German Research Foundation – Schwerpunktprogramm 2041 – 454012190 (S.B.E., G.T.); the Meta VCI Map consortium is supported by Vici grant 918.16.616 from ZonMw (G.J.B.) and by Veni grant (project 9150162010055) from ZonMW to JMB; National Institutes of Health (NIH), UCD ADRC NIH awards P30 AG10129 and P30 AG072972 (C.D.); V.V. is supported by JPND-funded E-DADS project (ZonMW project #733051106). ADNI data collection and sharing for this project was funded by the Alzheimer's Disease Neuroimaging Initiative (ADNI) (National Institutes of Health Grant U01 AG024904) and DOD ADNI (Department of Defense award number W81XWH-12-2-0012). ADNI is funded by the National Institute on Aging, the National Institute of Biomedical Imaging and Bioengineering, and through generous contributions from the following: AbbVie, Alzheimer's Association; Alzheimer's Drug Discovery Foundation; Araclon Biotech; BioClinica, Inc.; Biogen; Bristol-Myers Squibb Company; CereSpir, Inc.; Cogstate; Eisai Inc.; Elan Pharmaceuticals, Inc.; Eli Lilly and Company; EuroImmun; F. Hoffmann-La Roche Ltd and its affiliated company Genentech, Inc.; Fujirebio; GE Healthcare; IXICO Ltd.; Janssen Alzheimer Immunotherapy Research & Development, LLC.; Johnson & Johnson Pharmaceutical Research & Development LLC.; Lumosity; Lundbeck; Merck & Co., Inc.; Meso Scale Diagnostics, LLC.; NeuroRx Research; Neurotrack Technologies; Novartis Pharmaceuticals Corporation; Pfizer Inc.; Piramal Imaging; Servier; Takeda Pharmaceutical Company; and Transition Therapeutics. The Canadian Institutes of Health Research is providing funds to support ADNI clinical sites in Canada. Private sector contributions are facilitated by the Foundation for the National Institutes of Health (www.fnih.org). The grantee organization is the Northern California Institute for Research and Education, and the study is coordinated by the Alzheimer's Therapeutic Research Institute at the University of Southern California. ADNI data are disseminated by the Laboratory for Neuro Imaging at the University of Southern California.

Competing interests

F.B. is supported by the NIHR biomedical research center at UCLH. M.D. received honoraria for lectures from Bayer Vital and Sanofi Genzyme, Consultant for Hovid Berhad and Roche Pharma. G.T. has received fees as consultant or lecturer from Acandis, Alexion, Amarin, Bayer, Boehringer Ingelheim, BristolMyersSquibb/Pfizer, Daichi Sankyo, Portola, and Stryker outside the submitted work.

References

1. Dichgans Martin, Leys Didier. Vascular Cognitive Impairment. *Circulation Research*. 2017;120(3):573-591. doi:10.1161/CIRCRESAHA.116.308426
2. Wardlaw JM, Smith EE, Biessels GJ, et al. Neuroimaging standards for research into small vessel disease and its contribution to ageing and neurodegeneration. *The Lancet Neurology*. 2013;12(8):822-838. doi:10.1016/S1474-4422(13)70124-8
3. Duering M, Biessels GJ, Brodtmann A, et al. Neuroimaging standards for research into small vessel disease—advances since 2013. *The Lancet Neurology*. Published online May 23, 2023. doi:10.1016/S1474-4422(23)00131-X
4. Biesbroek JM, Weaver NA, Hilal S, et al. Impact of Strategically Located White Matter Hyperintensities on Cognition in Memory Clinic Patients with Small Vessel Disease. *PLOS ONE*. 2016;11(11):e0166261. doi:10.1371/journal.pone.0166261
5. Kloppenborg RP, Nederkoorn PJ, Geerlings MI, van den Berg E. Presence and progression of white matter hyperintensities and cognition: a meta-analysis. *Neurology*. 2014;82(23):2127-2138. doi:10.1212/WNL.0000000000000505
6. Coenen M, Kuijf HJ, Huenges Wajer IMC, et al. Strategic white matter hyperintensity locations for cognitive impairment: A multicenter lesion-symptom mapping study in 3525 memory clinic patients. *Alzheimer's & Dementia*. Published online December 12, 2022:alz.12827. doi:10.1002/alz.12827
7. Duering M, Gesierich B, Seiler S, et al. Strategic white matter tracts for processing speed deficits in age-related small vessel disease. *Neurology*. 2014;82(22):1946-1950. doi:10.1212/WNL.0000000000000475
8. ter Telgte A, van Leijsen EMC, Wiegertjes K, Klijn CJM, Tuladhar AM, de Leeuw FE. Cerebral small vessel disease: from a focal to a global perspective. *Nature Reviews Neurology*. 2018;14(7):387-398. doi:10.1038/s41582-018-0014-y
9. Salvalaggio A, De Filippo De Grazia M, Zorzi M, Thiebaut de Schotten M, Corbetta M. Post-stroke deficit prediction from lesion and indirect structural and functional disconnection. *Brain*. 2020;143(7):2173-2188. doi:10.1093/brain/awaa156
10. Foulon C, Cerliani L, Kinkingnéhun S, et al. Advanced lesion symptom mapping analyses and implementation as BCBtoolkit. *Gigascience*. 2018;7(3):1-17. doi:10.1093/gigascience/giy004
11. Talozzi L, Forkel SJ, Pacella V, et al. Latent disconnectome prediction of long-term cognitive-behavioural symptoms in stroke. *Brain*. Published online March 16, 2023:awad013. doi:10.1093/brain/awad013
12. Siddiqi SH, Kletenik I, Anderson MC, et al. Lesion network localization of depression in multiple sclerosis. *Nat Mental Health*. 2023;1(1):36-44. doi:10.1038/s44220-022-00002-y
13. Weaver NA, Zhao L, Biesbroek JM, et al. The Meta VCI Map consortium for meta-analyses on strategic lesion locations for vascular cognitive impairment using

lesion-symptom mapping: Design and multicenter pilot study. *Alzheimers Dement (Amst)*. 2019;11:310-326. doi:10.1016/j.dadm.2019.02.007
14. Jack CR, Barnes J, Bernstein MA, et al. Magnetic resonance imaging in Alzheimer's Disease Neuroimaging Initiative 2. *Alzheimers Dement*. 2015;11(7):740-756. doi:10.1016/j.jalz.2015.05.002
15. Hinton L, Carter K, Reed BR, et al. Recruitment of a community-based cohort for research on diversity and risk of dementia. *Alzheimer Dis Assoc Disord*. 2010;24(3):234-241. doi:10.1097/WAD.0b013e3181c1ee01
16. Case NF, Charlton A, Zwiers A, et al. Cerebral Amyloid Angiopathy Is Associated With Executive Dysfunction and Mild Cognitive Impairment. *Stroke*. 2016;47(8):2010-2016. doi:10.1161/STROKEAHA.116.012999
17. Pusswald G, Lehrner J, Hagmann M, et al. Gender-Specific Differences in Cognitive Profiles of Patients with Alzheimer's Disease: Results of the Prospective Dementia Registry Austria (PRODEM-Austria). *J Alzheimers Dis*. 2015;46(3):631-637. doi:10.3233/JAD-150188
18. Boomsma JMF, Exalto LG, Barkhof F, et al. Vascular Cognitive Impairment in a Memory Clinic Population: Rationale and Design of the "Utrecht-Amsterdam Clinical Features and Prognosis in Vascular Cognitive Impairment" (TRACE-VCI) Study. *JMIR Res Protoc*. 2017;6(4):e60. doi:10.2196/resprot.6864
19. Weaver NA, Kuijf HJ, Aben HP, et al. Strategic infarct locations for post-stroke cognitive impairment: a pooled analysis of individual patient data from 12 acute ischaemic stroke cohorts. *The Lancet Neurology*. 2021;0(0). doi:10.1016/S1474-4422(21)00060-0
20. Kuijf HJ, Biesbroek JM, De Bresser J, et al. Standardized Assessment of Automatic Segmentation of White Matter Hyperintensities and Results of the WMH Segmentation Challenge. *IEEE Trans Med Imaging*. 2019;38(11):2556-2568. doi:10.1109/TMI.2019.2905770
21. Biesbroek JM, Kuijf HJ, Weaver NA, et al. Brain Infarct Segmentation and Registration on MRI or CT for Lesion-symptom Mapping. *J Vis Exp*. 2019;(151). doi:10.3791/59653
22. Yeh FC. Population-based tract-to-region connectome of the human brain and its hierarchical topology. *Nat Commun*. 2022;13(1):4933. doi:10.1038/s41467-022-32595-4
23. Coenen M, Biessels GJ, DeCarli C, et al. Spatial distributions of white matter hyperintensities on brain MRI: A pooled analysis of individual participant data from 11 memory clinic cohorts. *NeuroImage: Clinical*. 2023;40:103547. doi:10.1016/j.nicl.2023.103547
24. Jiang J, Bruss J, Lee WT, Tranel D, Boes AD. White matter disconnection of left multiple demand network is associated with post-lesion deficits in cognitive control. *Nat Commun*. 2023;14(1):1740. doi:10.1038/s41467-023-37330-1
25. Schaefer A, Kong R, Gordon EM, et al. Local-Global Parcellation of the Human Cerebral Cortex from Intrinsic Functional Connectivity MRI. *Cerebral Cortex*. 2018;28(9):3095-3114. doi:10.1093/cercor/bhx179
26. Tian Y, Margulies DS, Breakspear M, Zalesky A. Topographic organization of the human subcortex unveiled with functional connectivity gradients. *Nat Neurosci*. 2020;23(11):1421-1432. doi:10.1038/s41593-020-00711-6
27. Cohen A, Soussand L, McManus P, Fox M. GSP1000 Preprocessed Connectome. Published online April 17, 2021. doi:10.7910/DVN/ILXIKS
28. Yeo BTT, Krienen FM, Sepulcre J, et al. The organization of the human cerebral cortex estimated by intrinsic functional connectivity. *J Neurophysiol*. 2011;106(3):1125-1165. doi:10.1152/jn.00338.2011
29. Neudorfer C, Butenko K, Oxenford S, et al. Lead-DBS v3.0: Mapping deep brain stimulation effects to local anatomy and global networks. *NeuroImage*. 2023;268:119862. doi:10.1016/j.neuroimage.2023.119862
30. Horn A, Reich M, Vorwerk J, et al. Connectivity Predicts deep brain stimulation outcome in Parkinson disease. *Annals of Neurology*. 2017;82(1):67-78. doi:10.1002/ana.24974
31. Fang-Cheng Yeh, Wedeen VJ, Tseng WYI. Generalized q-Sampling Imaging. *IEEE Trans Med Imaging*. 2010;29(9):1626-1635. doi:10.1109/TMI.2010.2045126
32. Hamdan S, More S, Sasse L, et al. Julearn: an easy-to-use library for leakage-free evaluation and inspection of ML models. *Gigabyte*. 2024;2024:1-16. doi:10.46471/gigabyte.113
33. Abraham A, Pedregosa F, Eickenberg M, et al. Machine learning for neuroimaging with scikit-learn. *Frontiers in Neuroinformatics*. 2014;8. Accessed March 28, 2022. https://www.frontiersin.org/article/10.3389/fninf.2014.00014
34. Poldrack RA, Huckins G, Varoquaux G. Establishment of Best Practices for Evidence for Prediction: A Review. *JAMA Psychiatry*. 2020;77(5):534-540. doi:10.1001/jamapsychiatry.2019.3671
35. Padmanabhan JL, Cooke D, Joutsa J, et al. A Human Depression Circuit Derived From Focal Brain Lesions. *Biological Psychiatry*. 2019;86(10):749-758. doi:10.1016/j.biopsych.2019.07.023
36. Bos D, Ikram MA. Research Aims in Clinical Medicine: Description, Identification, or Explanation. *World Neurosurgery*. 2022;161:240-244. doi:10.1016/j.wneu.2021.11.081
37. Omidvarnia A, Sasse L, Larabi DI, et al. Is resting state fMRI better than individual characteristics at predicting cognition? Published online April 25, 2023:2023.02.18.529076. doi:10.1101/2023.02.18.529076
38. Varoquaux G, Raamana PR, Engemann DA, Hoyos-Idrobo A, Schwartz Y, Thirion B. Assessing and tuning brain decoders: Cross-validation, caveats, and guidelines. *NeuroImage*. 2017;145:166-179. doi:10.1016/j.neuroimage.2016.10.038
39. Nadeau C, Bengio Y. Inference for the Generalization Error. *Machine Learning*. 2003;52(3):239-281. doi:10.1023/A:1024068626366
40. Vallat R. Pingouin: statistics in Python. *JOSS*. 2018;3(31):1026. doi:10.21105/joss.01026

41. Winkler AM, Ridgway GR, Webster MA, Smith SM, Nichols TE. Permutation inference for the general linear model. *Neuroimage*. 2014;92:381-397. doi:10.1016/j.neuroimage.2014.01.060
42. Markello RD, Hansen JY, Liu ZQ, et al. neuromaps: structural and functional interpretation of brain maps. *Nat Methods*. Published online October 6, 2022:1-8. doi:10.1038/s41592-022-01625-w
43. Margulies DS, Ghosh SS, Goulas A, et al. Situating the default-mode network along a principal gradient of macroscale cortical organization. *Proc Natl Acad Sci U S A*. 2016;113(44):12574-12579. doi:10.1073/pnas.1608282113
44. Fox MD, Snyder AZ, Vincent JL, Corbetta M, Van Essen DC, Raichle ME. The human brain is intrinsically organized into dynamic, anticorrelated functional networks. *Proceedings of the National Academy of Sciences*. 2005;102(27):9673-9678. doi:10.1073/pnas.0504136102
45. Fox MD, Zhang D, Snyder AZ, Raichle ME. The Global Signal and Observed Anticorrelated Resting State Brain Networks. *Journal of Neurophysiology*. 2009;101(6):3270-3283. doi:10.1152/jn.90777.2008
46. De Luca A, Kuijf H, Exalto L, Thiebaut de Schotten M, Biessels GJ. Multimodal tract-based MRI metrics outperform whole brain markers in determining cognitive impact of small vessel disease-related brain injury. *Brain Struct Funct*. 2022;227(7):2553-2567. doi:10.1007/s00429-022-02546-2
47. Frey BM, Petersen M, Schlemm E, et al. White matter integrity and structural brain network topology in cerebral small vessel disease: The Hamburg city health study. *Hum Brain Mapp*. 2021;42(5):1406-1415. doi:10.1002/hbm.25301
48. Schlemm E, Frey BM, Mayer C, et al. Equalization of Brain State Occupancy Accompanies Cognitive Impairment in Cerebral Small Vessel Disease. *Biological Psychiatry*. 2022;92(7):592-602. doi:10.1016/j.biopsych.2022.03.019
49. Pini L, Salvalaggio A, De Filippo De Grazia M, Zorzi M, Thiebaut de Schotten M, Corbetta M. A novel stroke lesion network mapping approach: improved accuracy yet still low deficit prediction. *Brain Communications*. 2021;3(4):fcab259. doi:10.1093/braincomms/fcab259
50. Friederici AD. The Brain Basis of Language Processing: From Structure to Function. *Physiological Reviews*. 2011;91(4):1357-1392. doi:10.1152/physrev.00006.2011
51. Corbetta M, Kincade JM, Ollinger JM, McAvoy MP, Shulman GL. Voluntary orienting is dissociated from target detection in human posterior parietal cortex. *Nat Neurosci*. 2000;3(3):292-297. doi:10.1038/73009
52. Shulman GL, McAvoy MP, Cowan MC, et al. Quantitative analysis of attention and detection signals during visual search. *J Neurophysiol*. 2003;90(5):3384-3397. doi:10.1152/jn.00343.2003
53. Alves PN, Forkel SJ, Corbetta M, Thiebaut de Schotten M. The subcortical and neurochemical organization of the ventral and dorsal attention networks. *Commun Biol*. 2022;5(1):1-14. doi:10.1038/s42003-022-04281-0
54. Astafiev SV, Shulman GL, Stanley CM, Snyder AZ, Van Essen DC, Corbetta M. Functional organization of human intraparietal and frontal cortex for attending, looking, and pointing. *J Neurosci*. 2003;23(11):4689-4699. doi:10.1523/JNEUROSCI.23-11-04689.2003
55. Schulz M, Malherbe C, Cheng B, Thomalla G, Schlemm E. Functional connectivity changes in cerebral small vessel disease - a systematic review of the resting-state MRI literature. *BMC Med*. 2021;19:103. doi:10.1186/s12916-021-01962-1
56. Ding JR, Ding X, Hua B, et al. Altered connectivity patterns among resting state networks in patients with ischemic white matter lesions. *Brain Imaging Behav*. 2018;12(5):1239-1250. doi:10.1007/s11682-017-9793-9
57. Dey AK, Stamenova V, Turner G, Black SE, Levine B. Pathoconnectomics of cognitive impairment in small vessel disease: A systematic review. *Alzheimer's & Dementia*. 2016;12(7):831-845. doi:10.1016/j.jalz.2016.01.007
58. SPRINT MIND Investigators for the SPRINT Research Group, Williamson JD, Pajewski NM, et al. Effect of Intensive vs Standard Blood Pressure Control on Probable Dementia: A Randomized Clinical Trial. *JAMA*. 2019;321(6):553-561. doi:10.1001/jama.2018.21442
59. Veronese N, Facchini S, Stubbs B, et al. Weight loss is associated with improvements in cognitive function among overweight and obese people: A systematic review and meta-analysis. *Neuroscience & Biobehavioral Reviews*. 2017;72:87-94. doi:10.1016/j.neubiorev.2016.11.017
60. Marek S, Tervo-Clemmens B, Calabro FJ, et al. Reproducible brain-wide association studies require thousands of individuals. *Nature*. Published online March 16, 2022:1-7. doi:10.1038/s41586-022-04492-9
61. Schilling KG, Li M, Rheault F, et al. Whole-brain, gray, and white matter time-locked functional signal changes with simple tasks and model-free analysis. *Proceedings of the National Academy of Sciences*. 2023;120(42):e2219666120. doi:10.1073/pnas.2219666120
62. Baller EB, Sweeney EM, Cieslak M, et al. Mapping the Relationship of White Matter Lesions to Depression in Multiple Sclerosis. *Biological Psychiatry*. 2023;0(0). doi:10.1016/j.biopsych.2023.11.010
63. Kletenik I, Cohen AL, Glanz BI, et al. Multiple sclerosis lesions that impair memory map to a connected memory circuit. *J Neurol*. 2023;270(11):5211-5222. doi:10.1007/s00415-023-11907-8

Table 1. Sample characteristics

Metric	*Stat*
Age in years, mean ± SD (n)	71.71 ± 8.87 (3485)
Female, n (%)	1737 (49.8)
Years of education, mean ± SD (n)	12.89 ± 4.45 (3485)
Patient ethnicity	
Afrocaribbean, n (%)	198 (5.7)
Asian, n (%)	237 (6.8)
Caucasian / European / White, n (%)	1620 (46.5)
Hispanic, n (%)	146 (4.2)
Other, n (%)	52 (1.5)
Diagnosis	
Subjective cognitive impairment	777 (22.30)
Mild cognitive impairment	1389 (39.86)
Dementia	1319 (37.85)
For dementia cases: probable etiology	
Alzheimer's dementia, n (%)	764 (57.9)
Vascular dementia, n (%)	85 (6.4)
Frontotemporal dementia, n (%)	44 (3.3)
Dementia with Lewy bodies, n (%)	24 (1.8)
Cardiovascular risk factors	
Current smoking, n (%)	499 (14.3)
Previous smoking, n (%)	459 (13.2)
Hypertension, n (%)	1714 (49.2)
Hypercholesterolemia, n (%)	1098 (31.5)
Diabetes mellitus, n (%)	492 (14.1)
BMI, mean ± SD (n)	25.28 ± 4.75 (640)
Comorbidities	
Atrial fibrillation, n (%)	98 (2.8)
History of prior stroke, n (%)	244 (7.0)
History of prior transient ischemic attack (TIA), n (%)	62 (1.8)
History of prior other vascular events, n (%)	715 (20.5)
Imaging	
WMH volume in ml, median [IQR] (n)	6.19 [14.21] (3485)
Cognitive function	
Mini-mental state examination, mean ± SD (n)	25.0 ± 4.7 (3327)
Attention / executive function, z, mean ± SD (n)	-1.12 ± 1.10 (3446)
Information processing speed, z, mean ± SD (n)	-0.96 ± 1.61 (2417)
Language, z, mean ± SD (n)	-1.08 ± 1.86 (2041)
Verbal memory, z, mean ± SD (n)	-1.48 ± 1.30 (3242)

Abbreviations: ml = milliliter, SD – standard deviation, z – harmonized z-score

Enhancing Cognitive Performance Prediction through White Matter Hyperintensity Disconnectivity Assessment: A Multicenter Lesion Network Mapping Analysis of 3,485 Memory Clinic Patients

Supporting Information

Marvin Petersen, Mirthe Coenen, Charles DeCarli, Alberto de Luca, Ewoud van der Lelij, Alzheimer's Disease Neuroimaging Initiative, Frederik Barkhof, Thomas Benke, Christopher P. L. H. Chen, Peter Dal-Bianco, Anna Dewenter, Marco Duering, Christian Enzinger, Michael Ewers, Lieza G. Exalto, Evan F. Fletcher, Nicolai Franzmeier, Saima Hilal, Edith Hofer, Huberdina L. Koek, Andrea B. Maier, Pauline M. Maillard, Cheryl R. McCreary, Janne M. Papma, Yolande A. L. Pijnenburg, Anna Rubinski, Reinhold Schmidt, Eric E. Smith, Rebecca M. E. Steketee, Esther van den Berg, Wiesje M. van der Flier, Vikram Venkatraghavan, Narayanaswamy Venketasubramanian, Meike W. Vernooij, Frank J. Wolters, Xu Xin, Andreas Horn, Kaustubh R. Patil, Simon B. Eickhoff, Götz Thomalla, J. Matthijs Biesbroek, Geert Jan Biessels, Bastian Cheng

Content

Methods

Supplementary figure S1 – Investigated white matter tracts of the HCP1065 atlas

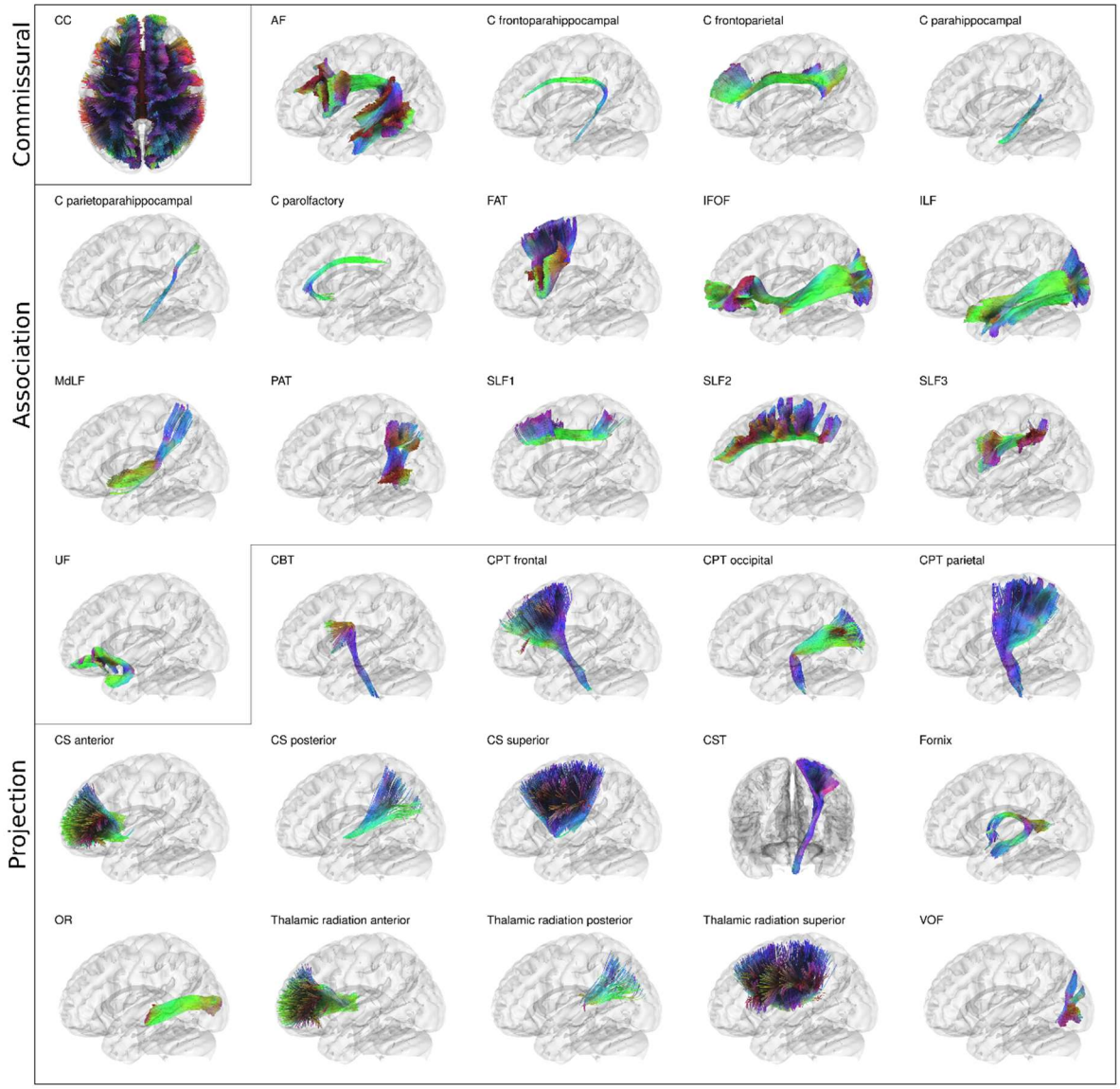

Anatomical depiction of the white matter tracts investigated, categorized into association, projection and commissural tracts. For paired tracts only left side examples are visualized. *Tract abbreviations*: Commissural tracts – CC = corpus callosum; Association tracts - AF = arcuate fascicle, C = cingulate, FAT = frontal aslant tract, IFOF = inferior fronto-occipital fasciculus, ILF = inferior longitudinal fasciculus, MdLF = middle longitudinal fasciculus, PAT = posterior aslant tract, SLF = superior longitudinal fasciculus, UF = uncinate fasciculus; Projection tracts – CBT = corticobulbar tract, CPT = corticopontine tract, CS = corticostriatal pathway, CST = corticospinal tract, FPT = frontopontine tract, F = fornix, OPT = occipitopontine tract, OR = optic radiation, VOF = Vertical occipital fasciculus.

Supplementary text S2 - Exploratory analyses

Correlation of lesion network mapping scores

To test for a structure-function-coupling of lesion network mapping scores, we correlated functional and structural lesion network mapping scores 1) across subjects per region of interest and 2) across regions of interests per subjects. Corresponding results can be found in *supplementary figure S13.*

Voxel-level lesion network maps

In addition, we generated voxel-level lesion network maps to identify white matter areas crucial for cognitive performance. This involved averaging the voxel-level connectivity maps of the ROIs significantly linked to cognitive domain scores. These maps, created for each combination of the four cognitive domains and two LNM modalities, highlight regions where connectivity links to cognitive variance. We then scaled these maps by the WMH frequency map, which reflects the prevalence of WMH in each voxel across the analysis sample. The resulting maps reveal regions where WMH most commonly contribute to variance in cognitive performance. The maps can be found in *supplementary figures S14 & S15.*

Results

Figure S3 – White matter hyperintensity distribution

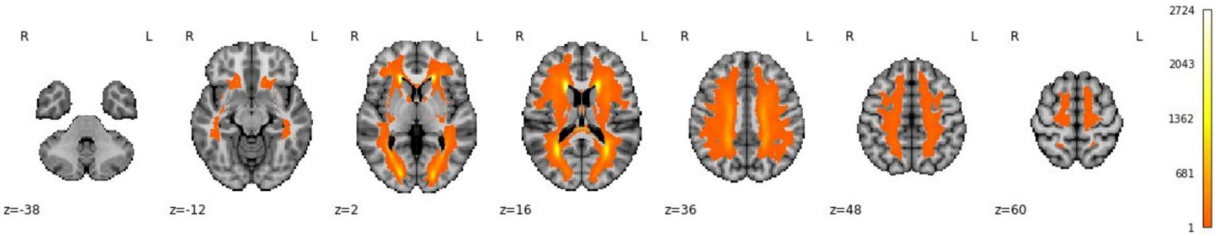

Heatmap indicating the frequency of white matter hyperintensities across the analysis sample.

Figure S4 – Predictive modelling analysis with explained variance (R^2, coefficient of determination) scoring

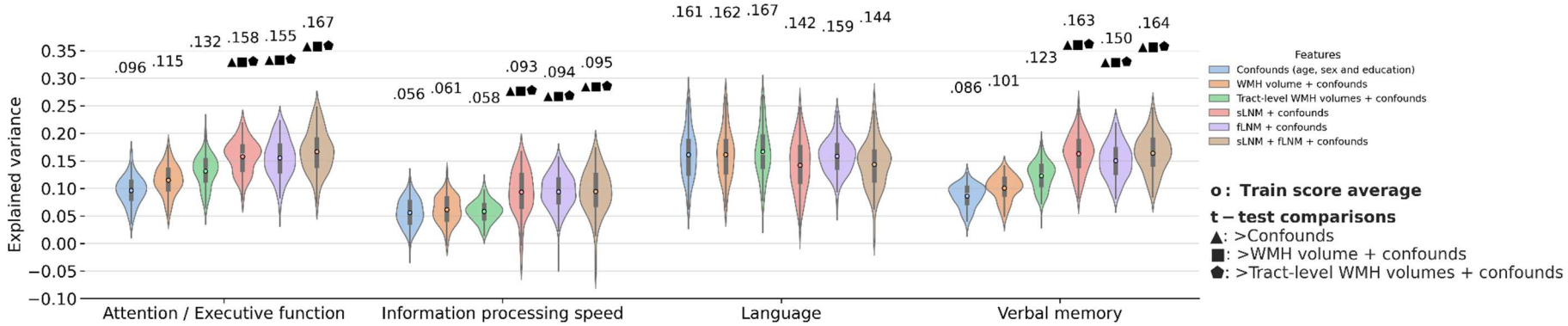

Violin plots illustrate prediction outcomes across cognitive domains. Each violin displays the distribution of explained variance of cognitive domain scores (10-fold cross-validation x 10 repeats = 100 folds → 100 Pearson correlations) for a model informed by a different feature set. The higher the explained variance, the higher the prediction performance. Blue: confounds (age, sex and education); orange: total WMH volume + confounds; green: tract-level WMH volumes + confounds; red: sLNM scores + confounds; purple: fLNM scores + confounds; brown: sLNM scores + fLNM scores + confounds. The average explained variance is indicated above each violin, with colored dots showing training score averages. Geometric symbols denote t-test results comparing LNM-based models against confound- and WMH volume-based models: ▲ indicates higher explained variance than confounds, ■ than WMH volume + confounds, ⬟ than tract-level WMH volume + confounds. Of note, a negative explained variance is possible using sum-of-squares formulation. A negative value indicates that the optimized model fits the data worse than a horizontal line representing the mean of the target variable.

Table S5 – Predictive modelling analysis results – Average negative mean squared error

	Attention / executive function	Information processing speed	Language	Verbal memory
Confounds (age, sex education)	-1.06219	-2.43104	-2.91271	-1.51663
WMH volume + confounds	-1.03992	-2.41763	-2.9114	-1.49302
Tract-level WMH volumes + confounds	-1.02051	-2.42529	-2.8931	-1.45587
sLNM + confounds	-0.98846	-2.33568	-2.98366	-1.38662
fLNM + confounds	-0.99139	-2.33465	-2.92767	-1.40741
sLNM + fLNM + confounds	-0.97774	-2.33223	-2.97935	-1.38486

Figure S6 – Region of interest-level averages of lesion network mapping scores

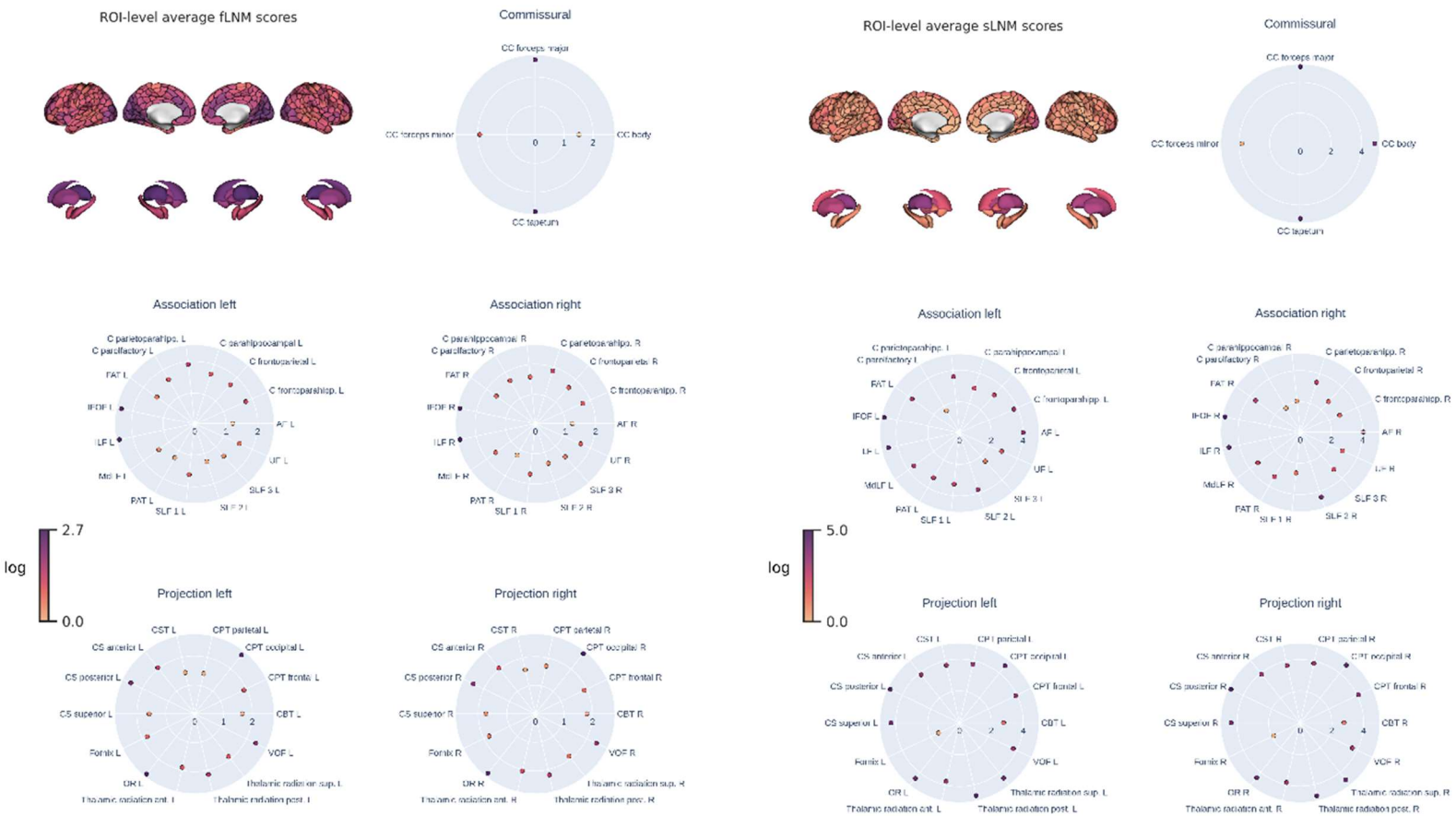

Region of interest-level average functional and structural lesion network mapping scores. Average lesion network mapping scores of gray matter regions of interest are mapped on the cortical surface and subcortical regions. For the white matter tracts, average lesion network mapping scores are displayed in radar plots. Radar plots display white matter tracts in alphabetical order starting at the 3 o'clock position.

Figure S7 – Tract-level functional lesion network mapping

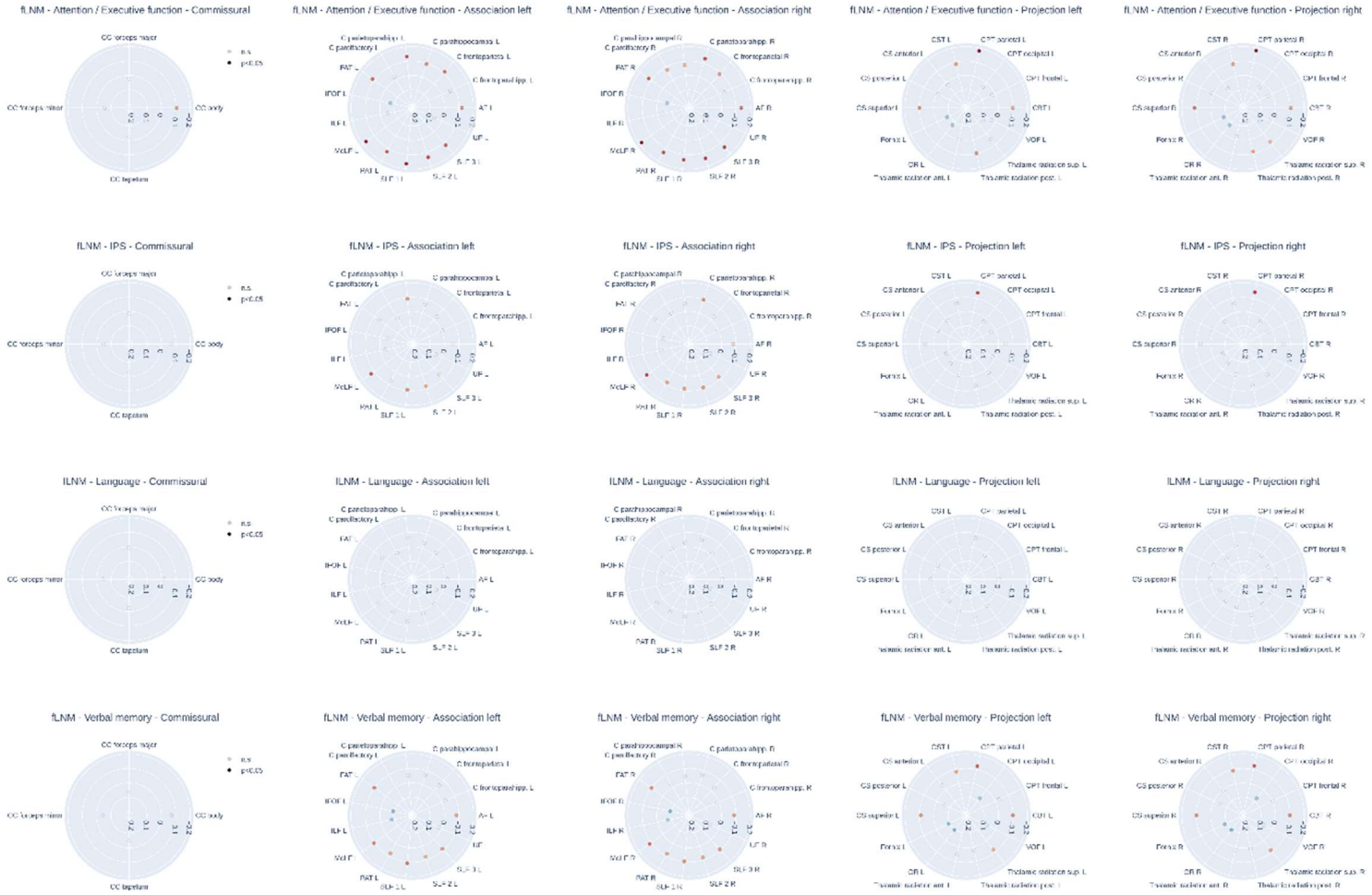

Radar plots display tract-level β coefficients from inferential statistics indicating the relationship between regional functional lesion network mapping scores and cognitive domain scores. This plot shows the associations for all tracts while in the main manuscript only the top 10 effects per combination of LNM modality and cognitive domain are featured. In contrast to the main manuscript, tracts are displayed in alphabetical order starting at the 3 o'clock position in the counterclockwise position. Red dots indicate a negative association (higher LNM score – lower cognitive domain score) and blue dots indicate a positive association (higher LNM score – higher cognitive domain score). Faintly colored dots indicate non-significant associations. Tracts with a significant association are displayed below the radar plots in alphabetical order. For paired tracts only left side examples are visualized.

Figure S8 – Tract-level structural lesion network mapping

Radial plots display tract-level β coefficients from inferential statistics indicating the relationship between regional structural lesion network mapping scores and cognitive domain scores. This plot shows the associations for all tracts while in the main manuscript only the top 10 effects per combination of LNM modality and cognitive domain are featured. In contrast to the main manuscript, tracts are displayed in alphabetical order starting at the 3 o'clock position in the counterclockwise position. Red dots indicate a negative association (higher LNM score – lower cognitive domain score) and blue dots indicate a positive association (higher LNM score – higher cognitive domain score). Faintly colored dots indicate non-significant associations. Tracts with a significant association are displayed below the radar plots in alphabetical order. For paired tracts only left side examples are visualized.

Figure S9 – Spatial correlations of region of interest-level β coefficients

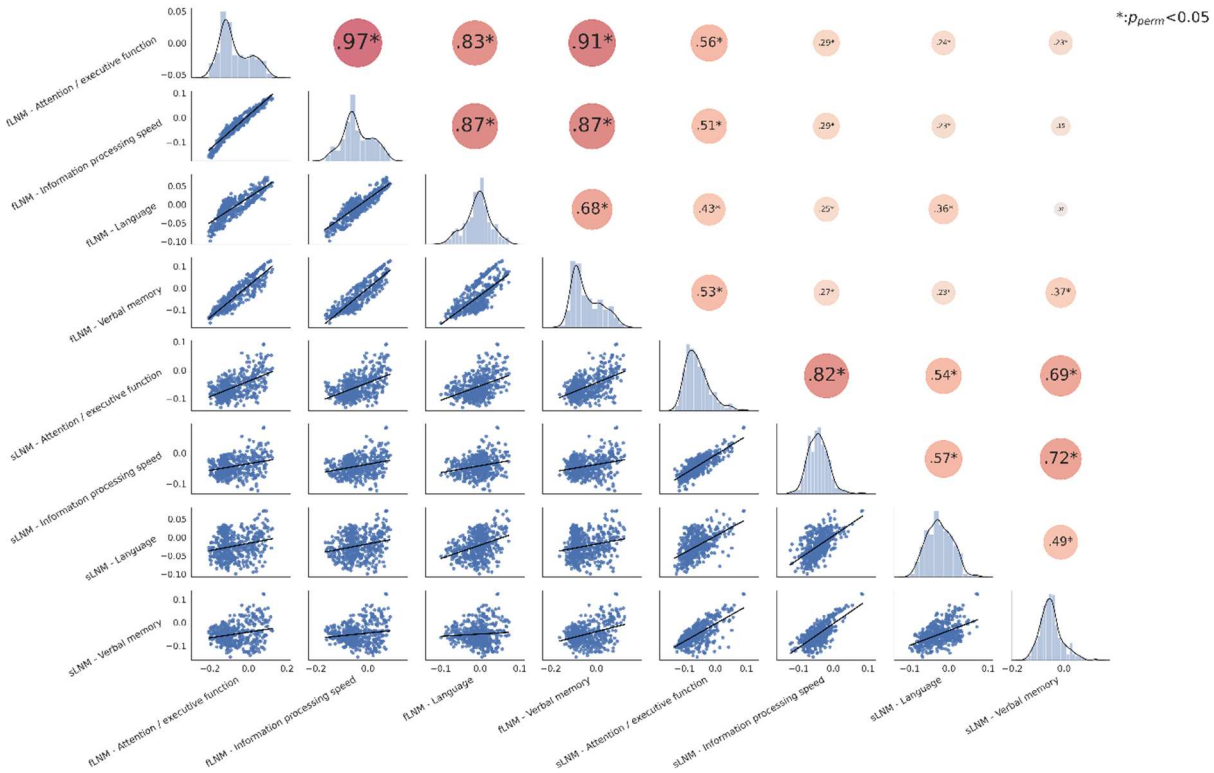

Spatial correlation matrix of all ROI-level effect maps (*β*). To investigate the spatial correspondence between effect maps of the ROI-level analysis, we performed Spearman correlations of each pair of maps. The upper triangle of the matrix displays spearman correlations with dot size and color representing the orientation and magnitude of the correlation coefficients. Asterisks highlight significant correlations after permutation testing and false discovery rate correction. The diagonal shows kernel density plots. The lower triangle illustrates the linear relationships via regression plots. Each dot of the regression plot corresponds with a ROI. *Abbreviations*: fLNM = functional lesion network mapping, p_{perm} = p-value obtained via comparison of empirical Spearman correlation to permutation-based null distribution, ROI = region of interest, r_{sp} = Spearman correlation, sLNM = structural lesion network mapping.

Figure S10 – Sensitivity analysis: Predictive modelling analysis

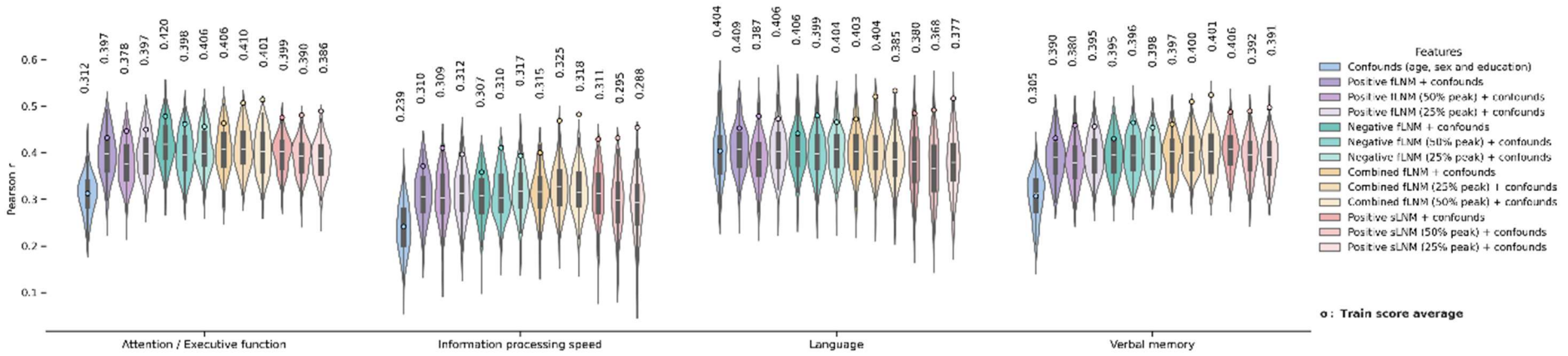

This plot corresponds with Figure 2 of the main manuscript but displays model performances informed by negative fLNM scores as well as LNM scores computed via different thresholding schemes alongside original LNM-informed models. Negative fLNM scores were obtained by only considering negative Pearson correlation coefficients within the WMH mask. Thresholding was performed by averaging only the highest 25% (25% peak) and highest 50% (50% peak) of intensity values of the ROI-level connectivity map in the WMH mask. For the negative fLNM scores, the lowest 25% and 50% voxel intensity values were averaged instead. Combined fLNM indicates models informed by positive and negative fLNM scores. *Abbreviations*: fLNM = functional lesion network mapping, sLNM = structural lesion network mapping, WMH = white matter hyperintensities of presumed vascular origin.

Figure S11 – Sensitivity analysis: Inferential statistics results of cortical and subcortical gray matter based on negative functional lesion network mapping scores

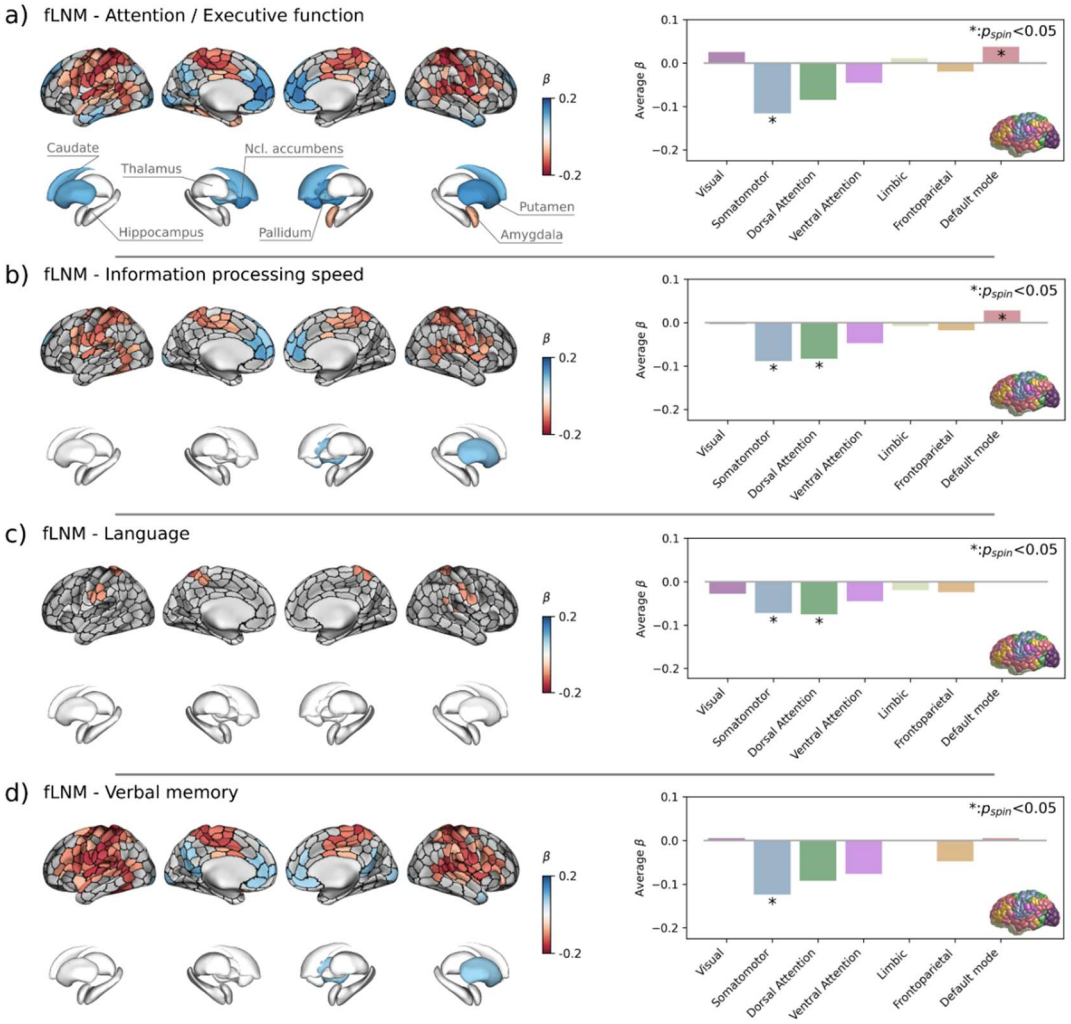

This plot corresponds with Figure 3 a) – d) of the main manuscript but in contrast displays regional associations of fLNM scores based on anticorrelations. Left: ROIs that were significantly associated with cognitive domain scores after family wise error-correction are highlighted by colors encoding *β*-coefficients from general linear models: a negative *β* (red) denotes that a higher regional LNM score, i.e., higher WMH disconnectivity, is associated to a lower cognitive domain performance; a positive *β* (blue) indicates that a higher regional LNM score is linked to a higher cognitive domain performance. Right: Barplots displaying the average *β* in the canonical (Yeo) resting state networks. The brain on the right indicates the regional distribution of the canonical resting state networks with colors corresponding to the bars. Statistical significance was assessed using spin permutations. Each row corresponds with a different combination of lesion network mapping modality and cognitive domain: a) fLNM – attention / executive function, b) fLNM – information processing speed, c) fLNM – language, d) fLNM – verbal memory. *Abbreviations*: fLNM = functional lesion network mapping, p_{spin} = p-value derived from spin permutations, ROIs = regions of interest, sLNM = structural lesion network mapping.

Figure S12 – Sensitivity analysis: Inferential statistics results of white matter tracts based on negative functional lesion network mapping scores

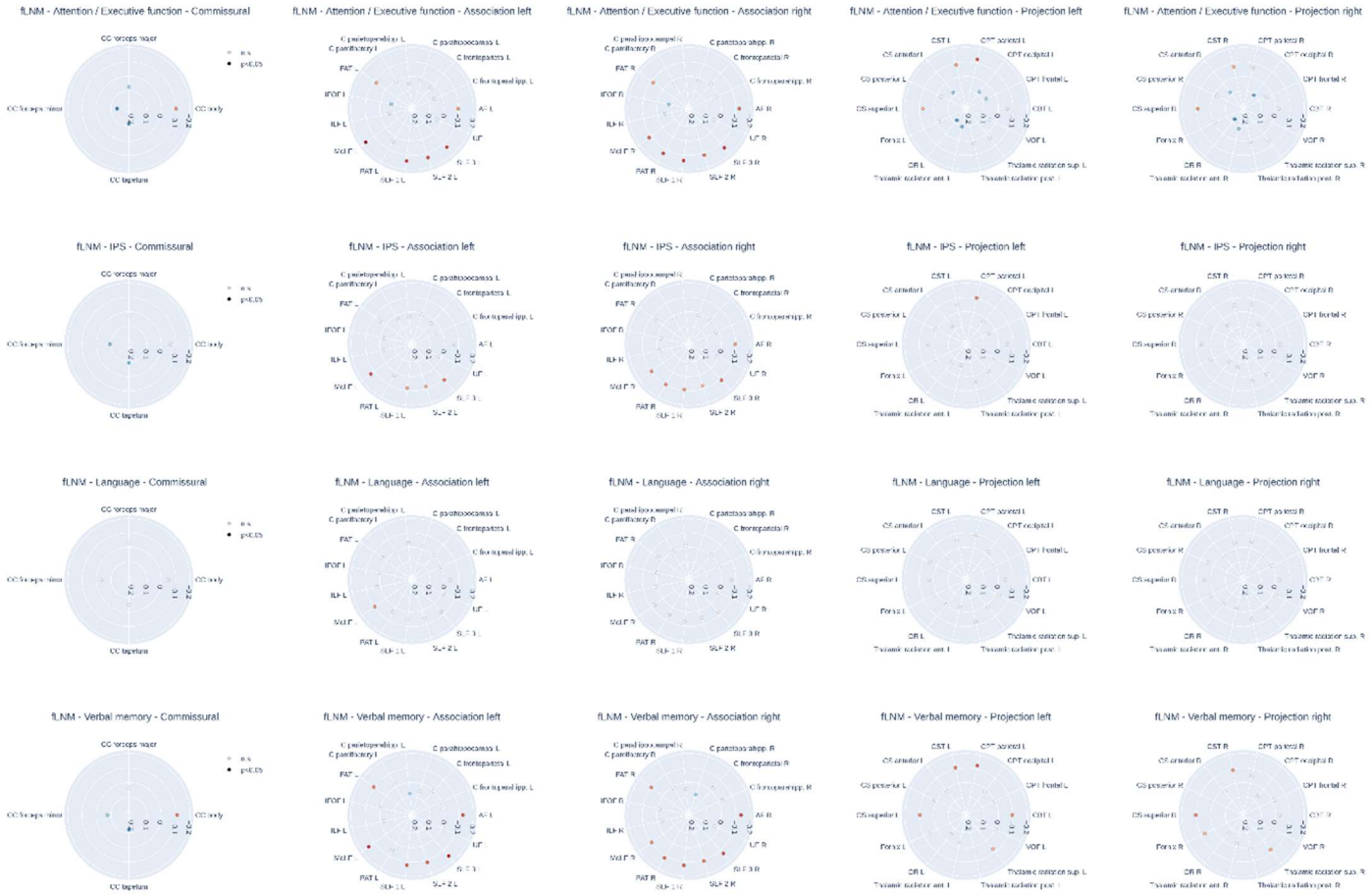

sLNM = structural lesion network mapping.

This plot corresponds with Figure 4 of the main manuscript but in contrast displays regional associations of fLNM scores based on anticorrelations. Tract abbreviations: Commissural tracts – CC = corpus callosum; Association tracts - AF = arcuate fascicle, C = cingulate, FAT = frontal aslant tract, IFOF = inferior fronto-occipital fasciculus, ILF = inferior longitudinal fasciculus, MdLF = middle longitudinal fasciculus, PAT = posterior aslant tract, SLF = superior longitudinal fasciculus, UF = uncinate fasciculus; Projection tracts – CBT = corticobulbar tract, CPT = corticopontine tract, CS = corticostriatal pathway, CST = corticospinal tract, CT = corticothalamic pathway, FPT = frontopontine tract, F = fornix, OPT = occipitopontine tract, OR = optic radiation, VOF = Vertical occipital fasciculus. *Abbreviations*: fLNM = functional lesion network mapping, n.s. = non-significant, p = p-value,

Figure S13 – Structure-function correlations of regional lesion network mapping scores

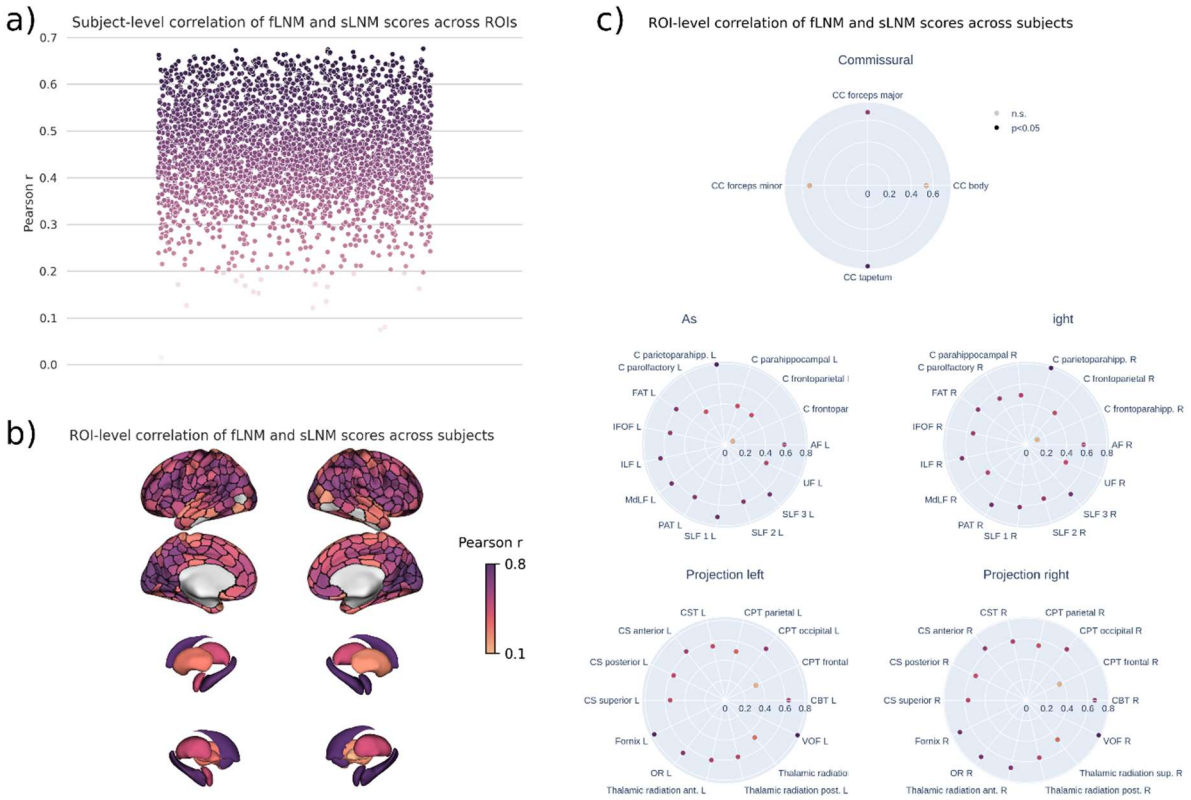

a) Swarmplot displaying the Pearson correlation of fLNM and sLNM scores across ROIs per subject. Each dot represents a subject and is colored by the Pearson correlation. b) and c) Pearson correlation of fLNM and sLNM scores across subjects per ROI. *Abbreviations*: fLNM = functional lesion network mapping, ROI = region of interest, sLNM = structural lesion network mapping.

Figure S14 - Voxel-level lesion network maps

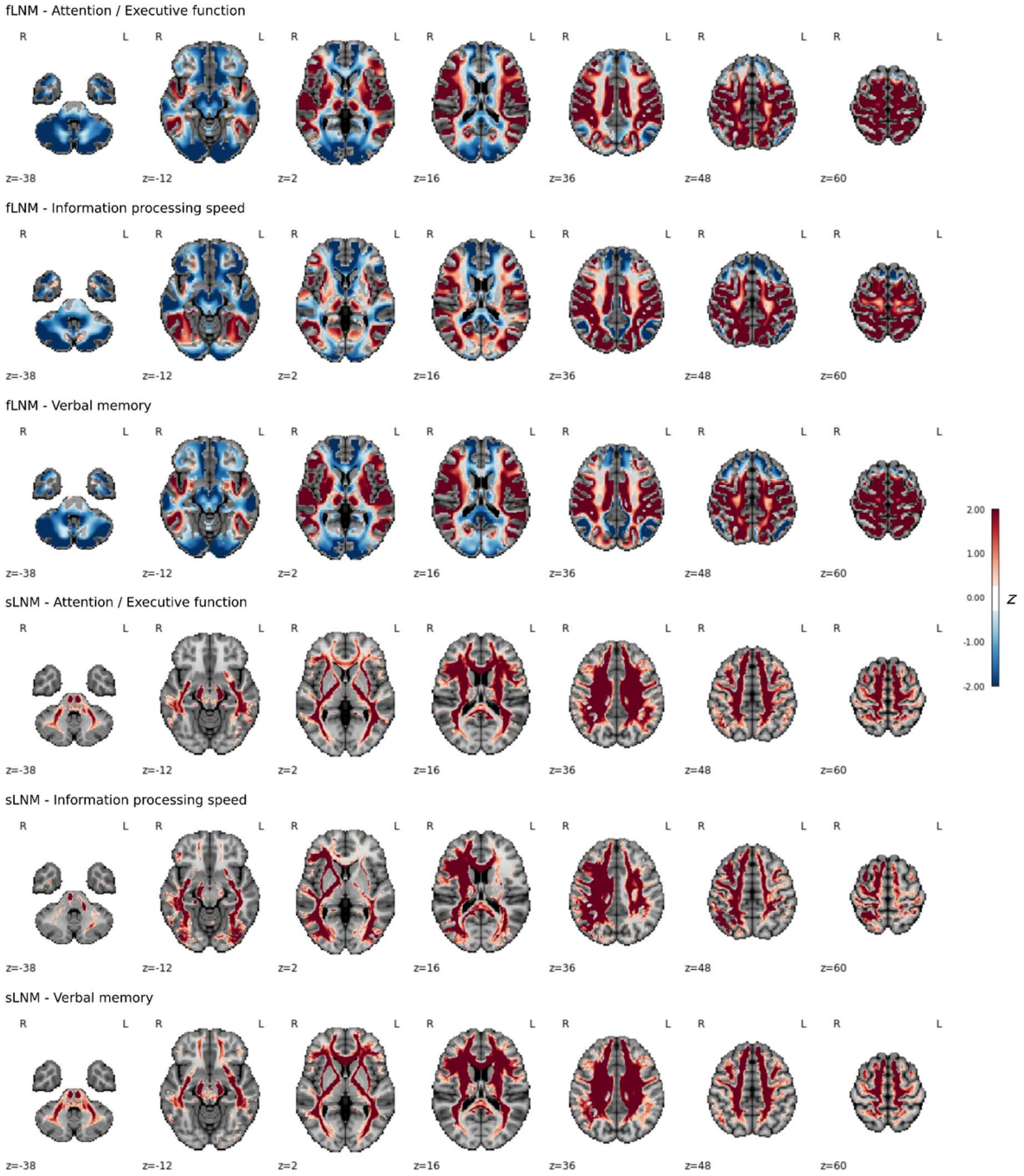

Voxel-level lesion network maps indicate the connectivity to regions of interest that significantly contribute to a cognitive domain. Each row corresponds to a different combination of lesion network mapping modalities (functional and structural) and cognitive domain scores. For the functional lesion network maps, positive z-scores indicate a positive Pearson correlation with the resting-state BOLD signal of the significantly associated ROIs. Negative z-scores indicate anticorrelated voxels and are highlighted in blue. For the structural lesion network maps, deeper red indicates that a voxel is connected by a higher amount of streamlines to significantly associated ROIs. *Abbreviations*: ROI = region of interest.

Figure S15 - Voxel-level lesion network maps scaled by the white matter hyperintensity distribution map

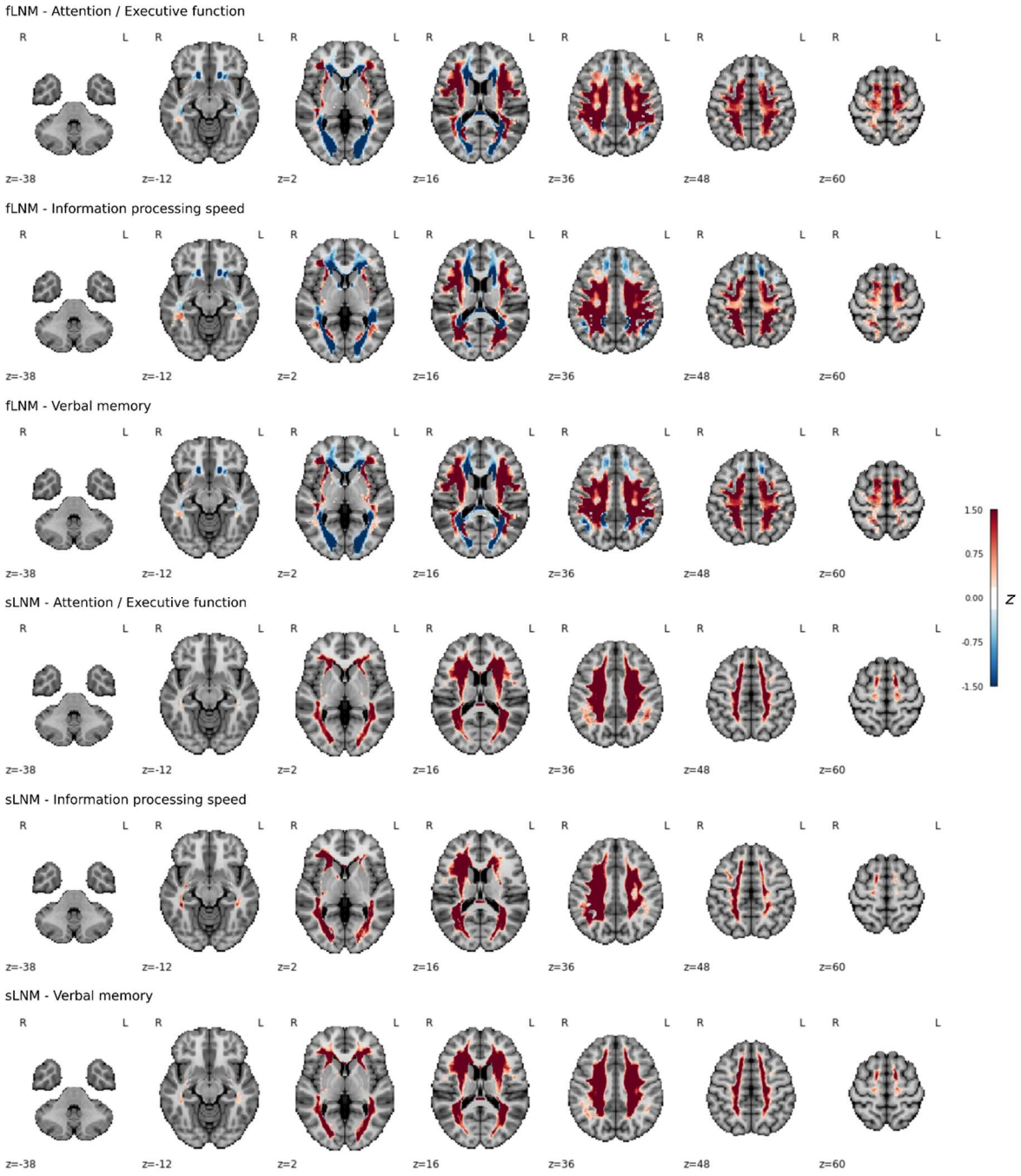

Voxel-level lesion network maps scaled by the WMH frequency map indicate the connectivity to regions of interest that significantly contribute to a cognitive domain and are likely lesioned by WMH. *Abbreviations*: ROI = region of interest, WMH = white matter hyperintensities of presumed vascular origin.

Discussion

Text S16 – Negative functional lesion network mapping scores / anticorrelations

The attention control networks are functionally contrasted by the default mode network which shows, instead of being engaged during externally focused tasks, increased activity during internally directed attention and self-referential processes.[1] As a result, the default mode network and the attention control networks are often found to be anticorrelated at rest.[2] This anticorrelation is thought to reflect a fundamental aspect of brain organization and the complex dynamic interplay between the networks is thought to be central for cognitive processing. Resting-state fMRI studies in CSVD patients suggest that WMH might affect the DMN and attention network interaction, particularly affecting anterior-posterior communication by disrupting long associative white matter fiber tracts.[3,4] Our findings indicate that stronger anticorrelation between the default mode network and WMH – reflected by more negative fLNM scores – correlates with reduced attention, executive function, and processing speed, supporting this hypothesis. Furthermore, by demonstrating enhanced predictive performance based on negative fLNM scores our results underscore the perception of anticorrelations yielding biologically and clinically meaningful information.

References

1. Greicius MD, Krasnow B, Reiss AL, Menon V. Functional connectivity in the resting brain: A network analysis of the default mode hypothesis. *Proc Natl Acad Sci U S A*. 2003;100(1):253-258. doi:10.1073/pnas.0135058100

2. Fox MD, Snyder AZ, Vincent JL, Corbetta M, Van Essen DC, Raichle ME. The human brain is intrinsically organized into dynamic, anticorrelated functional networks. *Proceedings of the National Academy of Sciences*. 2005;102(27):9673-9678. doi:10.1073/pnas.0504136102

3. Schulz M, Malherbe C, Cheng B, Thomalla G, Schlemm E. Functional connectivity changes in cerebral small vessel disease - a systematic review of the resting-state MRI literature. *BMC Med*. 2021;19:103. doi:10.1186/s12916-021-01962-1

4. Dey AK, Stamenova V, Turner G, Black SE, Levine B. Pathoconnectomics of cognitive impairment in small vessel disease: A systematic review. *Alzheimer's & Dementia*. 2016;12(7):831-845. doi:10.1016/j.jalz.2016.01.007

PNAS RESEARCH ARTICLE | NEUROSCIENCE OPEN ACCESS

Brain imaging and neuropsychological assessment of individuals recovered from a mild to moderate SARS-CoV-2 infection

Marvin Petersen[a,1,2], Felix Leonard Nägele[a,1], Carola Mayer[a], Maximilian Schell[a], Elina Petersen[b,c], Simone Kühn[d], Jürgen Gallinat[d], Jens Fiehler[e], Ofer Pasternak[f,g], Jakob Matschke[h], Markus Glatzel[h], Raphael Twerenbold[b,c,i,j], Christian Gerloff[a], Götz Thomalla[a], and Bastian Cheng[a]

Edited by Marlene Behrmann, University of Pittsburgh, Pittsburgh, PA; received October 12, 2022; accepted March 23, 2023

As severe acute respiratory syndrome coronavirus type 2 (SARS-CoV-2) infections have been shown to affect the central nervous system, the investigation of associated alterations of brain structure and neuropsychological sequelae is crucial to help address future health care needs. Therefore, we performed a comprehensive neuroimaging and neuropsychological assessment of 223 nonvaccinated individuals recovered from a mild to moderate SARS-CoV-2 infection (100 female/123 male, age [years], mean ± SD, 55.54 ± 7.07; median 9.7 mo after infection) in comparison with 223 matched controls (93 female/130 male, 55.74 ± 6.60) within the framework of the Hamburg City Health Study. Primary study outcomes were advanced diffusion MRI measures of white matter microstructure, cortical thickness, white matter hyperintensity load, and neuropsychological test scores. Among all 11 MRI markers tested, significant differences were found in global measures of mean diffusivity (MD) and extracellular free water which were elevated in the white matter of post-SARS-CoV-2 individuals compared to matched controls (free water: 0.148 ± 0.018 vs. 0.142 ± 0.017, $P < 0.001$; MD [10^{-3} mm^2/s]: 0.747 ± 0.021 vs. 0.740 ± 0.020, $P < 0.001$). Group classification accuracy based on diffusion imaging markers was up to 80%. Neuropsychological test scores did not significantly differ between groups. Collectively, our findings suggest that subtle changes in white matter extracellular water content last beyond the acute infection with SARS-CoV-2. However, in our sample, a mild to moderate SARS-CoV-2 infection was not associated with neuropsychological deficits, significant changes in cortical structure, or vascular lesions several months after recovery. External validation of our findings and longitudinal follow-up investigations are needed.

COVID-19 | neuroimaging | diffusion MRI | structural MRI | neuropsychological assessment

Significance

In this case–control study, we demonstrate that non-vaccinated individuals recovered from a mild to moderate severe acute respiratory syndrome coronavirus type 2 (SARS-CoV-2) infection show significant alterations of the cerebral white matter identified by diffusion-weighted imaging, such as global increases in extracellular free water and mean diffusivity. Despite the observed brain white matter alterations in this sample, a mild to moderate SARS-CoV-2 infection was not associated with worse cognitive functions within the first year after recovery. Collectively, our findings indicate the presence of a prolonged neuroinflammatory response to the initial viral infection. Further longitudinal research is necessary to elucidate the link between brain alterations and clinical features of post-SARS-CoV-2 individuals.

As the number of patients recovering from an acute infection with the severe acute respiratory syndrome coronavirus type 2 (SARS-CoV-2) grows, the study of its long-term consequences on health outcomes has gained much attention (1–4).

It is widely recognized that coronavirus disease 2019 (COVID-19) caused by SARS-CoV-2 not only leads to respiratory dysfunction but also impacts various other organ systems during the acute phase and well beyond (1, 5, 6). Neurological symptoms, such as headache, fatigue, memory, and attention deficits, may significantly impede well-being in individuals suffering from COVID-19 sequelae (4, 7, 8). Advancing our understanding of the underlying pathological mechanisms will be crucial for addressing future health care needs.

Different potential mechanisms have been suggested to be involved in the development and persistence of neurological symptoms in patients with COVID-19. Postmortem histopathological and molecular studies have demonstrated viral neurotropism, signs of neuroinflammation (9, 10), neurodegeneration (11), demyelination (12), axonal disruption (13), and micro- and macrovascular damage (14, 15). However, most studies were conducted in patients with severe COVID-19, whereas histopathological findings from individuals with mild to moderate courses are lacking.

In vivo studies applying modern brain imaging joined by comprehensive clinical and neuropsychological assessment are scarce. Recent preliminary evidence from the UK Biobank suggests cortical thickness reductions in the olfactory and limbic network, as well as neurocognitive decline in former COVID-19 patients, although these findings still need to be replicated in independent datasets (11). The majority of remaining studies focused on visually apparent pathological findings such as intracranial hemorrhage, stroke, or white matter hyperintensities in small case series or single case reports of more severely affected patients (16–19). Taken together, current evidence is of limited transferability to patients with a mild to moderate SARS-CoV-2 infection, therefore necessitating further investigations.

Preprint server: medrxiv (https://www.medrxiv.org/content/10.1101/2022.07.08.22277420v3.full).

This article is a PNAS Direct Submission.

[1]M.P. and F.L.N. contributed equally to this work.

[2]To whom correspondence may be addressed. Email: mar.petersen@uke.de.

This article contains supporting information online at https://www.pnas.org/lookup/suppl/doi:10.1073/pnas.2217232120/-/DCSupplemental.

Published May 23, 2023.

In order to address this research need, we studied 223 nonvaccinated individuals in median 289 d after recovery from mainly mild to moderate SARS-CoV-2 infections in a retrospective, cross-sectional case–control design. We leveraged advanced MRI techniques enabling the study of imaging phenotypes associated with neurodegeneration, atrophy, myelin/cellular disruption, inflammation, and vascular damage (20–23). Moreover, study participants received a comprehensive clinical and neuropsychological assessment. Building upon our previous multiorgan assessment in this cohort (1), here, we provide a detailed in vivo assessment of the cerebral white and gray matter, as well as neuropsychological outcomes in former COVID-19 patients.

Results

Sample Characteristics. We examined participants of the Hamburg City Health Study (HCHS) and its COVID Program. Imaging data were available for 230 post-SARS-CoV-2 individuals. Following quality assessment (QA), in total, 7 post-SARS-CoV-2 individuals had to be excluded, leaving 223 cases for propensity score matching with healthy controls who had passed QA. The results of the matching procedure are visualized in *SI Appendix*, Fig. S1. The final sample included 223 matched controls (93 female, age in years, mean ± SD, 55.74 ± 6.60) and 223 post-SARS-CoV-2 individuals (100 female, 55.54 ± 7.07; see Table 1). Of the latter, the majority had a mild to moderate course of COVID-19 (without symptoms, n = 7; mild symptoms, n = 125; moderate symptoms, n = 67), 18 were hospitalized, and none required mechanical ventilation or intensive care unit treatment. There were no significant differences between post-SARS-CoV-2 individuals and matched controls regarding age, sex, years of education, and cardiovascular risk factors.

Clinical Data. Although post-SARS-CoV-2 individuals showed nominally better test performances in Verbal Fluency (VF), Mini-Mental State Examination (MMSE), and clock drawing test (CDT) compared to matched controls, after Bonferroni correction for multiple comparisons, no significant group differences remained in any neuropsychological test score, including those associated with executive functioning, memory, psychosocial, and neurological symptom burden (Table 2).

Imaging. We first conducted analyses of covariance, adjusted for sex, age, and education, to test for group differences in imaging markers averaged across the entire white matter or cortical gray matter in the case of cortical thickness. A schematic illustration of the imaging markers under investigation is shown in Fig. 1. Post-SARS-CoV-2 individuals exhibited higher global extracellular free water and mean diffusivity (MD) in the cerebral white matter relative to matched controls, markers associated with immune activation and atrophy (mean ± SD, free water: 0.148 ± 0.018 vs. 0.142 ± 0.017, $F = 18.47$, $P_{bonf} < 0.001$; MD [10^{-3} mm^2/s]: 0.747 ± 0.021 vs. 0.740 ± 0.020, $F = 17.28$, $P_{bonf} < 0.001$) (Fig. 2 and *SI Appendix*, Table S1). To aid the biological interpretation, we converted the mean group differences in free water and MD to units of "years of healthy aging" using the estimates of linear regressions with age in the matched control group (free water: *beta* = 0.0009, $P < 0.001$, MD: *beta* = 0.000001, $P < 0.001$). Considering the mean differences between groups of 0.006 in free water and 0.000007 in MD, this resulted in group differences of 6.67 and 7 "years of healthy aging", respectively. While peak width of skeletonized mean diffusivity (PSMD) ($P_{uncorr} = 0.005$), a marker of cerebral small vessel disease, and cortical thickness ($P_{uncorr} = 0.01$) were nominally increased in post-SARS-CoV-2 individuals, both measures, as well as the remaining averaged imaging markers of white matter fiber structure, were not significantly different between groups after Bonferroni correction (Fig. 2 and *SI Appendix*, Table S1).

Table 1. Baseline characteristics of post-SARS-CoV-2 individuals and matched controls

	Post-SARS-CoV-2 individuals (N = 223)	Matched controls (N = 223)	P_{uncorr}
Demographics			
Age in years, mean ± SD	55.54 ± 7.07	55.74 ± 6.60	0.76
Female sex, N (%)	100 (44.8)	93 (41.7)	0.56
Education in years, mean ± SD	15.70 ± 2.56	15.67 ± 2.86	0.91
COVID-19-specific characteristics			
Self-reported disease severity at the time of infection			
Asymptomatic, N (%)	7 (3.1)		
Mild, N (%)	125 (56.1)		
Moderate, nonhospitalized, N (%)	67 (30.0)		
Moderate, hospitalized, without ICT, N (%)	18 (8.1)		
Days between the first positive SARS-CoV-2 PCR test and study enrollment, median (IQR)	289 (163, 318)		
Cardiovascular risk factors			
Hypertension*, N (%)	131 (58.7)	121 (54.3)	0.39
Dyslipidemia†, N (%)	54 (24.2)	51 (22.9)	0.82
Diabetes mellitus‡, N (%)	16 (7.2)	13 (5.8)	0.70
Smoking, ever, N (%)	107 (48.0)	105 (47.1)	0.92

Abbreviations: COVID-19 = coronavirus disease 2019, ICT = intensive care treatment, IQR = interquartile range, PCR = polymerase chain reaction, post-SARS-CoV-2 individuals = individuals who recovered from a severe acute respiratory coronavirus type 2 infection, SD = standard deviation.
*Prevalence of hypertension was defined as blood pressure ≥140/90 mmHg, intake of antihypertensive medication, or self-report.
†Prevalence of dyslipidemia was defined as LDL cholesterol/HDL cholesterol ratio >3.5 or intake of lipid-lowering therapies.
‡Prevalence of diabetes mellitus was defined as fasting blood glucose level >126 mg/dL or self-report.

To detect spatial patterns of brain structural alterations, we additionally performed vertex- and voxel-wise analyses of gray and white matter imaging markers. Vertex-wise comparisons of cortical thickness did not reveal significant differences between matched controls and post-SARS-CoV-2 participants. Voxel-wise statistics on the entire white matter skeleton, a representation of major white matter fiber bundles, revealed predominant free water and MD increases in the white matter skeleton of post-SARS-CoV-2 subjects encompassing all brain lobes, compared to very localized changes in other diffusion markers (Fig. 3 and *SI Appendix*, Table S2). More specifically, the conventional diffusion tensor imaging (DTI) markers fractional anisotropy (FA) and MD showed significant differences between groups, with FA increases in 0.8% and decreases in 1.2% of the skeleton in cases relative to healthy controls. MD was significantly increased in 41.3% and decreased in 0.1% of the skeleton of post-SARS-CoV-2 participants. Employing free-water imaging, post-SARS-CoV-2 individuals showed significant free-water elevations in 38.3% and reductions in 0.4% of the skeleton, as

Table 2. Results of clinical and neuropsychological assessments of post-SARS-CoV-2 individuals compared to matched controls

Clinical measure*	Post-SARS-CoV-2 individuals	Matched controls	P_{uncorr} †	P_{bonf} ‡	*F*
Neurocognition					
TMT-A in seconds	31.89 ± 10.60 (212)	33.71 ± 11.67 (190)	0.12	>0.99	2.40
TMT-B in seconds	68.50 ± 22.69 (212)	70.89 ± 25.57 (187)	0.37	>0.99	0.81
VF	28.03 ± 6.04 (212)	26.43 ± 7.15 (212)	0.02	0.14	5.94
WLR	8.52 ± 1.63 (210)	8.32 ± 1.61 (204)	0.25	>0.99	1.33
MMSE	28.37 ± 1.26 (211)	28.02 ± 1.72 (210)	0.02	0.19	5.34
CDT	6.75 ± 0.78 (212)	6.57 ± 1.03 (214)	0.04	0.37	4.20
Psychosocial symptom burden					
PHQ-9	3.94 ± 3.74 (212)	3.91 ± 3.77 (215)	0.97	>0.99	<0.01
GAD-7	2.94 ± 3.28 (212)	2.80 ± 3.06 (215)	0.67	>0.99	0.18
Neurological symptom burden					
PHQ-15§	2.13 ± 1.83 (212)	1.83 ± 1.73 (215)	0.09	0.82	2.86

Abbreviations: CDT = clock drawing test, GAD = general anxiety disorder, MMSE = Mini-Mental State Examination, PHQ = Patient Health Questionnaire, post-SARS-CoV-2 individuals = individuals who recovered from a severe acute respiratory coronavirus type 2 infection, SD = standard deviation, TMT-A = Trail Making Test Part A, TMT-B = TMT Part B, VF = verbal fluency, WLR = word list recall.
*Presented as mean ± SD (N).
†Uncorrected *P* values of analyses of covariance, adjusted for age, sex, and years of education.
‡Bonferroni-corrected *P* values of analyses of covariance, adjusted for age, sex, and years of education (considering 9 comparisons).
§PHQ-15 items: headache, dizziness, fatigue, and sleep disturbances.

well as FA of the tissue (FA_T) elevations in 3.3% of the skeleton, but no FA_T reductions. Alterations of the remaining diffusion markers were of even less spatial extent (<3%).

We complemented voxel-based approaches by an assessment of diffusion indices averaged within anatomically predefined white matter fiber tracts in a tract of interest analysis. The tract-of-interest approach revealed widespread effects of significantly higher MD and FW in multiple association, commissural, and projection tracts including the anterior thalamic radiation, the corpus callosum, cingular projections, the frontopontine tract, the inferior fronto-occipital fascicle, the optic radiation, the superior longitudinal fascicle, the striatal as well as thalamic projections, and the uncinate fascicle (Fig. 4). FA and FA_T also significantly differed in association and commissural tracts. Corresponding details to FA and FA_T results as well as boxplots displaying data of all tracts investigated are provided in *SI Appendix*.

Associations between Clinical and Imaging Data. Exploratory regression analyses were performed between clinical measures and averaged imaging markers that showed significant group differences, i.e., free water and MD.

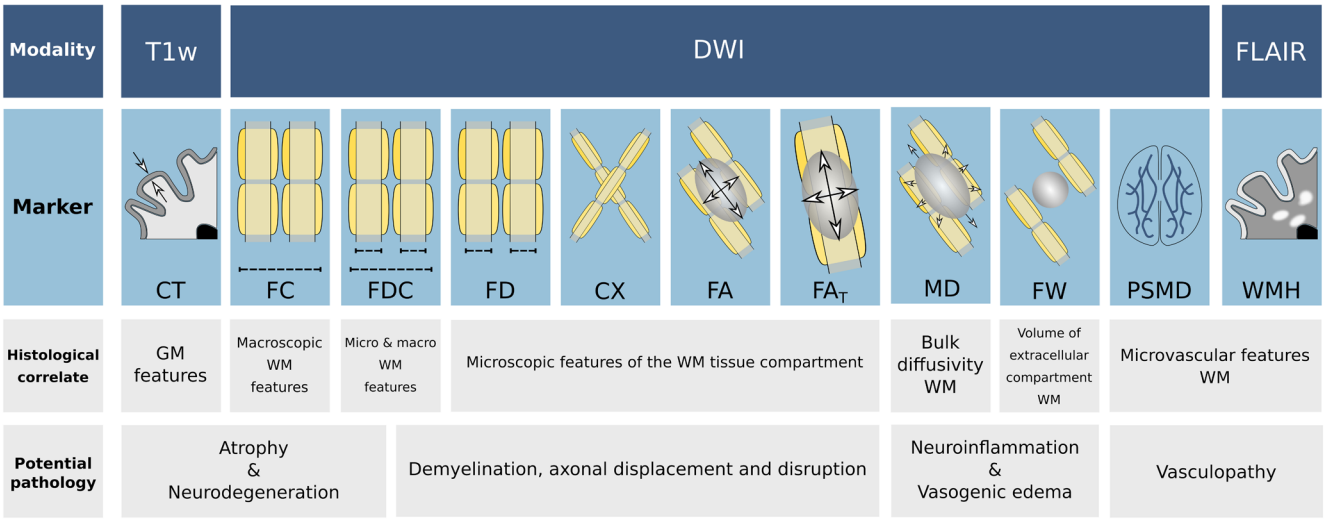

Fig. 1. Schematic illustration of the investigated imaging markers. To assess the cerebral gray and white matter, micro- and macrostructural imaging markers were derived. The first row of the schematic describes the imaging sequences utilized to derive the imaging markers below. The second row presents diagrammatic illustrations of the markers: CT was determined as the distance between the pial surface and white matter/gray matter boundary; FC represents the macroscopic white matter fiber-bundle diameter; FD reflects the microscopic intraaxonal volume; as the combinatorial measure of FC and FD, FDC simultaneously assesses micro- and macroscopic alterations of white matter tracts; CX measures the intricacy of fiber configurations within a voxel; FA measures the directional preference of diffusion; MD denotes the molecular diffusion rate; free-water imaging enables the adjustment of traditional diffusion tensor imaging markers for extracellular diffusion signal, which increases their tissue specificity (FA_T); FW represents the volume of the extracellular compartment; PSMD was calculated as the difference of the 95th and 5th percentile of skeletonized MD values; WMH load represents the white matter hyperintensity volume normalized by the total intracranial volume. Histological interpretations of the respective imaging markers and their potential sensitivity for pathologies are described in the third and fourth row, respectively. *Abbreviations*: CT = cortical thickness, CX = complexity, FA = fractional anisotropy, FA_T = FA of the tissue, FD = fiber density, FDC = fiber density and cross-section, FLAIR = fluid-attenuated inversion recovery, FW = free water, Log. FC = logarithm of fiber cross-section, MD = mean diffusivity, PSMD = peak width of skeletonized MD, WMH = white matter hyperintensity.

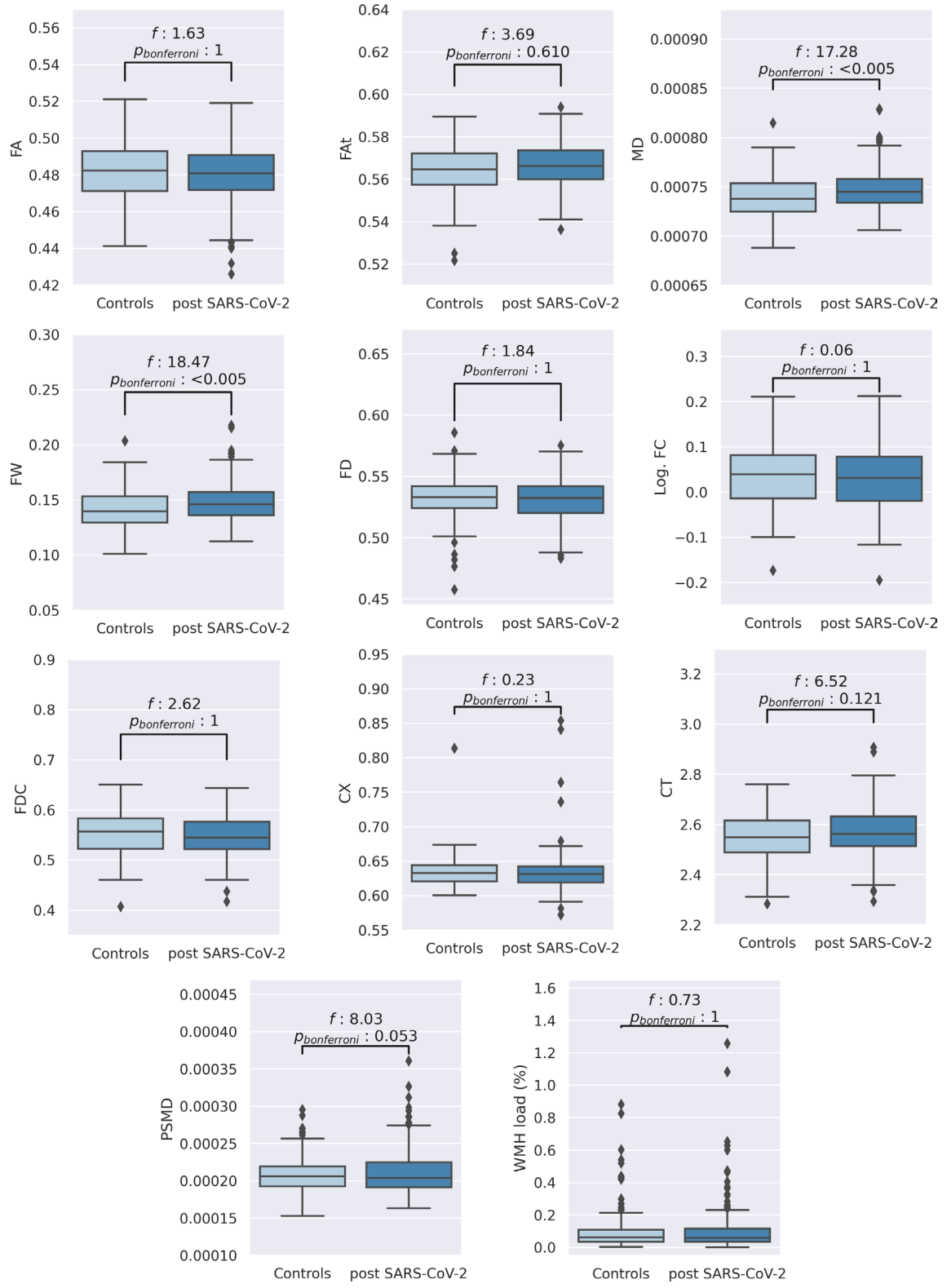

Fig. 2. Group comparison of neuroimaging indices on a global scale. Boxplots of averaged imaging measures and the corresponding statistical results (F-statistics and Bonferroni-corrected *P* values for 11 comparisons) from the ANCOVAs comparing matched controls with post-SARS-CoV-2 individuals adjusted for age, sex, and years of education. *Abbreviations*: CT = cortical thickness, CX = complexity, FA = fractional anisotropy, FA_T = FA of the tissue, FD = fiber density, FDC = fiber density and cross-section, FW = free water, Log. FC = logarithm of fiber cross-section, MD = mean diffusivity, post-SARS-CoV-2 = individuals who recovered from a severe acute respiratory coronavirus type 2 infection, PSMD = peak width of skeletonized MD, WMH = white matter hyperintensity.

Linear regression revealed a significant positive association of free water with Trail Making Test Part A (TMT-A) ($P = 0.008$) and Part B (TMT-B) ($P < 0.001$), as well as significant negative associations of free water with VF ($P = 0.003$) and Word List Recall (WLR) ($P < 0.001$) in the entire sample (*SI Appendix*, Table S3). MMSE, CDT, Patient Health Questionnaire-9 (PHQ-9), General Anxiety Disorder-7 (GAD-7), and PHQ-15 scores were not significantly correlated with free water. Moreover, we observed significant group × free-water interactions for VF ($P = 0.006$), WLR ($P = 0.02$), MMSE ($P = 0.02$), and CDT ($P = 0.04$). Post hoc Spearman

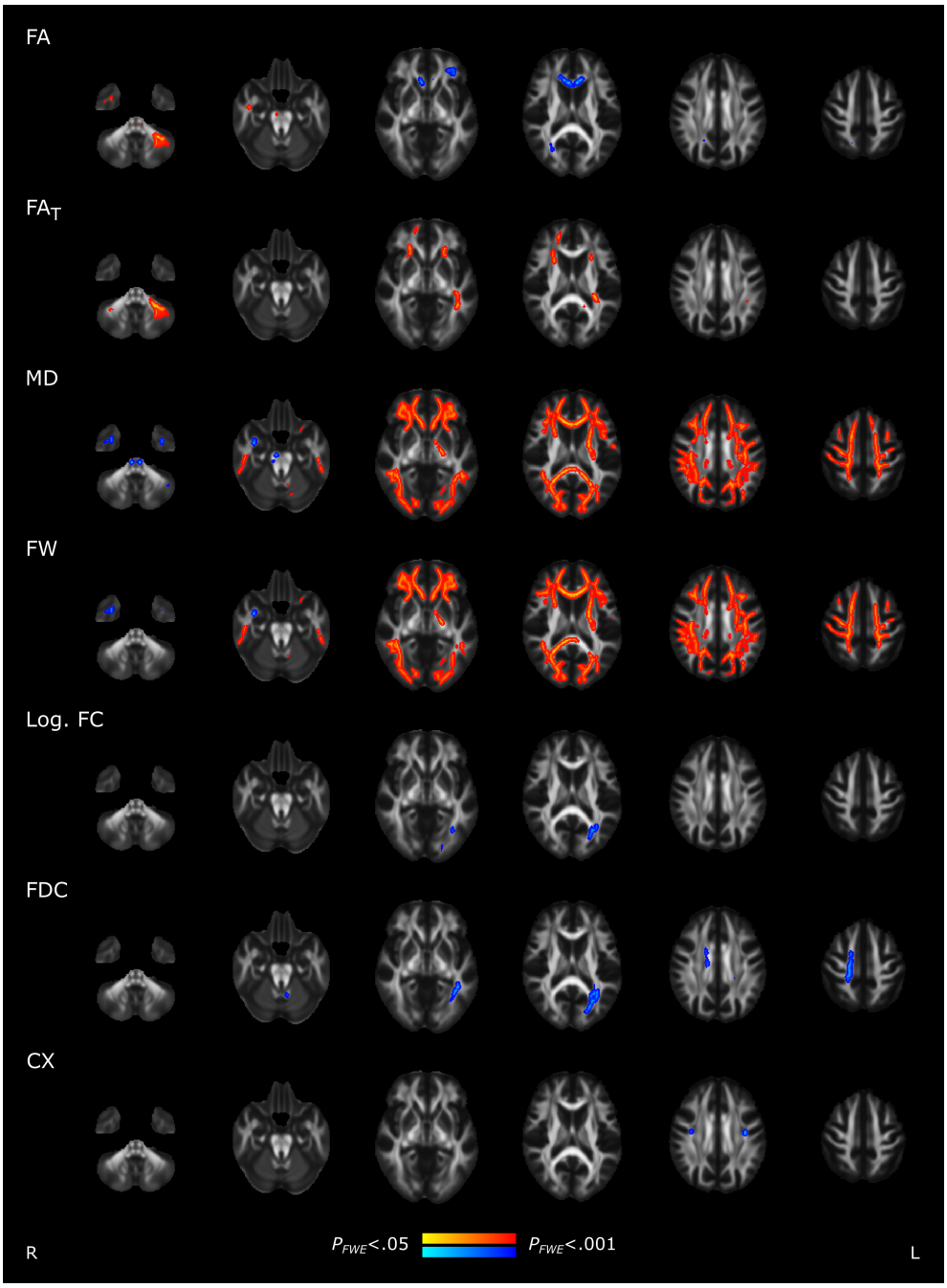

Fig. 3. Group comparison of skeletonized diffusion indices. Skeleton voxels that significantly differed between groups are highlighted by colors: post-SARS-CoV-2 individuals > matched controls, red; post-SARS-CoV-2 individuals < matched controls, blue. *Abbreviations*: CX = complexity, FA = fractional anisotropy, FA_T = FA of the tissue, FD = fiber density, FDC = fiber density and cross-section, FW = free water, FWE = family-wise error corrected, Log. FC = logarithm of fiber cross-section, MD = mean diffusivity, post-SARS-CoV-2 = individuals who recovered from a severe acute respiratory coronavirus type 2 infection.

correlations performed for matched controls and post-SARS-CoV-2 individuals, separately, confirmed positive associations with TMT-A (*rho* = 0.20, *P* = 0.004) and TMT-B (*rho* = 0.22, *P* = 0.001), as well as negative correlations with VF (*rho* = −0.23, *P* < 0.001) and WLR (*rho* = −0.25, *P* < 0.001) in the post-SARS-CoV-2 group. However, among all neuropsychological measures, free water was only significantly correlated with TMT-B (*rho* = 0.15, *P* = 0.04) in the group of matched controls (*SI Appendix*, Table S3 and Fig. S5).

Results for MD were very similar. Linear regression analyses showed significant positive associations of MD with TMT-A (*P* = 0.03) and TMT-B (*P* = 0.001), as well as negative associations of MD with VF (*P* = 0.01) and WLR (*P* < 0.001) in the combined group of matched controls and post-SARS-CoV-2 individuals. Further, significant group × MD interactions were present for TMT-A, VF, WLR, MMSE, and CDT (*SI Appendix*, Table S4). Post hoc Spearman correlations revealed significant positive correlations of MD with TMT-A (*rho* = 0.17, *P* = 0.01) and TMT-B (*rho* = 0.20, *P* = 0.005), as well as negative correlations of MD with VF (*rho* = −0.22, *P* = 0.001) and WLR (*rho* = −0.23, *P* < 0.001) in the post-SARS-CoV-2 group only. All other correlations were nonsignificant (*SI Appendix*, Table S4 and Fig. S6).

Additional regression analyses with age as the predictor of free water and MD showed significant positive associations of age with both imaging markers, as well as group × age interactions indicating stronger effects in post-SARS-CoV-2 individuals (please refer to *SI Appendix*, Table S5 and Fig. S7, for more detail).

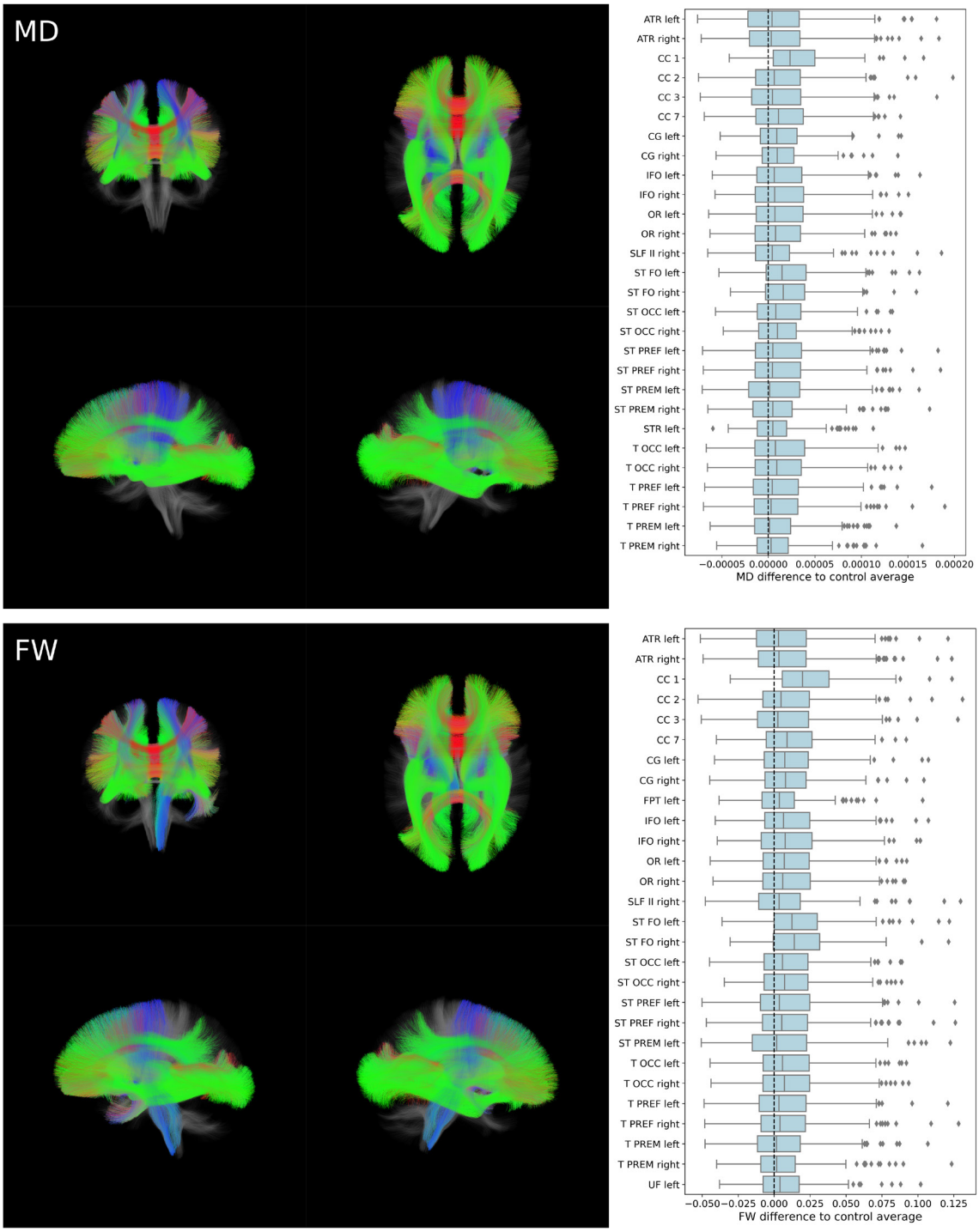

Fig. 4. Tract of interest analysis of mean diffusivity and free water. *Left*: 3D visualization of investigated white matter fiber tracts represented as streamline bundles. Tracts that significantly differed between groups are highlighted by colors encoding directionality. Presented perspectives are coronal, anterior to posterior (*Upper Left*); axial, superior to inferior (*Upper Right*); sagittal, left to right (*Lower Left*); sagittal, right to left (*Lower Right*). *Right*: Boxplots displaying differences of post-SARS-CoV-2 individuals to the control group average. Only data of tracts that significantly differed after Bonferroni correction (71 comparisons) are shown. Boxplots considering all tracts reconstructed by TractSeg can be found in *SI Appendix*. *Abbreviations*: ATR = anterior thalamic radiation, CC = corpus callosum, CG = cingulum, FPT = frontopontine tract, FW = free water, IFO = inferior fronto-occipital fascicle, MD = mean diffusivity, OR = optic radiation, post-SARS-CoV-2 = individuals who recovered from a severe acute respiratory coronavirus type 2 infection, SLF = superior longitudinal fascicle, ST FO = striato-fronto-orbital tract, ST OCC = striato-occipital tract, ST PREF = striato-prefrontal tract, ST PREM = striato-premotor tract, STR = superior thalamic radiation, T OCC = thalamo-occipital tract, T PREF = thalamo-prefrontal tract, T PREM = thalamo-premotor tract, UF = uncinate fascicle.

Prediction of a Past SARS-CoV-2 Infection Based on Imaging Markers. We examined the predictive capacity of derived imaging markers employing a supervised machine learning approach (Fig. 5). Free water (80.21%) and MD (79.38%) achieved the strongest median prediction accuracies. The median cortical thickness score was 45.95%. All investigated metrics but cortical thickness scored significantly better than null models for which the group assignment was randomly permuted.

Sensitivity Analyses. Analysis results remained stable if formerly hospitalized post-SARS-CoV-2 individuals were excluded and if

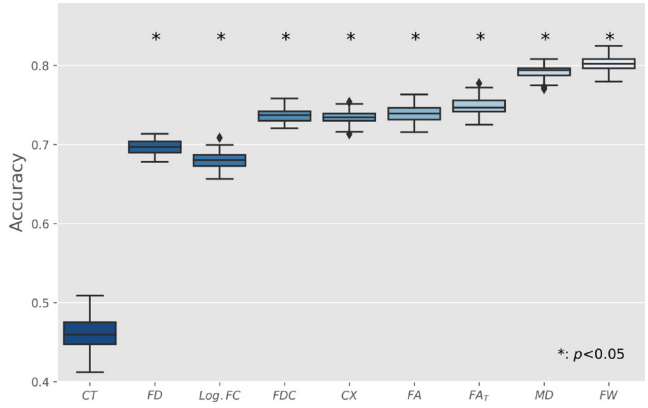

Fig. 5. Prediction of past SARS-CoV-2 infection based on imaging markers. To assess the diagnostic relevance of evaluated brain imaging markers, a supervised machine learning analysis was performed. The displayed boxplots represent the accuracy of logistic regression models trained on regional imaging metrics to predict past SARS-CoV-2 infection. Model training occurred in a 10-fold nested cross-validation setup and was repeated 100 times for each marker with different random split regimens. Asterisks indicate significant difference to null model predictions, which were based on group label permutation. Predictive models based on free water and MD reached a considerable accuracy of approximately 80% in predicting a past SARS-CoV-2 infection. By that, they outperformed other imaging markers under study. All models except those based on cortical thickness achieved a significantly better performance than null models. *Abbreviations*: CT = cortical thickness, CX = complexity, FA = fractional anisotropy, FA_T = FA of the tissue, FD = fiber density, FDC = fiber density and cross-section, FW = free water, Log. FC = logarithm of fiber cross-section, MD = mean diffusivity, PSMD = peak width of skeletonized MD, WMH = white matter hyperintensity.

post-SARS-CoV-2 individuals were stratified by recruitment route (*SI Appendix*).

Discussion

We investigated brain structural alterations and neuropsychological sequelae in a large sample of individuals who recovered from mainly mild to moderate COVID-19. At median 289 d after the acute infection, these individuals showed significantly higher average free water and MD in the white matter compared to matched healthy controls. In contrast, cortical thickness and markers of cerebral small vessel disease were not significantly different between groups. In addition, white matter diffusion indices successfully predicted a past SARS-CoV-2 infection. We did not detect neuropsychological deficits in post-SARS-CoV-2 individuals. Collectively, our study suggests that a mild to moderate SARS-CoV-2 infection is associated with subtle microstructural alterations in the cerebral white matter beyond the stage of acute infection.

A key aspect of COVID-19 neuropathology appears to be the dynamic response of the intrathecal immune system to the virus. Evidence of neuroinflammation was reported in histopathological and clinical studies of COVID-19 patients: virus invasion (24, 25), activation of glial cells (9, 26, 27), and a cytokine response in the cerebrospinal fluid accompanying neurological and psychiatric COVID-19 symptoms (10). In our study, we observed widespread increases of extracellular free water and MD in post-SARS-CoV-2 individuals encompassing all brain lobes. Supplementary analyses showed that these increases relate to approximately 7 "years of healthy aging" indicating a biologically relevant effect. Both free water and MD are sensitive to an activated immune response causing excessive extracellular free water and thus increased diffusivity (28–30). More specifically, microglia and astrocytes emit cytokines upon activation, inducing osmosis of water from the blood into the extracellular space (31, 32). Interestingly, endothelial dysfunction and subsequent vascular leakage due to persistent immune activation have been previously implicated in the pathophysiology of COVID-19 (33, 34). Taken together, it is conceivable that the observed increase in free water and MD could be an indirect sign of a prolonged neuroinflammatory reaction to a SARS-CoV-2 infection. Nevertheless, other possible mechanisms for changes in the extracellular space need to be considered.

Volume increases in the extracellular compartment might be accompanied by structural damage like demyelination as well as axonal disruption secondary to neuroinflammation. Free-water corrected diffusion markers enable further guidance in microstructural interpretations. While analyses of overall mean values showed no significant group differences in free-water corrected FA_T, voxel-wise statistics identified increased FA_T in corresponding frontal areas of post-SARS-CoV-2 individuals. Yet, these changes included only ~3% of the white matter skeleton, indicating either subtle or spatially limited effects localized to association tracts. Normal to increased FA_T in the presence of elevated free water suggests minor microstructural alterations like axonal compression or displacement rather than damage to myelin sheaths or axons which would rather lead to FA_T decreases (21). Moreover, fixel markers, which also model properties of the tissue compartment (35, 36), did not show group differences averaged across the entire white matter skeleton. Thus, in contrast to previous work demonstrating more widespread FA reductions in small samples of hospitalized COVID-19 cases (37–39), our findings suggest that white matter changes following a mild to moderate SARS-CoV-2 infection most likely reflect subtle increases in extracellular free water as opposed to structural neural damage.

Based on previous histopathological reports of vasculopathy in COVID-19 and higher ACE-2 expression in cells of the blood–brain barrier, we hypothesized that post-SARS-CoV-2 individuals would show alterations in imaging markers of small vessel disease burden (14). However, in our study, WMH (white matter hyperintensity) load was not significantly different, indicating that a mild to moderate course of COVID-19 does not lead to visually accessible vascular lesions (WMH) as previously reported (40). PSMD, an established imaging marker of small vessel disease more sensitive to microstructural changes (23), showed nominally higher values in post-SARS-CoV-2 individuals, but differences did not survive Bonferroni correction. Taken together, follow-up investigations are needed to understand whether subtle long-term vascular impairments will eventually increase the prevalence of cerebrovascular disease among COVID-19 convalescents (33).

Alterations of cortical gray and white matter commonly co-occur in neurological diseases (41, 42). Notably, this was not the case in our study. This is contrasted by a recent report on mildly affected COVID-19 subjects in the UK Biobank demonstrating longitudinal volumetric reductions in the gray matter in olfactory networks (11). On the other hand, a current cross-sectional study has shown gray matter volume increases in long-COVID patients compared to healthy controls (43). The discrepancies between these studies and our work may be due to general differences in recruitment strategies (general population vs enriched samples of individuals suffering from long-term sequelae) and study designs (longitudinal vs. cross-sectional), both of which likely affect the sensitivity to detect gray matter changes associated with a SARS-CoV-2 infection.

By providing scores of prediction accuracy, our machine learning analysis evaluated brain imaging markers for their diagnostic relevance. Logistic regression models based on free water and MD achieved a considerable accuracy of ~80% in predicting a past SARS-CoV-2 infection, outperforming other imaging markers under study. Of note, cortical thickness achieved the lowest

accuracy, not significantly differing from prediction by chance. The difference in accuracy between diffusion metrics and cortical thickness might highlight that in mild to moderate COVID-19, pathophysiological aspects are better detected by diffusion imaging–based techniques. Finally, the higher accuracy of fiber cross-section compared to cortical thickness—both morphometric measures—might imply that COVID-19-associated alterations preferably occur in the white matter.

We want to emphasize that our results represent average effects, i.e., not every mild to moderate affected COVID-19 patient may exhibit the reported changes. In addition, our results are based on a nonvaccinated cohort. As vaccination has been repetitively demonstrated to be a highly effective measure against COVID-19, vaccinated patients possibly exhibit less of the pathophysiological substrates identified in our study (44).

It is important to put the observed brain white matter alterations into a clinical perspective. Reported persisting clinical sequelae of COVID-19 include executive dysfunction, anxiety, depression, fatigue, muscle weakness, and sleep impairment (11, 45–47). In contrast, we found no significant difference for any cognitive domain, depression, anxiety, and neurological symptoms between groups. Similar to our previous finding in a larger, yet overlapping sample (1), nominally, post-SARS-CoV-2 individuals showed even better performances in MMSE, CDT, and VF compared to matched controls. Besides the absence or mild expression of the respective symptoms, other reasons, such as our relatively long follow-up period and a potential selection bias of highly motivated post-SARS-CoV-2 participants, as well as differing degrees of social deprivation as a result of country-specific pandemic control measures, may explain the discrepancy with other studies. Exploration of imaging–behavior interactions showed that relatively increased free water and MD were associated with worse executive performance (TMT-A/B), working memory (WLR), and VF in post-SARS-CoV-2 individuals, thus providing a preliminary pathophysiological link between neurocognitive deficits and brain alterations in individuals recovered from COVID-19. Clearly, more research is needed to increase our understanding of factors underlying the persistence of neurological symptoms in a subgroup of COVID-19 patients.

Strengths of this work lie in its considerable sample size; high-quality imaging and phenotypical data; a robust and reproducible image processing pipeline; the investigation happening at an early stage of the pandemic, potentially alleviating the problem of different COVID-19 strains and vaccinations as confounders; and a conservative statistical correction scheme to reduce the false-positive rate.

However, our study also exhibits limitations. Our investigation lacks information about SARS-CoV-2 strains as well as precise disease severity stratification beyond the self-reported information on hospitalization and subjective perception of disease intensity. In addition, we follow a cross-sectional observational study design unable to fully address premorbid group differences despite a rigorous matching procedure and insufficient to infer causality. Future longitudinal studies could not only elaborate on the trajectory of the identified microstructural white matter alterations but also address the question whether these findings are markers of increased susceptibility for the development of neurological sequelae. Finally, our correction scheme for multiple testing may not only be regarded as a study strength but also as overly conservative, considering the potential statistical dependencies between variables. We opted for this strategy, as we prioritized the minimization of false-positive findings. Nevertheless, we did report uncorrected P values and recognized nominal group differences in clinical and imaging markers to encourage future hypothesis-driven studies on neurological manifestations of COVID-19 with less conservative approaches.

We performed a comprehensive assessment of established neuroimaging markers for structural neural integrity to characterize neurobiological changes potentially underlying postacute COVID-19 neuropsychological sequelae after a mainly mild to moderate disease course. Our findings support the notion of a prolonged neuroinflammatory response indicated by subtle but widespread increases in extracellular free water and mean diffusivity in the white matter of COVID-19 convalescents. In contrast, we did not observe signs of cortical atrophy or macrostructural vascular damage. Importantly, despite identifying this characteristic imaging footprint, the investigated sample exhibited no marked neuropsychological symptoms 10 mo after SARS-CoV-2 infection. External validation and longitudinal investigations are needed to further clarify the clinical relevance of our findings.

Materials and Methods

Study Population. We examined participants of the HCHS COVID Program. A detailed description of the study design has been published previously (1). Post-SARS-CoV-2 participants 1] had a positive PCR test for SARS-CoV-2 and 2] were aged between 45 and 74 y at inclusion. Recruitment routes included both invitation upon laboratory-confirmed SARS-CoV-2 infection and self-referral of participants following newspaper announcement. Subsequent to recruitment, the participants underwent the study protocol of the HCHS (48)–including cranial MR imaging, neuropsychological testing, and a self-report questionnaire on COVID-19-associated symptoms. In addition, a healthy control group was sampled from the original HCHS cohort which was assessed prior to the SARS-CoV-2 pandemic (48). The previously reported matching procedure (1) considered confounders allowing for a comprehensive investigation of COVID-19 pathophysiology in multiple organ systems beyond the brain, including the lungs, heart, vasculature, and kidneys. In contrast to the previous procedure, we performed a 1:1 propensity score matching specifically accounting for confounds known to affect cognitive performance as well as indices derived from structural and diffusion MR imaging: the groups were matched for age, sex, and years of education as well as for the prevalence of arterial hypertension, diabetes mellitus, dyslipidemia, and smoking behavior using the matchit (v4.3.3) R package (49).

Ethics Approval. The local ethics committee of the Landesärztekammer Hamburg (State of Hamburg Chamber of Medical Practitioners, PV5131) approved the study, and written informed consent was obtained from all participants (1, 50).

Clinical Assessments. Cognitive testing was performed by a trained study nurse and included the MMSE (51), TMT-A/B (52), VF, and WLR subtests of the Consortium to Establish a Registry for Alzheimer's Disease Neuropsychological Assessment Battery (CERAD-Plus) (53), as well as the CDT (54). Psychosocial symptom burden was evaluated by the GAD-7 (anxiety) (55) and PHQ-9 (depression) (56). Moreover, self-reported neurological symptoms (headache, dizziness, fatigue, and sleep disturbances) were assessed by part of the PHQ-15 (57).

Brain Imaging. Image acquisitions have been described in detail before (50). Put briefly, 3D T1-weighted rapid acquisition gradient-echo sequence (MPRAGE, 0.83 × 0.83 × 0.94 mm), 3D T2-weighted FLAIR (0.75 × 0.75 × 0.9 mm), and single-shell diffusion MRI (2 × 2 × 2 mm, 64 noncollinear gradient directions, b = 1,000 s/mm^2) were acquired on a single 3T Siemens Skyra MRI scanner (Siemens, Erlangen, Germany). Detailed parameters can be found in *SI Appendix*.

An overview of the derived imaging markers for the gray and white matter can be found in Fig. 1. For a detailed account on image preprocessing, derivation of morphometric and diffusion indices, and QA, please refer to *SI Appendix* (58).

Following preprocessing, we derived conventional DTI markers of white matter microstructure, i.e., FA and MD, which have been extensively used in neuroscientific and neuropsychological research (59, 60). Free-water imaging was employed to model an extracellular free-water compartment, sensitive to immune activation (61) and atrophy (62), as well as a cellular tissue compartment (FA_T), more closely reflecting myelin and axonal alterations than their DTI equivalents (28). Fixel-based analysis, a multitissue model addressing more complex white matter

compositions, was used to derive metrics of fiber density, fiber-bundle cross-section (FC), fiber density and cross-section (FDC), and complexity (63). For further statistical analysis, diffusion markers were averaged across a representative skeleton of the entire white matter derived by tract-based spatial statistics as well as within 71 anatomical white matter fiber tracts reconstructed with TractSeg (64, 65). Finally, PSMD, a surrogate marker of cerebral small vessel disease, was calculated (23).

After cortical surface reconstruction with the Computational Anatomy Toolbox for SPM (CAT12), mean cortical thickness was estimated as a proxy for neurodegenerative processes (20, 66, 67). Normalized volumes of white matter hyperintensities (WMH load) were obtained by FSL's Brain Intensity AbNormality Classification Algorithm (BIANCA) with LOCally Adaptive Threshold Estimation (LOCATE) (68, 69).

Statistical Analysis. All statistical analyses were conducted in Python 3.9.1 (70, 71), CAT12 (66, 67, 72), as well as mrclusterstats (73). Statistical tests were two sided, with a $P < 0.05$ as significance threshold. In the case of averaged imaging and clinical data, *P* values were adjusted by Bonferroni correction for 11 and 9 comparisons, respectively. We chose this conservative correction scheme in order to minimize the possibility of false-positive findings. Additionally, sensitivity analyses were performed by 1] excluding post-SARS-CoV-2 individuals who had been hospitalized, and 2] stratifying the post-SARS-CoV-2 group by recruitment strategy, following the same procedures as described above.

Phenotypical data. Sample characteristics were compared between healthy controls and post-SARS-CoV-2 participants using χ^2 tests (binary) and two-sample *t* tests (continuous). Clinical variables were compared between groups in separate analyses of covariance (ANCOVA) adjusted for age, sex, and education.

Imaging. Statistical analysis of imaging parameters was conducted in two steps. First, global measures, i.e., mean skeletonized diffusion parameters, mean cortical thickness, WMH load, and PSMD, were compared between post-SARS-CoV-2 individuals and healthy controls in separate ANCOVAs, adjusted for age, sex, and education. In the case of FC and FDC, total intracranial volume served as an additional covariate. Next, in an effort to interrogate spatial patterns of brain structural alterations associated with a mild to moderate SARS-CoV-2 infection, we performed whole-brain voxel-wise permutation-based testing for skeletonized diffusion markers. Utilizing the same design matrices as in the ANCOVAs, we employed 5,000 permutations, threshold-free cluster enhancement, and family-wise error correction across multiple hypotheses. We supplemented voxel-wise statistics with a tract of interest approach by performing abovementioned ANCOVAs on the level of TractSeg-derived anatomical white matter tracts. Here, *P* values were adjusted by Bonferroni correction for 71 comparisons. Vertex-wise cortical thickness was statistically analyzed in a general linear model as implemented in CAT12 with family-wise error correction and a cluster threshold of 10.

Associations between clinical and imaging data. In case of significant group differences of averaged imaging markers, we performed exploratory regression analyses testing for associations between these imaging markers and neuropsychological scores in the entire sample. Moreover, group × imaging marker interactions were included in the regression model, and post hoc Spearman correlations were conducted for each group separately. As imaging markers are known to change as a function of age, we performed additional regression analyses with age in the matched control group to derive beta estimates for conversion of group differences in units of "years of healthy aging" in order to aid biological interpretation of our results. As we deemed these analyses exploratory, no correction for multiple comparisons was performed.

Machine Learning Prediction. To further evaluate their predictive capacities, all brain imaging markers calculated in the study were averaged within regions of interest where applicable (Desikan–Killiany cortical atlas parcels and TractSeg-derived anatomical white matter tracts) and propagated to a comparative supervised machine learning pipeline (scikit-learn v1.0.2) (65, 74, 75). Per marker, multivariate logistic regression models were trained to predict past COVID-19. Models were scored with prediction accuracy, and statistical significance was assessed via comparison to null model predictions. Further details are provided in *SI Appendix*.

Data, Materials, and Software Availability. Analysis codes and processed global imaging parameters data have been deposited in GitHub (See *SI Appendix*, Table S12; https://github.com/csi-hamburg/2022_petersen_naegele_postcovid_imaging/blob/main/global_imaging_markers.csv) (76). Personalized data from individual participants of the HCHS are not publicly available due to data protection regulations, but anonymized data can be accessed by interested researchers via a request to the HCHS steering committee based on a material transfer agreement.

ACKNOWLEDGMENTS. We wish to acknowledge all participants of the HCHS and cooperation partners, patrons, and the Deanery from the University Medical Center Hamburg–Eppendorf for supporting the HCHS. Special thanks apply to the staff at the Epidemiological Study Center for conducting the study. The participating institutes and departments from the University Medical Center Hamburg-Eppendorf contribute all with individual and scaled budgets to the overall funding. The HCHS is also supported by Amgen, Astra Zeneca, Bayer, BASF, Deutsche Gesetzliche Unfallversicherung, Deutsches Institut für Ernährungsforschung, the Innovative medicine initiative under grant number 116074 and the Fondation Leducq under grant number 16 CVD 03., Novartis, Pfizer, Schiller, Siemens, Unilever, and "Förderverein zur Förderung der HCHS e.V.". This work was funded by the Deutsche Forschungsgemeinschaft (DFG, German Research Foundation–SFB 936–178316478–C2 (M.P., F.L.N., C.M., G.T., and B.C.) and C7 (J.G. and S.K.) and SPP 204–454012190. This publication has been approved by the Steering Board of the HCHS.

Author affiliations: [a]Department of Neurology, University Medical Center Hamburg-Eppendorf, 20251 Hamburg, Germany; [b]Department of Cardiology, University Heart and Vascular Center, 20251 Hamburg, Germany; [c]Population Health Research Department, University Heart and Vascular Center, 20251 Hamburg, Germany; [d]Department of Psychiatry and Psychotherapy, University Medical Center Hamburg-Eppendorf, 20251 Hamburg, Germany; [e]Department of Neuroradiology, University Medical Center Hamburg-Eppendorf, 20251 Hamburg, Germany; [f]Department of Psychiatry, Brigham and Women's Hospital, Harvard Medical School, 202115 Boston, MA; [g]Department of Radiology, Brigham and Women's Hospital, Harvard Medical School, 202 Boston, MA; [h]Institute of Neuropathology, University Center Hamburg-Eppendorf, Hamburg, 20251 Gemany; [i]German Center for Cardiovascular Research, Partner site Hamburg/Kiel/Luebeck, 20251 Hamburg, Germany; and [j]University Center of Cardiovascular Science, University Heart and Vascular Center, 202115 Hamburg, Germany

Author contributions: M.P., F.L.N., G.T., and B.C. designed research; M.P., F.L.N., C.M., M.S., E.P., S.K., J.G., J.F., O.P., J.M., M.G., R.T., C.G., G.T., and B.C. performed research; M.P., F.L.N., C.M., M.S., E.P., and O.P. contributed new reagents/analytic tools; M.P. and F.L.N. analyzed data; G.T. and B.C. funding; and M.P., F.L.N., C.M., M.S., E.P., S.K., J.G., J.F., O.P., J.M., M.G., R.T., C.G., G.T., and B.C. wrote the paper.

Competing interest statement: J.G. has received speaker fees from Lundbeck, Janssen-Cilag, Lilly, Otsuka, and Boehringer outside the submitted work. J.F. reported receiving personal fees from Acandis, Cerenovus, Microvention, Medtronic, Phenox, and Penumbra; receives grants from Stryker and Route 92; is managing director of eppdata; and owns shares in Tegus and Vastrax, all outside the submitted work. C.G. reports personal fees from Abbott, Amgen, Bayer, Boehringer Ingelheim, Daiichi Sankyo, GlaxoSmithKline, Novartis, and Prediction Biosciences, outside the submitted work. G.T. has received fees as consultant or lecturer from Acandis, Alexion, Amarin, Bayer, Boehringer Ingelheim, BristolMyersSquibb/Pfizer, Daichi Sankyo, Portola, and Stryker, outside the submitted work. The remaining authors declare no conflicts of interest.

1. E. L. Petersen *et al.*, Multi-organ assessment in mainly non-hospitalized individuals after SARS-CoV-2 infection: The hamburg city health study COVID programme. *Eur. Heart J.* **43**, 1124–1137 (2022).
2. Y. Su *et al.*, Multiple early factors anticipate post-acute COVID-19 sequelae. *Cell* **185**, 881–895.e20 (2022).
3. B. Raman *et al.*, Medium-term effects of SARS-CoV-2 infection on multiple vital organs, exercise capacity, cognition, quality of life and mental health, post-hospital discharge. *EClinicalMedicine* **31**, 100683 (2021).
4. S. Mehandru, M. Merad, Pathological sequelae of long-haul COVID. *Nat. Immunol.* **23**, 194–202 (2022).
5. M. Ramos-Casals, P. Brito-Zerón, X. Mariette, Systemic and organ-specific immune-related manifestations of COVID-19. *Nat. Rev. Rheumatol.* **17**, 315–332 (2021).
6. A. Nalbandian *et al.*, Post-acute COVID-19 syndrome. *Nat. Med.* **27**, 601–615 (2021).
7. M. Taquet, J. R. Geddes, M. Husain, S. Luciano, P. J. Harrison, 6-month neurological and psychiatric outcomes in 236 379 survivors of COVID-19: A retrospective cohort study using electronic health records. *Lancet Psychiatry* **8**, 416–427 (2021).
8. A. Hampshire *et al.*, Cognitive deficits in people who have recovered from COVID-19. *EClinicalMedicine* **39**, 101044 (2021).
9. J. Matschke *et al.*, Neuropathology of patients with COVID-19 in Germany: A post-mortem case series. *Lancet Neurol.* **19**, 919–929 (2020).
10. O. M. Espíndola *et al.*, Inflammatory cytokine patterns associated with neurological diseases in Coronavirus Disease 2019. *Ann. Neurol.* **89**, 1041–1045 (2021).
11. G. Douaud *et al.*, SARS-CoV-2 is associated with changes in brain structure in UK Biobank. *Nature* **604**, 697–707 (2022).
12. I. I. Ismail, S. Salama, Association of CNS demyelination and COVID-19 infection: An updated systematic review. *J. Neurol.* **269**, 541–576 (2022).
13. M. G. Savelieff, E. L. Feldman, A. M. Stino, Neurological sequela and disruption of neuron-glia homeostasis in SARS-CoV-2 infection. *Neurobiol. Dis.* **168**, 105715 (2022).
14. J. Wenzel *et al.*, The SARS-CoV-2 main protease Mpro causes microvascular brain pathology by cleaving NEMO in brain endothelial cells. *Nat. Neurosci.* **24**, 1522–1533 (2021).

15. L.-A. Teuwen, V. Geldhof, A. Pasut, P. Carmeliet, COVID-19: The vasculature unleashed. *Nat. Rev. Immunol.* **20**, 389–391 (2020).
16. R. Manca, M. De Marco, P. G. Ince, A. Venneri, Heterogeneity in regional damage detected by neuroimaging and neuropathological studies in older adults with COVID-19: A cognitive-neuroscience systematic review to inform the long-term impact of the virus on neurocognitive trajectories. *Front. Aging Neurosci.* **13**, 646908 (2021).
17. S. Kremer, Neuroimaging in patients with COVID-19: A neuroradiology expert group consensus. *Eur. Radiol.* **32**, 3716–3725 (2022), 10.1007/s00330-021-08499-0 (12 April 2022).
18. S. G. Kandemirli *et al.*, Brain MRI findings in patients in the intensive care unit with COVID-19 infection. *Radiology* **297**, E232–E235 (2020).
19. S. Katal, S. Balakrishnan, A. Gholamrezanezhad, Neuroimaging and neurologic findings in COVID-19 and other coronavirus infections: A systematic review in 116 patients. *J. Neuroradiol.* **48**, 43–50 (2021).
20. C. R. Jack *et al.*, Tracking pathophysiological processes in Alzheimer's disease: An updated hypothetical model of dynamic biomarkers. *Lancet Neurol.* **12**, 207–216 (2013).
21. Y. Assaf, O. Pasternak, Diffusion tensor imaging (DTI)-based white matter mapping in brain research: A review. *J. Mol. Neurosci.* **34**, 51–61 (2008).
22. J. M. Wardlaw, C. Smith, M. Dichgans, Small vessel disease: Mechanisms and clinical implications. *Lancet Neurol.* **18**, 684–696 (2019).
23. E. Baykara *et al.*, A novel imaging marker for small vessel disease based on skeletonization of white matter tracts and diffusion histograms. *Ann. Neurol.* **80**, 581–592 (2016).
24. J. Meinhardt *et al.*, Olfactory transmucosal SARS-CoV-2 invasion as a port of central nervous system entry in individuals with COVID-19. *Nat. Neurosci.* **24**, 168–175 (2021).
25. R. Butowt, K. Bilinska, SARS-CoV-2: Olfaction, brain infection, and the urgent need for clinical samples allowing earlier virus detection. *ACS Chem. Neurosci.* **11**, 1200–1203 (2020).
26. M.-E. Tremblay, C. Madore, M. Bordeleau, L. Tian, A. Verkhratsky, Neuropathobiology of COVID-19: The role for Glia. *Front. Cell Neurosci.* **14**, 592214 (2020).
27. M. Schwabenland *et al.*, Deep spatial profiling of human COVID-19 brains reveals neuroinflammation with distinct microanatomical microglia-T-cell interactions. *Immunity* **54**, 1594–1610.e11 (2021).
28. O. Pasternak, N. Sochen, Y. Gur, N. Intrator, Y. Assaf, Free water elimination and mapping from diffusion MRI. *Magn. Reson. Med.* **62**, 717–730 (2009).
29. O. Pasternak *et al.*, Excessive extracellular volume reveals a neurodegenerative pattern in schizophrenia onset. *J. Neurosci.* **32**, 17365–17372 (2012).
30. Y. Wang *et al.*, Quantification of increased cellularity during inflammatory demyelination. *Brain* **134**, 3590–3601 (2011).
31. M. Schwartz, O. Butovsky, W. Brück, U.-K. Hanisch, Microglial phenotype: Is the commitment reversible? *Trends Neurosci.* **29**, 68–74 (2006).
32. E. Syková, C. Nicholson, Diffusion in brain extracellular space. *Physiol. Rev.* **88**, 1277–1340 (2008).
33. F. W. Chioh *et al.*, Convalescent COVID-19 patients are susceptible to endothelial dysfunction due to persistent immune activation. *Elife* **10**, e64909 (2021).
34. S. Krasemann *et al.*, The blood-brain barrier is dysregulated in COVID-19 and serves as a CNS entry route for SARS-CoV-2. *Stem Cell Rep.* **17**, 307–320 (2021), 10.2139/ssrn.3828200 (15 June 2022).
35. T. Dhollander *et al.*, Fixel-based analysis of diffusion MRI: Methods, applications. Challenges and opportunities. *Neuroimage* **241**, 118417 (2021).
36. M. Petersen *et al.*, Fixel based analysis of white matter alterations in early stage cerebral small vessel disease. *Sci. Rep.* **12**, 1581 (2022).
37. V. F. J. Newcombe *et al.*, Neuroanatomical substrates of generalized brain dysfunction in COVID-19. *Intensive Care Med.* **47**, 116–118 (2021).
38. Y. Qin *et al.*, Long-term microstructure and cerebral blood flow changes in patients recovered from COVID-19 without neurological manifestations. *J. Clin. Invest.* **131**, 147329 (2021).
39. S. Huang *et al.*, Persistent white matter changes in recovered COVID-19 patients at the 1-year follow-up. *Brain* **145**, 1830–1838 (2021).
40. L. Griffanti *et al.*, Adapting the UK biobank brain imaging protocol and analysis pipeline for the C-MORE multi-organ study of COVID-19 survivors. *Front. Neurol.* **12**, 753284 (2021).
41. L. Conforti, J. Gilley, M. P. Coleman, Wallerian degeneration: An emerging axon death pathway linking injury and disease. *Nat. Rev. Neurosci.* **15**, 394–409 (2014).
42. A. B. Storsve, A. M. Fjell, A. Yendiki, K. B. Walhovd, Longitudinal changes in white matter tract integrity across the adult lifespan and its relation to cortical thinning. *PLoS One* **11**, e0156770 (2016).
43. B. Besteher *et al.*, Larger gray matter volumes in neuropsychiatric long-COVID syndrome. *Psychiatry Res.* **317**, 114836 (2022).
44. D. R. Feikin *et al.*, Duration of effectiveness of vaccines against SARS-CoV-2 infection and COVID-19 disease: Results of a systematic review and meta-regression. *Lancet* **399**, 924–944 (2022).
45. A. Carfì, R. Bernabei, F. Landi; Gemelli Against COVID-19 Post-Acute Care Study Group, Persistent symptoms in patients after acute COVID-19. *JAMA* **324**, 603–605 (2020).
46. C. Huang *et al.*, 6-month consequences of COVID-19 in patients discharged from hospital: A cohort study. *Lancet* **397**, 220–232 (2021).
47. Z. Al-Aly, Y. Xie, B. Bowe, High-dimensional characterization of post-acute sequelae of COVID-19. *Nature* **594**, 259–264 (2021).
48. A. Jagodzinski, U. Koch-gromus, G. Adam, S. Anders, M. Augustin, Rationale and design of the hamburg city health study. *Eur. J. Epidemiol.* **35**, 169–181 (2019), 10.1007/s10654-019-00577-4.
49. D. Ho, K. Imai, G. King, E. A. Stuart, MatchIt: Nonparametric preprocessing for parametric causal inference. *J. Stat. Softw.* **42**, 1–28 (2011).
50. M. Petersen *et al.*, Network localisation of white matter damage in cerebral small vessel disease. *Sci. Rep.* **10**, 9210 (2020).
51. M. F. Folstein, S. E. Folstein, P. R. McHugh, "Mini-mental state". A practical method for grading the cognitive state of patients for the clinician. *J. Psychiatr. Res.* **12**, 189–198 (1975).
52. T. Tombaugh, Trail making test A and B: Normative data stratified by age and education. *Arch. Clin. Neuropsychol.* **19**, 203–214 (2004).
53. J. C. Moms *et al.*, The consortium to establish a registry for Alzheimer's Disease (CERAD). Part I. Clinical and neuropsychological assesment of Alzheimer's disease. *Neurology* **39**, 1159–1159 (1989).
54. K. I. Shulman, Clock-drawing: Is it the ideal cognitive screening test? *Int. J. Geriatr. Psychiatry* **15**, 548–561 (2000).
55. R. L. Spitzer, K. Kroenke, J. B. W. Williams, B. Löwe, A brief measure for assessing generalized anxiety disorder: The GAD-7. *Arch. Intern. Med.* **166**, 1092 (2006).
56. K. Kroenke, R. L. Spitzer, J. B. W. Williams, The PHQ-9: Validity of a brief depression severity measure. *J. Gen. Intern. Med.* **16**, 606–613 (2001).
57. K. Kroenke, R. L. Spitzer, J. B. W. Williams, The PHQ-15: Validity of a new measure for evaluating the severity of somatic symptoms. *Psychosom. Med.* **64**, 258–266 (2002).
58. M. Cieslak *et al.*, QSIPrep: An integrative platform for preprocessing and reconstructing diffusion MRI data. *Nat. Methods* **18**, 775–778 (2021).
59. R. J. Cannistraro *et al.*, CNS small vessel disease: A clinical review. *Neurology* **92**, 1146–1156 (2019).
60. K. Kamagata *et al.*, Diffusion magnetic resonance imaging-based biomarkers for neurodegenerative diseases. *Int. J. Mol. Sci.* **22**, 5216 (2021).
61. M. A. Di Biase *et al.*, Large-scale evidence for an association between peripheral inflammation and white matter free water in schizophrenia and healthy individuals. *Schizophr. Bull.* **47**, 542–551 (2021).
62. E. Ofori *et al.*, Free-water imaging of the hippocampus is a sensitive marker of Alzheimer's disease. *Neuroimage Clin.* **24**, 101985 (2019).
63. T. Dhollander *et al.*, Fixel-based analysis of diffusion MRI: Methods, applications. Challenges and opportunities. *Neuroimage* **241**, 118417 (2021).
64. S. M. Smith *et al.*, Tract-based spatial statistics: Voxelwise analysis of multi-subject diffusion data. *Neuroimage* **31**, 1487–1505 (2006).
65. J. Wasserthal, P. Neher, K. H. Maier-Hein, TractSeg–Fast and accurate white matter tract segmentation. *Neuroimage* **183**, 239–253 (2018).
66. R. Dahnke, R. A. Yotter, C. Gaser, Cortical thickness and central surface estimation. *Neuroimage* **65**, 336–348 (2013).
67. C. Gaser *et al.*, CAT–A computational anatomy toolbox for the analysis of structural MRI data. bioRxiv [Preprint] (2022). https://doi.org/10.1101/2022.06.11.495736 (Accessed 13 June 2022).
68. L. Griffanti *et al.*, BIANCA (Brain Intensity AbNormality Classification Algorithm): A new tool for automated segmentation of white matter hyperintensities. *Neuroimage* **141**, 191–205 (2016).
69. V. Sundaresan *et al.*, Automated lesion segmentation with BIANCA: Impact of population-level features, classification algorithm and locally adaptive thresholding. *Neuroimage* **202**, 116056 (2019).
70. R. Vallat, Pingouin: Statistics in Python. *JOSS* **3**, 1026 (2018).
71. P. Virtanen *et al.*, SciPy 1.0: Fundamental algorithms for scientific computing in Python. *Nat. Methods* **17**, 261–272 (2020).
72. R. A. Yotter, R. Dahnke, P. M. Thompson, C. Gaser, Topological correction of brain surface meshes using spherical harmonics. *Hum. Brain Mapp.* **32**, 1109–1124 (2011).
73. J.-D. Tournier *et al.*, MRtrix3: A fast, flexible and open software framework for medical image processing and visualisation. *Neuroimage* **202**, 116137 (2019).
74. A. Abraham *et al.*, Machine learning for neuroimaging with scikit-learn. *Front Neuroinform.* **8**, 14 (2014).
75. R. S. Desikan *et al.*, An automated labeling system for subdividing the human cerebral cortex on MRI scans into gyral based regions of interest. *Neuroimage* **31**, 968–980 (2006).
76. M. Petersen *et al.*, Global imaging *markers*. *Github*. https://github.com/csi-hamburg/2022_petersen_naegele_postcovid_imaging/blob/main/global_imaging_markers.csv. Accessed 21 April 2023.